



Mapping Millimetre-Scale Ground Deformation Over the Frank Slide and South Peak of Turtle Mountain, Alberta, Using Spaceborne InSAR Technology

Mapping Millimetre-Scale Ground Deformation over the Frank Slide and South Peak of Turtle Mountain, Alberta, Using Spaceborne InSAR Technology

S. Mei¹, V. Poncos² and C. Froese¹

¹Alberta Energy Resources Conservation Board/Alberta
Geological Survey

²Canadian Centre for Remote Sensing

August 2008

©Her Majesty the Queen in Right of Alberta, 2008
ISBN 0-7785-3859-1

The Energy Resources Conservation Board/Alberta Geological Survey (ERCB/AGS) and its employees and contractors make no warranty, guarantee or representation, express or implied, or assume any legal liability regarding the correctness, accuracy, completeness or reliability of this publication. Any digital data and software supplied with this publication are subject to the licence conditions. The data are supplied on the understanding that they are for the sole use of the licensee, and will not be redistributed in any form, in whole or in part, to third parties. Any references to proprietary software in the documentation, and/or any use of proprietary data formats in this release, do not constitute endorsement by the ERCB/AGS of any manufacturer's product.

When using information from this publication in other publications or presentations, due acknowledgment should be given to the ERCB/AGS. The following reference format is recommended:

Mei S., Poncos V. and Froese C. (2008): Mapping millimetre-scale ground deformation over the Frank Slide and South Peak of Turtle Mountain, Alberta, using spaceborne InSAR technology; Alberta Energy Resources Conservation Board, ERCB/AGS Earth Sciences Report 2007-09, 126 p.

Author address:

V. Poncos
Canada Centre for Remote Sensing
588 Booth Street
Ottawa, ON K1A 0Y7
(613) 947-1237
E-mail: vponcos@nrcan.gc.ca

Published August 2008 by:

Alberta Energy Resources Conservation Board
Alberta Geological Survey
4th Floor, Twin Atria Building
4999 – 98th Avenue
Edmonton, Alberta
T6B 2X3
Canada

Tel: (780) 422-1927
Fax: (780) 422-1918
E-mail: AGS-Info@ercb.ca
Website: www.ags.gov.ab.ca

Contents

Acknowledgments	vii
Abstract	viii
1 Introduction	1
2 InSAR Background	3
3 Data	4
3.1 Radarsat-1 Data.....	4
3.2 Digital Elevation Model (DEM) Data.....	9
4 CTM Processing Steps and Workflow	9
4.1 Selection of Input Data.....	11
4.2 Interferometric Processing	12
4.3 CTM Analysis	13
4.4 Statistical Evaluation of CTM Targets.....	21
4.4.1 Statistical Evaluation of Individual CTM Targets.....	21
4.4.2 Geostatistical Evaluation for Regional Deformation Pattern	24
5 Results and Interpretation	27
5.1 Overview of Deformation Processes.....	27
5.2 Ground Movement near South Peak/Saddle.....	32
5.3 Ground Movements in the Lower South Peak Area	39
5.4 Ground Movement in the Upper Slope of the Frank Slide.....	44
5.5 Ground Movement in the Lower Portion of the Frank Slide/Valley Bottom	47
6 Conclusions and Discussions	53
7 References	61
Appendix A: InSAR Theoretical Background	63
Appendix B: Interferograms and Coherence Maps	74

Tables

Table 1	Radarsat-1 sensor parameters	4
Table 2	Radarsat-1 imaging beam modes	5
Table 3	Radarsat-1 SLC data used by the present study and precipitation on the acquisition day.....	6
Table 4	Differential InSAR runs created and the respective perpendicular baselines	11
Table 5	Biases/offsets determined manually for co-registration referring to the master pixel (3469.84P, 5412.84L).....	12
Table 6	Parameters used for correction of the baseline–target geometry	13
Table 7	CTM targets identified for the lower South Peak area	41
Table 8	CTM targets identified in the lower portion of the upper slope of the Frank Slide	46
Table 9	Temporal and spatial correlation properties of phase components in PS-InSAR	68

Figures

Figure 1	Location map showing the Frank Slide on the eastern slope of Turtle Mountain, Alberta, Canada.....	2
Figure 2	RADARSAT-1 beam modes and beam positions	5
Figure 3	Perspective views of Turtle Mountain–Frank Slide generated using LiDAR DEM with a vertical exaggeration of two times	7
Figure 4	Perspective views of Turtle Mountain–Frank Slide generated using LiDAR DEM, with a vertical exaggeration of two times	8
Figure 5	Sunshade relief image showing the perspective view of the full feature LiDAR DEM.....	9

Figure 6	CTM control panel showing the processing chain.....	10
Figure 7	ROI selection window showing the CTM analysis AOI (yellow) and atmospheric correction ROI (red rectangle), displayed in the slant range coordinates.....	14
Figure 8	Average backscatter image generated by CTM analysis.....	15
Figure 9	Temporal coherence image generated by CTM analysis.....	16
Figure 10	DEM error image generated by CTM analysis.....	17
Figure 11	Deformation rate image generated by CTM analysis.....	18
Figure 12	Deformation rates for the CTM targets defined with a temporal coherence threshold value of 0.65.....	19
Figure 13	An example of plots showing the deformation model (averaging annual deformation), time series of wrapped phase, time series of unwrapped phase and deformation profile associated with a single target.....	20
Figure 14	An example of plots showing the deformation model (averaging annual deformation), time series of wrapped phase, time series of unwrapped phase and deformation profile associated with the same target shown in Figure 13.....	21
Figure 15	Crossplot of the temporal coherence and the standard error of the slope of the regression for the unwrapped phases for each CTM target identified with a temporal coherence threshold value of 0.65.....	22
Figure 16	CTM targets defined with a temporal coherence threshold value of 0.65 and a ratio of deformation rate to standard error greater than three.....	23
Figure 17	Histogram of CTM targets defined with a temporal coherence threshold value of 0.65 and a ratio of deformation rate to standard error greater than three.....	24
Figure 18	CTM targets defined with a threshold value of 0.65 and clustered within the lower Frank Slide.....	25
Figure 19	Histogram of deformation rate values of CTM targets clustered within the lower Frank Slide.....	25
Figure 20	CTM targets defined with a threshold value of 0.65 and clustered within the lower Frank Slide after removal of outliers.....	26
Figure 21	Histogram of deformation rate values of CTM targets clustered within the lower Frank Slide, after removal of outliers.....	27
Figure 22	Aerial view of the west side of the peak on Turtle Mountain showing South Peak, the saddle and North Peak.....	28
Figure 23	Close-up aerial view of toppling blocks and large boulders that comprise the saddle between North and South Peaks.....	29
Figure 24	Locations of the Frank, Hillcrest and Bellevue mines.....	30
Figure 25	View of the east side of Turtle Mountain illustrating the zones discussed in the following sections.....	31
Figure 26	Horizontal deformation vectors (with 95% confidence ellipses) representing deformations between 1982 and 2005 as determined from photogrammetric measurements.....	33
Figure 27	CTM targets identified for South Peak.....	34
Figure 28	Point profiles of wrapped phases and deformation estimates of Target sp1 on South Peak.....	35
Figure 29	Point profiles of wrapped phases and deformation estimates of Target sp2 on South Peak.....	36
Figure 30	Point profiles of wrapped phases and deformation estimates of Target sp3 on South Peak.....	37
Figure 31	Profiles of wrapped phases and deformation estimates of target sp4 on South Peak.....	38
Figure 32	Lower South Peak area and CTM targets.....	39

Figure 33	Plan view of the lower South Peak area with CTM targets.	40
Figure 34	Plan view of the eastern South Peak area with CTM targets.	41
Figure 35	CTM plots showing the deformation model (averaging annual deformation), time series of wrapped phase, time series of unwrapped phase and deformation profile associated with target esp4.	42
Figure 36	CTM plots showing the deformation model (averaging annual deformation), time series of wrapped phase, time series of unwrapped phase and deformation profile associated with target esp4.	43
Figure 37	CTM plots showing the deformation model (averaging annual deformation), time series of wrapped phase, time series of unwrapped phase and deformation profile associated with target esp4.	44
Figure 38	Perspective views to the west of Turtle Mountain–Frank Slide.	45
Figure 39	Plan view of the lower part of the upper slope of the Frank Slide with CTM targets.	46
Figure 40	View from the northeast of the east side of Turtle Mountain showing the apron of talus covering the eastern face of the mountain.	47
Figure 41	Deformation pattern of the lower part of the Frank Slide.	48
Figure 42	Sunshade relief image of the bare earth LIDAR DEM showing location of the Frank Mine (white polygon) and surface subsidence pits overlying its southern part.	50
Figure 43	Statistics and histogram of the targets detected in the red polygon as shown in Figure 42.	51
Figure 44	Deformation pattern of the eastern part of the Frank Slide.	52
Figure 45	Statistics and histogram of the targets detected in the red polygon shown in Figure 44.	52
Figure 46	Slope angle map of the Frank Slide.	55
Figure 47	Time series of wrapped phase values of Target up7 as shown in Figure 39.	56
Figure 48	Linear deformation model and resultant deformation estimates of Target up7 as shown in Figure 39.	57
Figure 49	Nonlinear deformation model obtained by smoothing with a 0.3 year kernel length and resultant deformation estimates of Target up7 as shown in Figure 39.	58
Figure 50	Nonlinear deformation model obtained by smoothing with a 0.5 year kernel length and resultant deformation estimates of Target up7 as shown in Figure 39.	59
Figure 51	Nonlinear deformation model obtained by piecewise linear fitting with a 0.3 year kernel length and resultant deformation estimates of Target up7 as shown in Figure 39.	60
Figure 52	Repeat pass InSAR geometry with an across track InSAR configuration.	65
Figure 53	Recommended temporal coherence threshold with regard to the number of interferograms used.	73
Figure 54	Interferogram (upper) and coherence (lower) images from Run 1.	75
Figure 55	Interferogram (upper) and coherence (lower) images from Run 2.	76
Figure 56	Interferogram (upper) and coherence (lower) images from Run 3.	77
Figure 57	Interferogram (upper) and coherence (lower) images from Run 4.	78
Figure 58	Interferogram (upper) and coherence (lower) images from Run 5.	79
Figure 59	Interferogram (upper) and coherence (lower) images from Run 6.	80
Figure 60	Interferogram (upper) and coherence (lower) images from Run 8.	81
Figure 61	Interferogram (upper) and coherence (lower) images from Run 9.	82
Figure 62	Larger area of Interferogram from Run 9 showing atmospheric effect.	83
Figure 63	Interferogram (upper) and coherence (lower) images from Run 10.	84
Figure 64	Larger area of Interferogram from Run 10 showing atmospheric effect.	85
Figure 65	Interferogram (upper) and coherence (lower) images from Run 11.	86

Figure 66	Larger area of Interferogram from Run 11.....	87
Figure 67	Interferogram (upper) and coherence (lower) images from Run 12.....	88
Figure 68	Interferogram (upper) and coherence (lower) images from Run 13.....	89
Figure 69	Larger area of Interferogram from Run 13.....	90
Figure 70	Interferogram (upper) and coherence (lower) images from Run 14.....	91
Figure 71	Interferogram (upper) and coherence (lower) images from Run 15.....	92
Figure 72	Larger area of interferogram from Run 15.....	93
Figure 73	Interferogram (upper) and coherence (lower) images from Run 16.....	94
Figure 74	Larger area of Interferogram from Run 16.....	95
Figure 75	Interferogram (upper) and coherence (lower) images from Run 17.....	96
Figure 76	Larger area of Interferogram from Run 17.....	97
Figure 77	Interferogram (upper) and coherence (lower) images from Run 18.....	98
Figure 78	Interferogram (upper) and coherence (lower) images from Run 19.....	99
Figure 79	Larger area of Interferogram from Run 19.....	100
Figure 80	Interferogram (upper) and coherence (lower) images from Run 20.....	101
Figure 81	Interferogram (upper) and coherence (lower) images from Run 21.....	102
Figure 82	Larger area of Interferogram from Run 21.....	103
Figure 83	Interferogram (upper) and coherence (lower) images from Run 22.....	104
Figure 84	Larger area of interferogram from Run 22 showing atmospheric effect.....	105
Figure 85	Interferogram (upper) and coherence (lower) images from Run 23.....	106
Figure 86	Larger area of interferogram from Run 23.....	107
Figure 87	Interferogram (upper) and coherence (lower) images from Run 24.....	108
Figure 88	Larger area of interferogram from Run 24.....	109
Figure 89	Interferogram (upper) and coherence (lower) images from Run 25.....	110
Figure 90	Larger area of interferogram from Run 25.....	111
Figure 91	Interferogram (upper) and coherence (lower) images from Run 26.....	112
Figure 92	Larger area of interferogram from Run 26.....	113
Figure 93	Interferogram (upper) and coherence (lower) images from Run 27.....	114
Figure 94	Interferogram (upper) and coherence (lower) images from Run 28.....	115
Figure 95	Larger area of Interferogram from Run 28.....	116

Acknowledgments

The authors thank Vernon Singhroy from Canadian Centre for Remote Sensing (CCRS) for technical review, Katrin Molch from CCRS for assistance in familiarization with EV-InSAR software and ordering and tasking the acquisition of Radarsat-1 data, and Robert Hawkins from CCRS in determining the line of sight direction of the Radarsat-1 sensor. The authors thank the Canadian Space Agency (CSA) for assistance in obtaining the Radarsat-1 SLC data, Francisco Moreno from Alberta Geological Survey in obtaining information for Turtle Mountain, and Glen Prior and Aimee Maxfield for editorial review.

Abstract

The Frank landslide was a catastrophic rock avalanche that took place in 1903 on the eastern slope of Turtle Mountain located in the southwestern Alberta, Canada. It buried a portion of the Town of Frank and claimed more than 70 lives. Thirty years later, studies of the remaining portions of the mountain documented another potential rock slide hazard that was estimated to involve a failure of 5 million m³ of rock in the area known as South Peak. The present study has applied Persistent/permanent Scatterers Interferometry SAR (PS-InSAR) technology to map ground deformation in the Frank Slide area using Radarsat-1 data and EarthView InSAR (EV-InSAR) Coherent Target Monitoring (CTM) software developed by Atlantis Scientific Inc (now MacDonald Dettwiler and Associates Ltd). The following are some results regarding the success of the application of spaceborne InSAR to map ground deformation over the Frank Slide area, using Radarsat-1 data acquired with Fine Beam 4 of the ascending pass from April 2004 to October 2006:

- On the upper portion of the mountain, foreshortening distortions associated with the incidence angle of the satellite beam mode used, the steep topography, shadow and decorrelation caused by irregular surficial talus movements, do not allow for reliable mapping of ground deformation in these areas. Although there were a small number of point targets extracted to map deformation on the west side of South Peak and on the upper Frank Slide, these points may not be representative of the deeper seated deformations of the rock slope, but rather isolated and discrete blocks or boulders. To obtain more reliable deformation data for the peak area, consideration may be given for also including Radarsat-1 data from the descending pass, although foreshortening distortions may persist with the descending pass as well. Likely, the greatest potential to map deformation for the peak area will be the future application of Radarsat-2, which is more flexible in both left and right-looking modes.
- The lower slope of the Frank Slide and the valley bottom are very well suited for the application of PS-InSAR for mapping ground deformations. Due to the bare and dry nature of the landscape and the slow systematic nature of the deformations, both slow creep of talus slopes and subsidence of the surface above abandoned underground coal mine workings were observed and quantified. On the talus-covered lower slopes of Turtle Mountain, the PS-InSAR results allow differentiation between recently deposited, more active talus and older, more stable debris. In addition, the ground surface above the Frank Mine was found to subside, in some areas, at an average rate of about 3.1 mm per year, relative to the reference area, which is located in the middle part of the Frank Slide, during the period from April 2004 to October 2006. This 3.1 mm/year represents the sum of movements attributable to (1) downslope creep of the 2001 talus and (2) coal mine subsidence. Some isolated targets, associated with pit holes caused by local collapsing of the Frank Mine, were found to subside at an annual rate of more than 20 mm per year in the line of sight of radar during this period. Upslope of the Frank Mine, a subsidence rate of more than 10 mm per year relative to the reference area, was detected for a group of targets located in the lower slope of the Frank Slide. For more than 100 years since the Frank landslide took place in 1903, speculation has been that ground movements induced by the underground coal mines at the foot of Turtle Mountain might have triggered the slide.
- In addition to providing quantification for an area where visual observations of subsidence had been made (the Frank Mine), an average rate of up to 3.2 mm/year relative to the reference area, was observed for some areas overlying the footprint of the abandoned Bellevue underground mine to the east. At the time of the preparation of this report, there was no published data on the subsidence of the ground surface in this area. Thus, the findings of this study may be important as a tool for Municipality of Crowsnest Pass to better understand the potential hazards associated with the Bellevue mine. Discussions with personnel from the municipality have verified that there

have been frequent collapses above the Bellevue Mine below roads and fields over the past few years and there is interest in the potential application of the technology to aid the municipality in mapping of the onset of collapse and proactively planning mitigation.

As all of the ground deformation monitoring equipment has been installed on the western side of South Peak near the top of the ridge, the PS-InSAR results discussed in this report provide new insights on deformation for other portions of Turtle Mountain that had previously not been monitored. Although there is currently no ground data to verify the results presented herein, these results provide valuable data that can be used to plan future monitoring programs. This may include the installation of prisms or differential GPS stations on the slopes above the coal mine workings or on the talus-covered slope below South Peak. Additional consideration is currently being given for the installation of a number of artificial corner reflectors below Third Peak or South Peak to both acquire new data and improve image co-registration for future PS-InSAR processing on Turtle Mountain. At this time, AGS has tasked continued Radarsat-1 F4F acquisitions for Turtle Mountain and intends to continue adding to the model on an annual basis to enhance the understanding of the complexities of movements on Turtle Mountain. Consideration is also being given to processing of an alternative beam mode that would allow for deformation mapping in the peak area of Turtle Mountain. This could either involve using a descending Radarsat-1 beam mode or utilizing the left and right looking capabilities of Radarsat-2 once it is in orbit and operational. Turtle Mountain would likely be an ideal case study for this enhanced feature of Radarsat-2 and the high resolution fine beam (3 m pixel size).

In addition, the theory, principles and algorithms related to implementation of PS-InSAR technology in EarthView InSAR Coherent Target Monitoring (CTM) software are reviewed and discussed. In addition to the processing steps available in CTM analysis, the present study has demonstrated a post-processing step that applies statistical and geostatistical analysis to discriminate reliable targets from false targets, and to differentiate between isolated point target movement and regional ground deformation. This also renders the present report as a useful reference manual for millimetre-scale ground deformation mapping using EarthView InSAR Coherent Target Monitoring (CTM) software.

1 Introduction

Turtle Mountain is located in the Rocky Mountains in southwestern Alberta in an area known as the Crowsnest Pass (Figure 1). In 1903, a catastrophic rock avalanche, the Frank landslide, occurred on the eastern slope of Turtle Mountain, burying a portion of the Town of Frank and claiming more than 70 lives. Thirty years later, studies of the remaining portions of the mountain by John Allan (1933) documented a potential rock slide hazard with an estimated volume of 5 million m³ originating from an area known as South Peak (Figure 1). Various attempts at monitoring this portion of the mountain were undertaken in the 1930s and 1980s. In 2003, on the centennial of the Frank landslide, the Government of Alberta committed \$1.1 million (CDN) to develop a real-time monitoring system over Turtle Mountain, and a warning and response plan for the Municipality of Crowsnest Pass. As a result, a wide range of sensors that measure displacement and tilt were installed around the cracks/fractures on South Peak. In addition to the sensor network, a number of studies, including various remote sensing studies, were also initiated to better understand the extent and rate of movements on South Peak and the rest of the mountain. The present study attempts to determine ground deformations over the Frank Slide and South Peak using a satellite based monitoring technique called Permanent/persistent Scatterer Interferometric Synthetic Aperture Radar (PS-InSAR) technology.

In the last 15 years, Interferometric Synthetic Aperture Radar (InSAR) has developed from theoretical concept to a technique that is being used at an increasing rate for a wide range of earth science fields. With a number of spaceborne SAR sensors available (ERS 1/2, Radarsat 1, JERS, ALOS), many high quality results from this technique have been obtained, demonstrating its potential as a powerful ground deformation measurement tool. In the last few years, the capability of InSAR has been considerably improved by using large stacks of SAR images acquired over the same area, instead of the classical two images used in the standard configurations. This multi-image InSAR technique was introduced as Permanent/persistent Scatterer Interferometric Synthetic Aperture Radar (PS-InSAR; Ferretti et al., 1999, 2000, 2001). With these advances, the InSAR techniques are becoming more and more quantitative geodetic tools for deformation monitoring, rather than simple qualitative tools. As a result, PS-InSAR technology was identified as a potentially useful technology for monitoring potential movements over Turtle Mountain, given its unique characteristics in terms of spatial density and high resolution deformation measurements (millimetre scale). In 2004 and 2005, Atlantis Scientific Inc. (2005) carried out an experimental study to demonstrate the potential application of PS-InSAR technology for the Turtle Mountain monitoring. This leads to the acquisition of Radarsat-1 data for 2004 and tasking the acquisition for 2005. In 2006, AGS, in collaboration with the Canadian Centre for Remote Sensing (CCRS), continued the InSAR monitoring of Turtle Mountain by using the available data acquired from 2001 to 2005 and tasking new acquisitions for 2006. This report documents the workflow, results and preliminary evaluation of the results obtained by AGS.

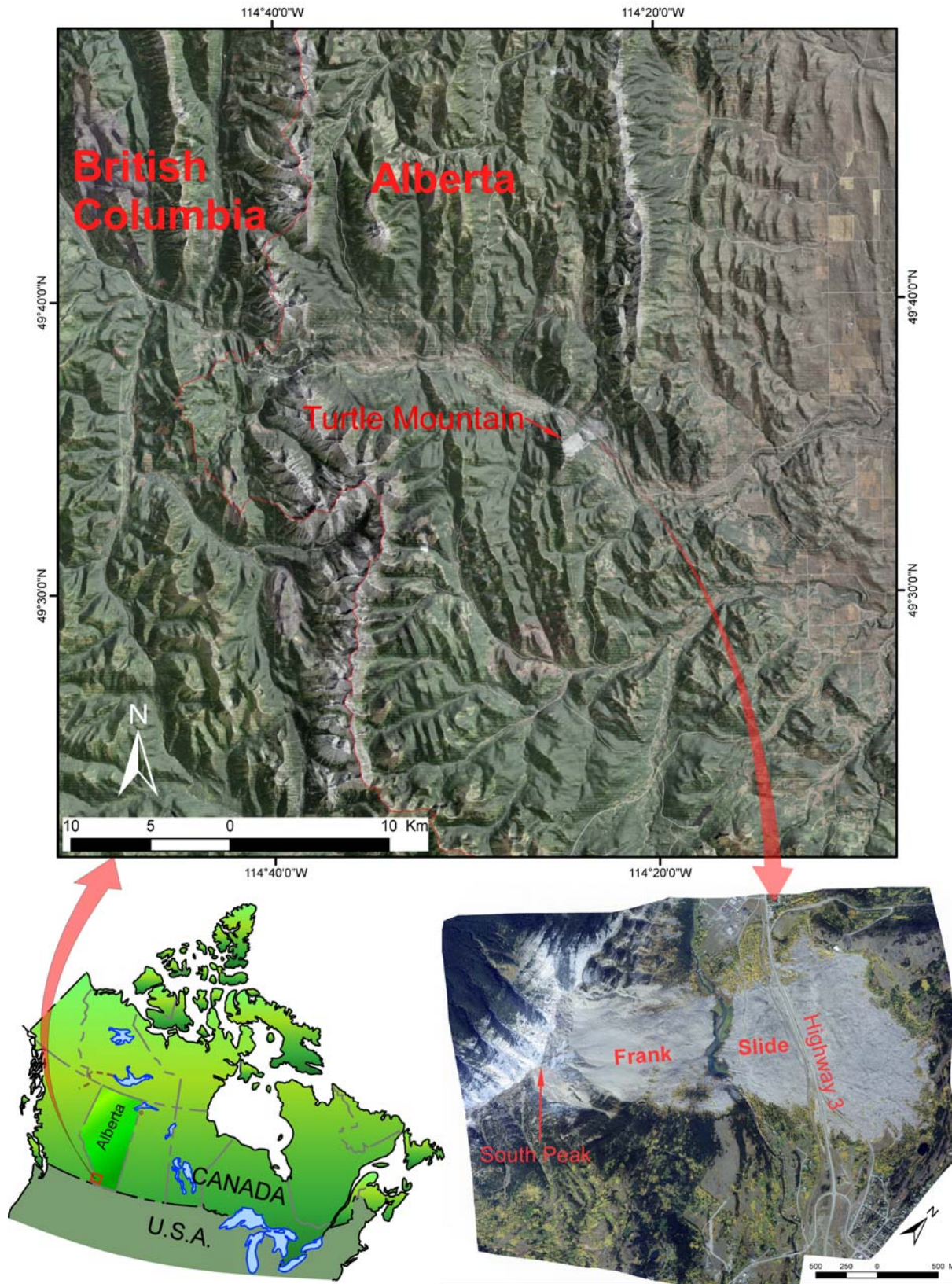


Figure 1. Location map showing the Frank Slide on the eastern slope of Turtle Mountain, Alberta, Canada.

2 InSAR Background

Radar, an acronym for Radio Detection and Ranging, is an active imaging technology that operates in the microwave portion of the electromagnetic spectrum. A radar sensor or antenna emits a series of electromagnetic pulses to the Earth's surface in the form of a sine wave, and detects the reflections of these pulses from the imaged ground targets. It records the strength of the signal, the time delay and the arrival phase of the pulse. Radar images are made up of pixels; the strength of the signal (defined as the amplitude) detected by a radar antenna defines the pixel brightness and is what we usually associate with a remotely sensed image. The time delay enables us to determine the distance from the radar antenna to the ground target, which is called "the range" in Radar terminology. The arrival phase makes it possible for Radar to detect millimetre-scale changes in the range (see below).

A satellite with an active microwave sensor allows us to image the Earth's surface along its pass; such a satellite typically orbits the Earth at an altitude of approximately 800 km. Each pixel in the acquired image has a specific size influenced by the radar sensor resolution on the ground imaged: the higher the resolution, the smaller the pixel size. To increase the image resolution, Synthetic Aperture Radar (SAR) technology has been developed to take advantage of the spacecraft movement and advanced signal processing techniques (called SAR focusing) to simulate a large antenna size.

The reflection of the electromagnetic pulses from an area on the ground, covered by the pixel in a SAR image, is recorded as both the intensity and arrival phase of the electromagnetic pulse. Accurate measurement of the arrival phase is possible because the radar signal is coherent. This coherence means the transmitted signal is generated from a stable local oscillator and the received signal has a precisely measurable phase difference in relation to the local reference phase (the transmitted oscillator phase). This gives SAR the capability to measure the change in the distance between the radar sensor on the satellite and the target on the ground—in phase or fractional wavelength—in addition to measuring the time delay of the electromagnetic pulse. Phase is a measure of how far the wave has traveled in units of wavelength. For example, if the signal has traveled by a wavelength then the phase has changed by 2π . Usually the phase can be accurately measured to about 10 % of the wavelength. This allows a much more accurate distance measurement than that using time delay. For example, for Radarsat-1 (C-band) with a wavelength of 56 mm, the change in the distance between the radar sensor on the satellite and the target on the ground can be measured to an accuracy in the order of millimetres (for example, $(56/2) \text{ mm} * 10\% = 2.8 \text{ mm}$). Compared with an 8.4 m resolution of the Fine Beam mode from the standard time delay measurement, this is about 3000 times more accurate.

However, there are millions of wavelengths between the radar sensor and the reflector on the ground, and the total number of wavelengths is not determined. Thus, the phase measurement is a relative measurement, and can be used only to tell the change in range from one measurement to the next. If two separate radar acquisitions are obtained with the same viewing geometry, or with a small distance between the two locations of the SAR platform over the same area, then, the phase difference between the two image acquisitions is related to the change in the range occurred between the two acquisitions. In turn, the change in the range between the two acquisitions is related to the change on the ground surface, or ground deformation. This forms the fundamental foundation on which Interferometric Synthetic Aperture Radar (InSAR) technology has been developed to extract information on ground deformation: by subtracting the phase of the second acquisition from that of the first acquisition, InSAR is capable of measuring the line of sight distance changes to a fraction of the wavelength of the radar sensor, and the magnitude of ground movement between two satellite passes can be measured to millimetre-scale accuracy. InSAR, which is a less commonly used synonym of InSAR, is usually reserved for airborne applications.

InSAR technology comes in different forms. These are—in order of the level of advancement and complexity—the following: Standard InSAR for DEM generation, Differential InSAR (DInSAR) for

ground deformation mapping and Permanent/Persistent Scatterer Interferometric Synthetic Aperture Radar (PS-InSAR) for displacements over individual coherent targets. A good understanding of the basic theory, principles and algorithms behind a Synthetic Aperture Radar (SAR), interferometric SAR (InSAR) and PS-InSAR is required to understand and evaluate the results from the PS-InSAR processing. The above review was meant only as a brief overview of the fundamental principles used to derive InSAR results. A more detailed theoretical background of Standard InSAR, DInSAR and PS-InSAR is presented in Appendix A. However, the review should not be considered exhaustive. For further information on the principles of SAR data acquisition, processing and analysis, as well as an in-depth discussion concerning theory and applications of SAR interferometry, the reader is referred to review books including Henderson and Lewis (1998), Franceschetti and Lanari (1999) and Hanssen (2001), and review papers including Gens and Genderen (1996), Bamler and Hartl, (1998), Massonnet and Feigl (1998) and Rosen et al. (2000).

3 Data

3.1 Radarsat-1 Data

The data used in the present study are Radarsat-1 Single Look Complex (SLC) data in the Committee on Earth Observation Satellites (CEOS) format processed by Canadian Space Agency (CSA). SLC is used because it has preserved both the amplitude and phase of the backscattered signal for each pixel in complex number format. Radarsat-1 is a Canadian remote sensing satellite that was launched in November 1995 and is currently in operation. Table 1 shows the main characteristics of the Radarsat-1 sensor.

Table 1. Radarsat-1 sensor parameters

Parameters	Value
Frequency / Wavelength	5.3GHz/C-band 5.6 cm
RF Bandwidth	11.6, 17.3 or 30.0 MHz
Transmitter Power (peak)	5 kW
Transmitter Power (average)	300 W
Maximum Data Rate	85 Mb/s (recorded) - 105 Mb/s (R/T)
Antenna Size	15m x 1.5m
Antenna Polarization	HH
Chirp Type	Linear FM down chirp
Pulse Repetition Frequency	1200-1400 Hz
Pulse Duration	42.0 u-sec
Pulse bandwidth	11.583 MHz, 17.282 MHz , 30.002 MHz
Orbit Altitude	793-821 kilometres
Orbit Inclination	98.6 degrees
Period	101 minutes
Ascending node	18:00 hours
Sun-synchronous	14 orbits per day
Repeat Pass	Every 24 days
North of 70 degrees N Coverage	Daily
North of 48 degrees N Coverage	Every 4 days
The Whole Earth (north of 80 degrees S)	Every 6 days
Ascending Pass Look Direction on Equator	78° (12° off East)
Descending Pass Look Direction on Equator	192° (12° off West)

Radarsat-1 is unique in its seven imaging beam modes possessing a diverse range of incident angles and swaths (33 beam positions; Figure 2). Table 2 lists the main characteristics of each beam mode.

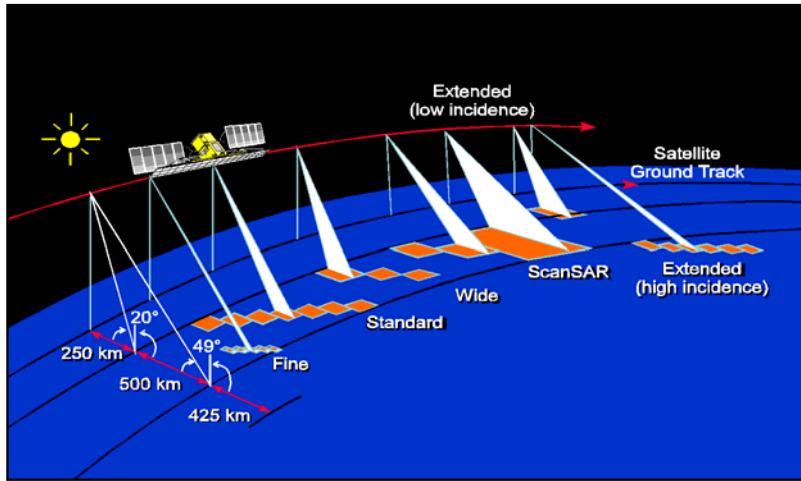


Figure 2. RADARSAT-1 beam modes and beam positions (from RADARSAT International (RSI), 1996).

Table 2. Radarsat-1 imaging beam modes

Beam Mode	Nominal resolution (m)	Number of positions	Swath width (km)	Look angles (degrees)
Fine	8	15	45	37–47
Standard	30	7	100	20–49
Wide	30	3	150	20–45
ScanSAR Narrow	50	2	300	20–49
ScanSAR Wide	100	2	500	20–49
Extended (H)	18-27	3	75	52–58
Extended (L)	30	1	170	10–22

In addition to the different beam modes with different look angles, SLC data are also acquired from two passes/look directions: the ascending pass that has a look direction about 8.5° off east and the descending pass that has a look direction about 8.5° off west at Turtle Mountain. Since InSAR measures the line of sight movement, it is critical to select the optimal combination of the pass (ascending or descending), beam mode and look angle. To avoid shadow, ideally the look direction should correspond to the aspect of the sliding slope and the look angle should be greater than the slope angle. The ideal combination of the look direction and angle should be close to the direction of motion to be measured; this requires some previous knowledge about the topography of the study area and historic land movement data. The availability of the SAR data is also vital, as a minimum number of acquisitions (15–20) are required to form a sufficient number of interferograms for CTM analysis and ensure the validation of statistical results.

Given the geometry of the north-trending Turtle Mountain and the northeastern facing slope of the Frank Slide, Atlantis Scientific Inc. (2005) decided to select an ascending pass in the Fine Beam mode with a relatively large incidence angle. As a result, the Fine Beam Mode 4 Far (F4F) track was selected as the best possible track for coherent target monitoring over Turtle Mountain, with the Fine Beam Mode 1 (F1) as a back-up beam. This resulted in scheduling and acquisition of Radarsat-1 SLC data for the years of

2004 and 2005. The Fine Beam mode is intended for applications that require the best spatial resolution available from the RADARSAT-1 system. The azimuth resolution is 8.4 m, with the range resolution being 9.1–7.8 m from F1 to F5. The F4F has a look angle ranging from 43.8° to 46.1° and the F1 from 36.8° to 39.9°.

To maximize the use of available Radarsat-1 data for the Turtle Mountain monitoring, the present study used the SLC data acquired from the selection of the F4F and F1 tracks by Atlantis Scientific Inc. (2005) at the planning stage. Table 3 lists the SLC data acquired for the CTM analysis. They are all from the Fine Beam 4 far range track, except the one acquired on April 19, 2004, which is from the Fine Beam 4 track. The precipitation on the day of acquisition, obtained from Alberta Department of Environment for the closest nearby weather station (Willoughby Ridge Station) is also included in Table 3. This weather station is located at 49° 33' north latitude and 114° 30' west longitude and at an elevation of 1783 m. It is about 7.1 km to the west of South Peak. The weather data from the Willoughby Ridge station are assumed to be representative of the weather for the Turtle Mountain area.

Table 3. Radarsat-1 SLC data used by the present study and precipitation on the acquisition day

Scene number	Acquisition Date	Beam Position	Daily Precipitation* (mm)
1	12/12/2000	F4F	1.8
2	1/5/2001	F4F	5.1
3	9/2/2001	F4F	0.3
4	9/26/2001	F4F	0
5	6/6/2004	F4F	4.1
6	6/30/2004	F4F	24.4
7	7/24/2004	F4F	0.5
8	8/17/2004	F4F	8.6
9	9/10/2004	F4F	1
10	10/4/2004	F4F	0
11	11/21/2004	F4F	0.3
12	12/15/2004	F4F	0
13	2/25/2005	F4F	0
14	3/21/2005	F4F	0
15	4/14/2005	F4F	7.6
16	5/8/2005	F4F	2.9
17	9/29/2005	F4F	18
18	11/16/2005	F4F	0
19	1/3/2006	F4F	0.2
20	5/3/2006	F4F	0.7
21	5/27/2006	F4F	9.8
22	4/19/2004	F4	0
23	6/20/2006	F4F	0
24	7/14/2006	F4F	0
25	8/7/2006	F4F	0
26	8/31/2006	F4F	0.4
27	9/24/2006	F4F	0
28	10/18/2006	F4F	0.9

*Data collected from the Willoughby Ridge station, which is 7.1 km to the west of the South Peak of Turtle Mountain.

Although the F4F and F1 tracks are good for the Frank Slide that occupies the lower portion of Turtle Mountain, the focus of the Turtle Mountain monitoring is actually over the upper part of the mountain that includes South Peak. The top of Turtle Mountain is a sharp ridge that extends from south to north (Figure 3). For both the F4F and F1 beams, the upper eastern slope of Turtle Mountain is in shadow (Figures 3 and 4). A close look of the top ridge shows a series of cracks extending from South Peak toward the north. These cracks are located on the west-facing slope near the top of the ridge. Since this slope is facing toward the sensor of the ascending pass, considerable foreshortening effects occur and, thus, degrade the imaging resolution for this critical area. As a result, the geometry of the top of Turtle Mountain poses considerable limitations to InSAR monitoring of ground movement using Radarsat-1 F4F and F1 beams.

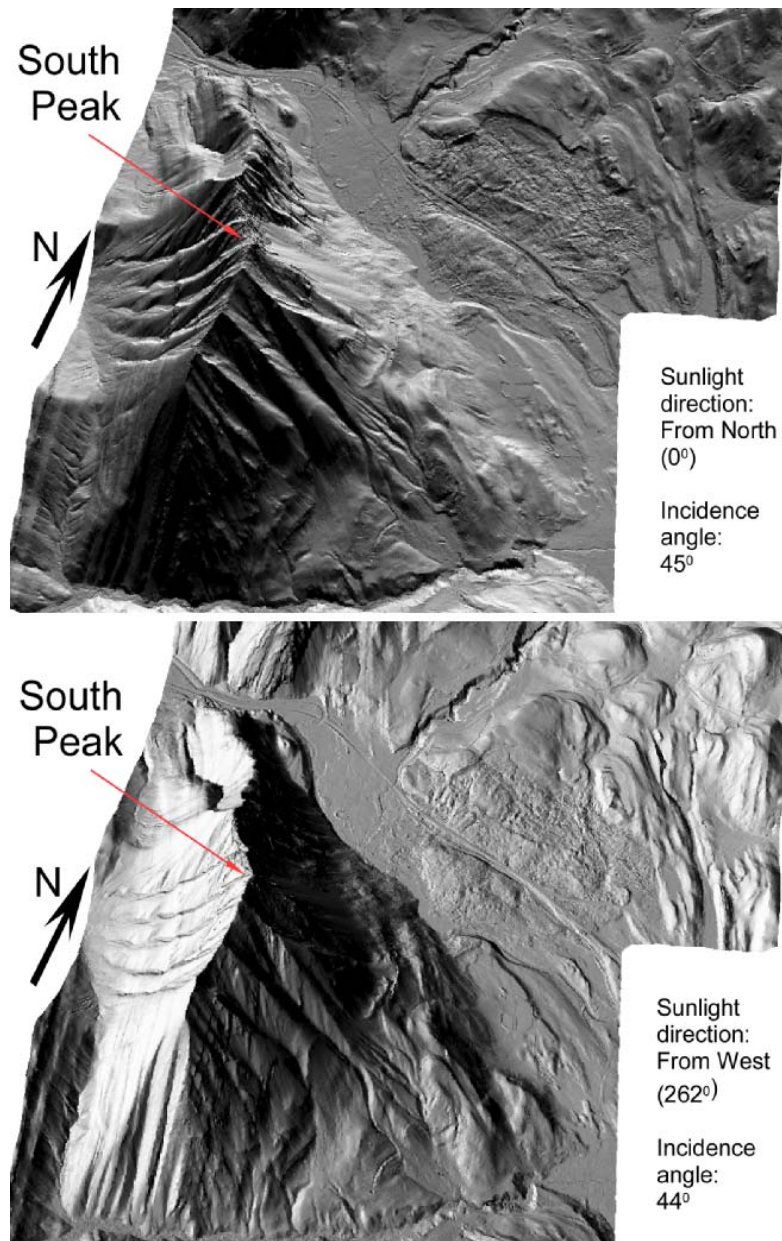


Figure 3. Perspective views of Turtle Mountain–Frank Slide generated using LiDAR DEM with a vertical exaggeration of two times. The lower view simulates the effect of the Fine Beam Mode 4 of the far range. It shows that shadow covers much of the upper eastern slope.

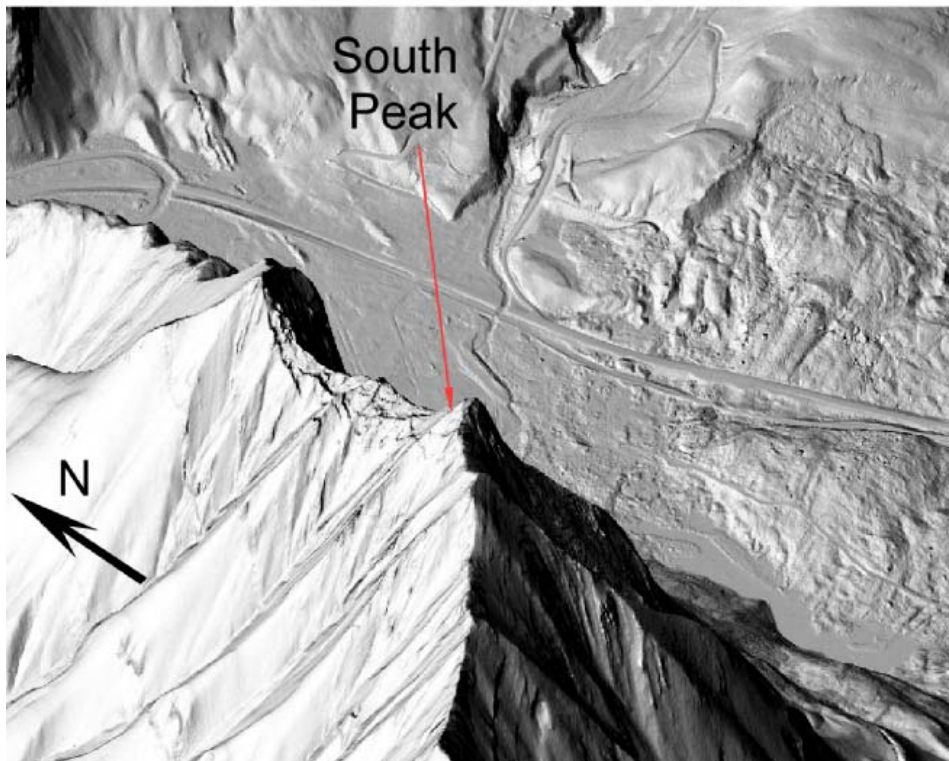
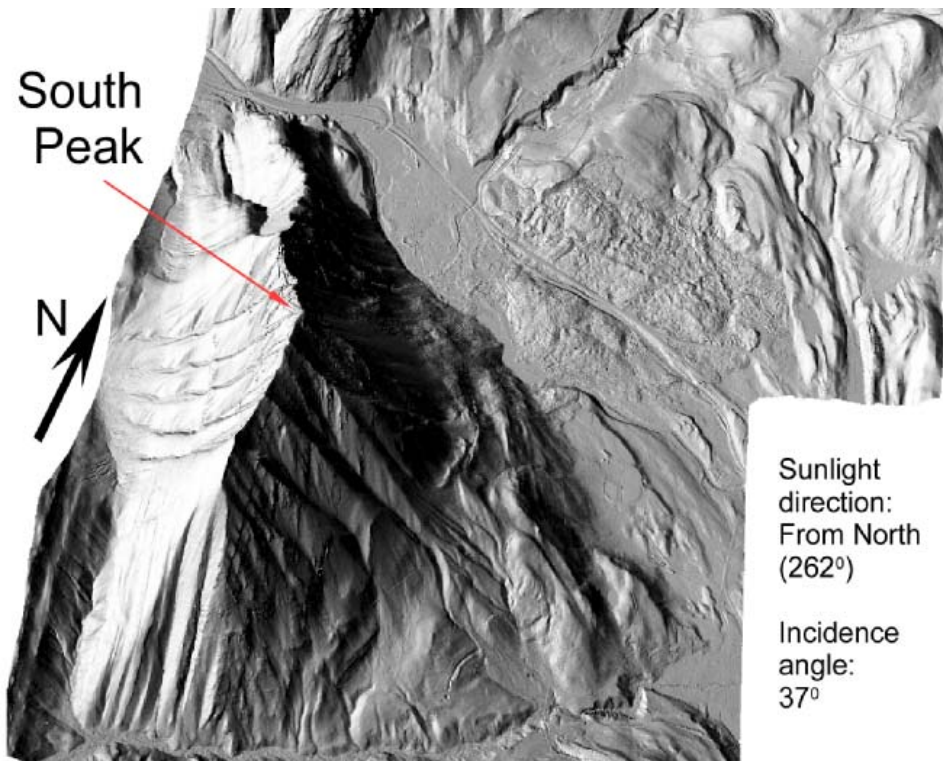


Figure 4. Perspective views of Turtle Mountain–Frank Slide generated using LiDAR DEM, with a vertical exaggeration of two times. The upper view simulates the effect of the Fine Beam Mode 1. It shows that shadow covers much of the upper eastern slope.

3.2 Digital Elevation Model (DEM) Data

To remove the topographic effect during the differential interferogram generation, a full feature Light Detection and Ranging (LiDAR) DEM was acquired from Airborne Imaging Inc. (Figure 5). This dataset was acquired through an airborne LiDAR survey that was carried out on July 24, 2005. A quality check indicates that the elevations at each LiDAR strip agreed with the surveyed elevations within 8 cm Root Mean Square (RMS) error or better. The data came in a 1 m grid format, and, due to the limitation of computation power was averaged to a 10 m grid to reduce the file size during interferometric processing. The full feature DEM is a digital surface model that includes the heights of buildings and trees (Figure 5).

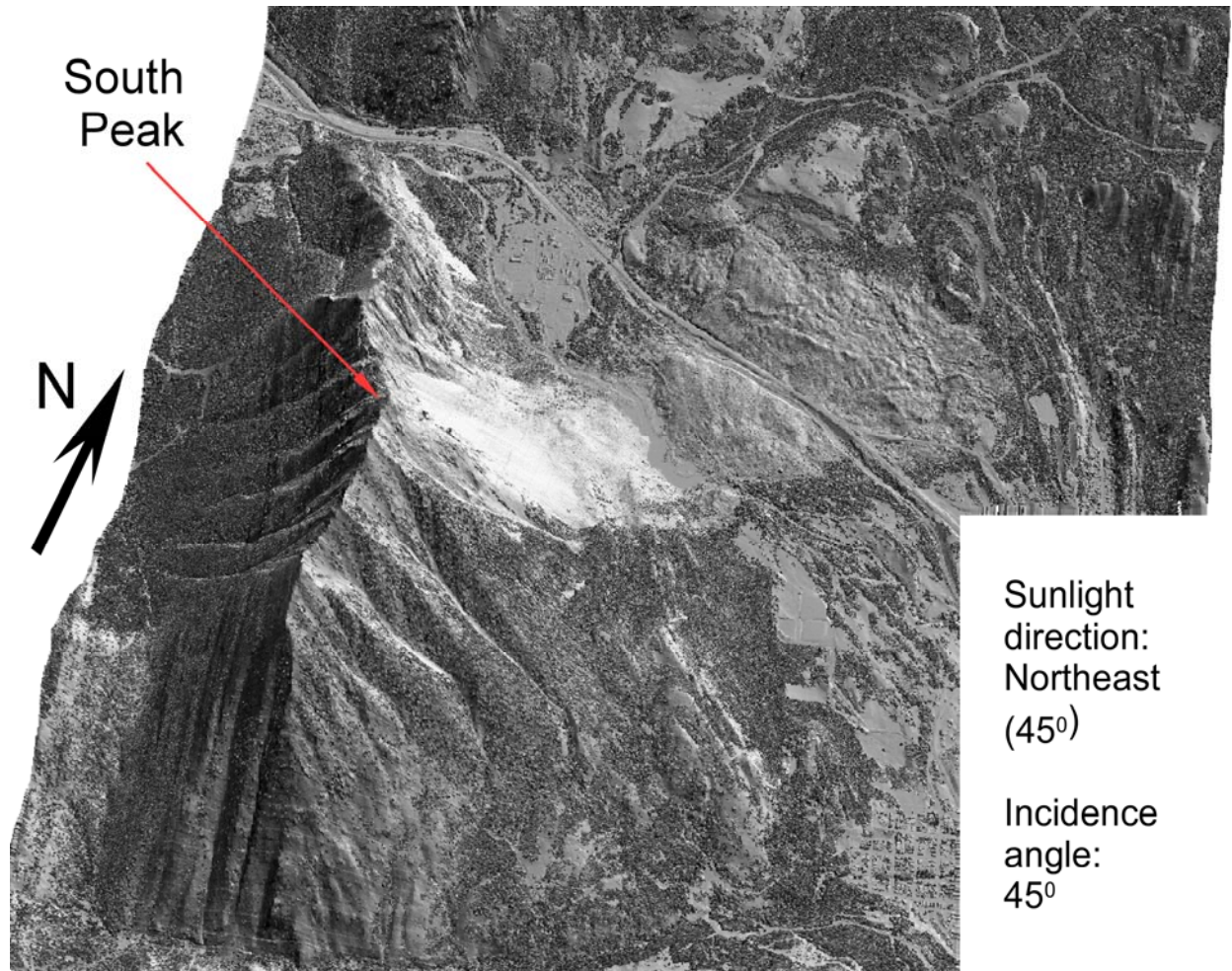


Figure 5. Sunshade relief image showing the perspective view of the full feature LiDAR DEM.

4 CTM Processing Steps and Workflow

The software used in this project for CTM analysis was EarthView InSAR (EV-InSAR) version 3.1 CTM Module. It is a commercial software package developed by Atlantis Scientific Inc., Canada (currently MacDonald Dettwiler and Associates Ltd). The design and development of EV-InSAR was supported in part by the RADARSAT User Development Program of the Canadian Space Agency (CSA). Generating interferograms and differential interferograms using available manual techniques is quite intensive and time consuming. EV-InSAR automates this process, making the generation of interferograms quick and more efficient. The step-by-step processing procedures, which include data entry, are controlled with the

help of a graphical user interface (GUI; Figure 6). The output from each processing step can be accessed easily through a console window. Figure 6 illustrates the processing chain for CTM analysis.

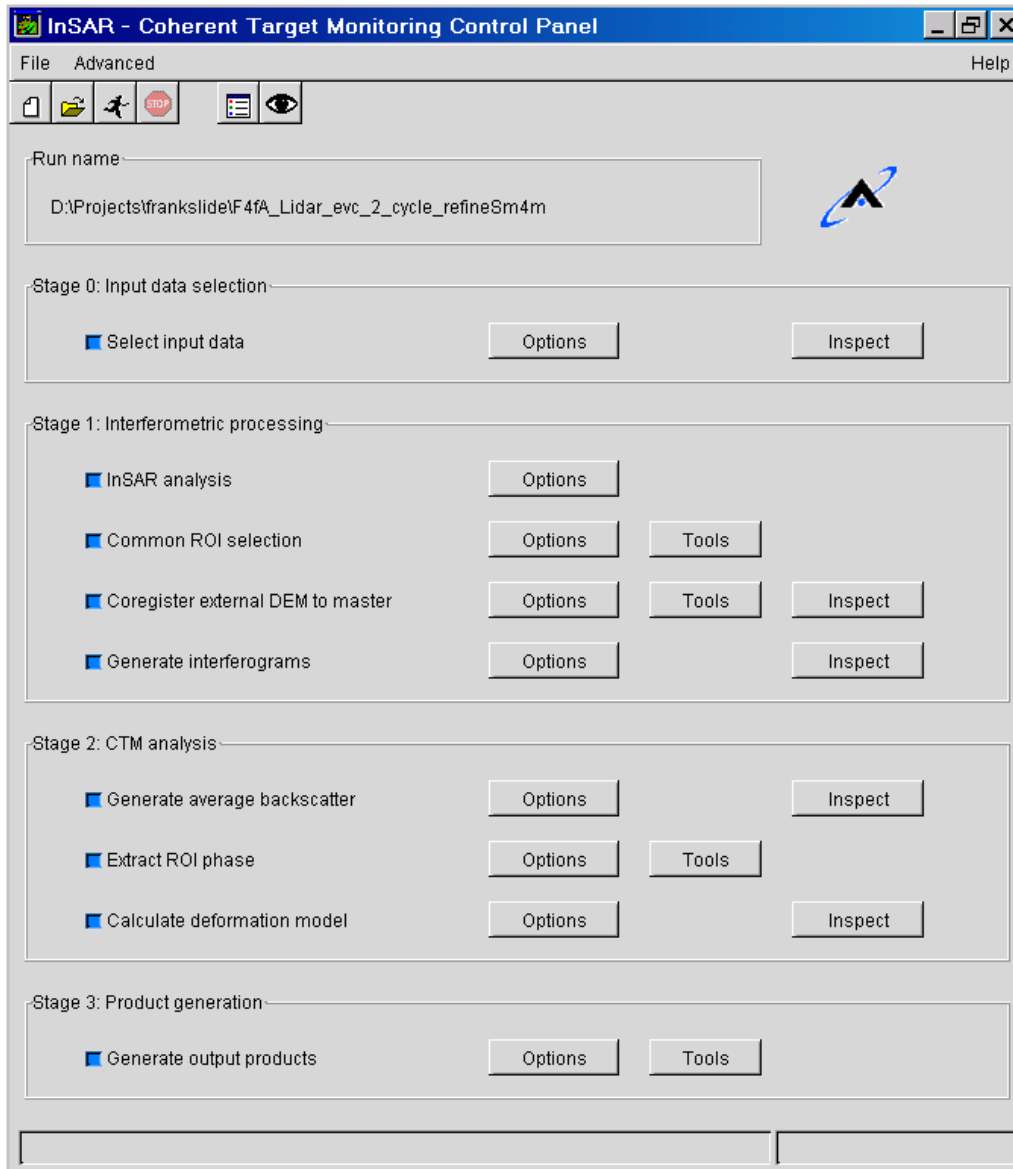


Figure 6. CTM control panel showing the processing chain.

The initial usability of EV-InSAR should not be overstated as processing in the background is quite complex. Due to the Python scripting language used, the error messages provided through the GUI interface are frequently unresponsive. Although more complex and extensive messages are provided through the Python interface, this information is useful only to an advanced Python programmer rather than a common user. The CTM processing steps are described below using the Turtle Mountain PS-InSAR monitoring project as an example. The emphasis is on identifying and discussing the most important decisions and problems facing each step. An additional step is included, as a post-CTM processing step in the workflow, in applying statistical and geostatistical analysis to evaluate the results for a large number of point targets obtained from the CTM analysis. This step is crucial in interpreting PS-InSAR results because it helps to discriminate the reliable targets from false targets, and to differentiate between isolated point target movements and regional ground deformation patterns.

4.1 Selection of Input Data

This step selects and inputs the master SAR image, slave images and a DEM for differential interferogram generation. A sufficient number of scenes need to be selected to obtain the desired temporal coherence threshold as illustrated in Figure 53 of Appendix A. Temporal decorrelation is less of a concern in selection of the data. The primary consideration for selecting the master image is that it gives reasonable baselines when combined with all the slave images. The ideal selection is that the master image is acquired near the middle of the temporal sequence and free of cloud/rain/snow during acquisition. The scene acquired on July 24, 2004 was chosen as the master image for interferogram generation because it gives rise to overall optimal baselines when paired with other image scenes. However, the disadvantage is that the weather data from the nearby Willoughby Ridge station indicate this station encountered 0.5 mm of rain on the acquisition day, even though it was clear of rain for July 22 and 23, 2004 and July 25 and 26, 2004 (Table 3). This step creates a set of Differential InSAR runs based on the data selected (Table 4).

Table 4. Differential InSAR runs created and the respective perpendicular baselines

Run number	Master-Slave image pair	Perpendicular baseline (m)
1	7/24/2004_12/12/2000	901.926
2	7/24/2004_1/5/2001	-1294.995
3	7/24/2004_9/2/2001	-2.4
4	7/24/2004_9/26/2001	303.7
5	7/24/2004_6/6/2004	-489.63
6	7/24/2004_6/30/2004	626.735
	7/24/2004 (Master)	0 (master)
8	7/24/2004_8/17/2004	90.258
9	7/24/2004_9/10/2004	0.365
10	7/24/2004_10/4/2004	573.99
11	7/24/2004_11/21/2004	-445.71
12	7/24/2004_12/15/2004	438.055
13	7/24/2004_2/25/2005	-47.39
14	7/24/2004_3/21/2005	-354.995
15	7/24/2004_4/14/2005	12.314
16	7/24/2004_5/8/2005	-179.226
17	7/24/2004_9/29/2005	695.558
18	7/24/2004_11/16/2005	304.997
19	7/24/2004_1/3/2006	-118.581
20	7/24/2004_5/3/2006	-154.225
21	7/24/2004_5/27/2006	459.577
22	7/24/2004_4/19/2004	250.35
23	7/24/2004_6/20/2006	-174.53
24	7/24/2004_7/14/2006	649.72
25	7/24/2004_8/07/2006	-62.95
26	7/24/2004_8/31/2006	-264.35
27	7/24/2004_9/24/2006	295.88
28	7/24/2004_10/18/2006	-213.869

4.2 Interferometric Processing

This stage produces a set of differential interferograms that are co-registered to the common master image, processed to a common region of interest (ROI) and ready for CTM analysis. This includes co-registration and resampling of the slave image, co-registration of the DEM to the master image, calculation of the interferometric phase, generating the correlation coherence image and correction of residual phase due to error in the input orbital geometric parameters.

Co-registration is fundamentally important as each slave image is required to be co-registered to the master image to an accuracy of 1/8 pixels to permit a successful interferometry. EV-InSAR automatically generates a set of tie-points between the master and slave images, based on cross-correlation of the master and slave image pair over a patch surrounding each tie-point. Then, a bi-cubic polynomial is fitted/calculated between the tie-points in the master image to those in the slave image. The bi-cubic coefficients are used to co-register the slave image to the master image. Although the co-registration process is automated, it may fail due to a number of reasons. In the case that a range bias between the master and slave images is too large, the automated algorithms may not determine the bias correctly. This causes a large number of tie-points to be rejected and results in an insufficient number of tie-points required for the polynomial fitting. As a result, both manual determination of the bias and an adjustment in the size of the tie-point grid are necessary. This is the case with runs 14–16 and 22 where both the range and azimuth biases have to be determined manually for co-registration (Table 5). The extremely large bias in Run 22 is due to the fact that this slave image is from F4 beam position whereas the master image is from F4F beam position.

Table 5. Biases/offsets determined manually for co-registration referring to the master pixel (3469.84P, 5412.84L)

Run number	Range bias	Azimuth bias
14	85	221
15	21	331
16	46	413
22	4379	11992

In addition, tie-points over decorrelated areas and water are not reliable and, as they may be detrimental to the polynomial fitting, should be excluded. Typically, good co-registration will result in an RMS tie-point error of less than 0.2 pixels and may be achieved with a relatively small number of reliable tie-points. To ensure that the image is sampled adequately, however, at least 20% of the available tie-points should be reliable and distributed uniformly across the study area.

During the generation of the differential interferogram, an attempt is made to automatically remove the flat-Earth phase based on the input baseline to target geometry using Equation [7] (Appendix A). An attempt is also made to automatically remove the elevation phase using the same baseline to target geometry and the input DEM, using Equation [11] (Appendix A). Since errors are inevitably present in the reported satellite positions, as provided in the master and slave image files, they result in an incomplete removal of both the flat-Earth phase and elevation phase. It is crucial to correct/remove the residual flat-Earth phase and elevation phase, as any error in the differential interferometric phase will propagate into the following coherence target analysis.

EV-InSAR provides a visual tool for identifying errors and adjusting the baseline geometry accordingly. Results can be examined with each correction of the baseline geometry until a satisfactory correction is obtained. EV-InSAR then calculates a new orbit for the Slave Satellite for the correction; this new geometry will be used to recalculate and remove the residual flat-Earth phase and residual elevation

phase. Although the removal of the residual phase is carried out in a visual environment, it is a difficult process due to noises caused by decorrelation and atmospheric effect. This process, requiring experience and patience, accounts for a major portion of the effort needed for the entire CTM analysis. Table 6 lists the corrections to the perpendicular baseline and the orbit Yaw parameter. The interferograms generated are included in Appendix B.

Table 6. Parameters used for correction of the baseline–target geometry

Run number	Master-Slave pair	Perpendicular baseline reported	Perpendicular baseline correction	Orbit Yaw correction
1	7/24/2004_12/12/2000	901.926	-155	-0.0012
2	7/24/2004_1/5/2001	-1294.995	-122	-0.0012
3	7/24/2004_9/2/2001	-2.4	-116	-0.0012
4	7/24/2004_9/26/2001	303.7	-122	-0.0015
5	7/24/2004_6/6/2004	-489.63	8	0
6	7/24/2004_6/30/2004	626.735	-2	0.0001
	7/24/2004_7/24/2004	Master		
8	7/24/2004_8/17/2004	90.258	-4	0
9	7/24/2004_9/10/2004	0.365	-7	0
10	7/24/2004_10/4/2004	573.99	-13	-0.0001
11	7/24/2004_11/21/2004	-445.71	12	-0.0003
12	7/24/2004_12/15/2004	438.055	14	0
13	7/24/2004_2/25/2005	-47.39	18	0.0001
14	7/24/2004_3/21/2005	-354.995	32	0
15	7/24/2004_4/14/2005	12.314	26	0.0003
16	7/24/2004_5/8/2005	-179.226	34	0.0004
17	7/24/2004_9/29/2005	695.558	33	-0.0001
18	7/24/2004_11/16/2005	304.997	54	0.0003
19	7/24/2004_1/3/2006	-118.581	-200	-0.0023
20	7/24/2004_5/3/2006	-154.225	-182	-0.0023
21	7/24/2004_5/27/2006	459.577	-180	-0.0023
22	7/24/2004_4/19/2004	250.35	-7	0
23	7/24/2004_6/20/2006	-174.53	-170	-0.0022
24	7/24/2004_7/14/2006	649.72	-180	-0.002
25	7/24/2004_8/07/2006	-62.95	-163	-0.002
26	7/24/2004_8/31/2006	-264.35	-155	-0.002
27	7/24/2004_9/24/2006	295.88	-155	-0.0023
28	7/24/2004_10/18/2006	-213.869	-143	-0.002

4.3 CTM Analysis

Upon completion of the interferometric processing, a time series of differential interferograms (see Appendix B) are generated such that

- all are registered with each other;
- all are processed to the same ROI; and
- orbital residual phase has been minimized using the residual phase removal tools.

These interferograms constitute the input data for the CTM analysis, which focuses on the temporal behaviour of each point target.

The first step for CTM analysis is to select the ROI for CTM analysis and the initial atmospheric/offset correction. The average phase of the initial atmospheric correction ROI is then subtracted from the interferometric phase and the resultant interferometric phase is then used to start the deformation model fitting. The ROI selection window in Figure 7 shows the backscatter image in the slant range coordinates. It is very important to select a stable area for the atmospheric correction ROI as the average phase for this area is assumed free of deformation phase in CTM analysis; this selection requires a priori knowledge of the study area. The CTM analysis area in this study is chosen from rows 1588 to 2451 and from columns 741 to 1851 in slant range coordinates (Figure 7). The atmospheric correction ROI (red rectangle in Figure 7) is selected as an area located within The Frank Slide at the foot of Turtle Mountain, ranging from row 2074 to 2115 and column 1258 to 1282 in slant range coordinates (Figure 7).

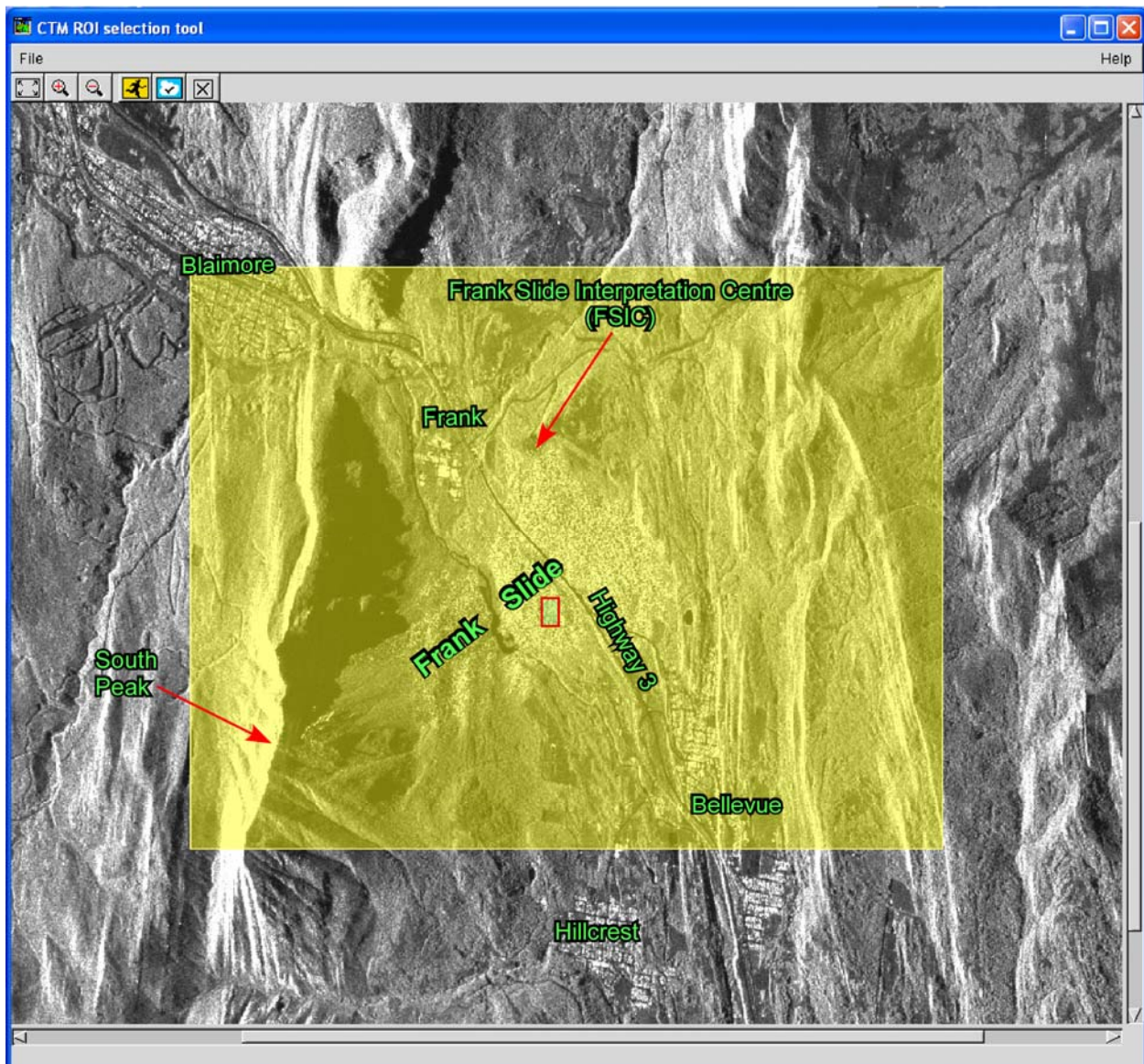


Figure 7. ROI selection window showing the CTM analysis AOI (yellow) and atmospheric correction ROI (red rectangle), displayed in the slant range coordinates.

The second step is CTM analysis that includes atmospheric correction, deformation rate modeling, DEM error estimation and temporal coherence calculation. It requires the user to input the search ranges of the deformation rate and the DEM error and, again, demands prior knowledge about the deformation and the accuracy of the DEM for the study area.

To avoid deterioration due to poor temporal baseline coverage, in the present study only the runs with scenes acquired from April 2004 to October 2006 are used. The resulting 23 runs/interferograms are from Run 5 to Run 28 (Tables 4 and 6). For CTM analysis in the present study, the deformation rate is defined as ranging from -56 mm per year to 56 mm per year in the radar line of sight, and the DEM error is defined as ranging from -25 m to 25 m. The atmospheric phase modeling used 2000 m as smooth length and a temporal coherence value of 0.65 as the threshold when averaging. CTM analysis produces an averaged backscatter image (Figure 8) and three types of results for each resolution cell: temporal coherence (Figure 9), DEM error estimated (Figure 10) and linear deformation rate (Figure 11).

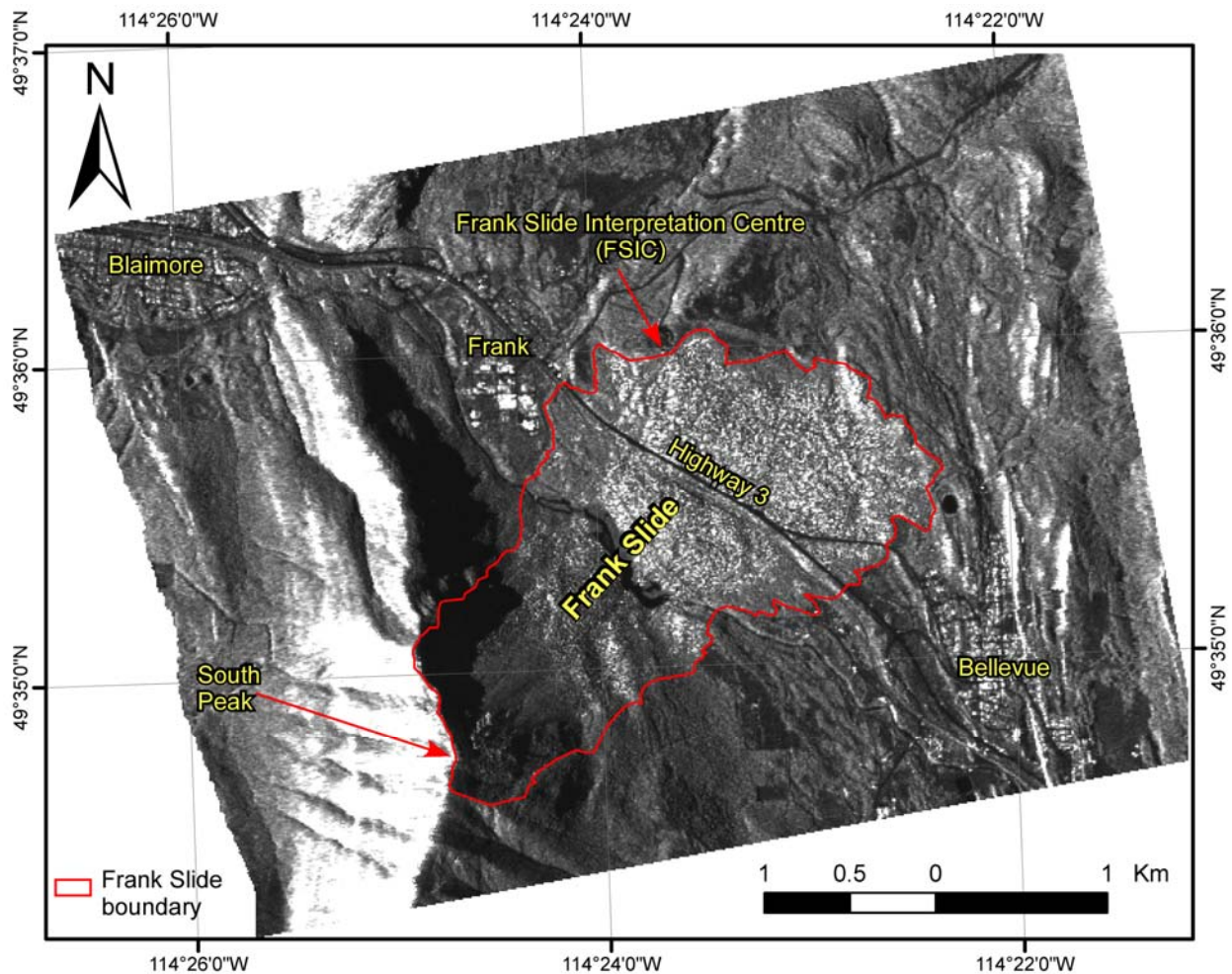


Figure 8. Average backscatter image generated by CTM analysis.

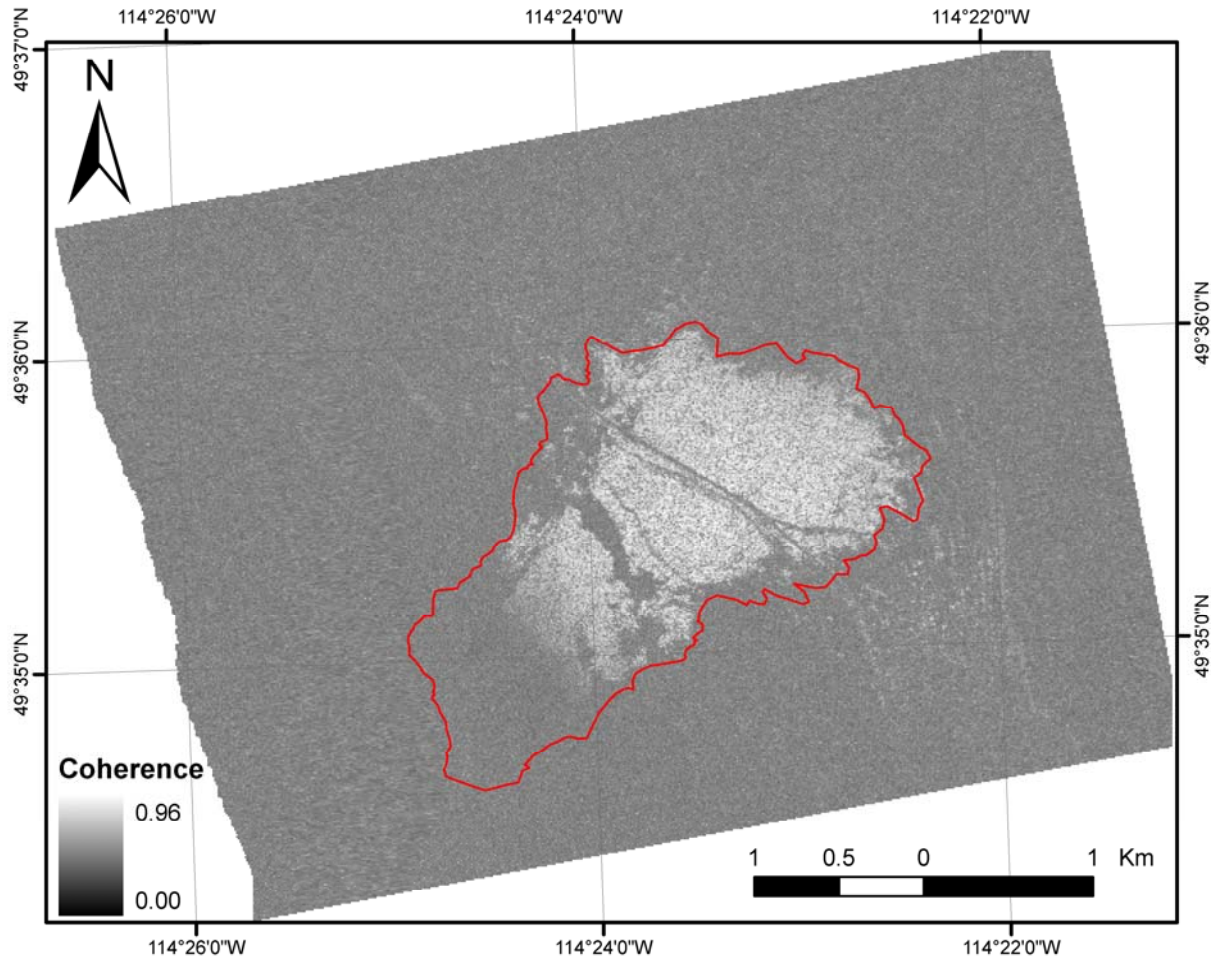


Figure 9. Temporal coherence image generated by CTM analysis. The Frank Slide boundary is outlined in red.

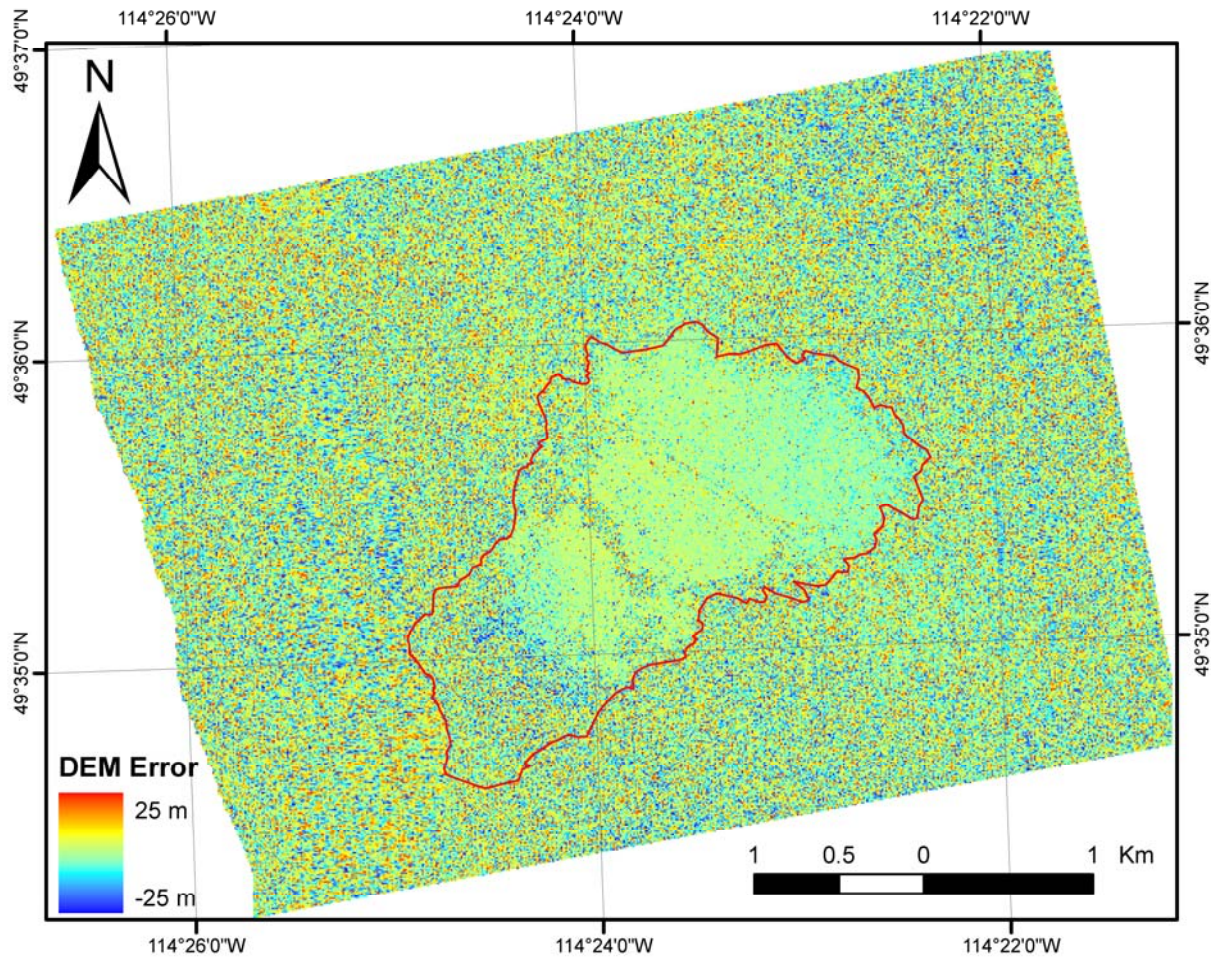


Figure 10. DEM error image generated by CTM analysis. The Frank Slide boundary is outlined in red.

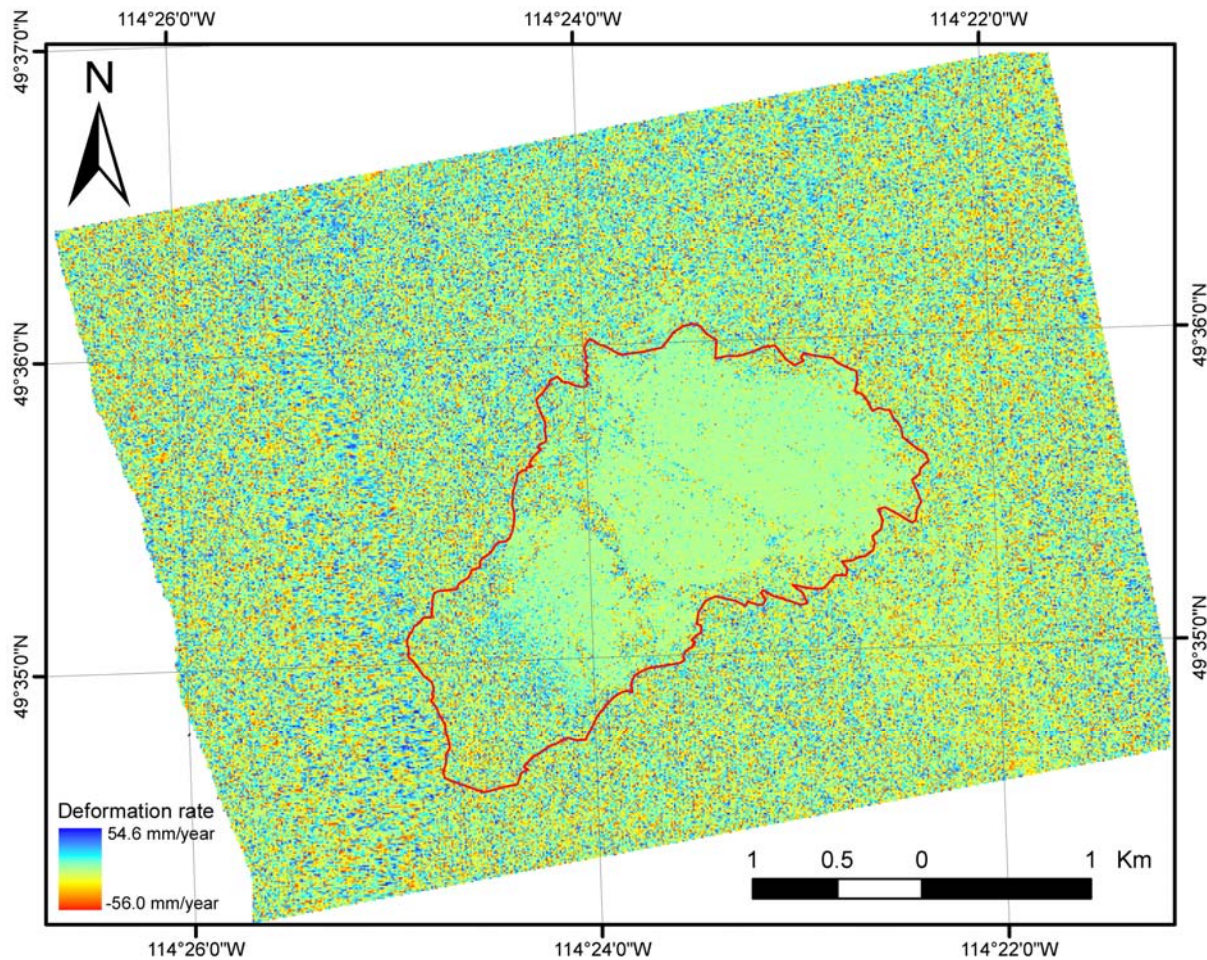


Figure 11. Deformation rate image generated by CTM analysis. The Frank Slide boundary is outlined in red.

As mentioned previously, only those points that have a temporal coherence value above a certain threshold can be regarded as coherent targets, and only the measurements obtained over the coherent targets can be considered for interpretation. In the present study, a coherence threshold of 0.65 is used for initial examination, based on the recommendation illustrated in Figure 53 (Appendix A). The targets obtained with this threshold are displayed in Figure 12 and colour-coded with the deformation rate. The deformation rate value represents the line of sight displacement relative to the stable and reference area (Figure 12); i.e., a negative deformation value is coded a reddish colour and indicates that the ground is moving toward the satellite and a positive value is coded a bluish colour and indicates that the ground is moving away from the satellite. A close examination of the targets reveals that 84% of the targets are concentrated over the lower two-thirds portion of the Frank Slide, and in this area, 98.6% of the targets are associated with an annual deformation rate ranging from -4 mm to 5 mm. A visual examination indicates most of the targets outside the Frank Slide (except the area to the southeast where the town of Bellevue is located) have a polarized annual deformation rate value (Figure 12); i.e., most of them are either greater than 5 mm or smaller than -4 mm. These targets are located mostly in shadow and vegetated or forested areas. In addition, they are not clustered according to their values but appear to be randomly distributed. These facts indicate that many of them might be identified as CTM targets by chance and, thus, simply represent noise. While some of these targets, which only represent isolated deformation events, may be associated with reliable deformation values, they act as random outliers for the evaluation of the regional deformation pattern.

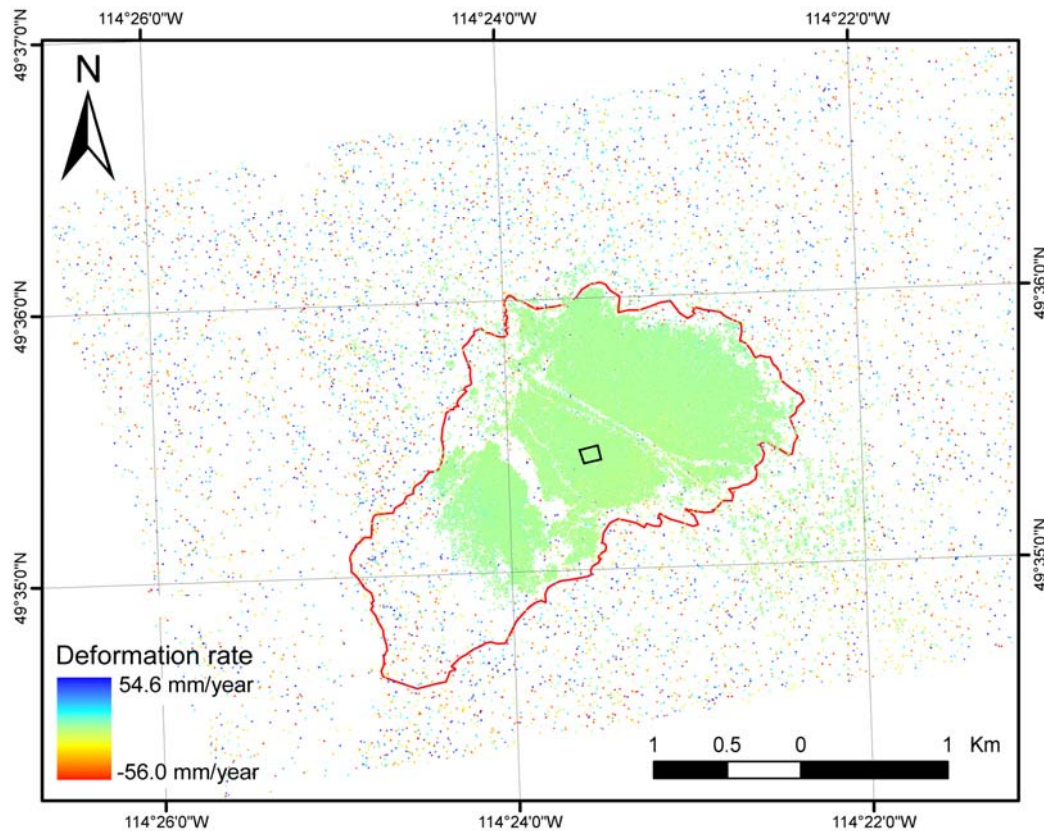


Figure 12. Deformation rates for the CTM targets defined with a temporal coherence threshold value of 0.65. The Frank Slide boundary is outlined in red and the reference area is denoted by the black rectangle.

For each target, CTM analysis produces four types of plots showing the deformation model (averaging annual deformation), time series of the wrapped phase, time series of the unwrapped phase and deformation profile (deformation versus year). Figure 13 shows an example of these outputs obtained by assuming the deformation is linear. For this target, the average deformation rate is estimated as 33.6 mm/per year and the temporal coherence 0.67. As mentioned previously, the EV_InSAR CTM module allows refinement of the linear model to achieve nonlinear deformation estimation. Figure 14 shows the refined version of these output plots using the smoothing refinement tool. The smooth length is defined as half year. The selection of a half year smoothing is due to the ground expansion with the winter to summer rise in temperature and contraction with the summer to winter decrease in temperature. With the refinement, the temporal coherence rises to 0.72 and the estimated average deformation rate decreases to 21.1 mm/per year. The decreased deformation rate is due to the use of a different deformation model for phase unwrapping; this can be observed by comparing the deformation profiles in Figure 13 and Figure 14. The refined model depicts a nonlinear deformation rate, and the direction of unwrapping of the three wrapped phase values from the year 2005 to 2006 is opposite to that of the linear model. The refinement also leads to many more point targets being identified as CTM targets with the same threshold. However, the refined nonlinear model cannot be confirmed for each target; this limits the validation of the refined targets.

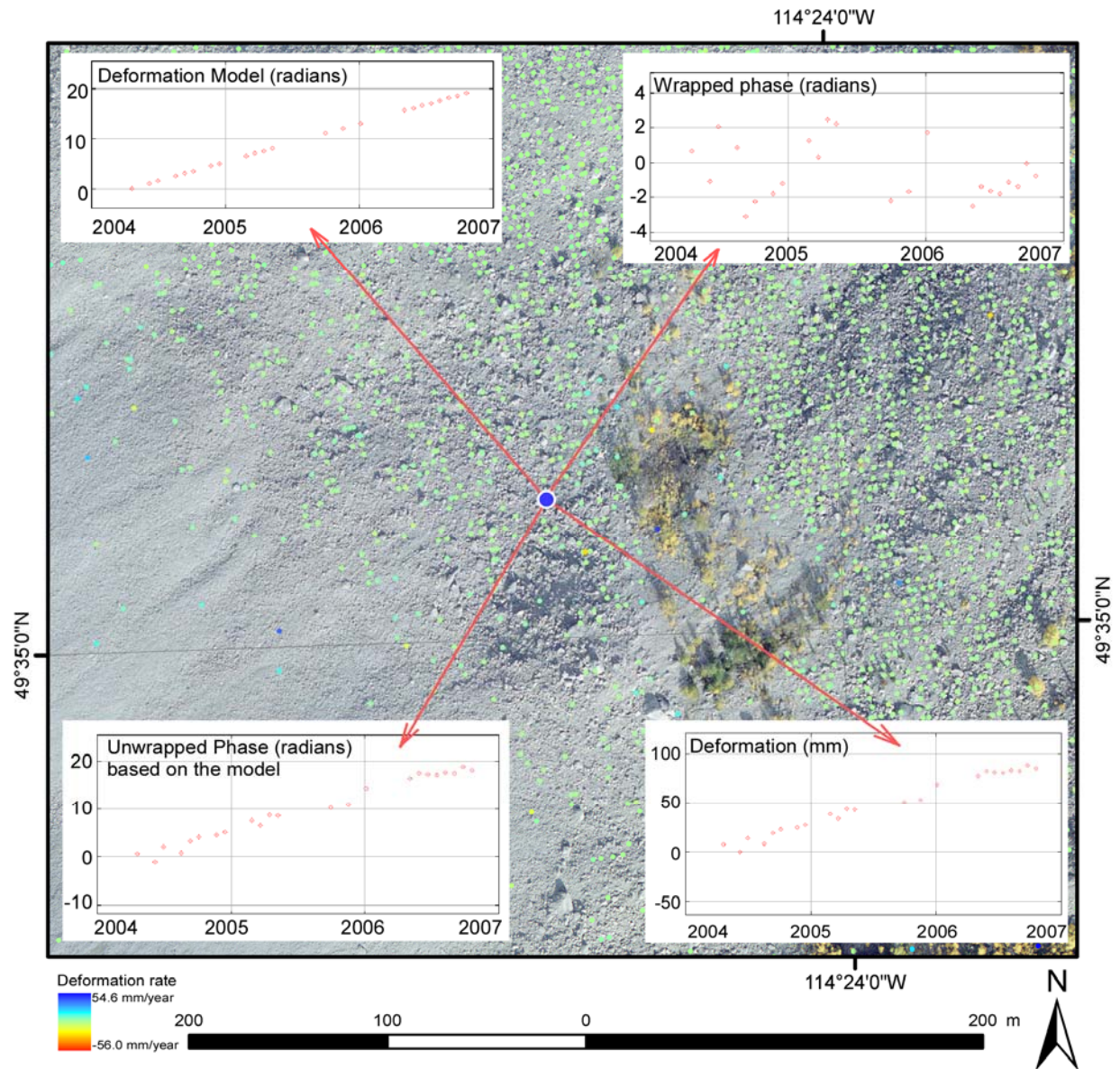


Figure 13. An example of plots showing the deformation model (averaging annual deformation), time series of wrapped phase, time series of unwrapped phase and deformation profile associated with a single target. The deformation is assumed to be linear.

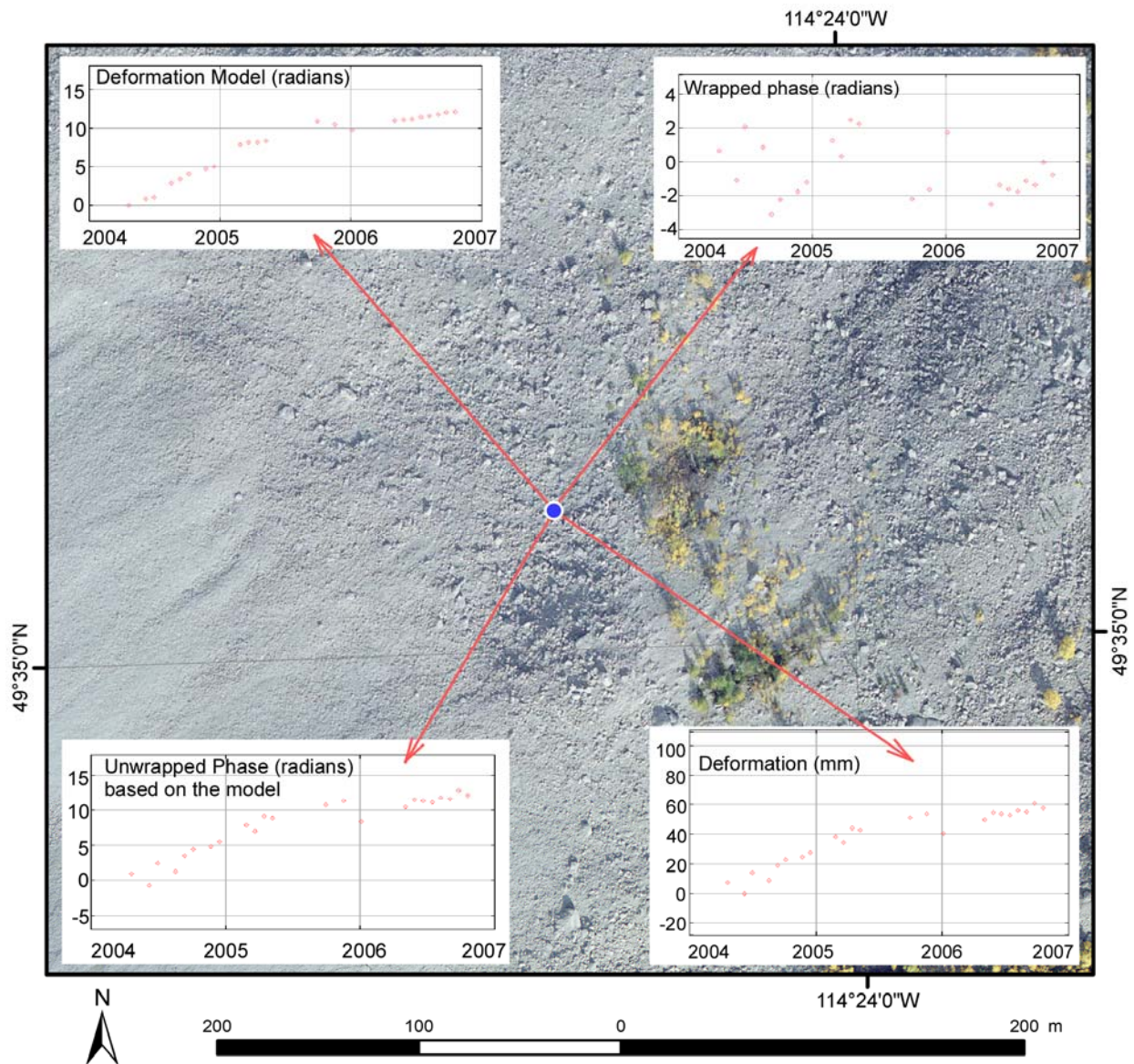


Figure 14. An example of plots showing the deformation model (averaging annual deformation), time series of wrapped phase, time series of unwrapped phase and deformation profile associated with the same target shown in Figure 13. The deformation is assumed to be nonlinear.

4.4 Statistical Evaluation of CTM Targets

4.4.1 Statistical Evaluation of Individual CTM Targets

Like differential Global Positioning System (GPS) measurements, all CTM measurements are relative measurements with respect to a reference area that is an assumed stable area and also used for the atmospheric correction (see Figures 7 and 12). The accuracy of CTM measurements depends on several factors, which include the number of images used, CTM targets density, climatic conditions, etc. Absolute measurements for CTM targets can be obtained only through calibration using ground control points (GCP). These GCPs may be obtained through differential GPS, optical levelling and thermal dilation surveying, etc. Once calibrated, measurements from the reliable/valid CTM targets can be used the same as data from other station-based surveying, including differential GPS, optical levelling and thermal

dilation. The advantages of PS-InSAR measurements are greatly increased density of measurements, larger coverage and cost effectiveness. These factors contribute to PS-InSAR's emergence as a competitive surveying tool for monitoring of millimetre-scale dynamic deformation processes.

However, as implied previously, some of the CTM targets are simply identified by chance due to inaccuracy of the deformation model, inherent weakness of the temporal coherence calculation and atmospheric disturbance, etc. The measurements on these targets are not reliable and should be excluded from the final interpretation. In PS-InSAR applications, the most crucial step is to assess the reliability of the targets and use only those targets that are reliable for interpretation.

Some of the false targets, such as those located in shadow, water (lakes and rivers) and forest canopies, can be located by visual examination. In these areas, the phases recorded are not reliable. The best way to evaluate an individual target is to examine the plot of its time series of wrapped phases, and compare it with the deformation model and unwrapped phases. For example, if the wrapped phases are tightly following a straight line within each phase cycle and the deformation is found to be linear, this may be a strong indication that the target is a coherent and moving target. CTM analysis usually generates hundreds of thousands of targets with a certain threshold of temporal coherence, and it is cumbersome to evaluate them by visually examining the point profile plot of each target. The solution to this is statistical analysis.

Statistical analysis is used here to quantify the noise level of the deformation rate measurement for each target. First, a linear regression is carried out for the unwrapped phases plotted against time, based on the linear model. The slope of the regression line represents the measured deformation rate. Then, the standard error of the slope of the regression line is calculated. The more rigidly the unwrapped phases follow the regression line, the smaller the standard error and the more reliable the target is presumed to be. Similar to the temporal coherence, standard error can be regarded as a measurement of reliability of the targets. Figure 15 shows that the standard error and temporal coherence are closely related; with a threshold value of 0.65, the standard errors are mostly below 5 mm. In addition, Figure 15 shows a small number of targets with a large standard error (defined as greater than 5 mm) that deviates from the correlation trend; this indicates the temporal coherence threshold of 0.65 is still associated with some remaining unreliable targets. These targets are associated with a temporal coherence that is smaller than 0.8. Although raising the temporal coherence threshold to 0.8 will eliminate these unreliable targets, it simultaneously eliminates many fairly reliable targets for the site of interest.

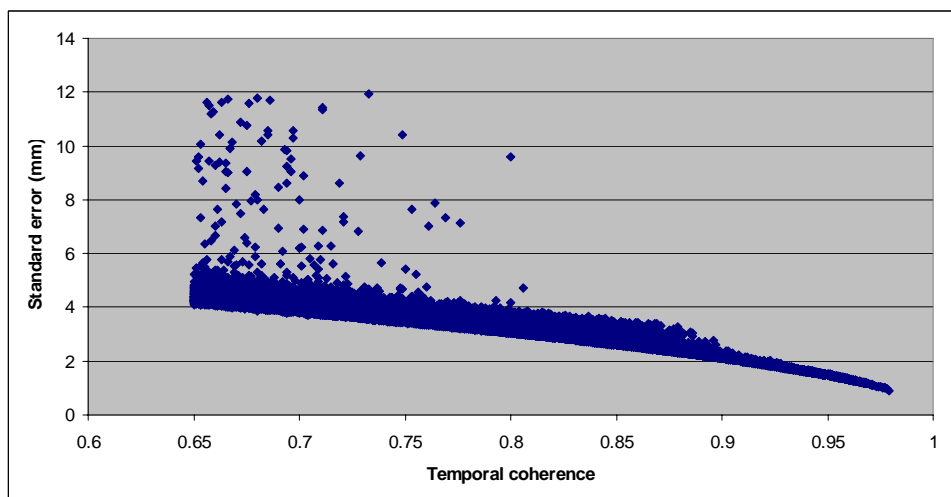


Figure 15. Crossplot of the temporal coherence and the standard error of the slope of the regression for the unwrapped phases for each CTM target identified with a temporal coherence threshold value of 0.65.

The targets can also be evaluated by treating the deformation rate as a signal and examining its strength relative to the standard error. The strength of the deformation signal can be quantified by dividing the deformation rate by the standard error. If the deformation rate (the slope value of the regression line) is greater than a certain threshold (e.g., three times the standard error) this could indicate that the signal level is strong enough to make the deformation rate a reliable measurement. Figure 16 shows the targets with a deformation value that is greater than three times the standard error.

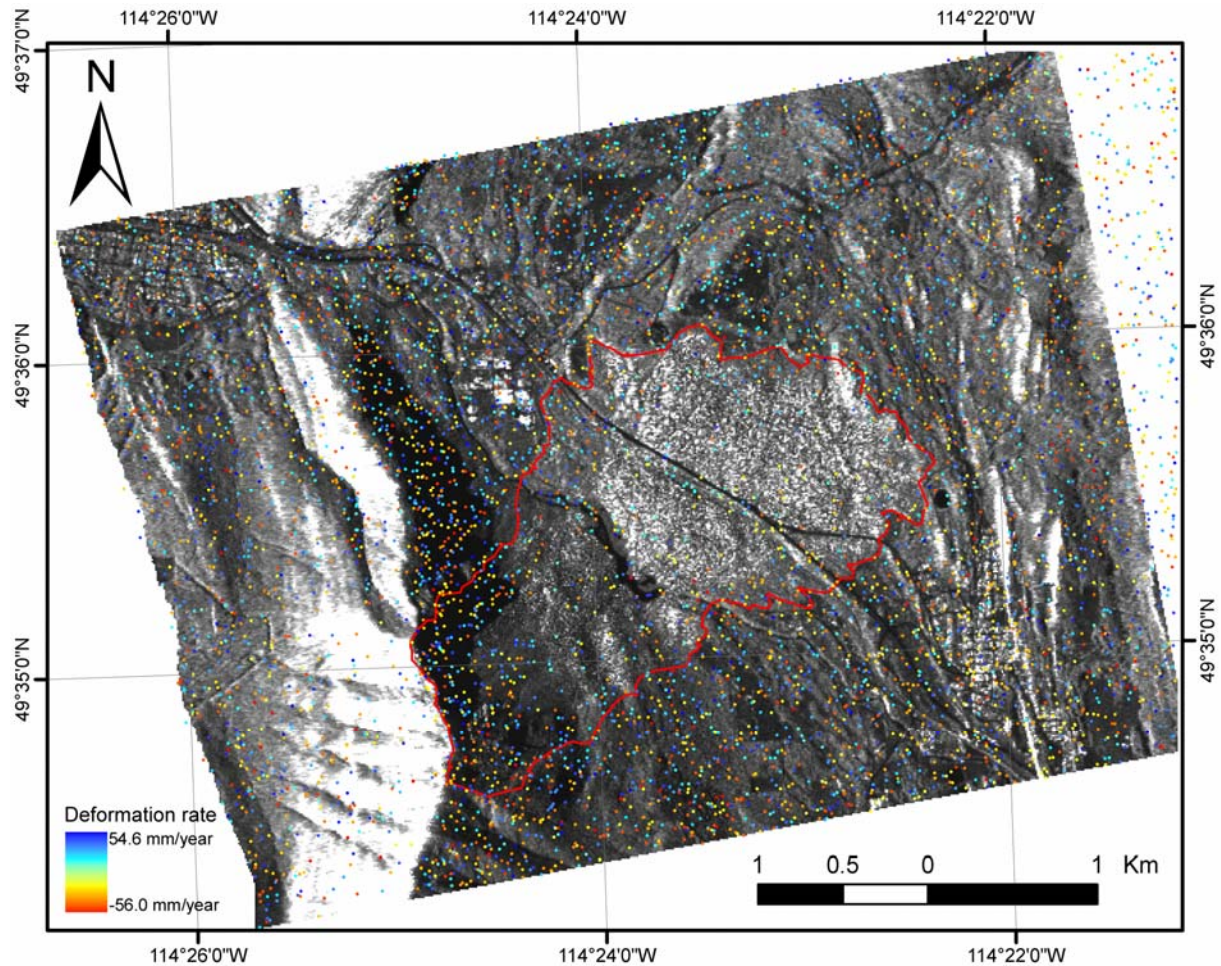


Figure 16. CTM targets defined with a temporal coherence threshold value of 0.65 and a ratio of deformation rate to standard error greater than three. The Frank Slide boundary is outlined in red.

Two observations can be made by examining Figure 16. One observation is that some of targets are located in shadow, water (lakes and rivers) and forest canopies. Some of these points are selected as CTM targets by chance because the phase returned from these areas is not reliable. They are false targets and should be excluded. This indicates that this statistical method for selecting the reliable targets depends on the land cover type and should be used in combination with visual examination of terrain conditions. Only those targets that are located on exposed rocks and buildings can be considered. The second observation is that most of the targets located in the lower two-thirds of the Frank Slide are not picked up by this statistical analysis. These targets are located in a highly coherent area (compare Figures 9 and 12) and thus, most of them are reliable targets. However, they are not identified by the statistical analysis because they are located in a relatively stable area and have a very small deformation rate value or a weak deformation signal. This can be confirmed by examining the histogram of the identified targets using the statistical analysis (Figure 17). The histogram clearly shows that the targets picked up with the statistical

analysis have an absolute annual deformation rate that is greater than 10 mm. In the stable area, only those targets with a deformation rate greater than 10 mm are picked up by the statistical analysis. This indicates that the selection method using the strength of deformation signal does not work for stable areas or areas where the deformation rate is very small (close to zero). It also should be noted that this analysis requires a minimum number of at least 20 observations for each target to make a reliable assessment whether the deformation rate measurement exceeds the noise level.

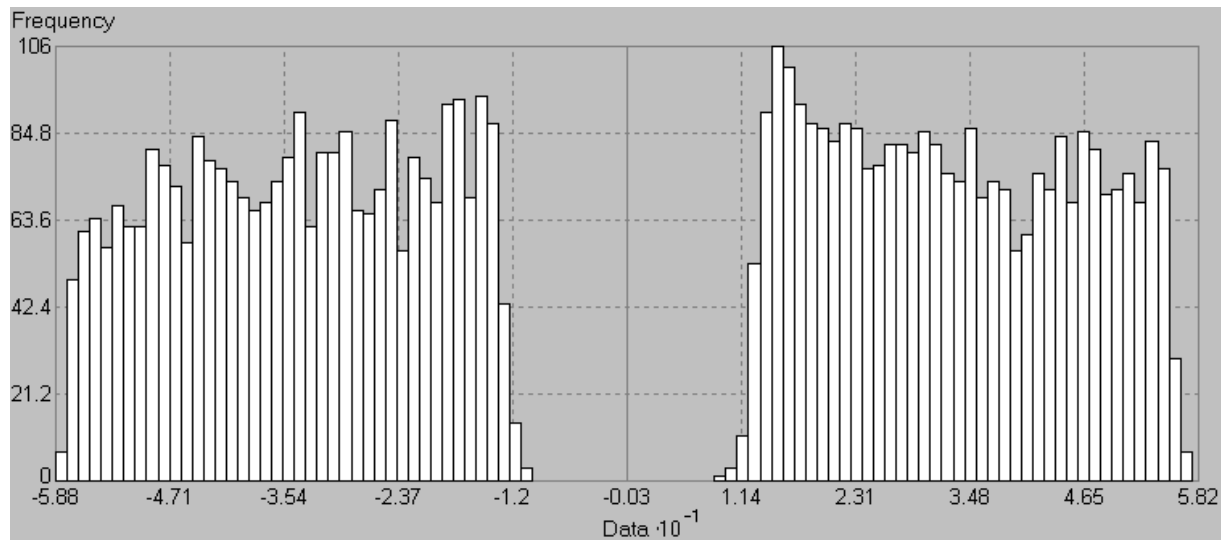


Figure 17. Histogram of CTM targets defined with a temporal coherence threshold value of 0.65 and a ratio of deformation rate to standard error greater than three.

4.4.2 Geostatistical Evaluation for Regional Deformation Pattern

The advantages in great density and large coverage also render the PS-InSAR a multiscale surveying tool for ground deformation. In addition to focusing on measurements over isolated point targets, it is the regional deformation pattern that becomes the focus of interest in most applications. The regional deformation pattern can be obtained by interpolating measurements from isolated point targets using geostatistical analysis.

For evaluation of the regional deformation pattern, only clusters of targets over a high temporal coherence area should be considered. Within each of these clusters, a small number of targets may still be associated with uncommon and/or polarized deformation values. These uncommon values—even though they may be found to be valid targets—should be treated as outliers when the regional deformation pattern is the focus of interest, as they represent only isolated local displacement events. These targets can be identified and removed using geostatistical analysis. Figure 18 shows the targets clustered within the lower two-thirds of the Frank Slide and Figure 19 shows the histogram of the deformation values. These targets are located in the coherent area, as shown in Figure 9, and, thus, can be used for deformation pattern analysis.

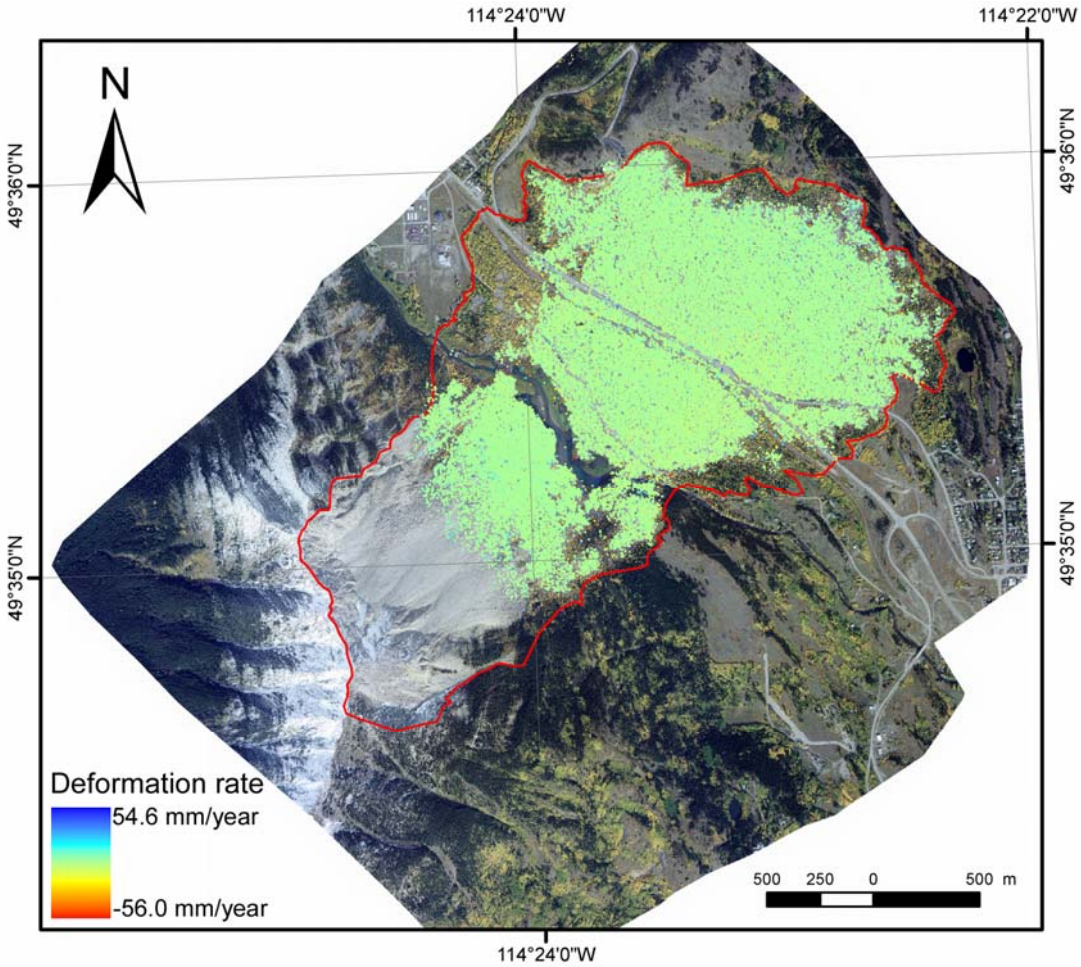


Figure 18. CTM targets defined with a threshold value of 0.65 and clustered within the lower Frank Slide. The Frank Slide boundary is outlined in red.

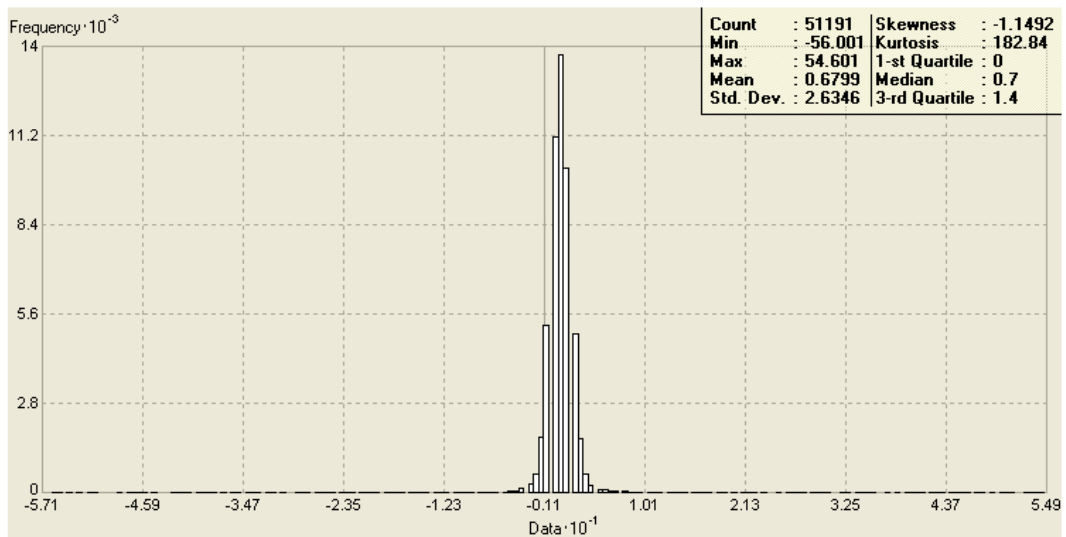


Figure 19. Histogram of deformation rate values of CTM targets clustered within the lower Frank Slide.

The histogram of the deformation values (Figure 19) shows that a small amount of values contributes to an extremely thin tail on both side of the histogram. Most of these values are located more than two standard deviations away from the mean (0.68 mm) and are found mostly to be distributed in the marginal areas in spatial distribution and randomly distributed according to the value. They represent global outliers and should be removed from the analysis when the regional deformation pattern is the focus of interest. Figure 20 shows the targets within the lower two-thirds of the slide after removal of the global outliers and Figure 21 shows the new histogram of the deformation rate values. The deformation pattern become clear after removal of the outliers (compare Figures 18 and 20).

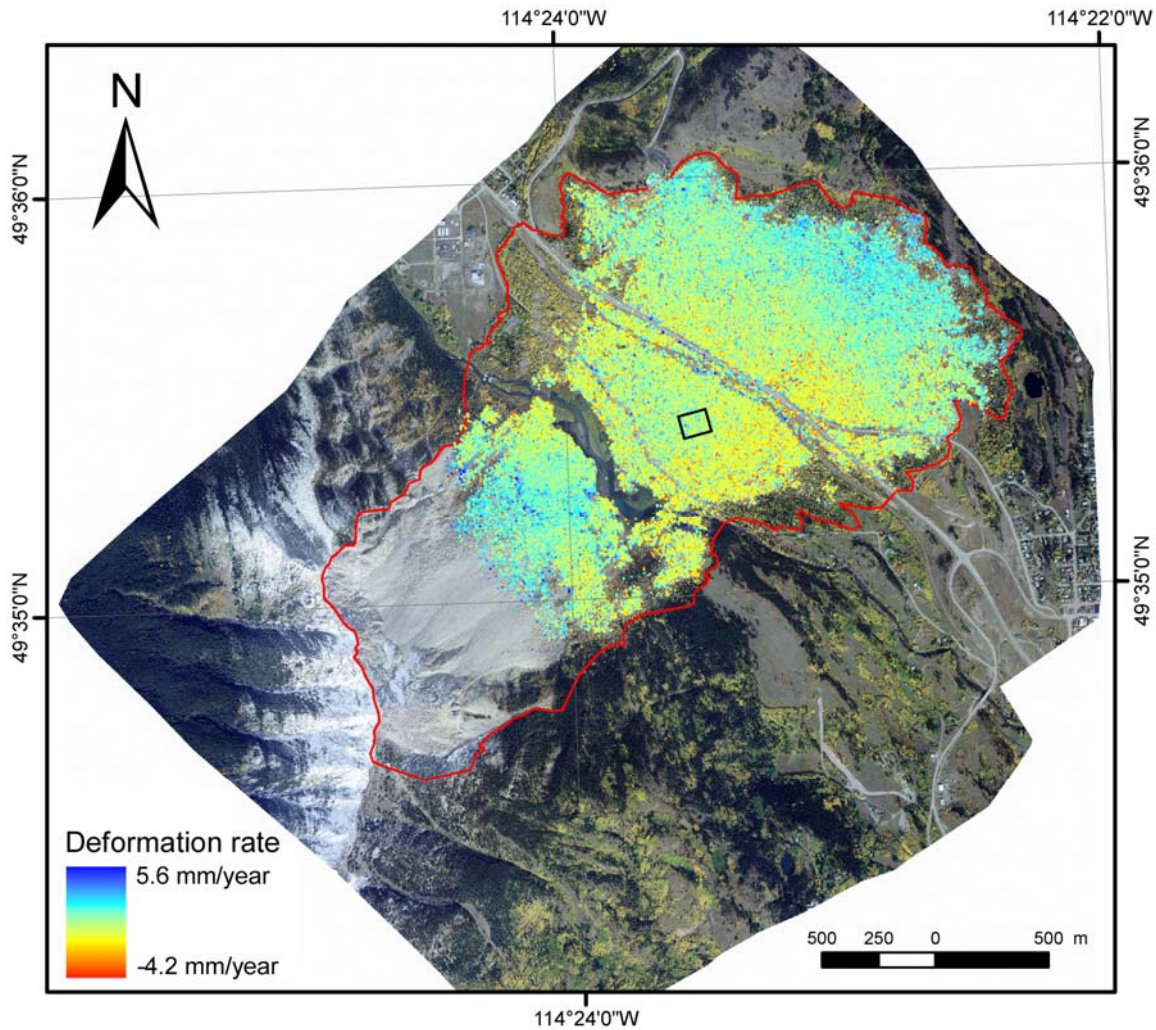


Figure 20. CTM targets defined with a threshold value of 0.65 and clustered within the lower Frank Slide after removal of outliers. The Frank Slide boundary is outlined in red and the reference area is denoted by the black rectangle.

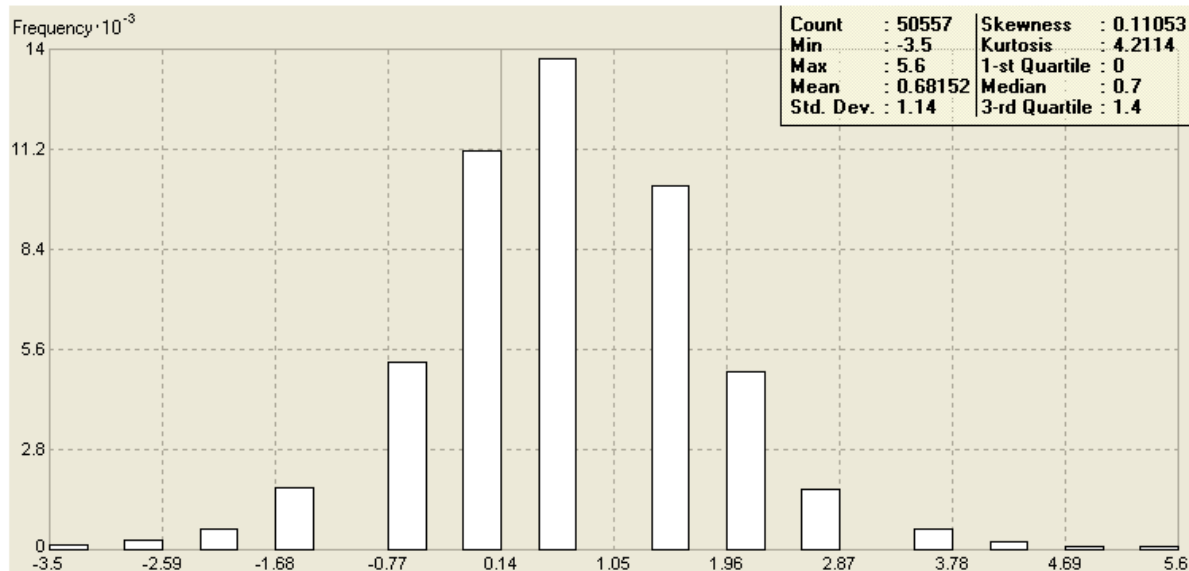


Figure 21. Histogram of deformation rate values of CTM targets clustered within the lower Frank Slide, after removal of outliers. The discreteness of the values is due to the search template that uses a fixed increment values for the deformation rate in CTM analysis.

5 Results and Interpretation

5.1 Overview of Deformation Processes

Prior to reviewing the results of the PS-InSAR analysis at Turtle Mountain, a discussion of the observed movement and processes is necessary. In broad terms, there are three main types of ground deformation observed in the Frank Slide: rock slope movements, talus slope movements and coal mine subsidence. The following discusses these types of deformations and provides visual examples as a basis for the discussion of the results obtained from the PS-InSAR analysis.

Rock Slope Movements: The rock slope movements are defined as deformations of intact blocks of rock on the mountain and are assumed to represent materials that are moving for the first time. These movements can be classified either as discrete, localized features that topple and fall near the crest of unstable areas, or deeper-seated systematic deformations that encompass hundreds of thousands to millions of cubic metres of rock mass that either move by sliding and/or rotation. At Turtle Mountain, we see examples of both movements at the crest of the mountain on the South Peak and saddle areas (Figure 22). At the top of the saddle—the headwall of the 1903 slide—there are large wedges and blocks left unsupported by the 1903 slide and these blocks have slowly moved toward the east since that time. On an annual basis localized blocks or series of blocks are observed to topple and fall into the debris of the 1903 slide. An aerial view of this area is shown in Figure 23.



Figure 22. Aerial view of the west side of the peak on Turtle Mountain showing South Peak, the saddle and North Peak. The view is looking toward northeast.



Figure 23. Close-up aerial view of toppling blocks and large boulders that comprise the saddle between North and South Peaks. The view is to the south.

Beginning in 1933, numerous studies have been undertaken on South Peak to understand the rate, extent and style of movement for a potential large, deep-seated rock slide with an estimated volume of 5 million m^3 . Since 2003, a network of sensors has been installed and studies undertaken to understand the processes that are ongoing at South Peak and the rest of the mountain. An overview of this network and studies are provided by Moreno and Froese (2006) and Froese and Moreno (2007). Since then, an understanding of the movement rates and patterns on South Peak are slowly being realized. A more thorough treatment of the characterization of deep-seated rock slope movement at South Peak is discussed in a following section.

Talus Slope Movements: Below the steep cliffs formed by the 1903 landslide headwall are aprons of colluvium that are comprised of approximately 30 million m^3 of rock debris. Recent deposits range from blocks and boulders that fall into the 1903 debris on an annual basis to a relatively large deposit of many thousands of cubic metres that was deposited as the result of a large rock slide in the vicinity of North Peak in 2001. These deposits consist of gravel-size particles to very large boulders (up to many metres in diameter) that rest at quasi-stable angles after deposition and slowly move downslope due to gravity and seasonal changes in moisture and temperature. Specific aspects of these movements will be discussed in relation to the PS-InSAR results in Section 5.5.

Coal Mine Subsidence: In the early 1900s, there was significant underground coal mining activity in the Crowsnest Pass. Mines were typically excavated using room and pillar mining techniques where large portions of a coal seam were mined by hand and the coal removed via horse-drawn pull carts. After the completion of mining, the large rooms were abandoned and left supported by pillars of intact coal. Over time, as the integrity of these pillars decayed, the roofs of the rooms would slowly yield, leading to subsidence at the surface. Often, pillars were robbed to improve yield from the mines, additionally destabilizing the mine workings. In some cases, this slow deformation is a gradual process that eventually leads to collapse at the surface. In the vicinity of Turtle Mountain, there were three main mines: Frank Mine, Hillcrest Mine and Bellevue Mine (Figure 24). Specific discussion of deformations associated with the Frank and Bellevue mines is discussed in Section 5.5.

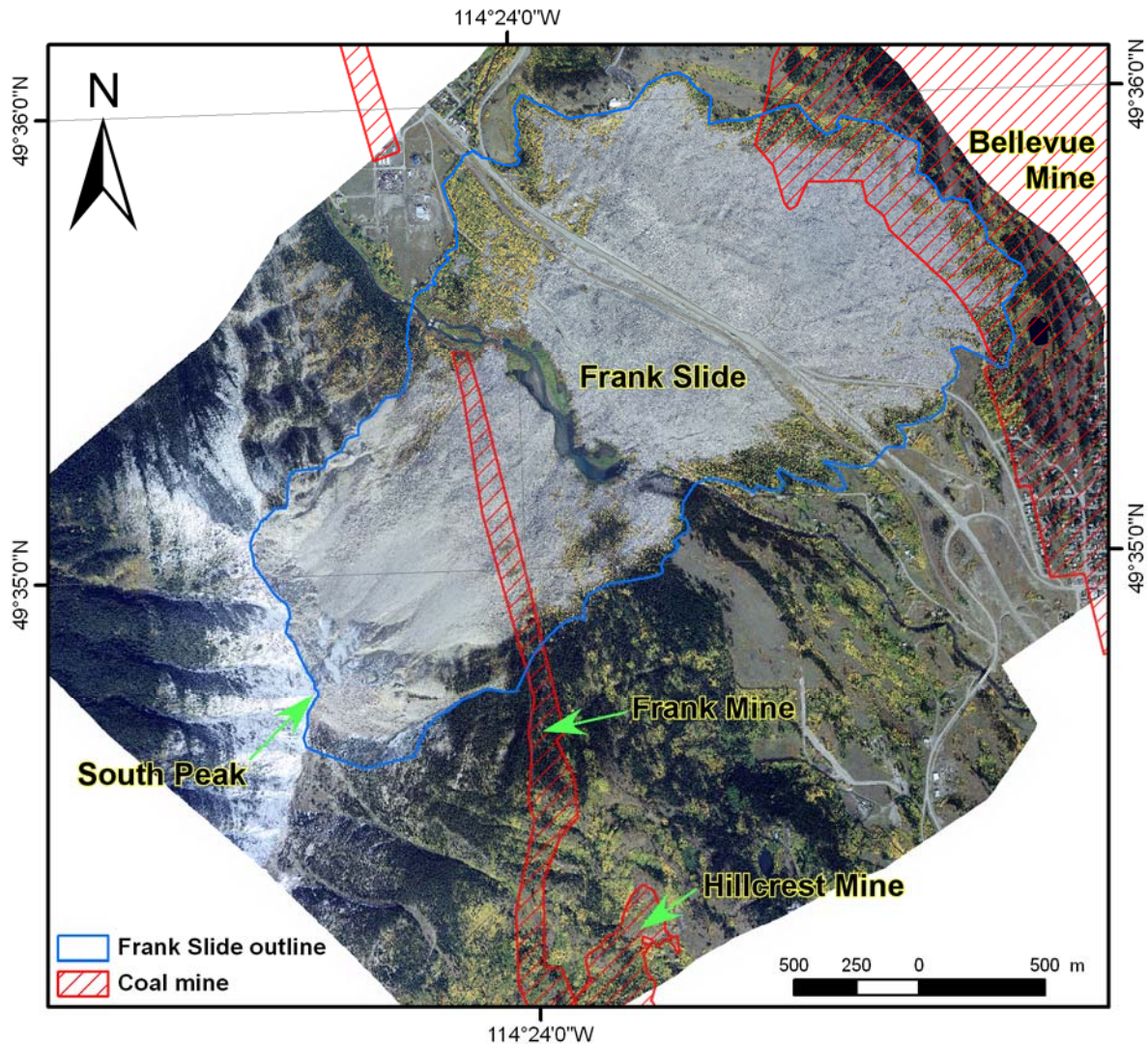


Figure 24. Locations of the Frank, Hillcrest and Bellevue mines.

The following discussion will be divided into five specific areas: Peak (South Peak and Saddle), Upper Slope Frank Slide, Lower South Peak, Lower Slope Frank Slide (Colluvium) and Valley Bottom (Figure 25). Regarding the quality of data obtained from the PS-InSAR analysis, these five areas can be classified into two groups that are strikingly different in temporal coherence and number of CTM targets that can be identified. The Lower Slope Frank Slide (Colluvium) and Valley Bottom are characterized by good temporal coherence (compare Figures 9 and 25) and contain more than 95% of CTM targets, obtained

with a coherence threshold of 0.65, within all of the five areas. This is because the base of the valley is covered by bare, dry rock and any deformations are likely very slow and systematic as the materials have had over 100 years to settle since their deposition in 1903. In contrast, the other three areas, including South Peak, Lower South Peak and Upper Slope Frank Slide (Figure 25), contain only sparsely distributed targets. Reasons for the lower quality data from the upper portion of mountain are due to the effects of steep topography on the radar returns and on the variability of deformations of more active colluvium on the upper slopes. On the west side of the mountain, there are significant distortions of the data returns of the satellite due to a phenomenon called foreshortening. As explained previously, the foreshortening effect contributes to the low number of CTM targets on the west facing slope of South Peak. On the upper portions of the eastern side of the peak, there are portions of the mountain that are in the satellite's "blind spot" and only a shadow is visible in the backscatter images. Similar to shadow from optical light sources, shadowing with radar occurs when the slope facing away from the radar is so steep that no reflection can occur. This means that no suitable information is available related to motion. Another reason for the low number of targets for the Upper Slope Frank Slide could be that the exposed areas experienced frequent, irregular surficial movement of rock fragments/debris due to gravity and seasonal changes in precipitation/moisture and temperature and, thus, are not as temporally coherent as the lower Frank Slide (Figure 9). In addition, the upper slope of the Frank Slide is also different from the Lower South Peak area in that it is covered by much finer debris. As a result, it may look smooth to the radar sensor. This also causes inadequate signal return from the smooth surface (i.e., energy is reflected away by the smooth surface). Regardless of these adverse factors, some targets—although sparse—are identified for these areas and provide clues to possible ground movements.

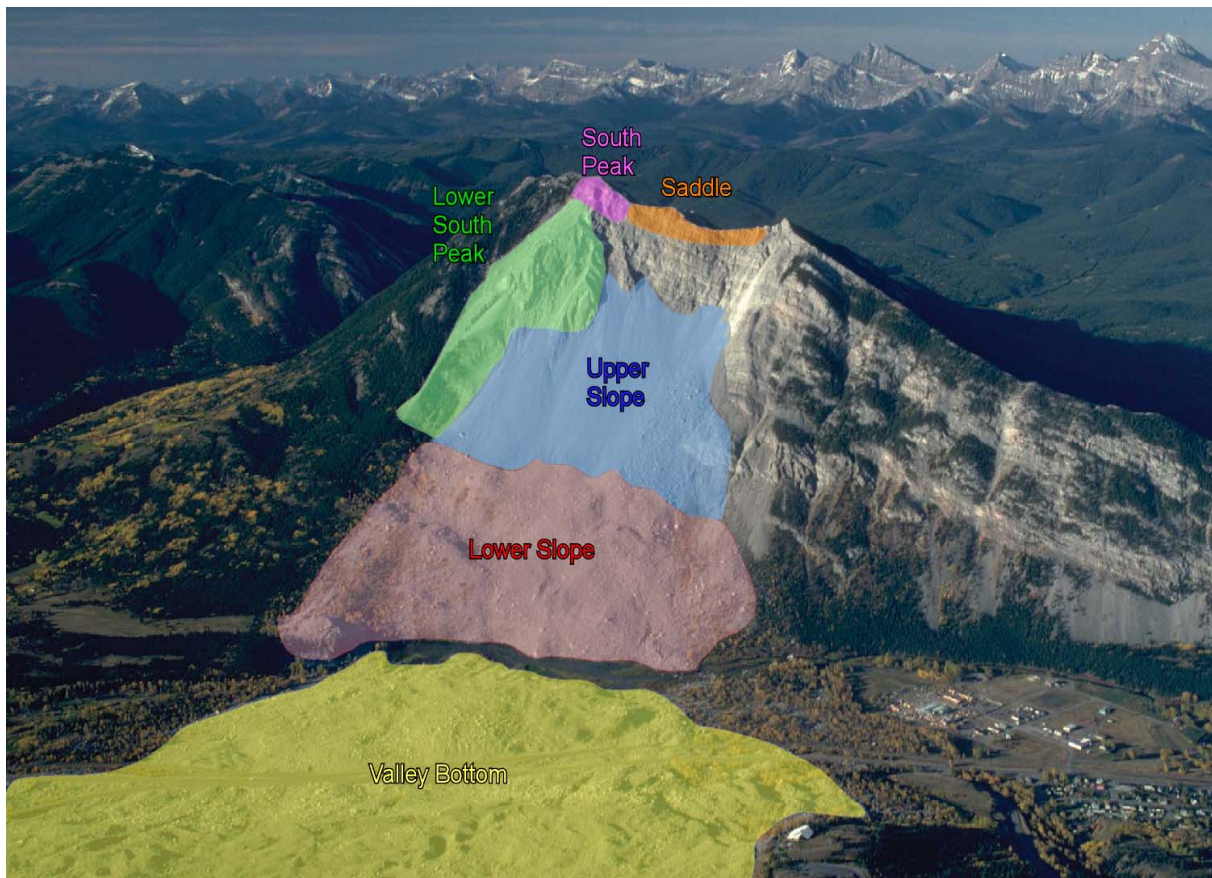


Figure 25. View of the east side of Turtle Mountain illustrating the zones discussed in the following sections.

In light of the PS-InSAR measurements, three types of movements have been identified in these areas: movement of loose rock fragments/debris on the surface, deep-seated movement of the entire ground as a whole block beneath the loose rock fragments and a combination of the two. The first type of movement is herein referred to as **surficial movement**. It is usually an irregular and periodic downslope movement that can be attributed to combination of gravity and processes that include the freeze-thaw process, precipitation, rainfall-runoff and wind. The second type of movement is herein referred to as **ground movement**. The ground movement is systematic movement responding to the force of regional stress that acts over a long time. PS-InSAR techniques are designed for identifying ground movement, which is also the focus of the present study. As discussed above, the surficial movement causes temporal decorrelation and, thus, can hinder the identification of the ground movement. In addition, it is possible that the movement of a target represents a combination of the two; e.g., the slow surficial movement of a target is induced by and superimposed upon the underlying ground movement. All of these three types of movements are represented by the PS-InSAR results.

5.2 Ground Movement near South Peak/Saddle

As indicated previously, the bedrock movements at South Peak have been the focus of periodic monitoring since 1933 and intensive studies since 2003. One of the monitoring approaches uses photogrammetry, and the details of the analysis are outlined by Chapman (2006). A series of photogrammetric targets was installed in the early 1980s by the University of Calgary (Fraser, 1983). Twenty-four targets were installed to give broad coverage around the area of South Peak, including points considered to be stable to the west and south, and areas that were considered to be more active to the north and on the east side of South Peak. The concept behind the approach was that a large number of targets would be installed and photographed over time by low-level photogrammetric flights at the same scale and under the same constraints, so that the relative movements of the array could be determined using a point-movement-localization procedure (Chapman, 2006). As shown in Figure 26, movement rates detected in horizontal directions indicate that deformations of up to 88 mm were observed on the east side of South Peak, with movements on the larger mass—between South Peak and Crack 1 (see Moreno and Froese, 2006, Figure 8)—ranging between 19–42 mm in the years 1982–2005. These rates correspond to average deformations of 0.9–3.2 mm/year over the 23 year period (Moreno and Froese, 2006). Due to the rugged and unstable nature of the saddle area between South and North peaks, there is no quantifiable data available to understand the rates of deformation. Specifically in the Saddle area, remote sensing data would be an ideal solution for monitoring due to the area's rugged and unstable nature. Figure 26 shows that movements for each photogrammetric target are different in both magnitude and direction, indicating the complexity of deformations of the peak, which is likely subjected to a combination of sliding-along bedding, toppling on the eastern face and possibly rotation due to movements to the east.

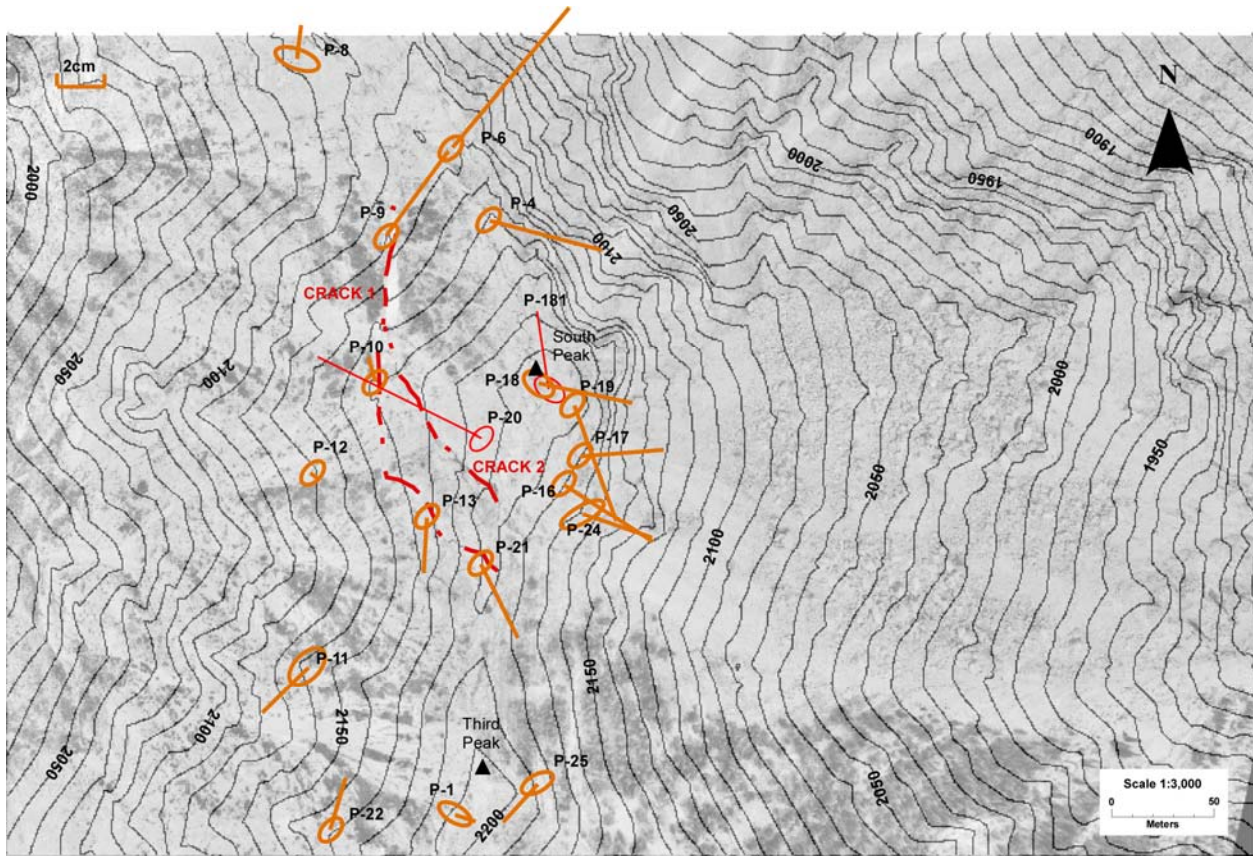


Figure 26. Horizontal deformation vectors (with 95% confidence ellipses) representing deformations between 1982 and 2005 as determined from photogrammetric measurements (after Moreno and Froese, 2006). Lines extending from ellipses represent direction and amount of movement (note bar represents 2 cm of movement in upper left corner).

With the selection of the F4F ascending beam mode, and an incidence angle ranging between 43.8 and 46.1 degrees, the satellite line of sight is close to the direction perpendicular to the face of the saddle and South Peak, and, therefore, is subject to distortions of the signal backscattered to the satellite. This distortion, known as foreshortening, can occur when a steep slope is essentially perpendicular to the line of sight of the satellite and many points on the slope appear to be the same distance from the satellite. The SAR will then interpret all of these points to be compressed into one pixel on the slope, even though they come from many different locations. Due to the effects of extensive foreshortening, the detection of large quantities of coherent targets around the peak area is difficult and the physical location of the targets detected questionable. Therefore, no reliable data have been gained with the CTM analysis to aid in understanding the systematic deformations of the peak; rather, just discrete measurements of blocks or boulders in the peak area.

For the South Peak area, four CTM targets are identified and all of them have a temporal coherence greater than 0.65 and a deformation rate to standard deviation error ratio greater than 3 (Figure 27). The deformation rate is measured in the line of sight of the radar sensor. In case of the fine beam 4 far ascending mode used in this study, the line of sight of the radar sensor for Turtle Mountain is around azimuth 81.5° and its depression angle is around 45° . This line of sight direction is close to the downslope direction of the eastern slope of Turtle Mountain. A positive value of the deformation rate indicates that the target is moving away from the radar sensor in the line of sight and coded with a bluish colour. All of the four targets indicate movement away from the sensor, or downslope movement, from April 2004 to October 2006. The deformation rate is about 23 mm per year and becomes greater toward the eastern

margin. Although the four specific targets are shown on Figure 27, the locations where these results are derived are questionable, due to extensive foreshortening and uncertainty associated with co-registration. Based on the results of previous monitoring of photogrammetric targets on South Peak, maximum deformations in horizontal directions (Figure 26) of an average of 3.5 mm/year have been reported (with deformation rates of less than 1 mm/year being more typical; Moreno and Froese, 2006). These photogrammetric measurements are measured in different directions in a horizontal plane (Figure 26) and cannot be compared directly with the PS-InSAR results that are in the radar line of sight direction. In addition, the uncertainty associated with the photogrammetric measurements remains questionable. However, the reported rates on the four CTM targets generally appear greater than the photogrammetric measurements. This may indicate that these targets represent only discrete blocks toppling off of the east side of the peak or boulders on the lower east peak (see Figure 23 for the fracture intensity). These results may not represent the systematic, deep-seated deformations of the peak itself as an entire block.

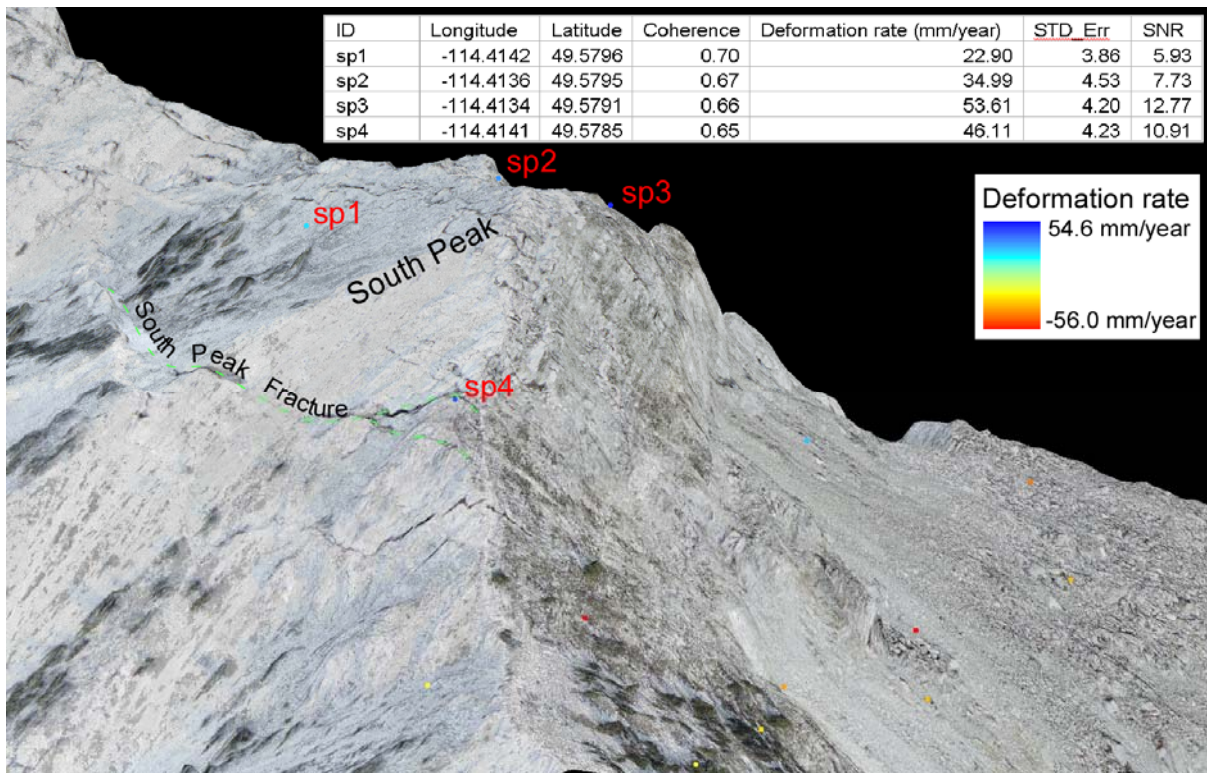


Figure 27. CTM targets identified for South Peak (view to northeast). In the insert table, STD_err stands for standard error of the deformation rate, obtained from a linear regression of the unwrapped phase values for each point target. SNR represents signal to noise ratio calculated as the ratio of the deformation rate to its standard error. The longitude and latitude coordinates are based on North American Datum (NAD) 83.

For the measurements of targets representing discrete blocks, the deformation rate represents the average and long term displacement trend. Short term and periodic movements can occur due to seasonal change in temperature and precipitation. Figures 28 to 31 show the wrapped phase and deformation profiles of the four targets. The deformation profiles suggest that short-term and periodic movements exist and are superimposed on the long-term deformation trend. These short-term undulations can be estimated—by examining both the deformation profiles (Figures 28 to 31) and the standard error of the unwrapped phases (Figure 27)—as up to approximately 4 mm in magnitude off the long-term deformation trend. These trends are consistent with those observed on instrumentation with accelerations in the spring due to snow melt and with lower levels of deformation observed in the winter under frozen ground conditions.

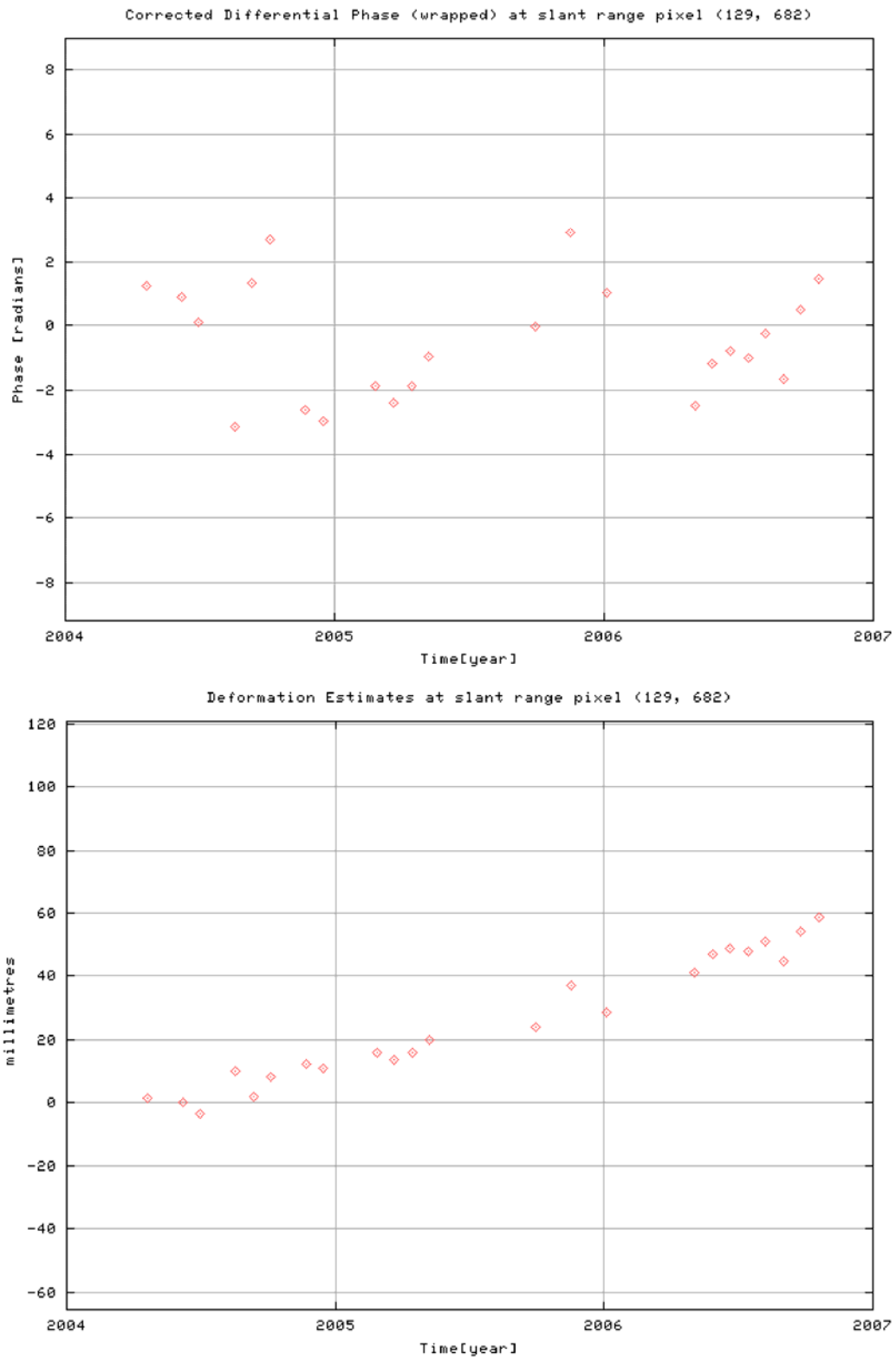


Figure 28. Point profiles of wrapped phases and deformation estimates of Target sp1 on South Peak.

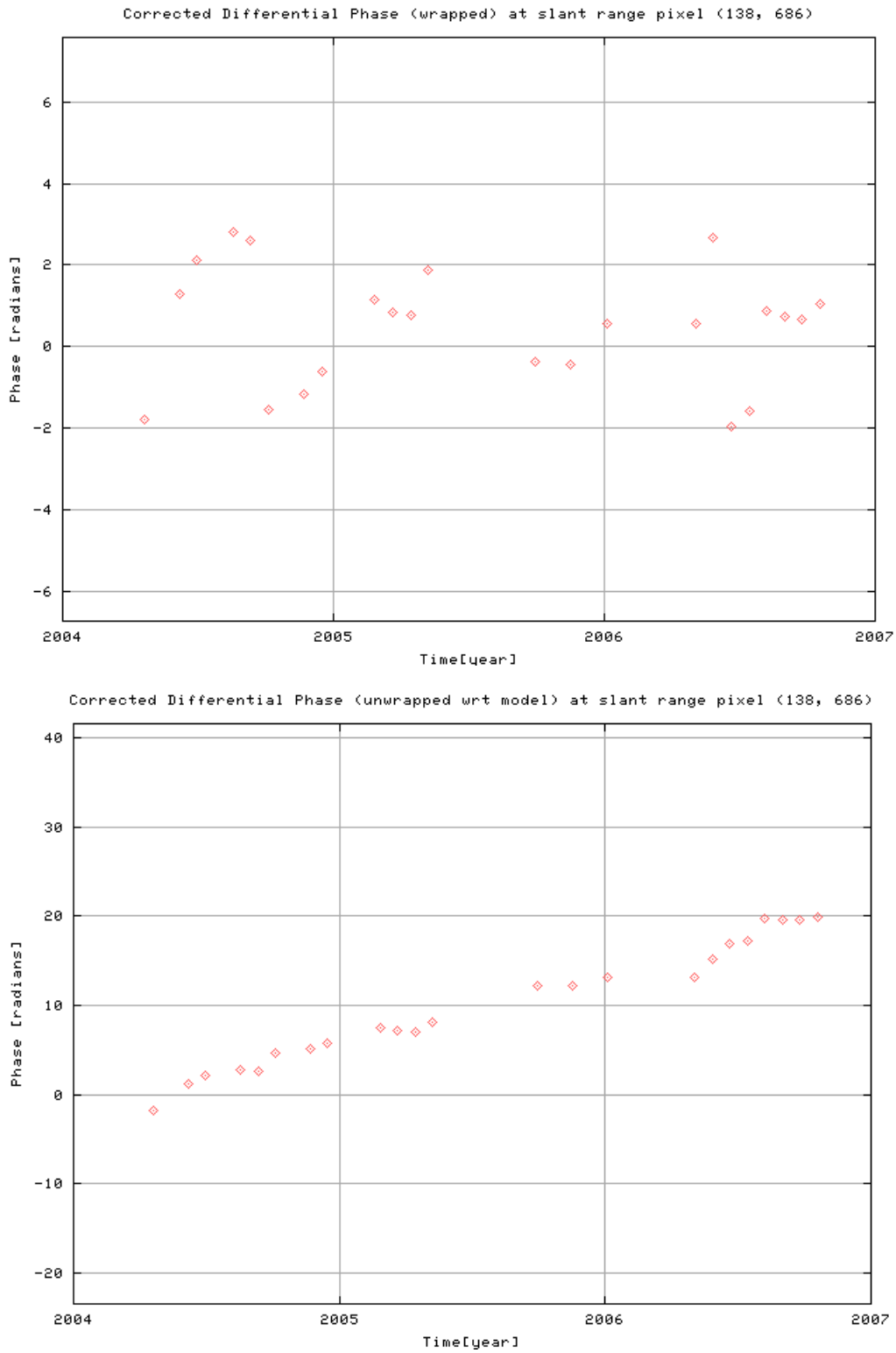


Figure 29. Point profiles of wrapped phases and deformation estimates of Target sp2 on South Peak.

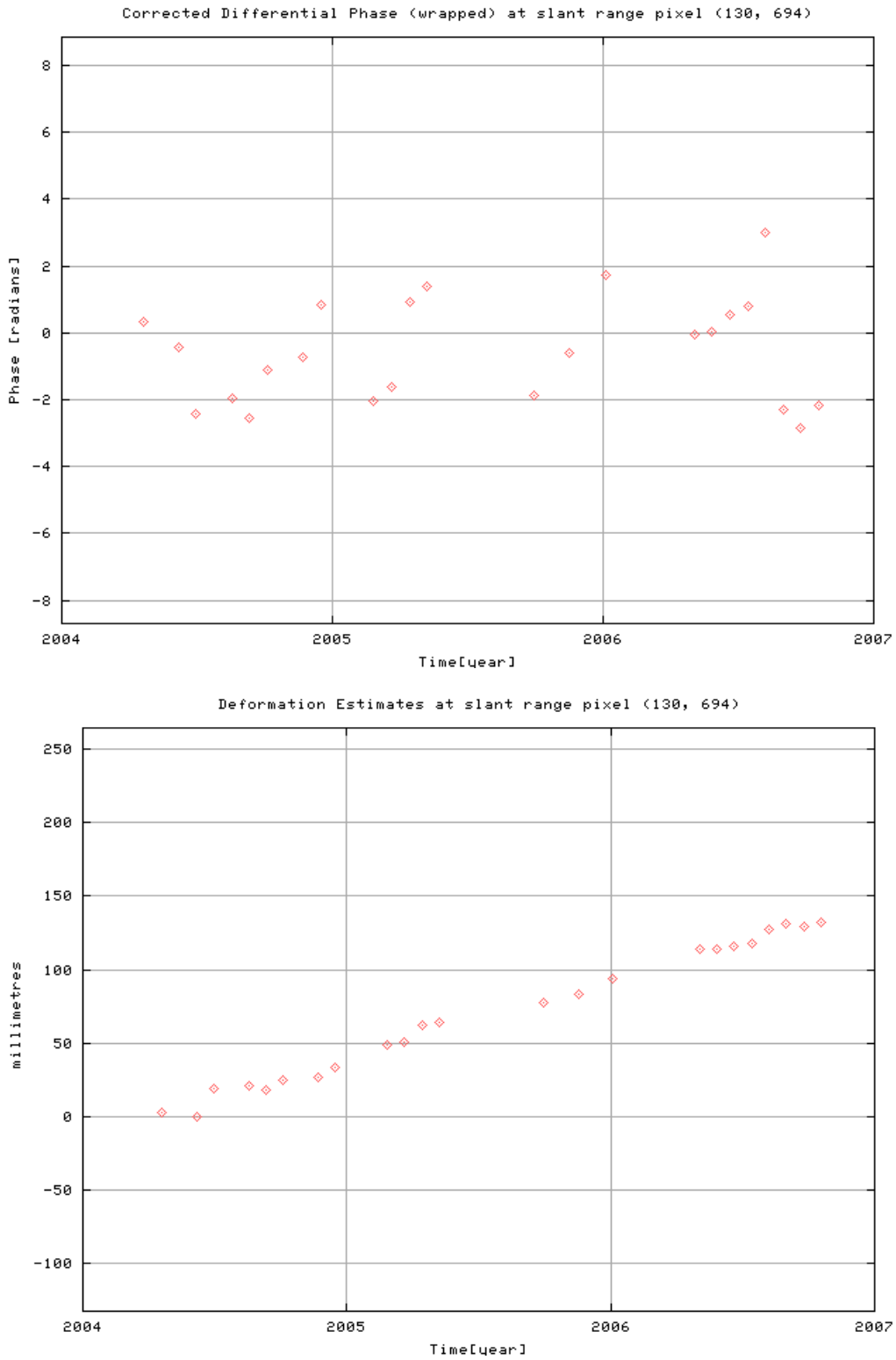


Figure 30. Point profiles of wrapped phases and deformation estimates of Target sp3 on South Peak.

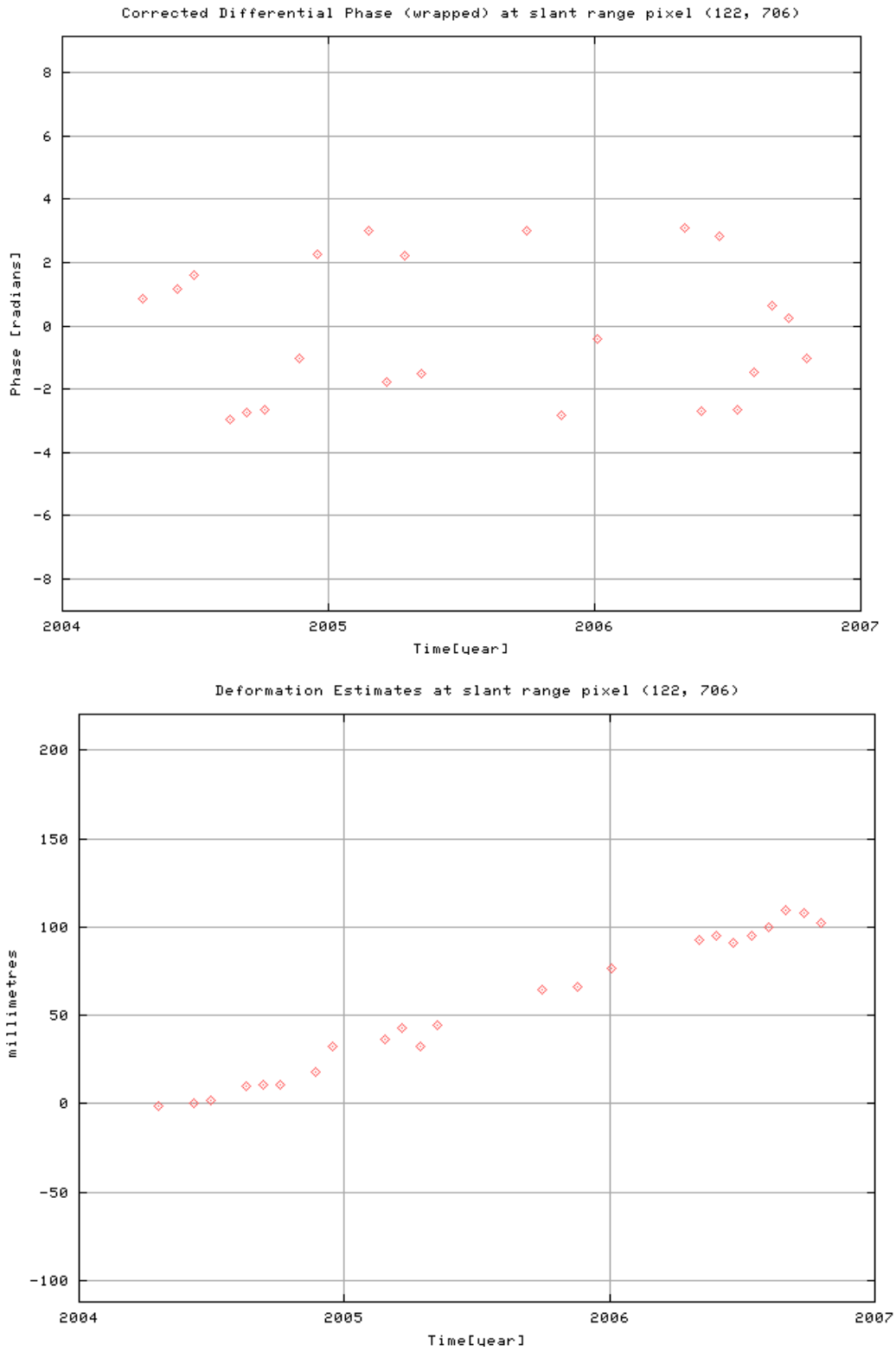


Figure 31. Profiles of wrapped phases and deformation estimates of target sp4 on South Peak.

5.3 Ground Movements in the Lower South Peak Area

To the east of and directly below South Peak there is a hump-like area on the upper part of the eastern slope of Turtle Mountain (Figure 32). This area, forming part of the core of the Turtle Mountain anticline, is extensively fractured and covered with talus derived from the cliffs above. It is herein called the Lower South Peak area. The southern part of this area is covered by loose rock debris and the northern part is dominated by the exposed bedrock surface. While most of the upper portion of the eastern slope of Turtle Mountain is in shadow to the line of sight of radar, a few spots scattered over the lower portion of the Lower South Peak area are still visible to the radar sensor (Figure 33). As a result, nine CTM targets are identified for the Lower South Peak area such that all of them have a temporal coherence greater than 0.65 and a deformation rate to standard error ratio greater than 3. These targets are located in spots that are believed to be exposed to the radar sensor (Figure 33).

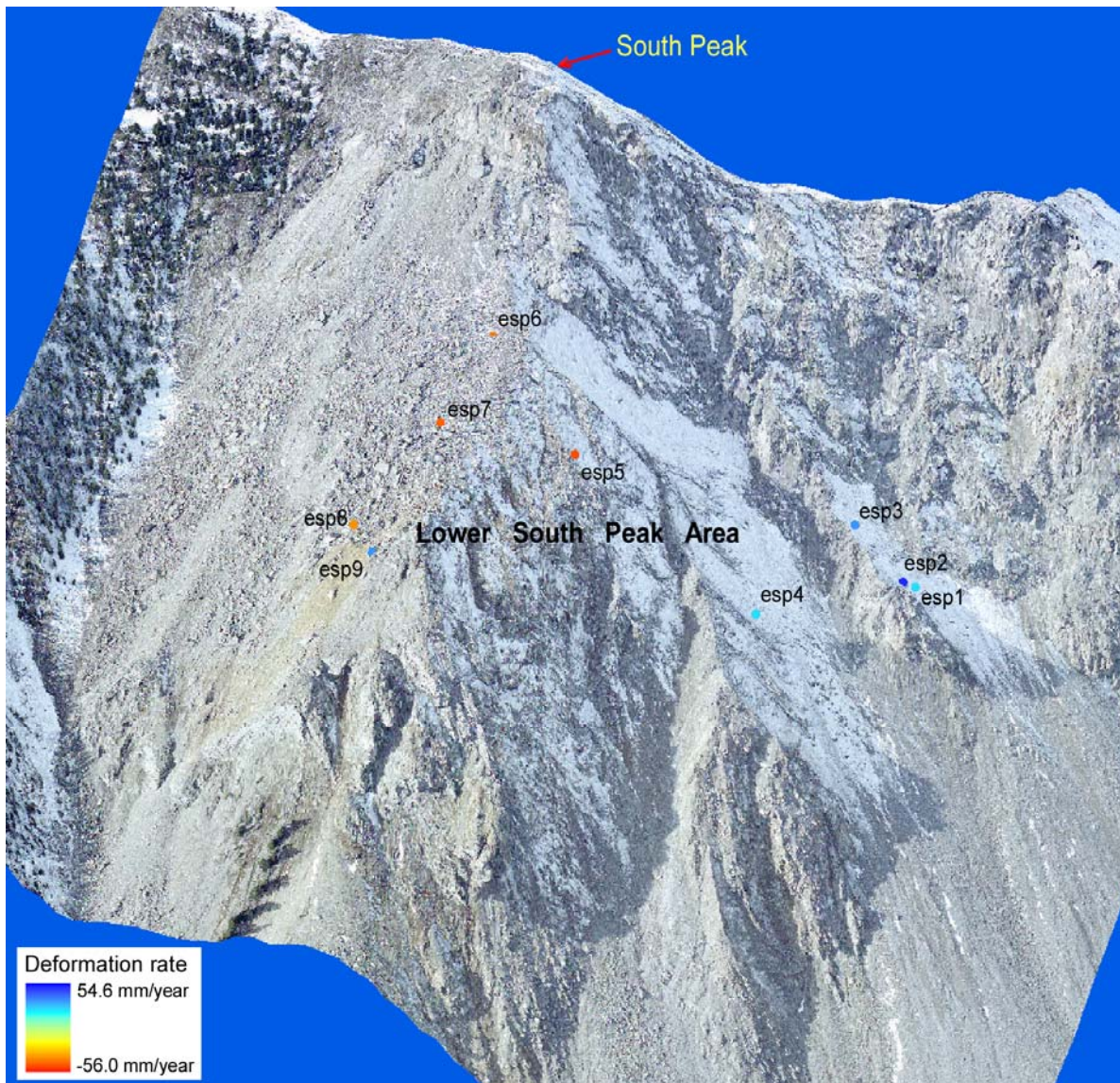


Figure 32. Lower South Peak area and CTM targets (view to west).

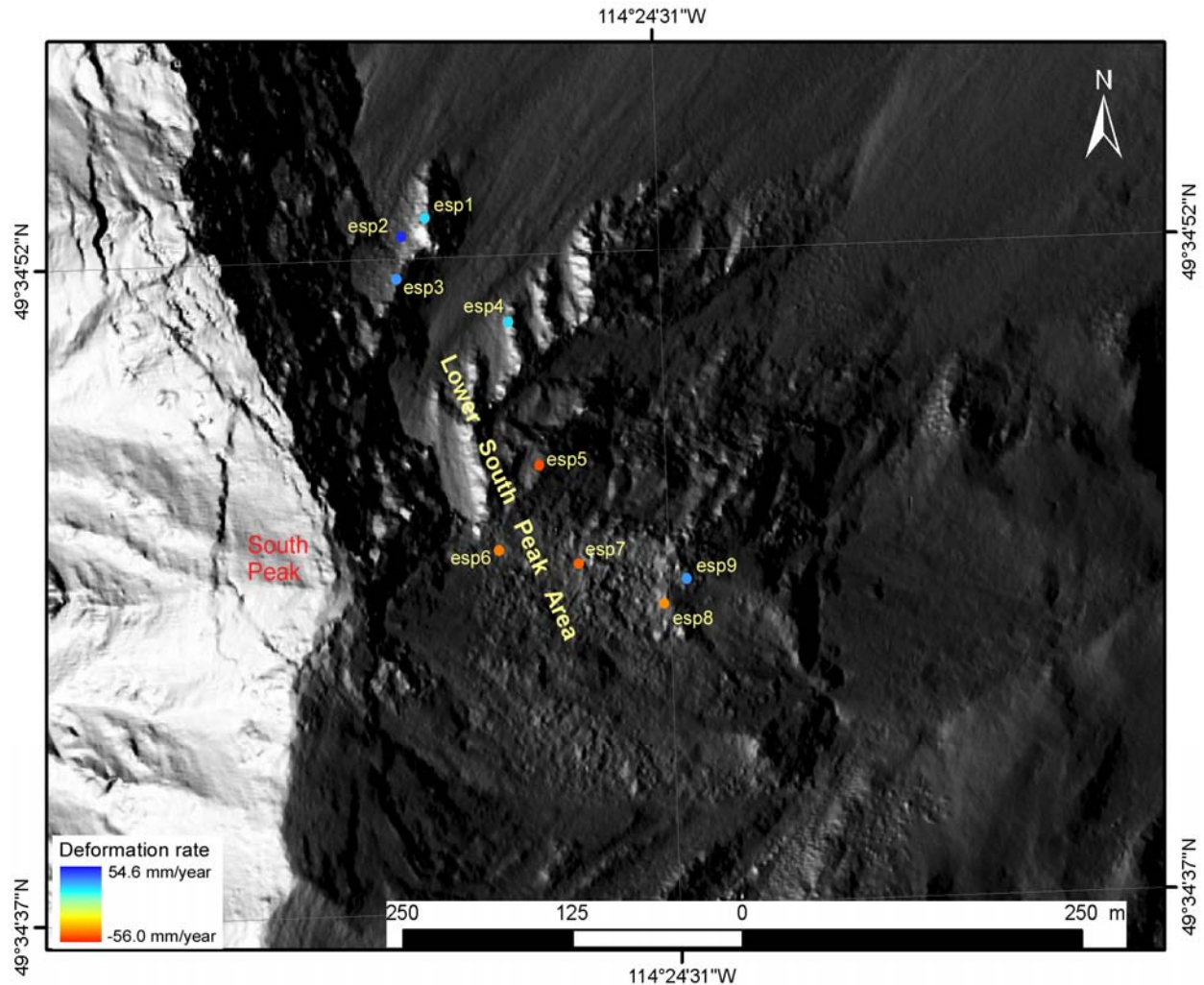


Figure 33. Plan view of the lower South Peak area with CTM targets. The view is generated using LiDAR DEM by simulating the sunshade effect of the Fine Beam Mode 4 of the far range. It shows that shadow covers much of the upper eastern slope.

The deformation rates obtained from the targets in the Lower South Peak area are included in Table 7. Interestingly, four of the targets indicate a movement toward the sensor, which could suggest an upward or upslope movement. This upward movement could not be explained by any known processes. A close examination indicates that the southern part of the Lower South Peak area is a slope facing south to southeast covered by loose talus. The northern part is a slope facing away from the sensor and is represented by exposed bedrock surfaces. The southern part could be dominated by surficial and downslope movement of talus on the surface. This might suggest that the deformation measurements from these targets represent only surficial movements of the slowly creeping talus layer. One possible explanation of the toward-sensor movement could be that the targets are moving downslope toward the south, which is nearly perpendicular to the radar line of sight. If the downslope movement is in the direction as indicated by red arrows in Figure 34, it will cause shortening of the distance between the radar sensor and the target (the line of sight direction is indicated by the yellow arrow, Figure 34). Three of the four abnormal targets, targets esp6 to esp8, are located in the southern area. Very likely, the displacement measurements from these targets simply indicate a southward downslope movement of the surficial talus blanket. Although target esp5 appears located on the exposed bedrock surface, southward movement could also be an explanation for its toward-sensor movement.

Table 7. CTM targets identified for the lower South Peak area.

ID	Longitude (NAD 83)	Latitude (NAD 83)	Coherence	Deformation Rate (mm/year)	STD_Err	SNR
esp1	-114.412651	49.581426	0.66	22.98	4.13	5.57
esp2	-114.412903	49.581311	0.68	53.44	4.23	12.63
esp3	-114.412965	49.581035	0.71	33.48	3.81	8.78
esp4	-114.411837	49.580743	0.70	23.00	4.32	5.33
esp5	-114.411573	49.579825	0.66	-51.12	4.66	-10.98
esp6	-114.412010	49.579287	0.70	-40.83	4.08	-10.01
esp7	-114.411208	49.579187	0.66	-45.39	4.17	-10.90
esp8	-114.410348	49.578913	0.67	-38.00	4.23	-8.98
esp9	-114.410116	49.579072	0.66	32.91	4.30	7.66

STD_err stands for standard error of the deformation rate, obtained from a linear regression of the unwrapped phase values for each point target. SNR represents signal to noise ratio calculated as the ratio of the deformation rate to its standard error.

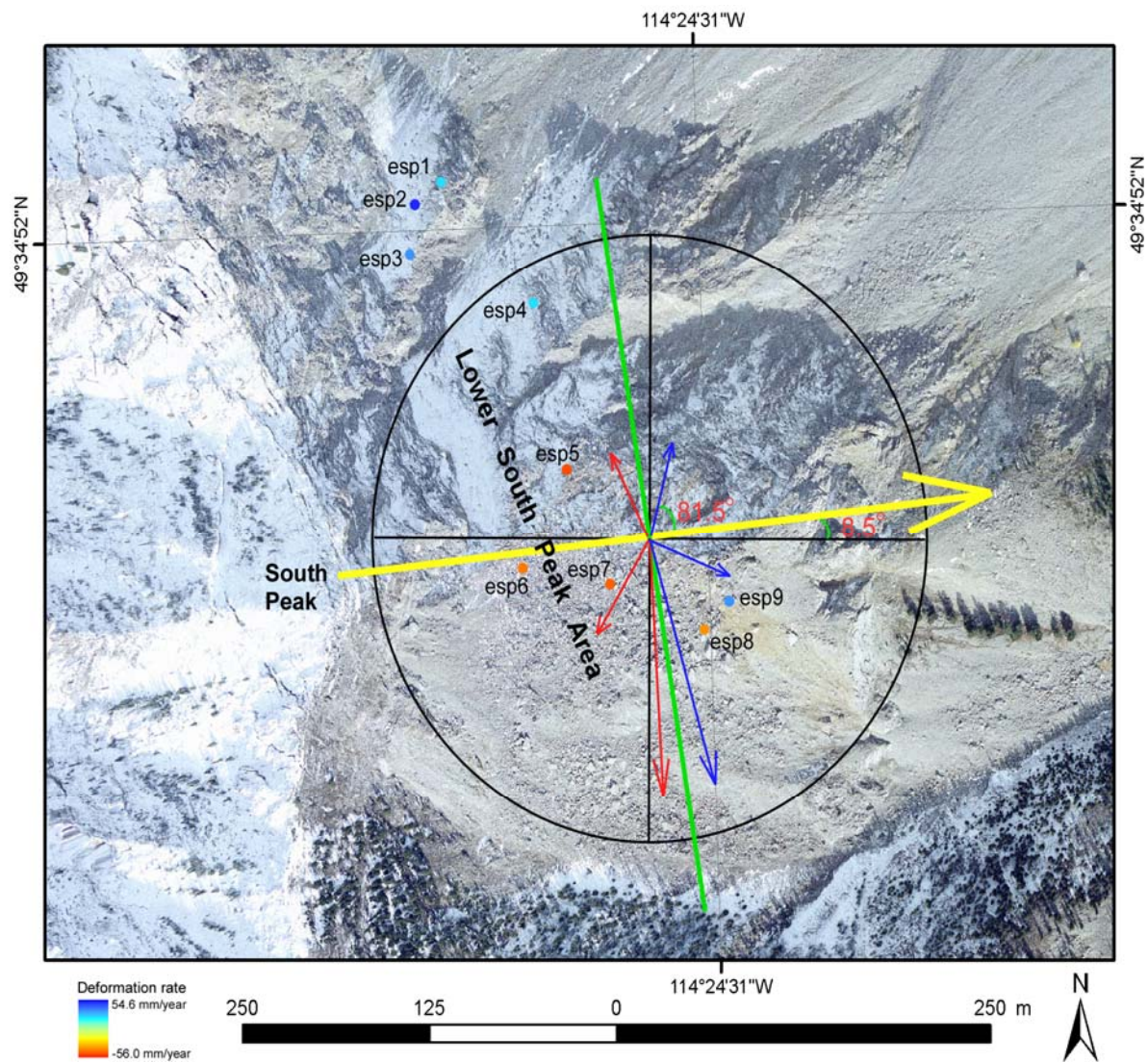


Figure 34. Plan view of the eastern South Peak area with CTM targets. The yellow arrow indicates the radar line of sight direction, and the green line is perpendicular to the yellow arrow. The red arrows indicate the downslope movements toward the sensor, and the blue arrows movements away from the sensor.

The targets from the northern part of the Lower South Peak area include targets esp1 to esp4; all of them indicate an eastward downslope movement, or movement away from the sensor, at an annual rate ranging from 23 to 53 mm per year (Table 7). A closer examination was made for Target esp4 using several refined nonlinear deformation models and the results are displayed in Figures 35 to 37. The results from the model refinement were found to be almost identical to those obtained from the linear model, which may indicate the high reliability of the measurement. The results all indicate that Target esp4 moved downslope nearly 58 mm from April 2004 to October 2006. However, it is not certain whether the measurements from Target esp4, as well as those from targets esp1 to esp3, are representative of the overall ground movement of the northern part of the Lower South Peak area as this area is extensively fractured. More targets are needed for conclusive evaluation of the ground movement of the Lower South Peak area.

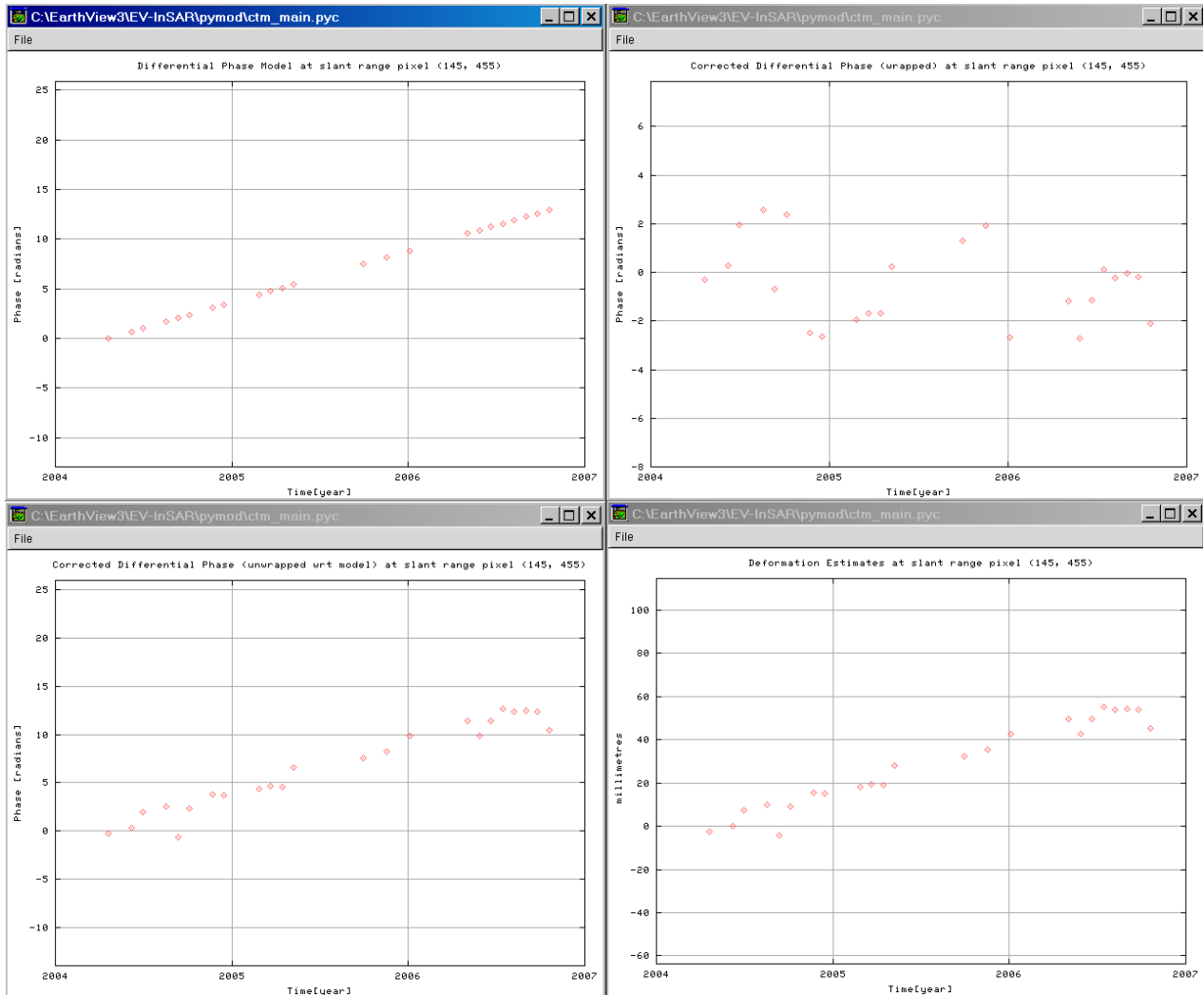


Figure 35. CTM plots showing the deformation model (averaging annual deformation), time series of wrapped phase, time series of unwrapped phase and deformation profile associated with target esp4. The deformation model used is linear.

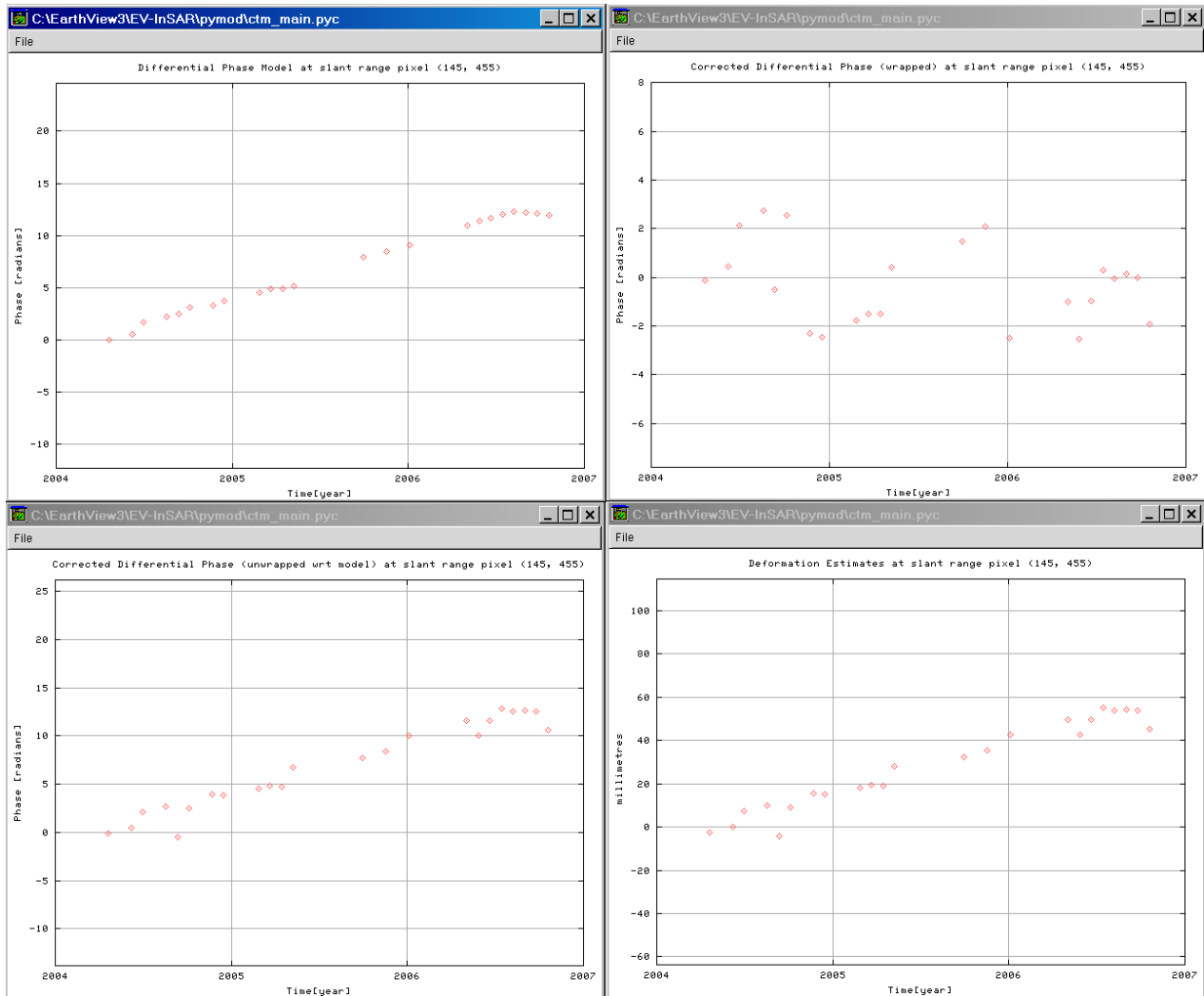


Figure 36. CTM plots showing the deformation model (averaging annual deformation), time series of wrapped phase, time series of unwrapped phase and deformation profile associated with target esp4. The deformation model is nonlinear and was obtained by smoothing the wrapped phase values using a half-year smooth length.

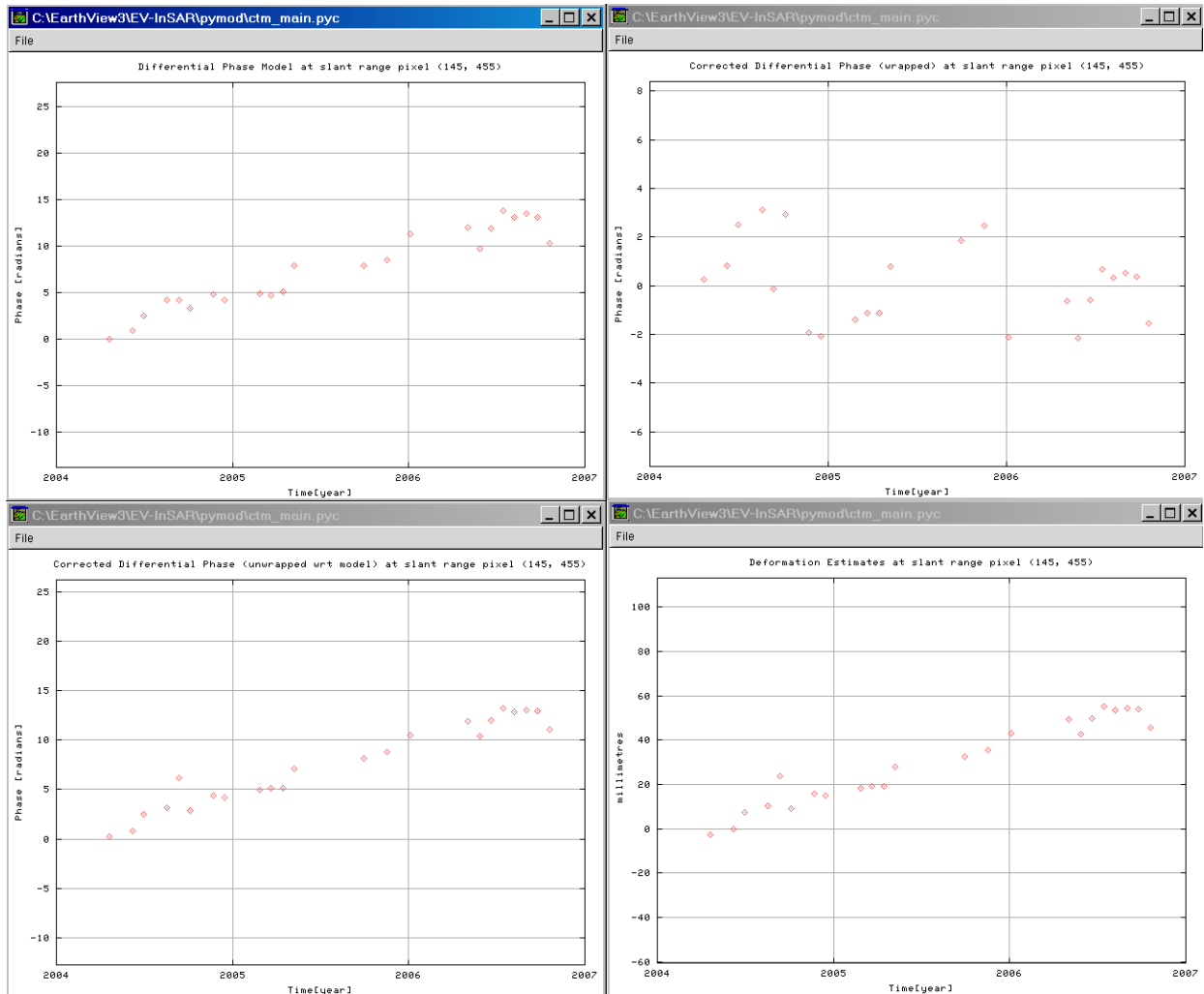


Figure 37. CTM plots showing the deformation model (averaging annual deformation), time series of wrapped phase, time series of unwrapped phase and deformation profile associated with target esp4. The deformation model is nonlinear and was obtained by applying piecewise linear fitting the wrapped phase values using a 0.3 year kernel length.

5.4 Ground Movement in the Upper Slope of the Frank Slide

As discussed in Section 5.1, the upper slope of the Frank Slide is mostly in shadow to the sight of radar sensor (Figure 38), making this area unsuitable for monitoring deformation using the F4F ascending beam mode. In addition, the local incident angle of radar signal is close to 90° on the upper slope, and the upper slope is characterized by fine debris (Figure 38); these two combined factors cause the slope to look smooth to the radar signal, even if it may be partly exposed to the sight of the radar sensor. This means that the radar signals will be mostly reflected away from the sensor and few of them are backscattered. As a result, most of the PS-InSAR measurements within this area may not be reliable. Nevertheless, some targets in the lower part of this area that are exposed to the radar sensor (Figure 39) indicate downslope movement away from the radar sensor (Table 8). These movements are likely indicative of the slow downslope creep of the talus apron on the upper portion of the Frank Slide. The PS-InSAR mapped talus deformations on the lower portion of the Frank Slide are discussed in Section 5.5.

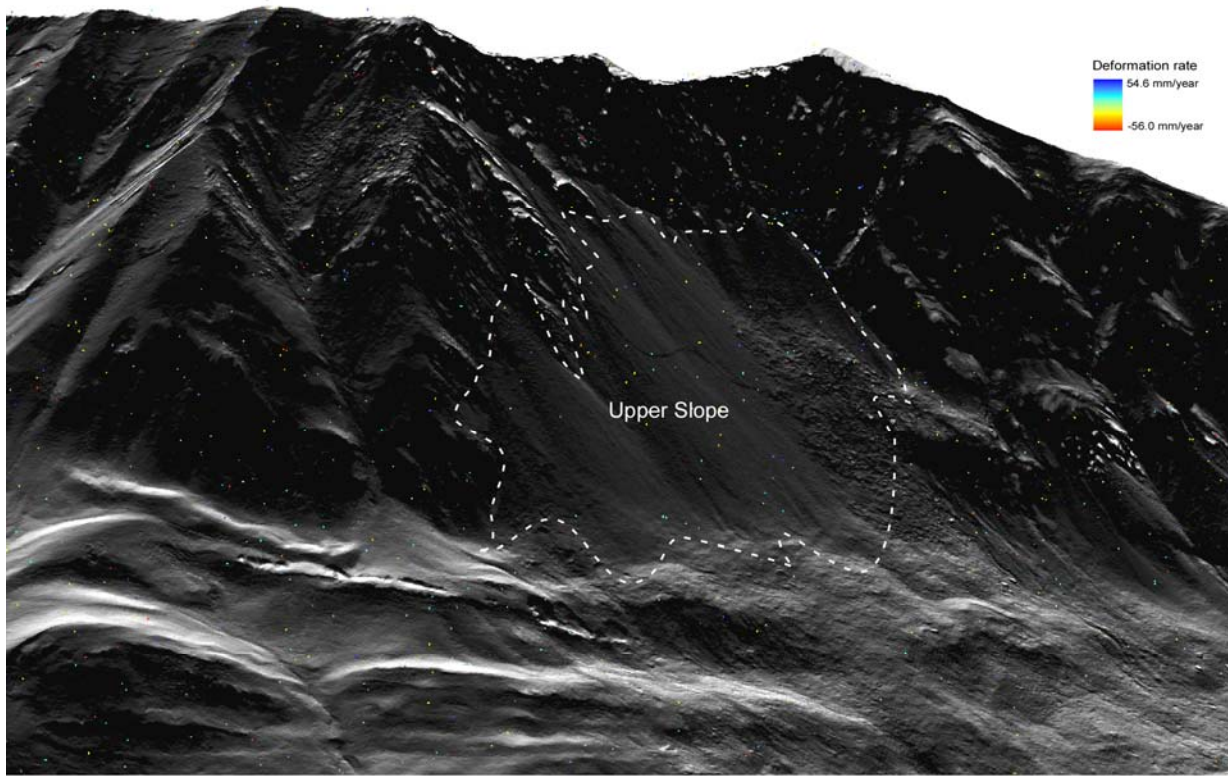


Figure 38. Perspective views to the west of Turtle Mountain–Frank Slide. The upper view simulates the effect of the Fine Beam Mode 4 of the far range. It illustrates that shadow covers much of the upper slope of the Frank Slide.

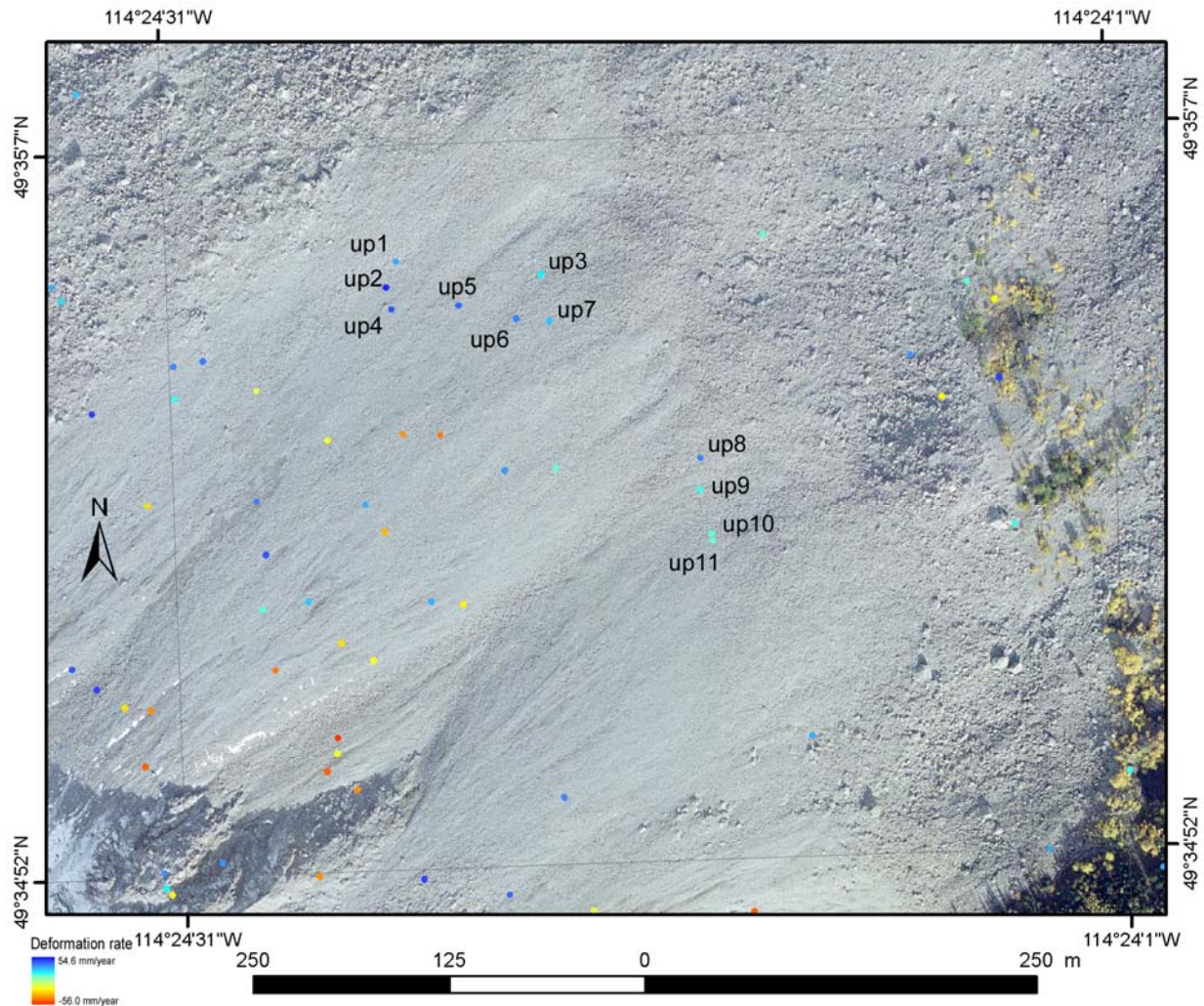


Figure 39. Plan view of the lower part of the upper slope of the Frank Slide with CTM targets.

Table 8. CTM targets identified in the lower portion of the upper slope of the Frank Slide.

ID	Longitude (NAD 83)	Latitude (NAD 83)	Coherence	Deformation rate (mm/year)	STD_Err	SNR
up1	-114.408238	49.584656	0.66	31.05	4.26	7.30
up2	-114.408340	49.584511	0.67	51.56	4.25	12.13
up3	-114.406964	49.584559	0.67	17.76	4.04	4.40
up4	-114.408296	49.584381	0.66	45.80	4.32	10.60
up5	-114.407710	49.584394	0.66	42.62	4.22	10.10
up6	-114.407204	49.584310	0.65	36.55	4.70	7.78
up7	-114.406909	49.584295	0.70	25.93	3.91	6.63
up8	-114.405620	49.583479	0.65	37.25	4.22	8.82
up9	-114.405631	49.583298	0.68	14.49	4.11	3.52
up10	-114.405543	49.583037	0.69	13.11	4.16	3.15
up11	-114.405536	49.582993	0.70	12.16	3.99	3.05

5.5 Ground Movement in the Lower Portion of the Frank Slide/Valley Bottom

The lower slope/valley portion of the Frank Slide is characterized by deformations associated with the gradual downslope movement of talus and surface subsidence associated with abandoned coal mine workings. Figure 40 provides an aerial view of the eastern face of Turtle Mountain, from the northeast, showing the features that will be the basis for discussion of the PS-InSAR results.

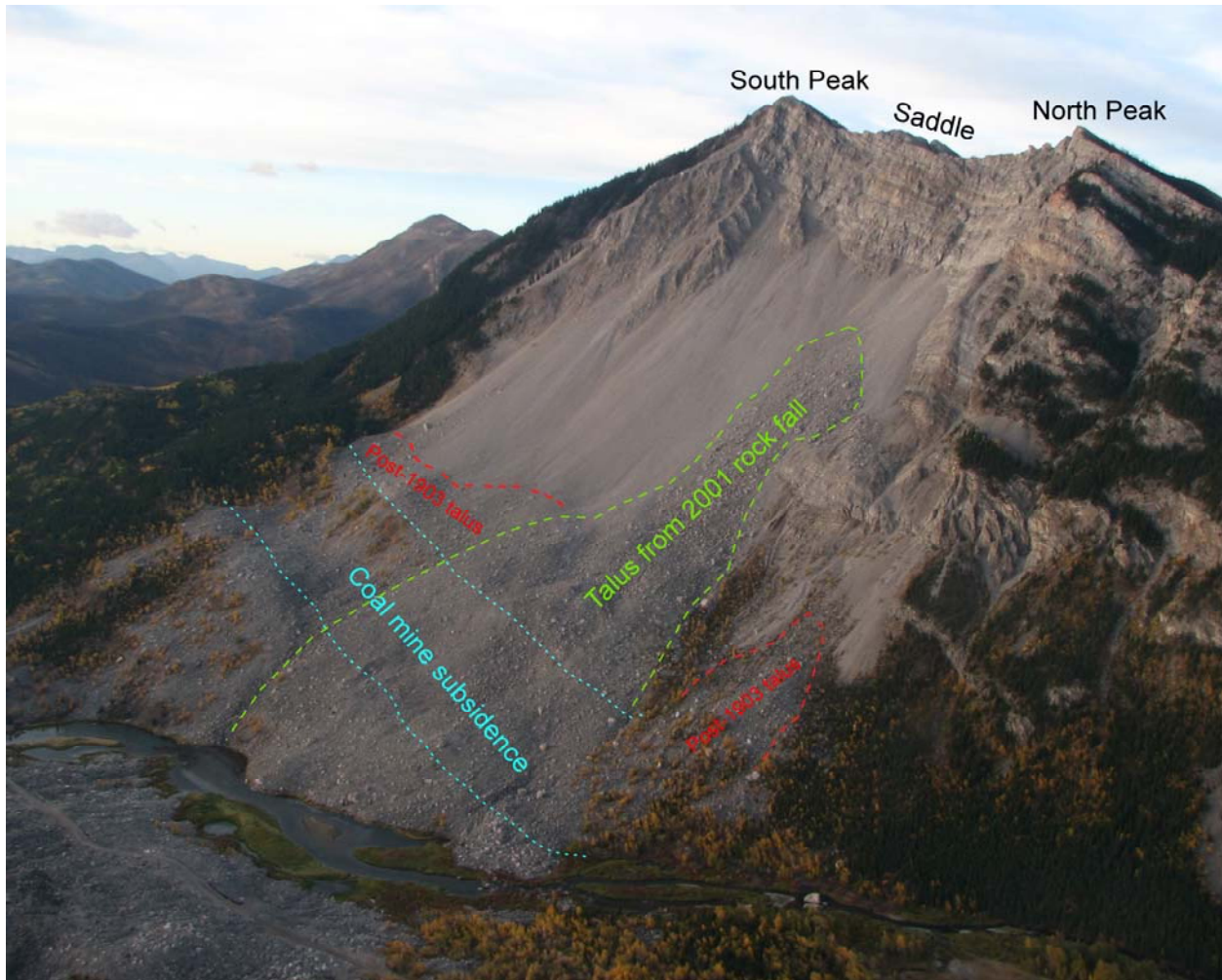


Figure 40. View from the northeast of the east side of Turtle Mountain showing the apron of talus covering the eastern face of the mountain. Post-1903 talus predates the 2001 rock fall and postdates the 1903 landslide.

The lower part of the Frank Slide, which occupies two-thirds of the entire slide area, is mostly covered by exposed rock fragments that have been in this location for more than 100 years. It occupies the bottom of the valley and has a gentle topography. As a result, the surficial movement of the rock fragments are minimal. This, combined with the fact that the rock covering the valley bottom is nonvegetated and generally dry, leads to the high coherence and identification of more than 95% of the CTM targets for the Frank Slide area. Due to their great density and excellent coverage, the PS-InSAR measurements for this area as a whole can be used for reliable restoration of the deformation pattern. Figure 41 shows the deformation pattern generated by applying Kriging interpolation to the deformation rates of CTM targets. The western and eastern margins of the slide area subsided at an annual rate of up to 6.4 mm/year, relative to the south eastern portion of the central part of the valley bottom, from April 2004 to October 2006. A

discussion of these results in relation to the specific deformation processes is provided in the following sections.

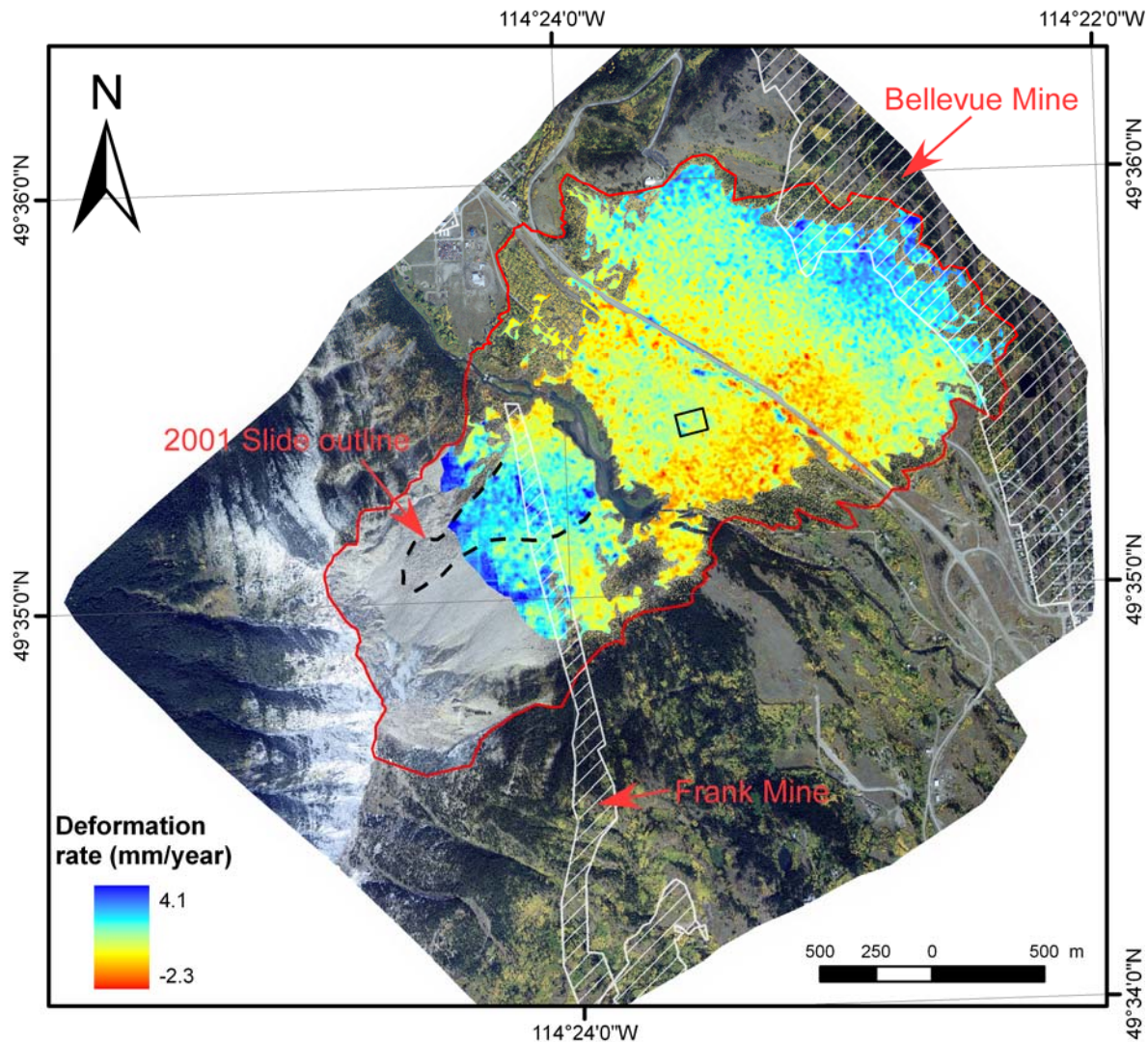


Figure 41. Deformation pattern of the lower part of the Frank Slide. The area marked by white strips indicates the location of underground coal mines. The Frank Slide boundary is outlined in red and the reference area is denoted by the black rectangle.

Lower Slope Talus: In this area, post-1903 talus, composed of rockfall debris from the South Peak and Saddle areas, sits above and upslope of the coal mine workings and continues to shift in response to gravitational forces and thermal fluctuations (Figure 40). As can be seen in Figure 39 and Table 8, several targets in this area show a downslope movement rate of more than 10 mm/year in the radar line of sight. The deformation patterns on Figure 41 indicate a subsidence rate of up to 6.4 mm/year, relative to the central part of the valley bottom, upslope of the Frank Mine subsidence, while the rates of movement decrease to near zero downslope of the subsidence feature (except for the area of the 2001 slide). This difference in deformation rates and patterns is likely due to (1) downslope adjustments in the younger (post-1903) talus and (2) coal mine subsidence undermining the talus, leading to accelerated deformation rates upslope of the Frank Mine.

2001 Slide Debris: In June 2001, a large rock slide originated on the 1903 slide headwall, near North Peak, and deposited boulders onto the lower slope of the Frank Slide, extending into the Crowsnest River. The colluvium associated with the 2001 event is outlined on Figure 40 and has an estimated volume of 6,000 m³ (C. Bunce, personal communication, 2007). As the talus derived from the 2001 event is much younger than that of the 1903 slide, it is expected to be more mobile. As observed from the CTM results on Figure 41, this area is associated with a relatively higher subsidence rate.

Coal Mine Subsidence: Since the Frank landslide took place in 1903, speculation for more than 100 years has been that ground movements induced by the underground coal mines at the foot of Turtle Mountain might have triggered the slide. By overlying the location of underground mines with the deformation pattern obtained from the PS-InSAR analysis, it becomes clear that the two subsiding areas mapped using PS-InSAR coincide with the locations of the Frank and Bellevue underground coal mines (Figure 41). Between 1901 and 1918, mining of an underground coal seam near the toe of Turtle Mountain was undertaken, with the portion of the seam within the extent of the 1903 slide being mined between 1901 and 1903. Frank mine was mined using large shafts (chambers) separated by pillars of intact coal for support (McConnell and Brock, 1904). After mining of the coal was completed, the mine was not backfilled. While there have been no formal studies into the condition of the mine workings, a series of sinkholes have developed at the surface in areas where the crown of the mine has collapsed. Figure 42 shows a series of collapse pits at the surface to the south of the PS-InSAR deformation map. In addition, a subsidence trough can be visually identified overlying the Frank Mine under the talus apron of the 1903 slide (Figure 40).

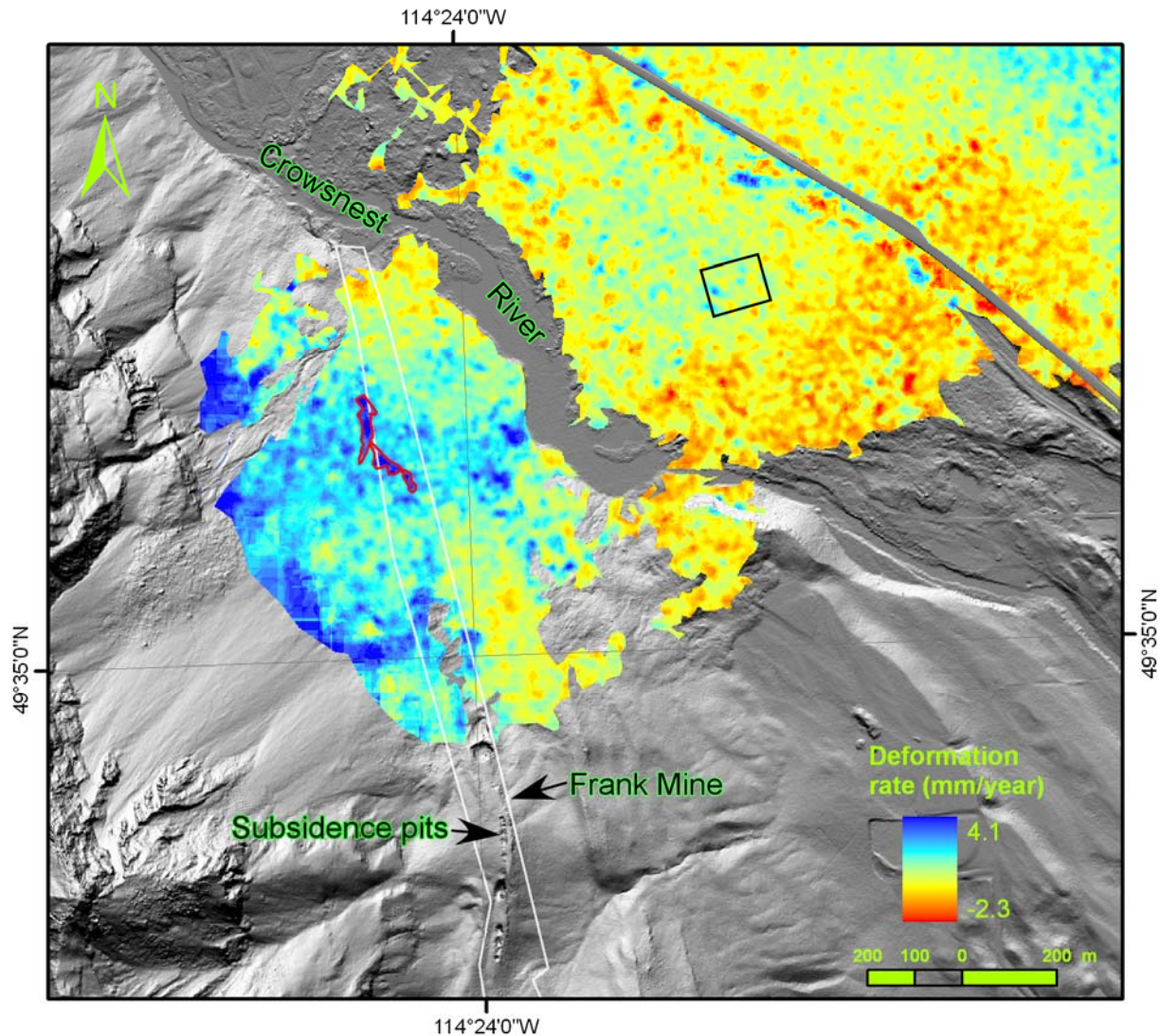


Figure 42. Sunshade relief image of the bare earth LIDAR DEM showing location of the Frank Mine (white polygon) and surface subsidence pits overlying its southern part. The red polygon denotes a subsidence area in the northern part of the Frank Mine and the black rectangle indicates the reference area.

To this day, no monitoring of the rate of the Frank Mine subsidence has been undertaken. The PS-InSAR deformation map indicates an area in the northern part of the Frank Mine that has an average ground movement rate of 3.1 mm/year relative to the reference area (red polygon in Figure 42; Figure 43). This 3.1 mm/year represents the sum of movements attributable to (1) downslope creep of the 2001 talus and (2) coal mine subsidence.

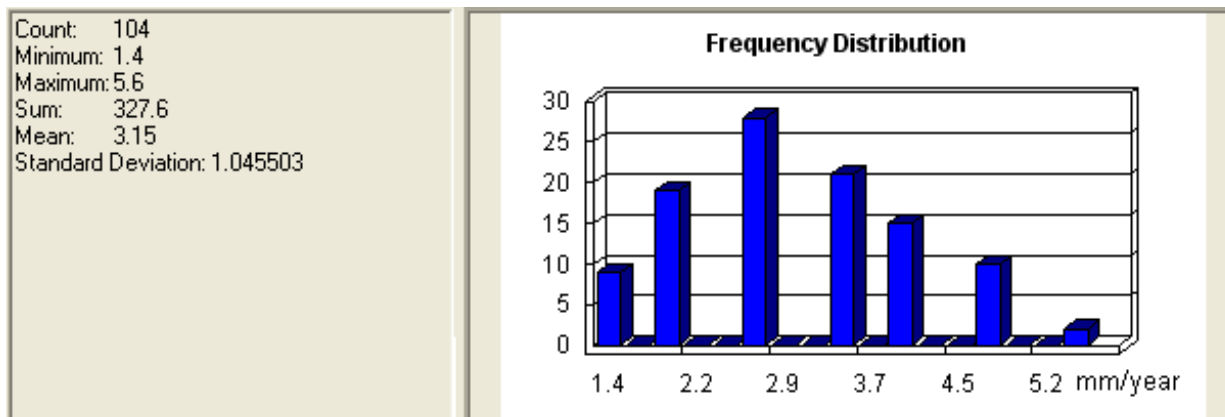


Figure 43. Statistics and histogram of the targets detected in the red polygon as shown in Figure 42.

In addition to average regional subsidence, subsidence for individual targets over the Frank Mine is also detected. Figures 13 and 14 show one of the targets that overlie the Frank Mine at the foot of Turtle Mountain. Figure 13 shows the result with a linear deformation model, indicating that this target moved about 90 mm in the radar line of sight direction. Figure 14 shows the result with a refined nonlinear deformation model, indicating that this target moved about 60 mm in the radar line of sight. These two numbers convert to 63.6 mm and 42.4 mm of vertical subsidence, respectively, occurring during April 2004–October 2006. Like this data point, many tens of other similar points have been used to generate the systematic deformation plot provided in Figures 41 and 42, which provide the first quantitative data for the subsidence overlying the coal mine workings of the old Frank Mine.

As seen on Figure 44, there are also ground deformations mapped by the PS-InSAR that correspond to the footprint of the Bellevue Mine that is located on the eastern side of the valley bottom and below the eastern extent of the Frank Slide. For example, for the area indicated by the red polygon in Figure 44, an average subsidence of 3.2 mm/year relative to the reference area has been observed (Figure 45). At the time of writing this report, no published evidence of vertical subsidence associated with the Bellevue Mine had been documented. In conversations with personnel from the Municipality of Crowsnest Pass, it was indicated that within the past few years there have been increasing instances of subsidence collapse pits opening up at the surface below roads and in fields above the Bellevue Mine workings; however, no specific monitoring is being undertaken.

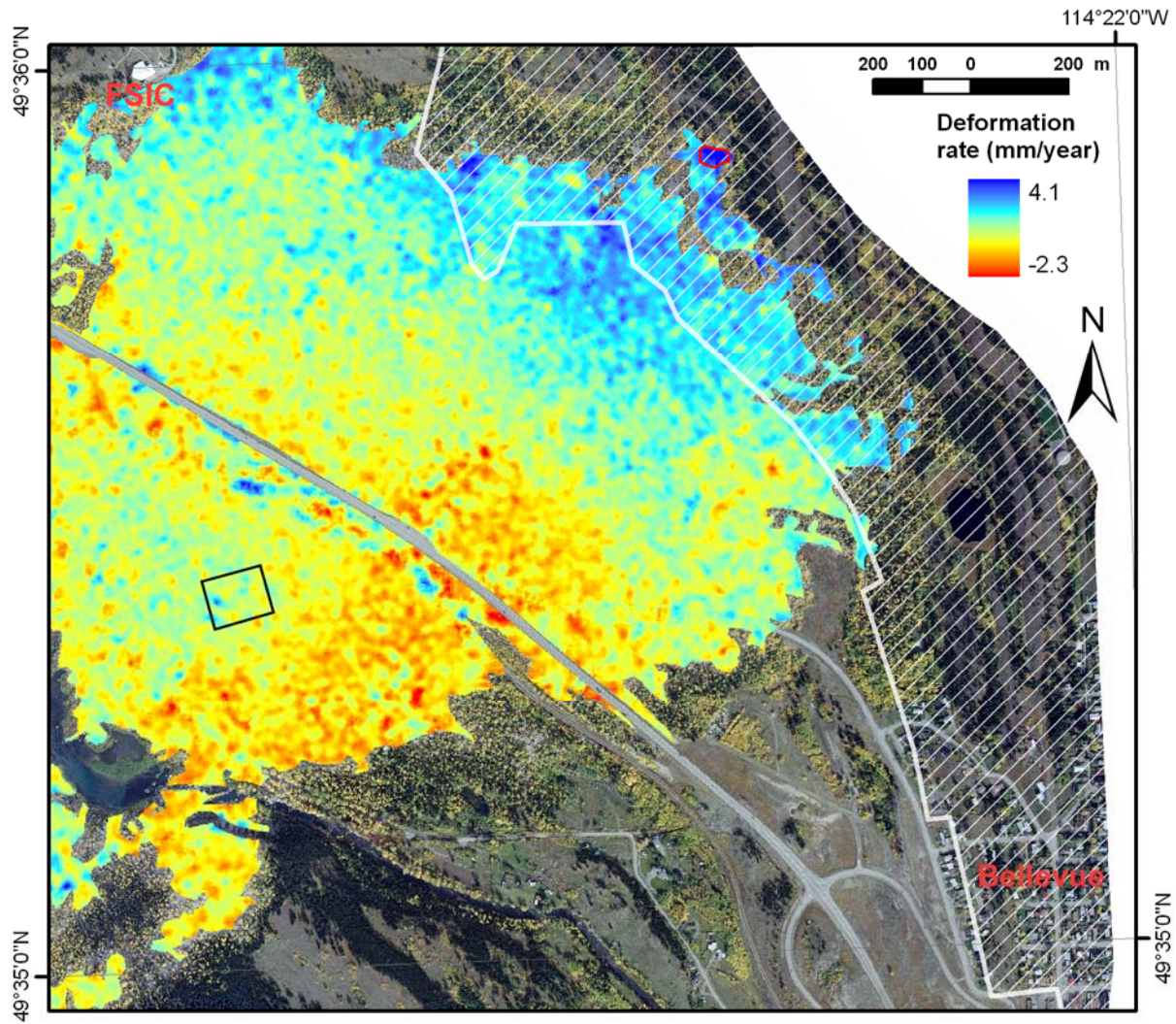


Figure 44. Deformation pattern of the eastern part of the Frank Slide. The red polygon indicates an area above the Bellevue Mine, which is marked by white stripes. The black rectangle denotes the reference area.

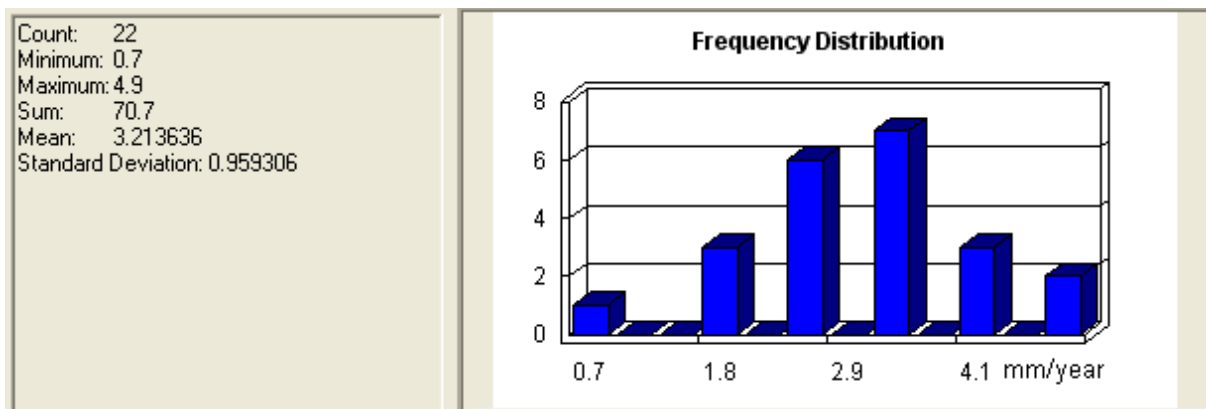


Figure 45. Statistics and histogram of the targets detected in the red polygon shown in Figure 44.

6 Conclusions and Discussions

This study has applied PS-InSAR technology to millimetre-scale ground deformation mapping in the Frank Slide area using EarthView InSAR Coherent Target Monitoring (CTM) software. It confirms that PS-InSAR has become a high-resolution (millimetre scale) surveying tool for regional land deformation mapping.

On the upper portion of Turtle Mountain, foreshortening distortions associated with the incidence angle of the satellite beam mode used and the steep topography do not allow for reliable mapping of deformation in these areas (see below for more details). Although there were a small number of moving targets extracted on the west side of South Peak and on the upper Frank Slide, these points may not be representative of the deeper seated deformations of the rock slope, but rather, isolated movements of small, discrete blocks or boulders. To obtain more reliable deformation data for the peak area, a combination of both ascending and descending beam Radarsat-1 data may be used, although foreshortening distortions may persist. It is likely that the future flexibility of Radarsat-2 in viewing angles in both a left and right-looking mode could help to remedy some of the problems.

The lower slopes of the Frank Slide and the valley bottom are very well suited for the application of PS-InSAR for mapping ground deformations. Due to the bare and dry nature of the landscape and the slow systematic nature of the deformations, both slow creep of talus slopes and subsidence of the surface above the abandoned underground coal mine workings were observed. The ground surface above the Frank Mine was found to be subsiding at an annual rate of up to 3.1 mm per year relative to the reference area (Figure 42) from April 2004 to October 2006. This 3.1 mm/year represents the sum of movements attributable to (1) downslope creep of the 2001 talus and (2) coal mine subsidence. For more than 100 years since the Frank landslide took place in 1903, speculation has been that ground movements induced by the underground coal mine at the foot of Turtle Mountain might have triggered the slide. The PS-InSAR results in this study provide the quantitative evidence for the subsidence induced by the underground coal mines from April 2004 to October 2006, but do not shed light on 1903 conditions.

In addition to providing quantification for an area where visual observations of subsidence had been made (the Frank Mine), average deformations of up to 3.2 mm/year relative to the reference area (Figure 44) were observed overlying the footprint of the abandoned Bellevue underground mine to the east. At the time of the preparation of this report, there were no published data on the subsidence of the ground surface in this area. The findings of this study may be an important tool for the municipality to better understand the potential hazards associated with the Bellevue Mine.

As much of the monitoring effort to this time on Turtle Mountain has focussed on the South Peak area, the PS-InSAR results related to the Frank Slide have not been calibrated with any ground control points due to lack of data from other conventional surveying tools, including differential GPS. The PS-InSAR results provide information on ground deformation over a much larger area than the current ground monitoring network on Turtle Mountain. Thus, The PS-InSAR results can aid in identifying optimal sites for additional ground monitoring stations.

In addition to the results discussed above regarding deformation of the Turtle Mountain area, insights regarding the processing software and methods were also realized. For any type of implementations of PS-InSAR including CTM, some false targets always result. As a result, an additional post-processing step is necessary to discriminate the reliable targets from false targets. This report has demonstrated a useful approach that uses statistical and geostatistical analysis to evaluate the reliability of CTM targets and differentiate between isolated point target movement and regional ground deformation.

It needs to be pointed out that the usefulness of PS-InSAR is considerably limited by the adverse geometry and surficial loose debris of Turtle Mountain, including its South Peak. The limitations are further explained below:

The top ridge of Turtle Mountain is sharp and trending roughly north-south (Figure 46). The western slope is facing toward the radar sensor and the slope angle is close to the slope angle of the front surface of the radar microwave signal. This leads to severe foreshortening effects. As a result, very few targets (only 4) can be identified for this area.

The upper part of the eastern slope of Turtle Mountain is dipping at an angle ranging from 33° to 60° (Figure 46). The top portion of this slope is a steep cliff with a slope angle range from 47° to 87° (Figure 46). This geometry causes most of the upper part of the eastern slope to be in shadow relative to the radar sensor. As a result, no reliable targets can be found for most of the eastern slope.

Although a small number of scattered spots over the Lower South Peak area are exposed to the radar sensor, its southern part is dominated by periodic downslope movement of loose rock fragments/debris, probably in response to physical weathering and precipitation. This causes considerable temporal decorrelation.

In addition, the main part of the upper slope of the Frank Slide is covered by fine debris. This, combined with the east-dipping geometry, causes the slope to look smooth to the radar signal.

To sum up, the geometry of the South Peak area of Turtle Mountain renders it an unsuitable site for PS-InSAR application using Radarsat-1 data, due to the foreshortening effect, the shadow, decorrelation caused by loose surficial debris and smoothness effect. However, the lower part of the Frank Slide is ideal for PS InSAR application and reliable deformation measurements have been successfully obtained.

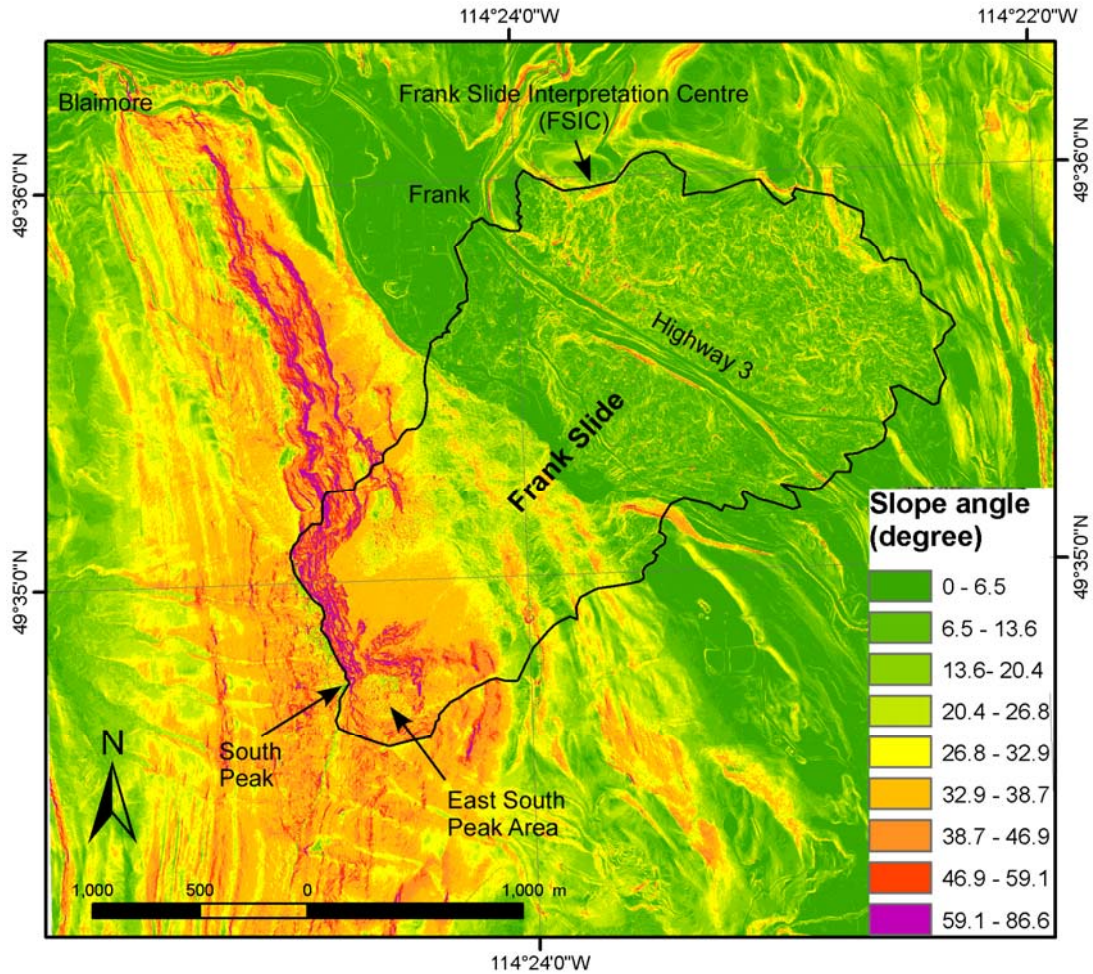


Figure 46. Slope angle map of the Frank Slide. The black line outlines the Frank Slide boundary.

Other limitations are inherent in the EarthView InSAR CTM software. First, the algorithm used for calculation of the temporal coherence might lead to a high coherence value for areas that have minimum signal returns. These areas include shadow, water bodies and smooth surfaces. As a result, a considerably large number of false targets are created for these areas. Second, a linear deformation model used in CTM analysis also limits its use. If the deformation is not linear, which is not uncommon, then, the measurement is not accurate. Although a nonlinear model can be achieved in the EarthView InSAR CTM software, it is actually based on the refinement of the results obtained from the linear model. Furthermore, the refinement algorithm is very sensitive to the wrapped phase values and the parameter selection for the smoothing kernel length. Figures 47 to 51 show the resultant deformation estimates are considerably different with different refinement parameters, using Target up7 as an example (see Figure 39 for its location). It suggests that previous knowledge about the true deformation model is required to assess the validity of the refinement parameters. This limits the use of a nonlinear deformation model refinement tool, as a priori knowledge of deformation is often inadequate and difficult to achieve with conventional surveying tools. Also, the refinement algorithm in CTM appears far from being robust and reliable. Regardless of all these weaknesses, EV-InSAR CTM still stands as a useful deformation mapping tool in the case of favourable land cover type and geometry.

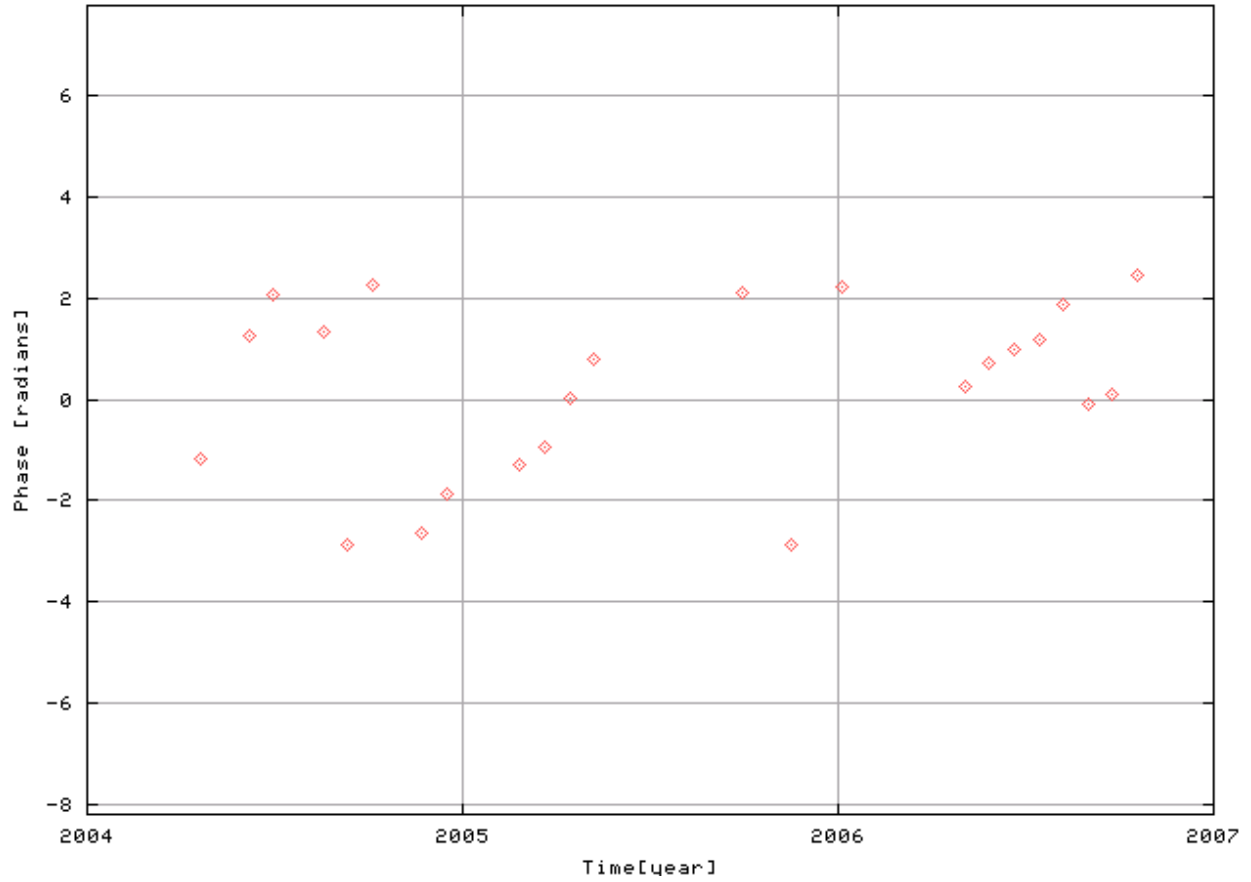


Figure 47. Time series of wrapped phase values of Target up7 as shown in Figure 39.

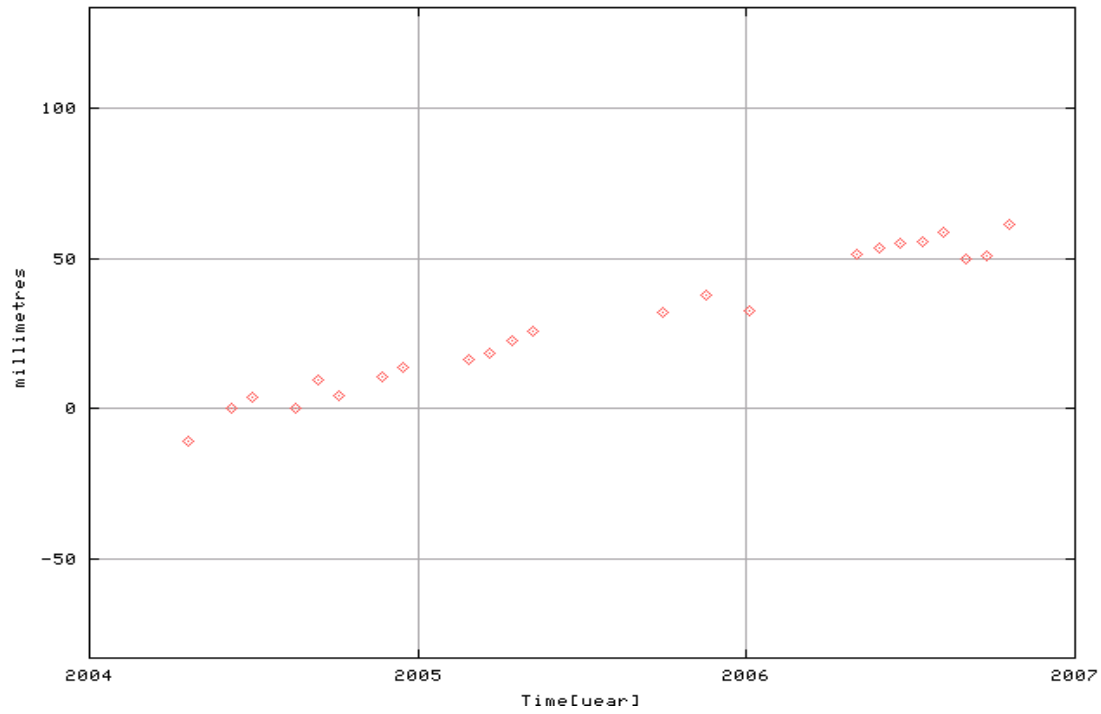
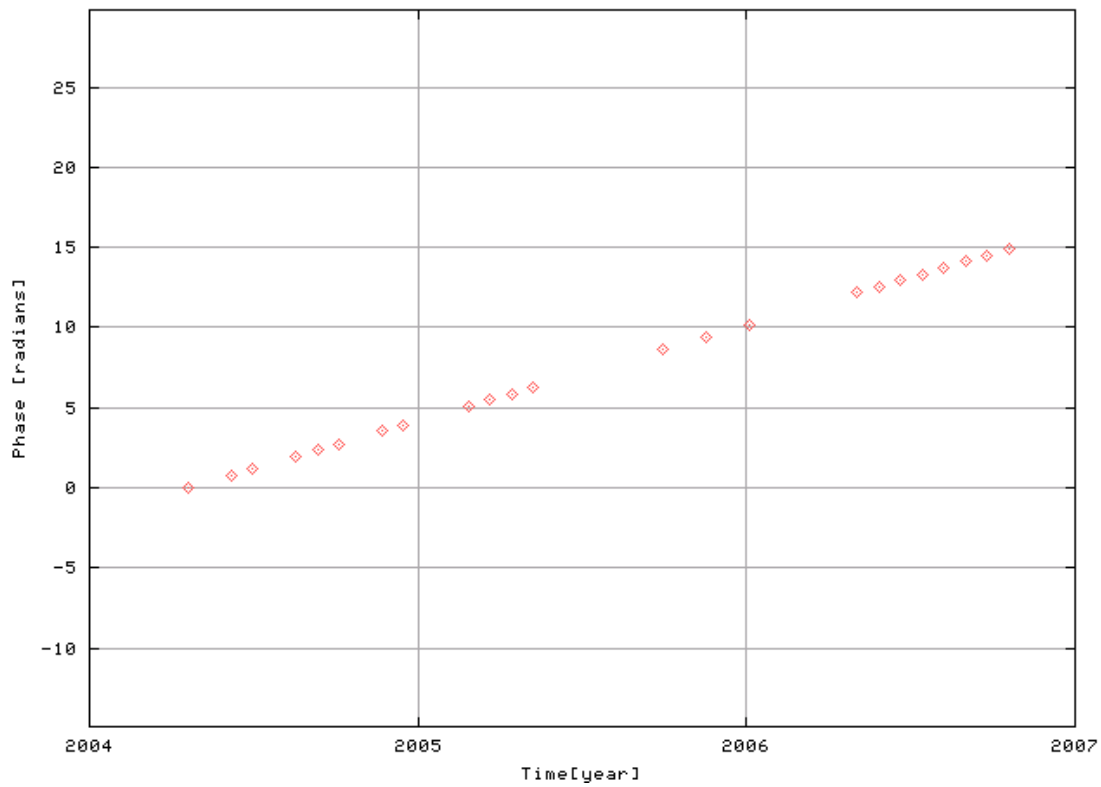


Figure 48. Linear deformation model and resultant deformation estimates of Target up7 as shown in Figure 39.

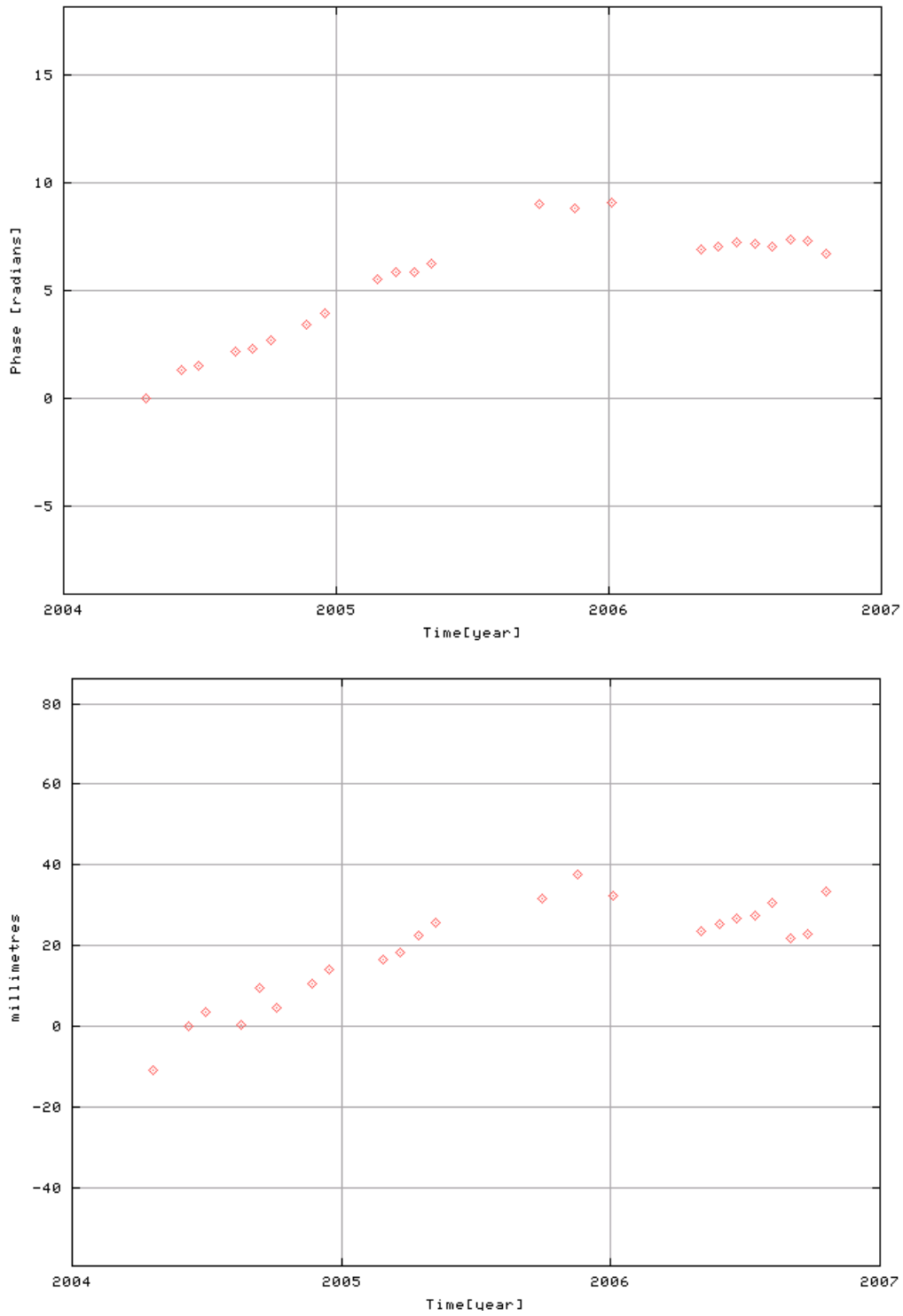


Figure 49. Nonlinear deformation model obtained by smoothing with a 0.3 year kernel length and resultant deformation estimates of Target up7 as shown in Figure 39.

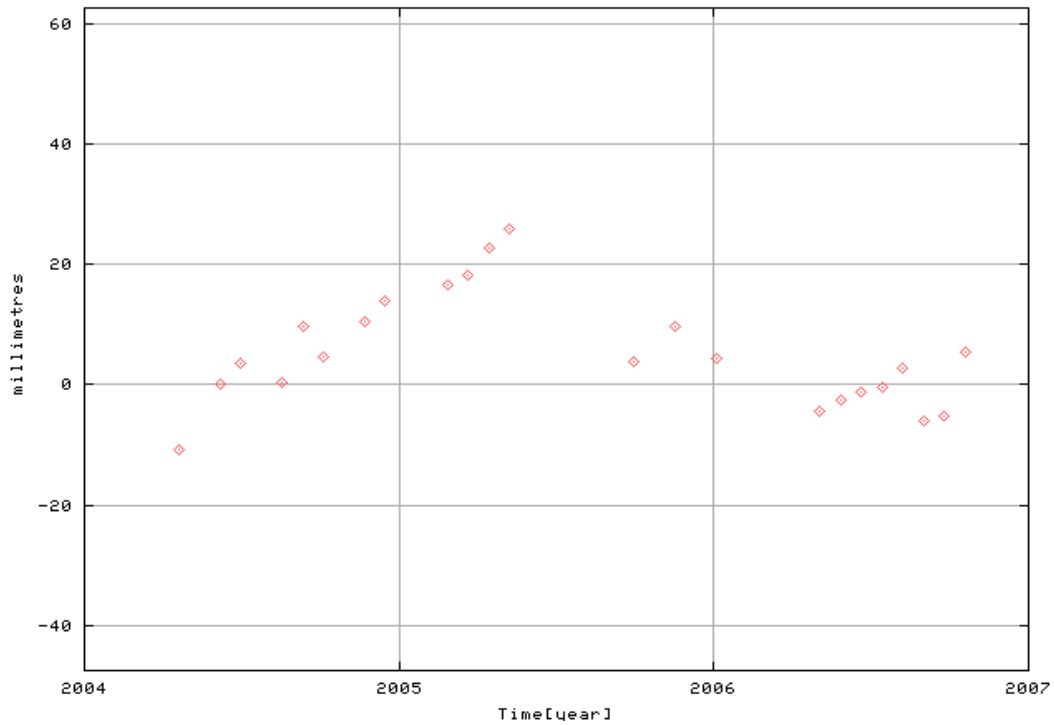
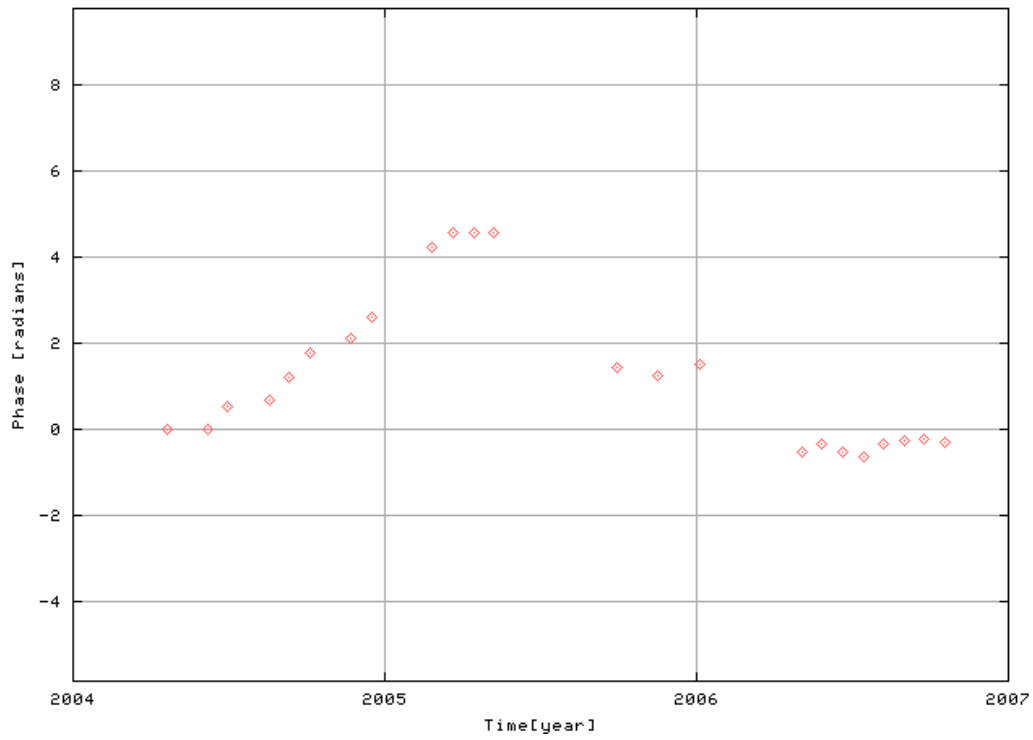


Figure 50. Nonlinear deformation model obtained by smoothing with a 0.5 year kernel length and resultant deformation estimates of Target up7 as shown in Figure 39.

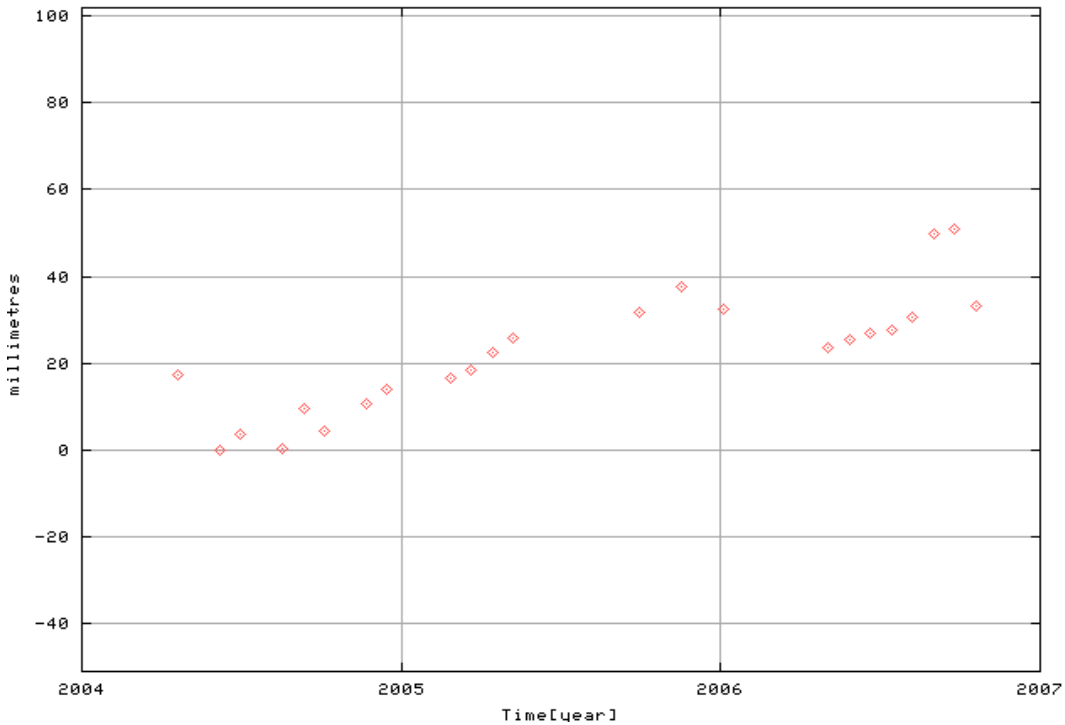
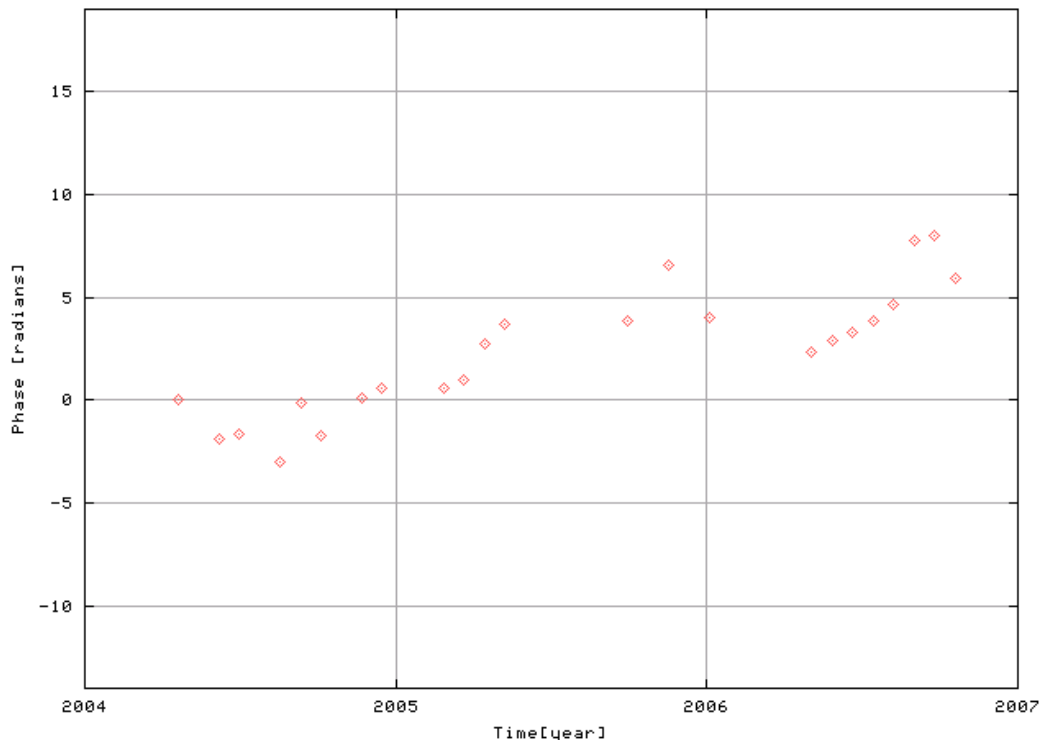


Figure 51. Nonlinear deformation model obtained by piecewise linear fitting with a 0.3 year kernel length and resultant deformation estimates of Target up7 as shown in Figure 39.

7 References

- Allan, J.A. (1933): Third report on the stability of Turtle Mountain for Department of Public Works, Government of Alberta, Edmonton, Alberta; Department of Geology, University of Alberta, 28 p.
- Atlantis Scientific Inc. (2004): EV-InSAR version 3.1 user's guide; Atlantis Scientific Inc., 317 p.
- Atlantis Scientific Inc. (2005): Frank Slide, Alberta InSAR monitoring: set-up and demonstration for 2004/2005; unpublished report prepared for Alberta Geological Survey, 35 p.
- Bamler, R. and Hartl, P. (1998): Synthetic aperture radar interferometry; *Inverse Problems*, v. 14, p. R1–R54.
- Berardino, P., Fornaro, G., Lanari, R. and Sansosti, E. (2002): A new algorithm for surface deformation monitoring based on small baseline differential SAR interferograms; *Institute of Electrical and Electronics Engineers, Transactions on Geoscience and Remote Sensing*, v. 40, no. 11, p. 2375–2383.
- Chapman, M.A. (2006): Deformation monitoring of Turtle Mountain by high-precision photogrammetry, epoch 5; unpublished report prepared for Alberta Geological Survey, 37 p.
- Colesanti, C., Ferretti, A., Novali, F., Prati, C. and Rocca, F. (2003a): SAR monitoring of progressive and seasonal ground deformation using the permanent scatterers technique; *Institute of Electrical and Electronics Engineers, Transactions on Geoscience and Remote Sensing*, v. 41, no. 7, p. 1685–1701.
- Colesanti, C., Ferretti, A., Prati, C. and Rocca, F. (2003b): Monitoring landslides and tectonic motions with the permanent scatterers technique; *Engineering Geology*, v. 68, p. 3–14.
- Duro, J., Inglada, J., Closa, J., Adam, N. and Arnaud, A. (2003): High resolution differential interferometry using time series of ERS and Envisat SAR data; *Proceedings of the Third International Workshop on ERS SAR Interferometry (FRINGE 2003)*, Frascati, Italy, ESA SP-550 (on CD-ROM).
- Ferretti, A., Prati, C. and Rocca, F. (1999): Permanent scatterers in SAR interferometry; *International Geoscience and Remote Sensing Symposium*, Hamburg, Germany, Abstract, p. 1–3.
- Ferretti, A., Prati, C. and Rocca, F. (2000): Nonlinear subsidence rate estimation using permanent scatterers in differential SAR interferometry; *Institute of Electrical and Electronics Engineers, Transactions on Geoscience and Remote Sensing*, v. 38, no. 5, p. 2202–2212.
- Ferretti, A., Prati, C. and Rocca, F. (2001): Permanent scatterers in SAR interferometry; *Institute of Electrical and Electronics Engineers, Transactions on Geoscience and Remote Sensing*, v. 39, no. 1, p. 8–20.
- Franceschetti, G. and Lanari, R. (1999): *Synthetic Aperture Radar Processing*; CRC Press, New York, New York, 307 p.
- Fraser, C.S. (1983): Deformation of Turtle Mountain by high precision photogrammetry; *Alberta Environment Research Management Division, Report L0-83*, 43 p.
- Froese, C.R. and Moreno, F. (2007): Turtle Mountain field laboratory (TMFL) part 1: overview and summary of activities; *Proceedings of the First North American Conference on Landslides*, Colorado, Abstract, 10 p.
- Gens, R. and Genderen, J. L.V. (1996): SAR interferometry—issues, techniques, applications; *International Journal of Remote Sensing*, v. 17, no. 10, p. 1803–1835.

- Graham, L.C. (1974): Synthetic interferometer radar for topographic mapping; Proceedings of the Institute of Electrical and Electronics Engineers, v. 62, no. 6, p. 763–768.
- Hanssen, R.F. (2001): Radar Interferometry Data Interpretation and Error Analysis; Kluwer Academic Publishers, Dordrecht, Netherlands, 308 p.
- Henderson, F.M. and Lewis, A.J., ed. (1998): Principles and applications of imaging radar; Manual of Remote Sensing (3rd edition), v. 2, John Wiley & Sons, Inc., New York, New York, 750 p.
- Massonnet, D. and Feigl, K.L. (1998): Radar interferometry and its application to changes in the Earth's surface; Review of Geophysics, v. 36, p. 441–500.
- McConnell, R.G. and Brock, R.W. (1904): Report on the great landslide at Frank, Alberta, Canada; Department of the Interior (Canada) Annual Report, 1902-1903, Part 8, 17 p.
- Moreno, F. and Froese, C.R. (2006): Turtle Mountain field laboratory: monitoring and research summary report, 2005; Alberta Energy and Utilities Board, EUB/AGS Earth Sciences Report 2006-07, 88 p.
- Rabus, B., Eineder, M., Roth, A. and Bamler, R. (2003): The shuttle radar topography mission—a new class of digital elevation models acquired by spaceborne radar; ISPRS Journal of Photogrammetry and Remote Sensing, v. 57, p. 241–262.
- RADARSAT International (RSI) (1996): RADARSAT geology handbook; unpublished manual, 70 p.
- Rosen, P.A., Hensley, S., Joughin, I.R., Li, F.K., Madsen, S.N., Rodriguez, E. and Goldstein, R.M. (2000): Synthetic aperture radar interferometry; Proceedings of the Institute of Electrical and Electronics Engineers, v. 88, p. 333–376.
- Usai, S. (2003): A least squares database approach for SAR interferometric data; Institute of Electrical and Electronics Engineers, Transactions on Geoscience and Remote Sensing, v. 41, no. 4, p. 753–760.
- Werner, C., Wegmuller, U., Strozzi, T. and Wiesmann, A. (2003): Interferometric point target analysis for deformation mapping; Proceedings of the Institute of Electrical and Electronics Engineers, International Geoscience and Remote Sensing Symposium, Toulouse, France, v. 7, p. 4362–4364.
- Zebker, H.A. and Goldstein, R.M. (1986): Topographic mapping from interferometric synthetic aperture radar observations; Journal of Geophysical Research, v. 91, no. B5, p. 4993–4999.
- Zebker, H.A. and Villasenor, J. (1992): Decorrelation in interferometric radar echoes; Institute of Electrical and Electronics Engineers, Transactions on Geoscience and Remote Sensing, v. 30, no. 5, p. 950–959.
- Zebker, H.A., Werner, C.L., Rosen, P.A. and Hensley, S. (1994): Accuracy of topographic maps derived from ERS-1 interferometric radar; Institute of Electrical and Electronics Engineers, Transactions on Geoscience and Remote Sensing, v. 32, no. 4, p. 823–836.

Appendix A: InSAR Theoretical Background

To understand and evaluate the results from PS-InSAR processing, it is necessary to review and discuss the basic theory, principles and algorithms behind a Synthetic Aperture Radar (SAR), interferometric SAR (InSAR) and PS-InSAR. Any implementation software should provide a straightforward demonstration of the standard InSAR and PS-InSAR processing workflow; however, the complexity of the theory, principles and algorithms involved are hidden behind the highly simplified graphical user interface (GUI). This review, which should not be considered exhaustive, focuses on implementing PS-InSAR technology using EV-InSAR Coherent Target Monitoring (CTM) software. For further details on the principles of SAR data acquisition, processing and analysis, as well as an in-depth discussion concerning theory and applications of SAR interferometry, we recommend the books of authors such as Henderson and Lewis (1998), Franceschetti and Lanari (1999) and Hanssen (2001), and the papers of authors such as Gens and Genderen (1996), Bamler and Hartl, (1998), Massonnet and Feigl (1998) and Rosen et al. (2000).

Radar

Radar is an acronym for Radio Detection and Ranging. It is an active imaging technology and operates in the microwave portion of the electromagnetic spectrum. A radar antenna emits a series of electromagnetic pulses and detects the reflections of these pulses from imaged ground targets. It records both the strength of the signal and the two-way travel time of the pulse. The strength of the signal (amplitude) defines the pixel brightness and is what we usually associate with a radar image. The time delay enables us to determine the range or distance from the antenna to the ground target.

Radar Phase

The radar antenna also records the arrival phase of the signal. This is possible because the radar signal is coherent, which means the transmitted signal is generated from a stable local oscillator and the received signal has a precisely measurable phase difference in relation to the local reference phase (the transmitted oscillator phase). This renders Radar with the capability to measure the range in phase or fractional wavelength, in addition to measuring the time delay. Phase is a measure of how far the wave has traveled in units of wavelength. For example, if the signal has traveled by a wavelength then the phase has changed by 2π . Usually phase can be accurately measured to about 10 % of the wavelength. This allows a much more accurate distance measurement. For example, for Radarsat-1 (C-band) with a wavelength of 56 mm, the range can be measured to accuracy in the order of millimetres (for example, $56/20 = 2.8$ mm). This is about 3000 times more accurate than the 8.4 m resolution for the standard time delay measurement; however, there are millions of wavelengths between the radar system and the reflector on the ground and the total number of wavelengths is not determined. Thus, the phase measurement is a relative measurement, and can be used only to tell the change in range from one measurement to the next.

The phase measured by the radar antenna depends on several factors: the distance from the SAR sensor to the ground surface, the surface scattering effect on the incident electromagnetic wave, the atmospheric delay along the signal path and the phase noise. The signal phase contribution of a single SAR acquisition can be expressed as the following equation:

$$\phi = \phi_{scattering} + \phi_{atmosphere} + \frac{4\pi}{\lambda} r + \phi_{noise} \quad [1]$$

where $\phi_{scattering}$ is the phase related to the scattering effect of the target; λ is the wavelength, r is the distance between the sensor and the target; $\frac{4\pi}{\lambda}r$ is the phase contributed by the two-way distance between the sensor and the target; $\phi_{atmosphere}$ is the phase contributed by the atmosphere.

For simplicity, one may ignore the phase contributed by the atmosphere ($\phi_{atmosphere}$) and the phase noise (ϕ_{noise}). The phase is then proportional to range. At some range, the radar signal hits a scatterer and is reflected back to the SAR antenna. The arrival phase is recorded to a pixel in the SAR image. This range to the reflection point contributes to the phase of the target at that pixel in the following way. As the

signal hits the target, the phase (ϕ) = $\frac{2\pi}{\lambda}r$. By the time it has arrived at the receiver, the signal has

traveled a distance $2r$, so the phase-range relation is actually $\phi = \frac{4\pi}{\lambda}r$. Note that the phase is wrapped for

every distance of the wavelength (λ) in the range. For Radarsat-1 the wavelength is 5.6 cm. As the range to the pixel's scattering centre is random at the scale of the radar wavelength, the phase related to the range is essentially random with a single SAR system. The target scattering effect also contributes to the phase measured by the antenna. Since the target scattering properties are independent from point to point on the ground, the phase related to the scattering effect is also random. In addition, the radar signal returned to the radar antenna is recorded for every resolution element (e.g., about 8 x 8 m in size for Radarsat-1 Fine Beam 4) in a SAR image and its phase value is the coherent sum of the echoes from all scattering interactions in that resolution element. The exact way in which the contributions from the different scatterers are added up in the observed signal is not predictable. As a result, the phase recorded in a single SAR image is, in general, quite random and of no practical purpose on its own.

Synthetic Aperture Radar (SAR)

The range resolution of a radar signal can be improved by managing the bandwidth of the transmitted pulse. The azimuth resolution of the signal detected by an antenna is inversely proportional to the length of the antenna. A longer antenna can obtain more information about imaged objects and thus improve the resolution. To increase the image resolution in the azimuth direction, the Synthetic Aperture Radar technology uses spacecraft movement and advanced signal processing techniques (called SAR focusing) to simulate a large antenna size. Graham (1974) first demonstrated this technology that improves the azimuth resolution from the 4.5 km beam width for the single pulse to approximately 5 m. Since then, several algorithms have been developed for SAR focusing. A focused radar image is composed of many pixels, each representing the backscatter for the corresponding area of the ground surface. One of the SAR imagery products called Single Look Complex (SLC) has preserved both the amplitude and phase of the backscattered signal for each pixel in complex number format. InSAR mainly uses the phase information. The Radarsat-1 SAR data used in this study were processed (focused) to the SLC format by the Canadian Space Agency (CSA).

SAR Interferometry

As explained previously, the phase in a SAR image is effectively random because its value is generated as the sum of hundreds of elementary returns from all scatterers within the resolution cell. If two separate radar acquisitions are acquired with the same viewing geometry, or with a small distance between the two locations of the SAR platform (called the baseline B in Figure 52) over the same area, however, the summing of the contributions from individual scatterers due to scattering effect is largely the same so that the phase difference between the two image acquisitions is not random (see below). This can either be realized by using two physically separate antennas mounted on the same platform (single-pass interferometry) or two passes of the same antenna (repeat-pass interferometry; Figure 52).

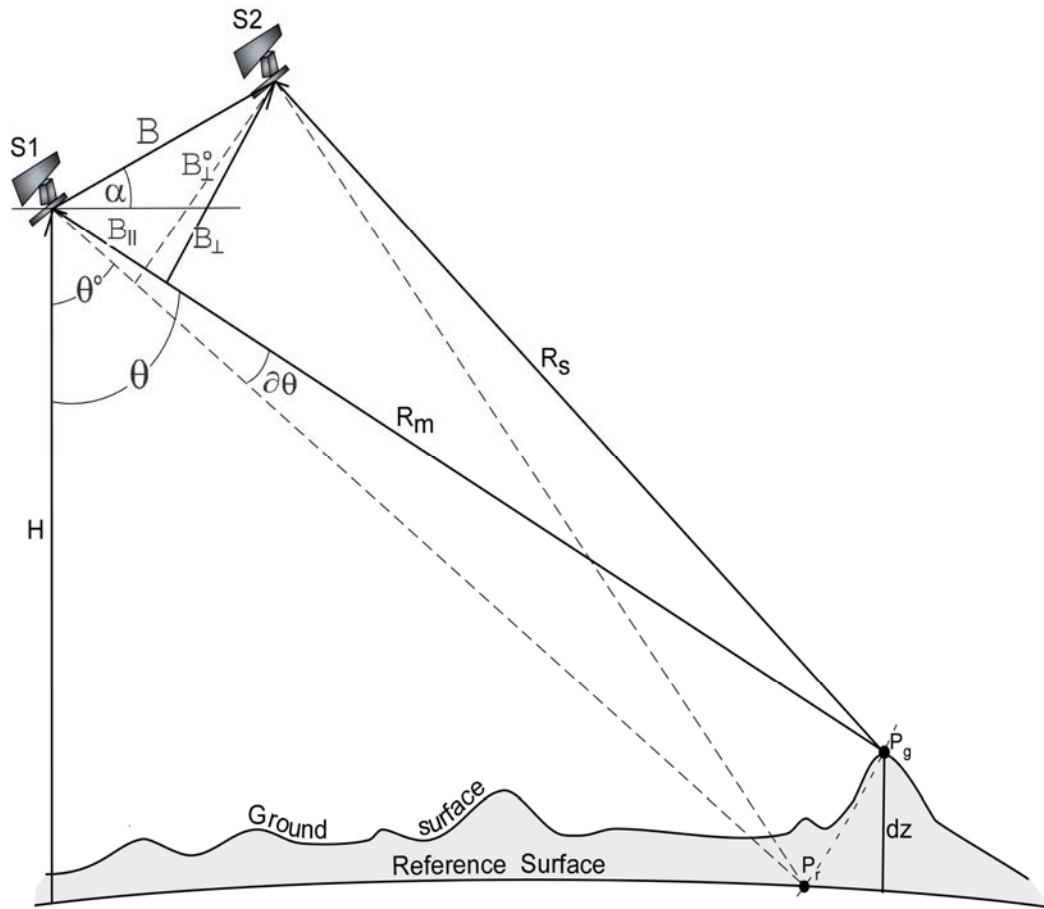


Figure 52. Repeat pass InSAR geometry with an across track InSAR configuration (Flight paths perpendicular into plane). B is called the baseline representing the distance between the two antennas. B_{\perp} and B_{\parallel} are called perpendicular and parallel baseline, respectively. α is the angle between the baseline and the horizontal plane, and θ is the look angle of the sensor. P_g is the ground location of the target and P_r is the location of the target on the reference surface. P_g and P_r have the same range distance from the sensor. H is the sensor altitude and dz is the height of the target above the reference surface. R_m and R_s are the distances from the sensor to the target for the two acquisitions.

Subtracting the phase of the second image from the first forms an interferogram. The interferometric phase in an interferogram can be expressed as:

$$\Delta\phi = \Delta\phi_{scattering} + \Delta\phi_{atmosphere} + \frac{4\pi}{\lambda} \Delta r + \phi_{noise} \quad [2]$$

where $\Delta r = R_s - R_m$ (Figure 52). If the surface scattering effect is the same for the two images then its phase contribution is cancelled in the calculation of the interferometric phase ($\Delta\phi_{scattering} = 0$). Assume that the atmosphere is also the same for the two acquisitions (e.g., when the two acquisition are taken simultaneously) and, thus, $\Delta\phi_{atmosphere} = 0$. Then, the remaining interferometric phase contains only information that is closely related to the difference in distances from the surface to the two SAR locations:

$$\Delta\phi = \frac{4\pi}{\lambda} \Delta r \quad [3]$$

If surface motion occurs between the acquisition times of the two imaging passes of the SAR platform then it contributes to a local phase shift in the interferometric phase:

$$\Delta\phi = \frac{4\pi}{\lambda} \Delta r + \frac{4\pi}{\lambda} \Delta d \quad [4]$$

where Δd is the displacement of the target in the line of sight of the radar signal that occurred during the two acquisitions.

Such deformation can be estimated directly as a fraction of the wavelength and its contribution to the phase is independent of the satellite separation. The ideal condition for deformation detection occurs when the two satellites are in the same position in space (i.e., $\Delta r = 0$) so that only deformation will cause phase shifts in the interferometric phase:

$$\Delta\phi = \frac{4\pi}{\lambda} \Delta d \quad [5]$$

However, the ideal condition is never observed in practice. When the two antenna positions are separated by some distance in the plane perpendicular to the antenna motion, called the interferometric baseline (Figure 52), different points on the surface will be at slightly different relative positions from the antennas. This will generate interferometric phase due to the surface topography as well as deformation. The interferometric phase caused by topography can be divided into the phase contributed by a reference Earth surface and that by the elevation above it. In reality, the interferometric phase is the sum of contributions from different processes (Zebker et al., 1994; Ferretti et al., 2000; Hanssen 2001):

$$\Delta\phi = \phi_{flat_earth} + \phi_{elevation} + \phi_{displacement} + \Delta\phi_{atmosphere} + \phi_{noise}, \quad [6]$$

where ϕ_{flat_earth} is the flat-Earth phase contributed by the reference Earth surface, $\phi_{elevation}$ is the phase contributed by the elevation of the target above the reference surface, $\phi_{displacement}$ is a phase contribution due to a possible movement of the target in the line of sight (LOS) direction, $\Delta\phi_{atmosphere}$ is a phase resulting from changes in the atmospheric delay processes along the signal path between the two acquisitions, and ϕ_{noise} is the phase noise that includes the term $\Delta\phi_{scattering}$ in equation [2].

Depending on the application, the second, third and fourth terms on the right hand side of equation [6] may be considered useful information or noise. The flat-Earth phase ϕ_{flat_earth} is a deterministic component and can be calculated (Zebker and Goldstein, 1986; Hanssen 2001) by the following equation:

$$\phi_{flat_earth} = \frac{4\pi}{\lambda} B \sin(\theta^0 - \alpha), \quad [7]$$

where B is the baseline, θ^0 is the look angle found for the reference surface and α is the angle between the baseline and the horizon (see Figure 52).

Under the condition that there is no displacement ($\phi_{displacement} = 0$) and $\Delta\phi_{atmosphere} + \phi_{noise}$ is negligible, then,

$$\Delta\phi = \phi_{flat_earth} + \phi_{elevation} \quad [8]$$

Equation [8] is the key equation used by one of the InSAR applications called standard InSAR, the purpose of which is to derive a digital elevation model (DEM). Knowing the satellite-ground target geometry involved, elevation can be derived using the following equations (Zebker and Goldstein, 1986; Hanssen, 2001):

$$\phi_{elevation} = \Delta\phi - \phi_{flat_earth} \quad [9]$$

$$dz = \frac{\lambda R_m \sin(\theta^0)}{4\pi B_{\perp}^0} \phi_{elevation} \quad [10]$$

where $B_{\perp}^0 = B \cos(\theta^0 - \alpha)$, λ is the radar wavelength, R_m is the range or the distance between the radar and the target on the ground, θ^0 is the look angle for the reference point (Figure 52), B_{\perp} is the perpendicular baseline and dz is the surface elevation above a reference elevation (see Figure 52). Zebker et al. (1994) demonstrated that an accuracy of 1–10 m can be achieved for the elevation, and the DEM obtained from the shuttle radar topography mission is a good example (Rabus et al., 2003).

In the study of surface displacements, which is the case for the present study, equation [6] is used to remove the topographic phase contribution from the signal. To do this, the imaged topography must be known either from a digital elevation model (DEM), or be estimated from a separate interferogram for DEM generation. In the case that a DEM is used, the phase contributed by the elevation can be calculated by rearranging Equation [10]:

$$\phi_{elevation} = \frac{4\pi B_{\perp}^0}{\lambda R_m \sin \theta^0} dz \quad [11]$$

The interferometric phase after removal of topographic phase (including flat-Earth phase and elevation phase) is called differential interferometric phase. Due to the inevitable error present in any digital elevation model, the removal of elevation phase is never perfect. As a result, the equation for the differential interferometric phase is

$$\phi_{differential} = \phi_{displacement} + \Delta\phi_{atmosphere} + \phi_{dem_error} + \phi_{noise} \quad [12]$$

where ϕ_{dem_error} represents the residual phase due to DEM error after the elevation phase removal. If the last three terms in equation [12] are negligible, then, the displacement in the line of sight direction of radar (Δd) can be calculated as

$$\Delta d = \frac{\lambda}{4\pi} \phi_{displacement} \cong \frac{\lambda}{4\pi} \phi_{differential} \quad [13]$$

Equation [13] is the equation used by another type of InSAR application called Differential InSAR (DInSAR), the focus of which is to derive ground deformation from two radar acquisitions from repeat passes.

Persistent/permanent Scatterers Interferometry (PS-InSAR)

Differential InSAR relies heavily on fringe patterns in a differential interferogram to reveal deformation patterns. It is limited by changes in ground surface reflectivity, which is called decorrelation (Zebker and Villasenor, 1992), and atmospheric delay processes. Decorrelation could cause ϕ_{noise} in equation [12] to increase to a level that renders the equation [13] invalid and thus, makes the accurate measurement of deformation impossible. This will cause the interferogram to lose fringe patterns and be too noisy to interpret. The change in the atmospheric conditions between the repeat pass acquisitions could also easily cause $\Delta\phi_{atmosphere}$ to be too large to be negligible, thus masking entire deformation fringe patterns. In addition, a low accuracy of DEM will also generate residual topographic effects in the differential interferogram.

However, even for the case when decorrelation in most locations has destroyed the fringe patterns and the atmospheric perturbation is present in an interferogram, there are still many isolated point-like targets in the interferogram that return the energy from the SAR sensor coherently. On these targets, the phase due to changes in their scattering properties (included in ϕ_{noise} of equation [12]) is negligible and accurate measurement of deformation can still be derived, if the $\Delta\phi_{atmosphere}$ and ϕ_{dem_error} in equation [12] can be eliminated or reduced to an acceptable level. These targets are called coherent targets and the subject of a new suite of InSAR techniques called Persistent/permanent Scatterer Interferometry (PS-InSAR).

PS-InSAR was first introduced in the late 1990's as Permanent Scatterer (PS) technique (Ferretti et al., 1999). Instead of analyzing the phase in the spatial domain like DInSAR, the phase of isolated coherent points is analyzed as both a function of time and space. It uses SAR data from multiple acquisitions over a long period and creates a stack of differential interferograms that have a common master image. By using such a large number of acquisitions, the atmospheric signal and DEM error phase can be estimated and corrected for the coherent targets. This technique bypasses the problem of geometrical and temporal decorrelation encountered in DInSAR by considering only point-like scatterers. It offers a convenient processing framework that enables the use of all acquired images (even with large baselines), and a parameter estimation strategy for interferograms with low spatial coherence (Colesanti et al., 2003a, b; Ferretti et al., 2000, 2001).

PS-InSAR separates the atmospheric change phase ($\Delta\phi_{atmosphere}$), deformation phase ($\phi_{displacement}$) and DEM error phase (ϕ_{dem_error}) in equation [12] by exploiting their difference in spatial and temporal correlation properties (Table 9).

Table 9. Temporal and spatial correlation properties of phase components in PS-InSAR

Phase	Temporal	Spatial	Acquisition Geometry
$\phi_{displacement}$	Correlated in time	Correlated in space	Independent of baseline
ϕ_{dem_error}	Constant in time	Uncorrelated in space	Proportional to baseline
$\Delta\phi_{atmosphere}$	Uncorrelated in time	Correlated in space	Independent of baseline
ϕ_{noise}	Uncorrelated in time	Uncorrelated in space	Independent of baseline

PS-InSAR solves equation [12] with the following steps. First, targets that have a minimal ϕ_{noise} are detected and identified as coherent targets by using multiple interferograms. Then, the atmospheric change phase ($\Delta\phi_{atmosphere}$) is estimated on the coherent targets and removed from the differential phase ($\phi_{differential}$) for each interferogram. Finally, the deformation phase ($\phi_{displacement}$) and DEM error phase (ϕ_{dem_error}) are estimated using the time series of the atmosphere corrected phases for each target and an iterative scheme to maximize the temporal coherence of the target (Ferretti et al., 2001). The final results of PS-InSAR are millimetre scale, relative measurement of deformation in the line of sight direction on the identified targets with respect to a reference target.

After it was demonstrated that it is possible to reduce atmospheric artifacts and to obtain highly precise estimates despite decorrelation, by using a large number of acquisitions, a number of related techniques, including Coherent Target Monitoring (CTM; Atlantis Scientific Inc., 2004), Interferometric Point Target Analysis (IPTA; Werner et al., 2003), Stable Point Network Analysis (SPNA; Duro et al., 2003), Small Baseline Subset Approach (Berardino et al., 2002; Usai, 2003) and Corner Reflector Interferometry, have been developed. These techniques seek to implement the PS technique by using modified approaches.

EV_InSAR Coherent Target Monitoring (CTM) Analysis

As mentioned previously, Coherent Target Monitoring (CTM) analysis is one of the PS-InSAR implementations and is used in the present study. It was developed by Atlantis Scientific Inc., which is currently affiliated with Microsoft. Like any other PS-InSAR implementation, CTM requires a set of multitemporal differential interferograms as inputs. The residual phase associated with removal of the flat-Earth phase and elevation phase should be minimized as possible in these interferograms. These interferograms are registered with each other using a common master image and are processed to the same region of interest (ROI). They contain a time series of differential phases for each pixel used for CTM analysis.

As indicated in equation [12], the phase due to deformation is still combined with the atmospheric change phase and DEM error phase in each differential interferogram. The processing algorithms for separating/estimating each term on the right side of equation [12], as used by CTM analysis, are briefly described below (Atlantis Scientific Inc., 2004).

Initial Atmospheric Change Phase Estimation

This involves choosing a stable region near the suspected deformation area of interest. In the stable region, the deformation phase ($\phi_{displacement}$) is assumed to be zero. Since DEM error phase (ϕ_{dem_error}) can be modelled as a random process and the phase noise (ϕ_{noise}) is random in space, averaging of the differential phase ($\phi_{differential}$) over the stable region will minimize the DEM error phase (ϕ_{dem_error}) and phase noise (ϕ_{noise}), and leave behind only the atmospheric change phase ($\Delta\phi_{atmosphere}$). Within a small study area (a few square kilometres), the atmospheric change can be assumed to be constant. As a result, the initial estimation of the atmospheric change phase ($\Delta\phi_{atmosphere}$) is obtained by averaging the differential interferometric phase ($\phi_{differential}$) over the stable region.

Estimation of the DEM error phase and deformation phase

The atmospheric phase change ($\Delta\phi_{atmosphere}$), estimated by averaging the differential interferometric phase ($\phi_{differential}$) over the stable region, is removed from the differential phase for each interferogram. The phase left behind is the atmospheric corrected differential phase ($\phi_{differential_atmosphere_corrected}$):

$$\phi_{\text{differential_atmosphere_corrected}} = \phi_{\text{displacement}} + \phi_{\text{dem_error}} + \phi_{\text{noise}} \quad [14]$$

where the phase noise (ϕ_{noise}) term represents a general noise that could include the residual atmospheric change phase due to imperfect removal of the atmospheric change phase ($\Delta\phi_{\text{atmosphere}}$).

At each point in the coregistered interferograms the time series of the atmospheric phase-corrected differential phase is compared with a linear model of an assumed deformation rate (v) and a model of an assumed DEM error (dz) for that point. First, a two-dimensional search grid for the DEM error and deformation-rate values is used, with the user-defined range ($\pm v_{\text{maximum}}, \pm dz_{\text{maximum}}$) and increment values ($\Delta v, \Delta dz$) for searches in both the DEM error and deformation rate. Based upon the SAR geometry for each interferogram, the value of the change in phase with respect to height is known (Equation 11). Thus, given an assumed DEM error (dz) in the search, the associated DEM error phase ($\phi_{\text{dem_error}}$) can be calculated for each pixel in each interferogram (see Equation 11). Then, the wrapped deformation phase ($\phi_{\text{displacement}}$) can be calculated as:

$$\phi_{\text{displacement}} = \phi_{\text{differential_atmosphere_corrected}} - \phi_{\text{dem_error}} + \phi_{\text{noise}} \quad [15]$$

The acquisition date (T_i) for each SLC image is known, so, given an assumed deformation template (v) in the search an estimate of the modelled deformation phase (unwrapped) can be interpolated for each pixel in each interferogram:

$$\phi_{i_model} = \frac{4\pi}{\lambda} v T_i, \quad i = (1, \dots, n) \quad [16]$$

where n is the total number of the interferograms used for CTM analysis. Assuming a deformation rate value, the unwrapped deformation phase can be obtained by unwrapping the wrapped phase ($\phi_{\text{displacement}}$) along the modelled deformation slope, which is defined by the assumed deformation rate at each pixel, in each interferogram. This is done by adjusting the wrapped phase ($\phi_{\text{displacement}}$) with a multiple of 2π such that the resultant deformation phase ($\phi_{i_displacement_unwrapped}$) matches the model (ϕ_{i_model}) in a minimum least squares sense. As a result, for each pair of DEM error value and deformation rate/slope value, a phase residual can be calculated for each pixel in each interferogram:

$$\phi_{i_residual} = \phi_{i_differential_atmosphere_corrected} - \phi_{i_model} - \phi_{i_dem_error} \quad [17]$$

Then, the time series of the residual phases of each pixel are used to calculate a temporal coherence value (γ) for the pixel:

$$\gamma = \frac{\sqrt{\left(\sum_i^n \cos(\phi_{i_residual})\right)^2 + \left(\sum_i^n \sin(\phi_{i_residual})\right)^2}}{n}, \quad i = (1, \dots, n) \quad [18]$$

where n is the total number of the interferograms used for CTM analysis. For each pixel, a temporal coherence value (γ) is calculated with each pair of DEM error value and deformation rate/slope value

assumed in the search. This gives rise to many temporal coherence values (γ) for each pixel. The DEM error value and the deformation slope value of the pair that gives the highest temporal coherence ($(v, dz) \bullet \gamma_{\text{maximum}}$) are used for the estimation of the DEM error phase ($\phi_{\text{dem_error}}$) and the wrapped deformation phase ($\phi_{\text{displacement}}$) for that pixel, using equation 11 and 15 respectively, and the maximum temporal coherence value is used as the estimate of the temporal coherence value for that pixel as well.

Atmospheric Correction Refinement

The atmospheric correction, calculated by averaging the differential interferometric phase over the stable reference region, is only an initial estimate. This estimate can be refined with an iterative scheme. First, estimates for a DEM error phase ($\phi_{\text{dem_error}}$), a deformation phase ($\phi_{\text{displacement}}$) and a temporal coherence value (γ) are obtained for each pixel as described in the previous section. Then, an estimate of the atmospheric change phase ($\Delta\phi_{\text{atmosphere}}$) can be calculated for each pixel in each interferogram:

$$\Delta\phi_{\text{atmosphere}} = \phi_{\text{differential}} - \phi_{\text{displacement}} - \phi_{\text{dem_error}} \quad [19]$$

Then, the atmospheric change phase ($\Delta\phi_{\text{atmosphere}}$) is averaged over the area. Different from the averaging for obtaining the initial estimate of the atmospheric change phase ($\Delta\phi_{\text{atmosphere}}$), the averaging for atmospheric correction refinement is carried out only over the targets that have a temporal coherence above a threshold. The reason is that only the targets with a high temporal coherence allow reliable estimates. Then, the newly estimated atmospheric change phase ($\Delta\phi_{\text{atmosphere}}$) is subtracted from the original differential interferograms to obtain a new estimate of the atmospheric corrected differential phase ($\phi_{\text{differential_atmosphere_corrected}}$). Finally, the atmospheric corrected differential phase ($\phi_{\text{differential_atmosphere_corrected}}$) is again compared with the model as described in the previous section, and a refined set of estimates for the DEM error phase ($\phi_{\text{dem_error}}$), the wrapped deformation phase ($\phi_{\text{displacement}}$) and the temporal coherence value (γ) are obtained for each pixel in each interferogram. The two processing steps, estimating the DEM error phase and deformation phase and Atmospheric Correction Refinement, can be repeated until the improvement in estimation of the atmospheric change phase ($\Delta\phi_{\text{atmosphere}}$) stops. At the end, the unwrapped deformation phase is used to calculate the time series of the cumulative deformation at each pixel in the line of sight of the radar sensor using the following equation:

$$\Delta d_i = \frac{4\pi}{\lambda} \phi_{i_displacement_unwrapped}, \quad i = (1, \dots, n) \quad [20]$$

where n is the total number of the interferograms used for CTM analysis.

Deformation Model Refinement

This is an optional processing step in CTM analysis. The deformation model used in the estimation of the DEM error phase and deformation phase, as described previously, is a linear model. In actuality, the true physical deformations could be nonlinear. This implies that there is a weakness in the model-based approach for deformation estimates in current PS-InSAR application. If the assumed deformation model does not fit the actual deformation trend, the deformation estimate will not be reliable. To cope with nonlinear deformation, EarthView InSAR CTM uses an approach that refines an existing linear model. It assumes that the linear model is sufficiently close to a good solution, including producing a reasonable

estimate of the DEM error. Then, a nonlinear model is fitted to the time series of the deformation phase estimates that result from the linear model. Three types of nonlinear model refinements are currently implemented: “simple smoothing,” “piecewise linear fit” and “polynomial fit.”

“Simple smoothing” is a nonparametric fit that is carried by locally smoothing the time series of the wrapped deformation phases estimated from the previous iteration. The nonlinear model is formed by simple unwrapping (assume all phase jumps are less than π in absolute value) of the smoothed phase and the unwrapped deformation phases from the previous iteration of the linear model are updated accordingly. “Piecewise linear” fit is implemented by locally linear-fitting the time series of the wrapped deformation phases estimated from the previous iteration. The nonlinear model is obtained by simple unwrapping of the wrapped phases of local linear-fitting and the unwrapped deformation phases from the previous iteration of linear model are updated. “Polynomial fit” fits a polynomial to the unwrapped deformation phase values from the linear model to form the new nonlinear model. The unwrapped deformation phases from the previous iteration of the linear model remain the same.

As indicated by Equation 17 and 18, the calculation of the temporal coherence is dependent on the modelled deformation phase (ϕ_{i_model}). Consequently, the above-mentioned three deformation model refinements lead to an update to the temporal coherence due to the change of the modelled deformation phase (ϕ_{i_model}) associated with the new nonlinear model. The updated temporal coherence value is systematically higher than that from the linear model, as the modelled deformation phase (ϕ_{i_model}) with the refinement is closer to the atmospheric corrected differential phase ($\phi_{i_differential_atmosphere_corrected}$) in each interferogram.

Coherent Targets and Temporal Coherence

As mentioned previously, the phase value recorded for each pixel is the coherent sum of the echoes from all scattering interactions in that resolution element. Since the phase contribution of each element depends on the viewing angle, the interferometric phase will be influenced by the baseline. A nonzero baseline will lead to a nonzero scattering change phase ($\Delta\phi_{scattering}$) in Equation 2. When the baseline increases, the scattering change phase ($\Delta\phi_{scattering}$) will also increase, so does the phase noise (ϕ_{noise}) in the interferometric phase in Equation 6. This is called geometric decorrelation. The pixels affected by geometric decorrelation usually contain an extended target or multiple equally contributing point-like targets. These pixels account for the majority of the pixels in a study area with vegetation and are also subject to temporal decorrelation, which is related to the scattering property change over time. However, there are some image pixels that have a scattering mechanism that is dominated by a single point-wise element (i.e., much smaller than the image pixel). Since the phase contribution of the dominant point-like element overwhelms the coherent sum of all other scattering elements present within the same sampling cell, the interferometric phase of these pixels is only slightly affected by geometric decorrelation. In addition, if the dominant scatterers correspond to objects, the scattering property of which does not vary in time (e.g., portions of man-made structures and exposed bare rocks), temporal decorrelation is also negligible. This will lead to minimum phase noise (ϕ_{noise}). These targets are called coherent or permanent/ persistent targets. They are the focus of PS-InSAR because reliable deformation measurement can be obtained only over the coherent targets.

By using a large number of interferograms (at least 10), the phase behaviour in time of the pixels can be examined. Then, the pixels can be discriminated based on their phase coherence in time, and a subset of stable pixels can be identified as coherent targets. Different methods have been developed for identifying

the coherent targets. In Earth View InSAR CTM, the stability of phase over time is characterized by the temporal coherence value (γ), which is calculated using Equation 18.

The phase residual ($\phi_{residual}$) in equations 17 and 18 is related to the scattering change phase ($\Delta\phi_{scattering}$) and phase noise (ϕ_{noise}). If the phase residual ($\phi_{residual}$) does not change over time, it indicates a perfect coherence target that is not affected by geometric and temporal decorrelation, and the temporal coherence (γ) will be 1. The more unstable the phase residual ($\phi_{residual}$) over time, the lower the temporal coherence (γ) value. However, even a random phase change over time will give rise to a nonzero temporal coherence. For a scatterer with random phase, the temporal coherence based on N images will be about $1/N$ (Atlantis Scientific Inc., 2004). Due to the deformation phase and DEM error phase estimation and removal process inherent in the calculation of the coherence, a high coherence value could result even though the underlying phase is random. As a result, it is recommended that only those targets with a temporal coherence value above a certain threshold, which is four standard deviations greater than the expected temporal coherence value assuming the phase is random (Atlantis Scientific Inc., 2004), may be considered valid coherent targets. This temporal coherence threshold is related to the number of interferograms used. Figure 53 shows the temporal coherence threshold versus the number of interferograms as recommended by Atlantis Scientific Inc. (2004).

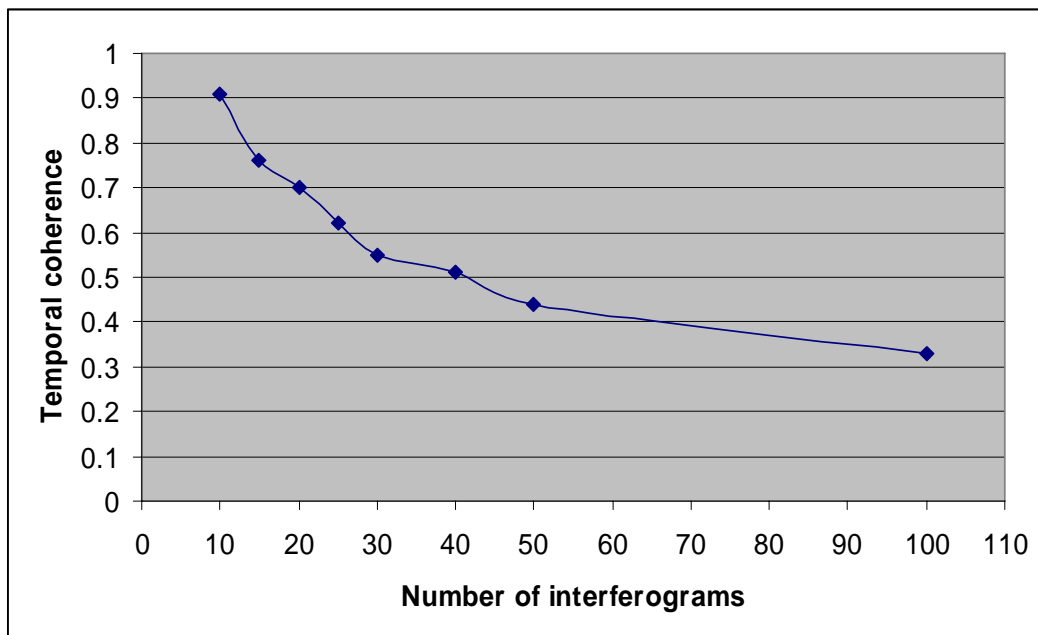


Figure 53. Recommended temporal coherence threshold with regard to the number of interferograms used (based on data from Atlantis Scientific Inc., 2004).

The temporal coherence calculation relies on the deformation model used. This is a weakness in the model based approach used in current PS-InSAR applications. If the assumed deformation model does not fit the actual deformation pattern, the temporal coherence may be underestimated and many coherent targets may remain unidentified. The deformation model refinement, as described previously, usually leads to a higher temporal coherence and, thus, many more targets identified as the coherent targets. However, this could also lead to false identification of coherent targets. Selecting the optimal deformation model is very challenging and requires some a priori knowledge about the deformation history.

Appendix B: Interferograms and Coherence Maps

During the generation of the interferogram, there are two types of residual phase that needs to be removed. The first is the phase information due to the flat (or slightly curved) Earth's surface, and it is common to both differential interferometry and standard interferometry (e.g., DEM generation). The automatic flat-Earth phase removal during the generation of the interferogram is not complete due to inaccuracies in the reported orbital information of the satellite platforms and deviations of the target from the Earth model used. In addition to the flat-Earth phase, a differential interferogram may also contain some residual topographic phase due to the uncertainty in the baseline-target geometry, and inaccuracies in coregistration of the master image to the DEM as well.

The key to the complete removal of the residual phases is to accurately correct the baseline geometry. The correction of the baseline geometry is perfect when the flat-Earth phase is completely removed. This is because the flat-Earth phase is very sensitive to errors in the master and slave orbit modeling. For example, an error of 5 m in the perpendicular baseline will cause a serious flat-Earth phase slope across the interferogram in the case of C-band data, such as ERS and RADARSAT. Although EV-InSAR provides a tool with a visualized environment for adjusting the baseline, it is very challenging to visually identify the fringes caused by residual phase, due to decorrelation and atmospheric masking. Also, it requires some a priori knowledge of the target to differentiate between the fringes of residual phase and those of true features.

There are two methods for accomplishing the visual removal of the flat-Earth phase: one is by looking at the large view of interferograms for the flat-Earth phase removal and correction of the slave orbit; the other focuses on the smaller area of direct interest. Examining large views help to correctly model the flat-Earth phase, but may fail when a large portion of the view is too decorrelated to see the fringes. Focusing on smaller area of direct interest has the advantage of correctly constraining the process by incorporating existing knowledge about the stable area, but may miss the big picture of the flat-Earth fringes, which results in incomplete removal of the flat-Earth phase. The incomplete removal of the flat-Earth phase, in turn, leads to inaccurate modeling of the baseline geometry. During the visual removal of the flat-Earth phase, the authors tried to incorporate both methods. In this Appendix, all the differential interferograms are presented. For some of the interferograms, both a large and a small view of the interferograms are included, for the reader's benefit.

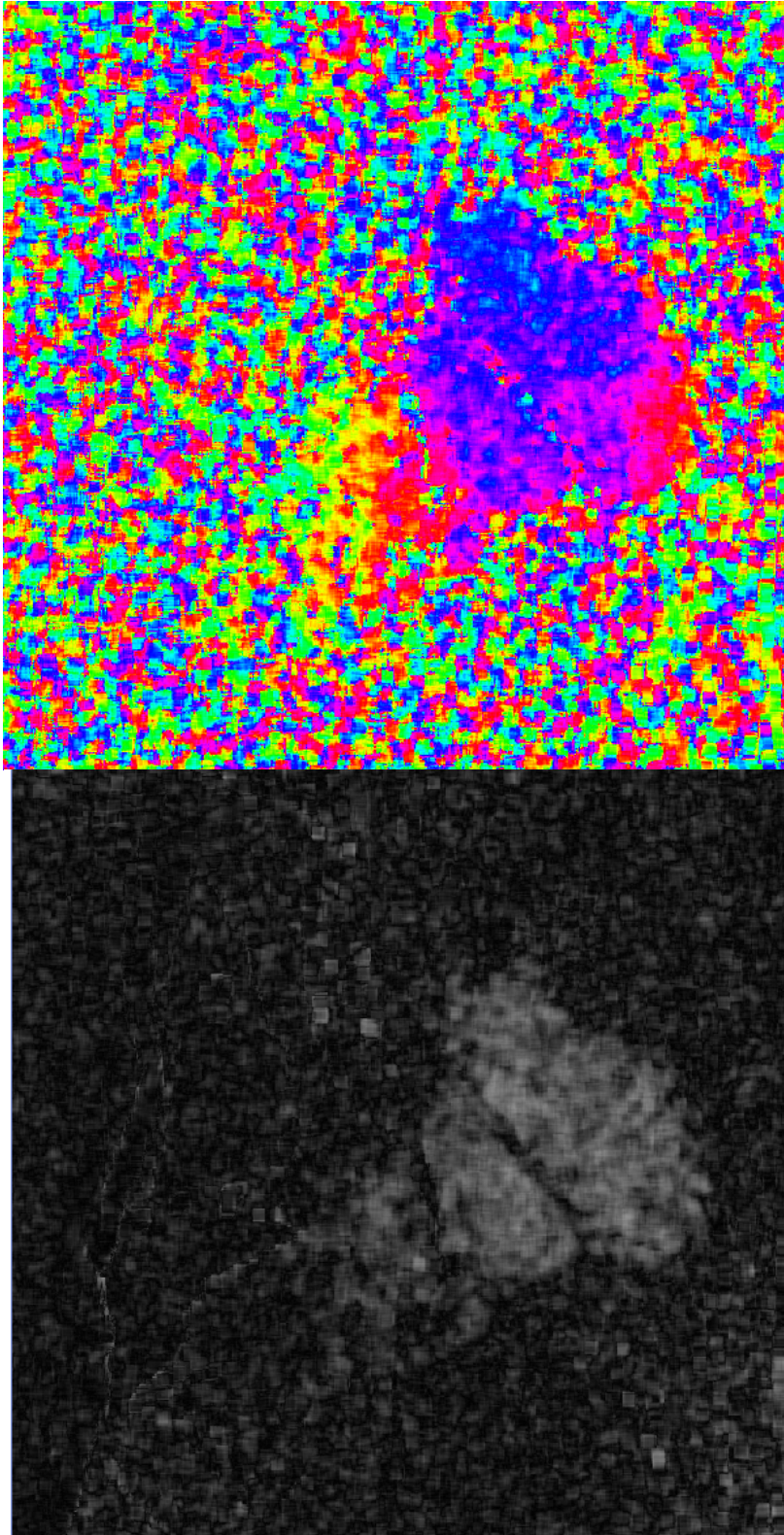


Figure 54. Interferogram (upper) and coherence (lower) images from Run 1. See Appendix B text for details.

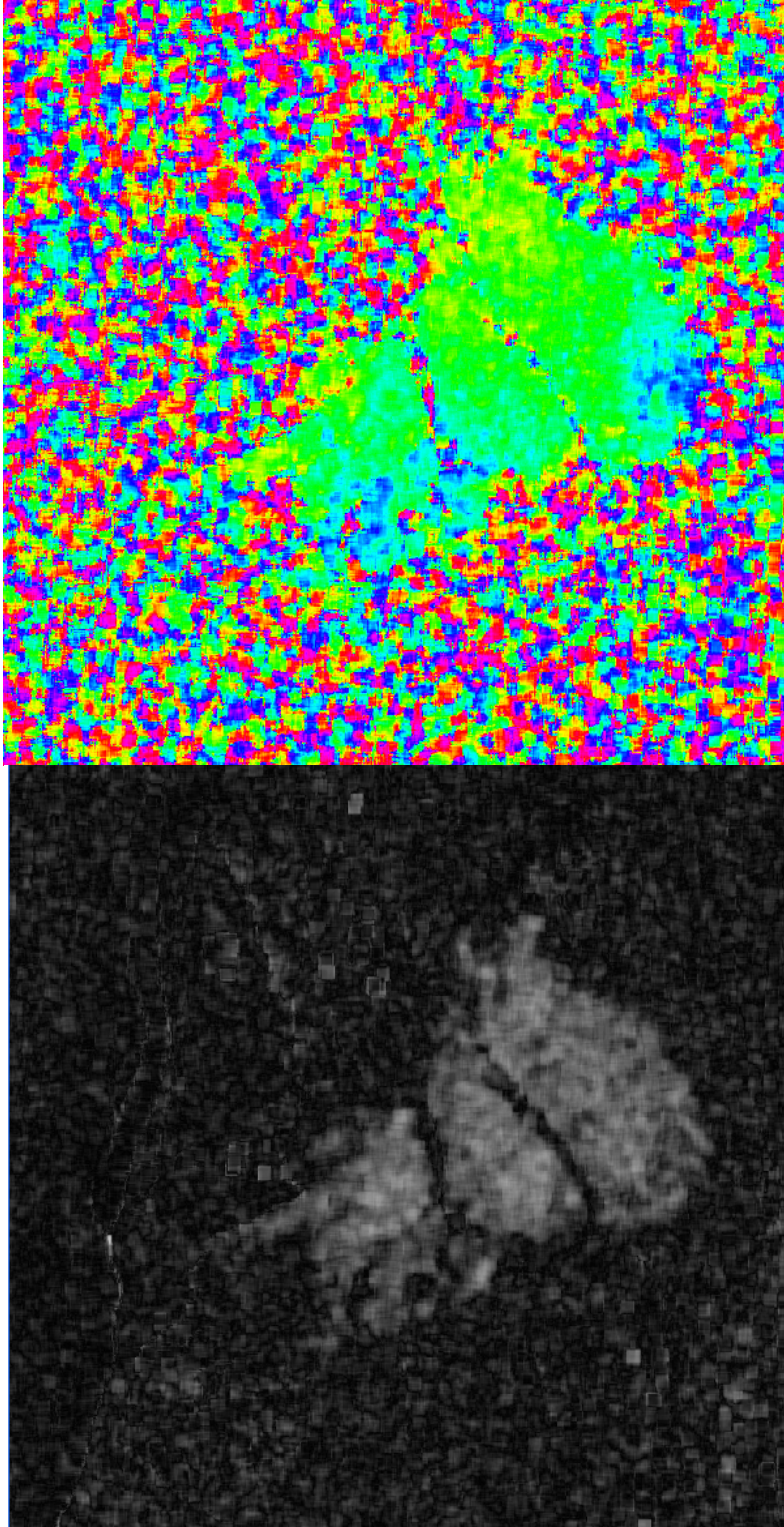


Figure 55. Interferogram (upper) and coherence (lower) images from Run 2. See Appendix B text for details.

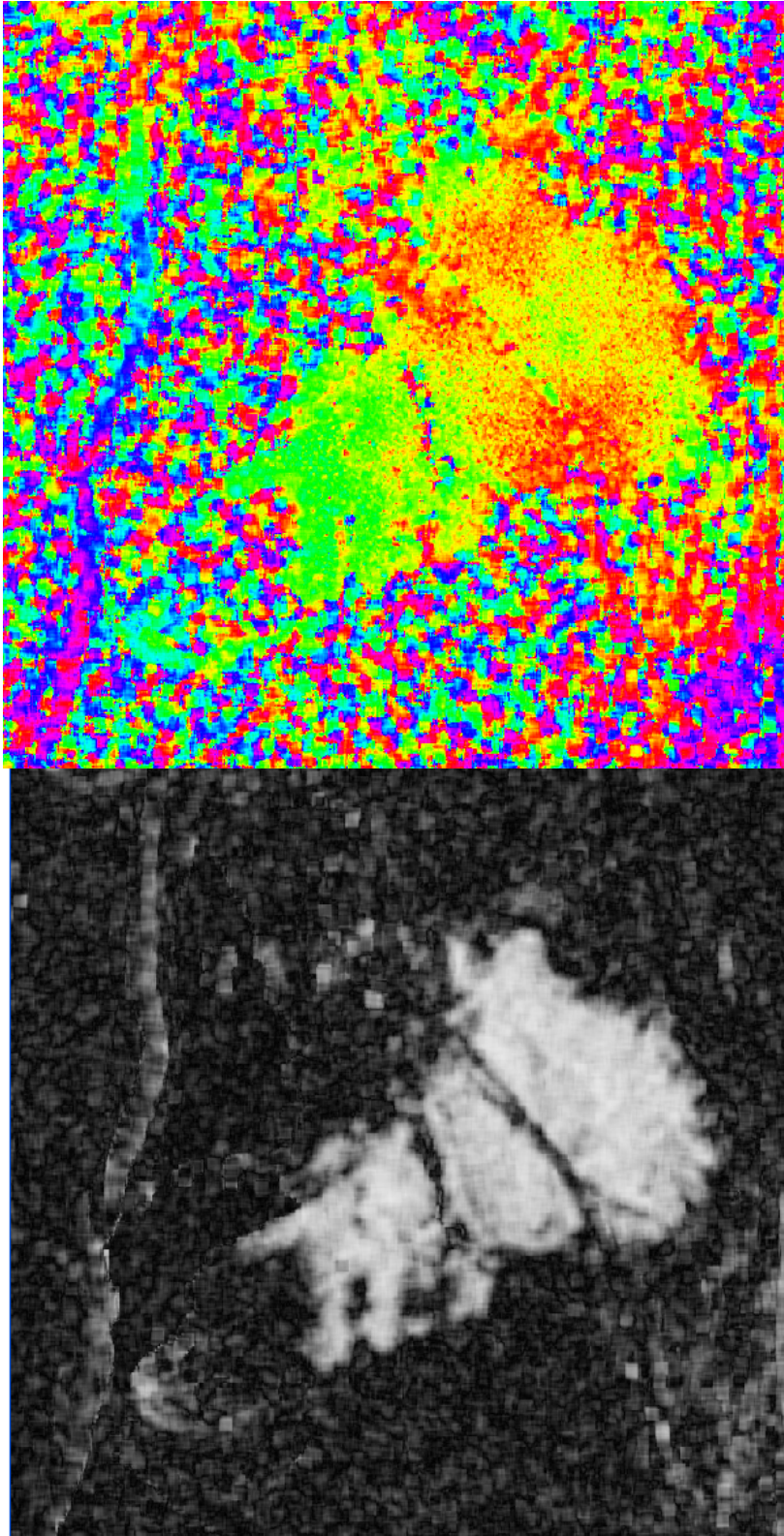


Figure 56. Interferogram (upper) and coherence (lower) images from Run 3. See Appendix B text for details.

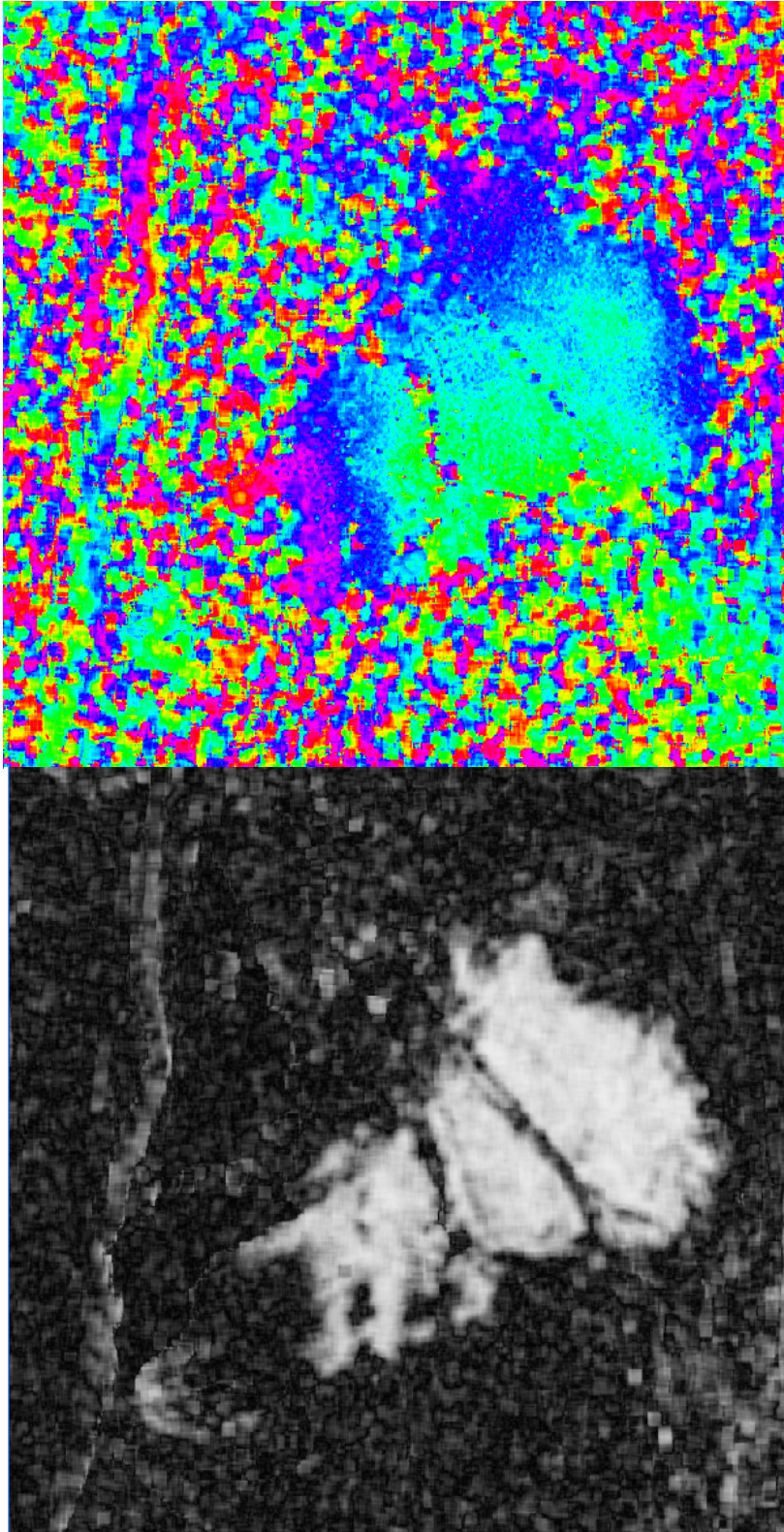


Figure 57. Interferogram (upper) and coherence (lower) images from Run 4. See Appendix B text for details.

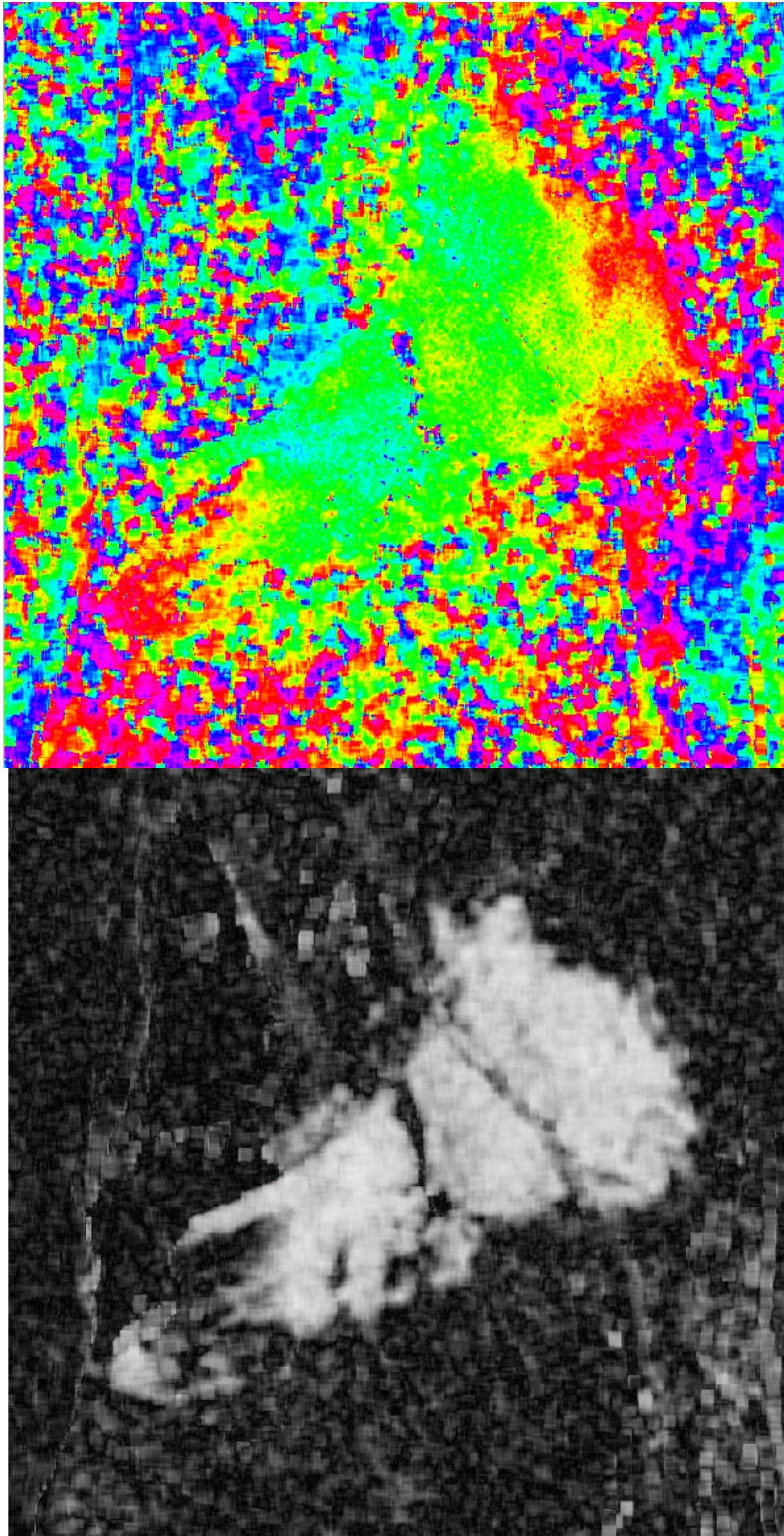


Figure 58. Interferogram (upper) and coherence (lower) images from Run 5. See Appendix B text for details.

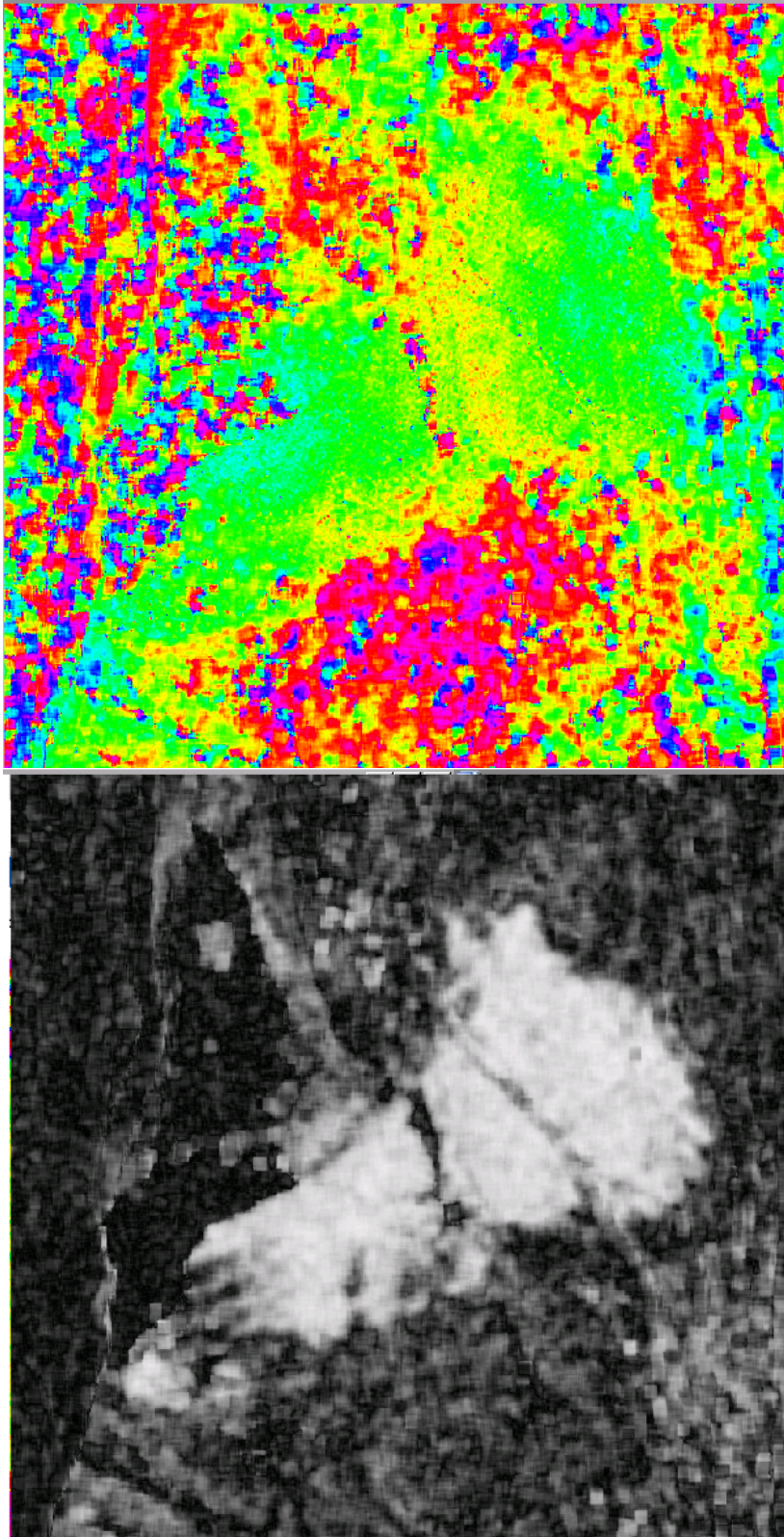


Figure 59. Interferogram (upper) and coherence (lower) images from Run 6. See Appendix B text for details.

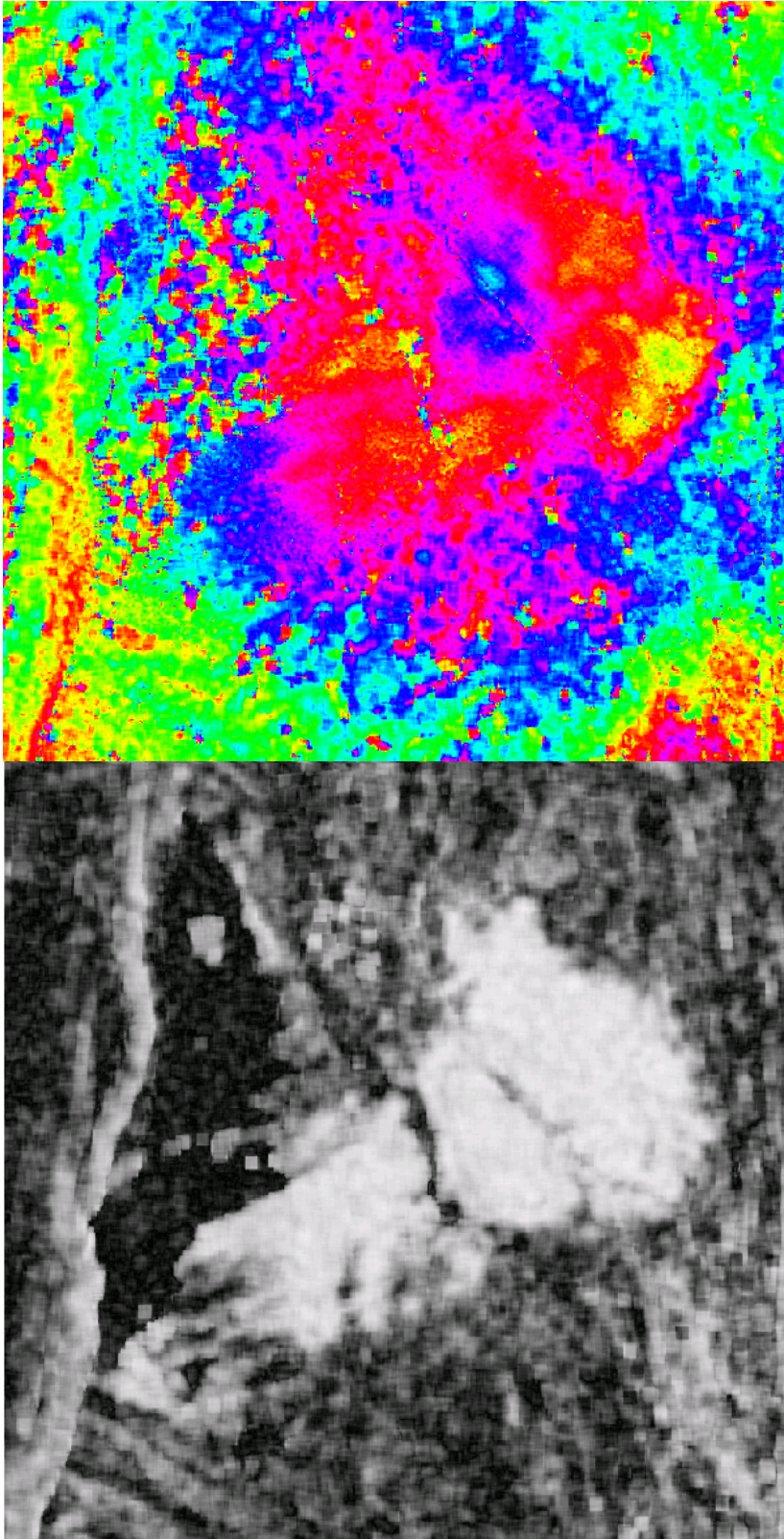


Figure 60. Interferogram (upper) and coherence (lower) images from Run 8. See Appendix B text for details.

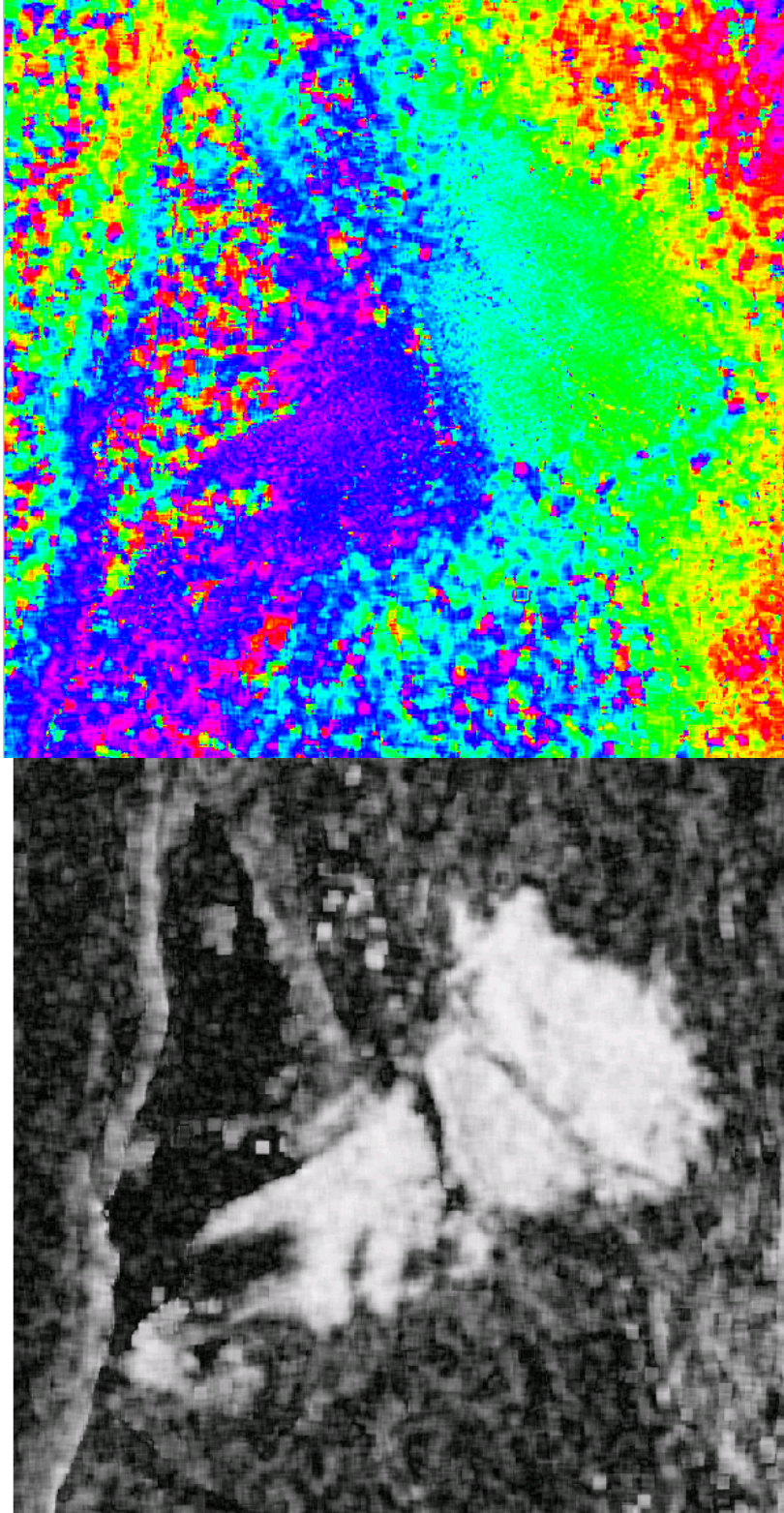


Figure 61. Interferogram (upper) and coherence (lower) images from Run 9. See Appendix B text for details.

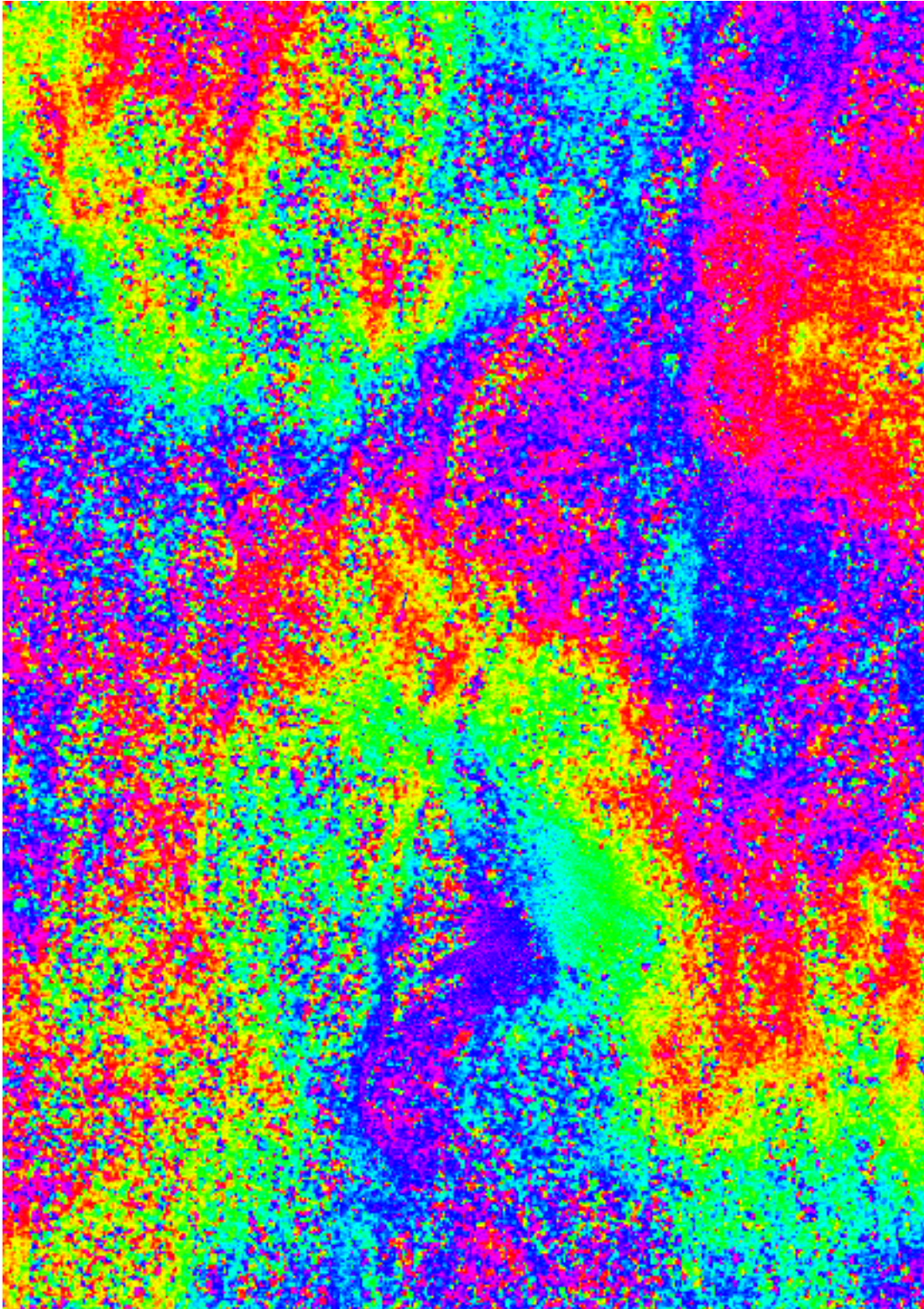


Figure 62. Larger area of Interferogram from Run 9 showing atmospheric effect. See Appendix B text for details.

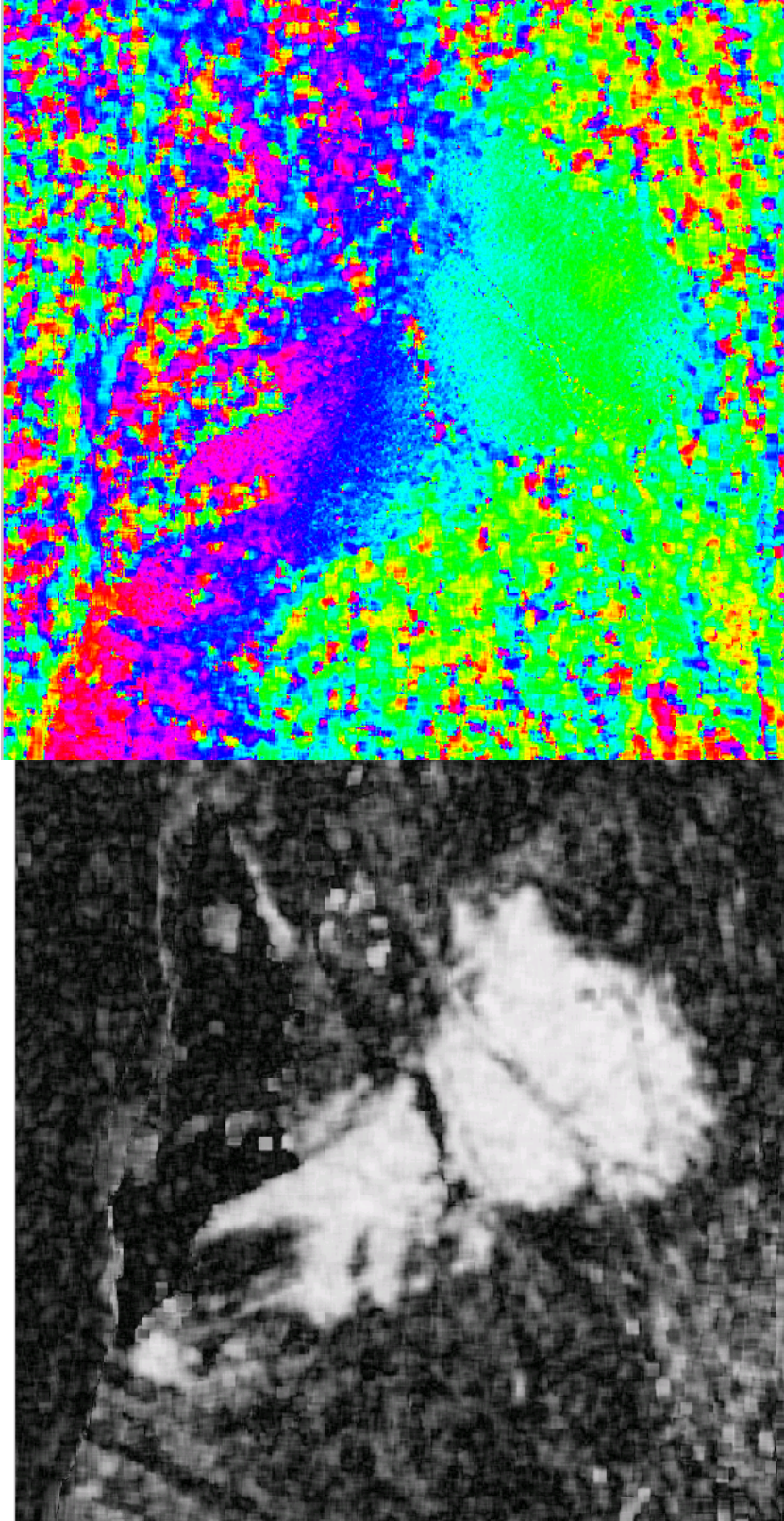


Figure 63. Interferogram (upper) and coherence (lower) images from Run 10. See Appendix B text for details.

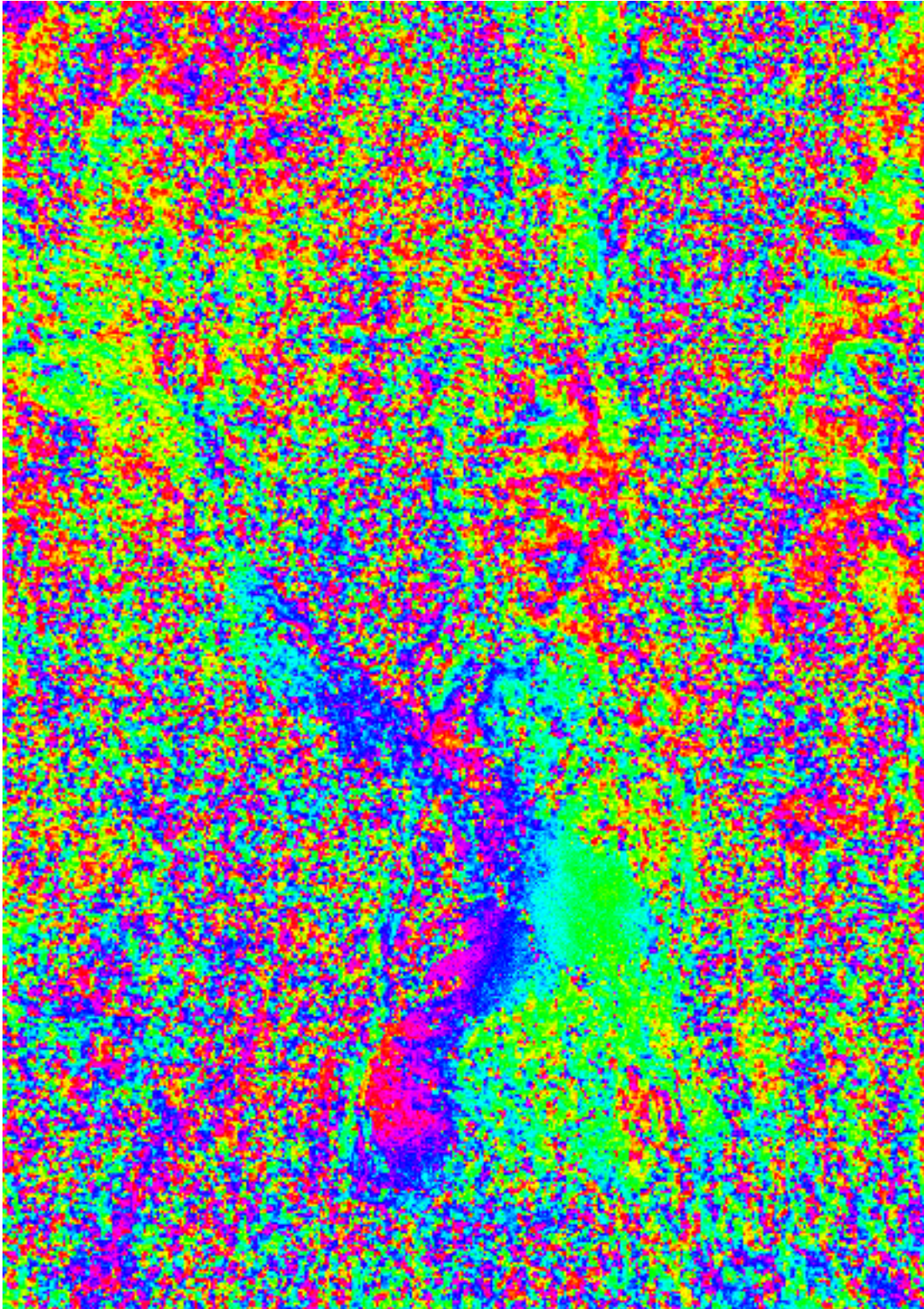


Figure 64. Larger area of Interferogram from Run 10 showing atmospheric effect. See Appendix B text for details.

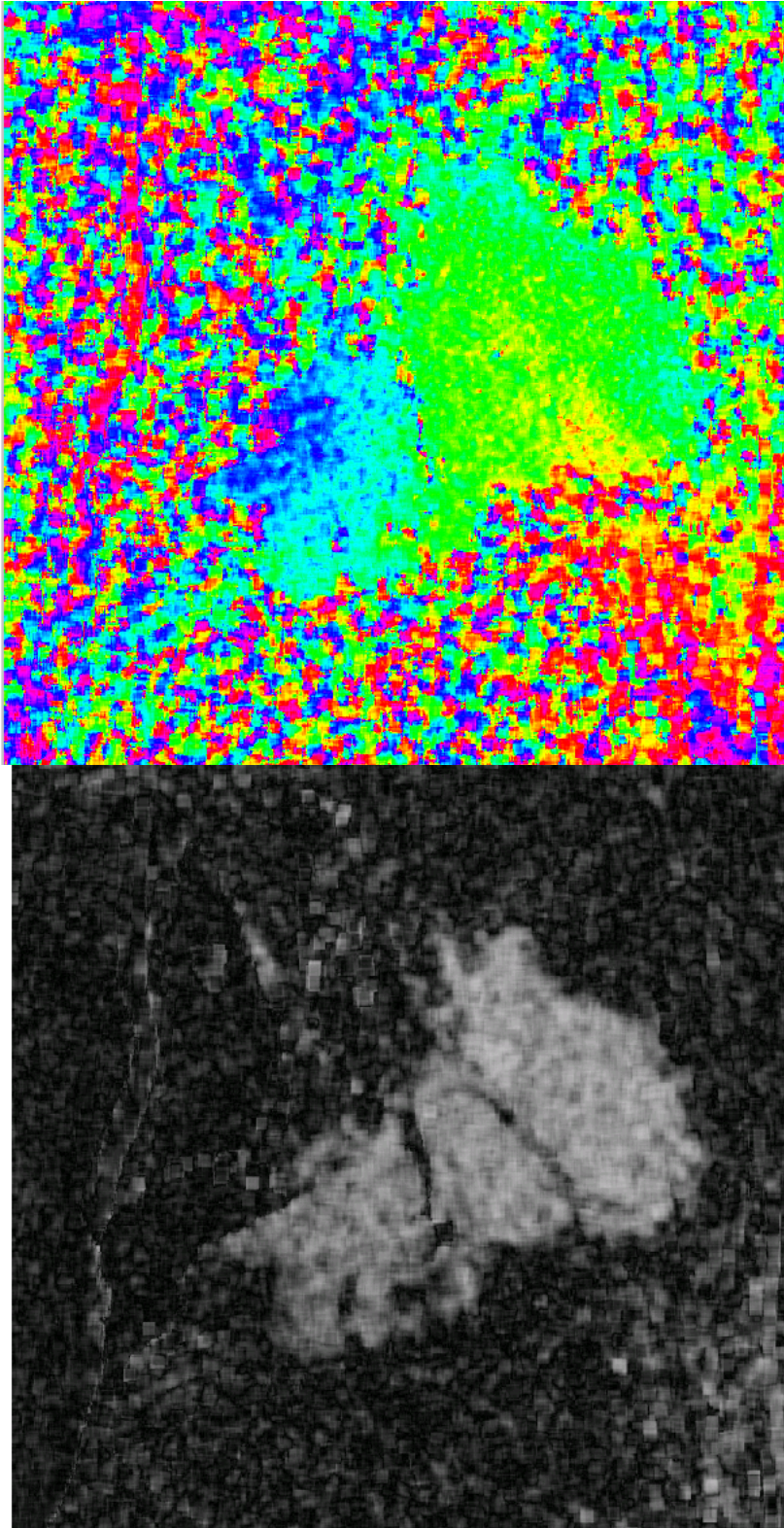


Figure 65. Interferogram (upper) and coherence (lower) images from Run 11. See Appendix B text for details.

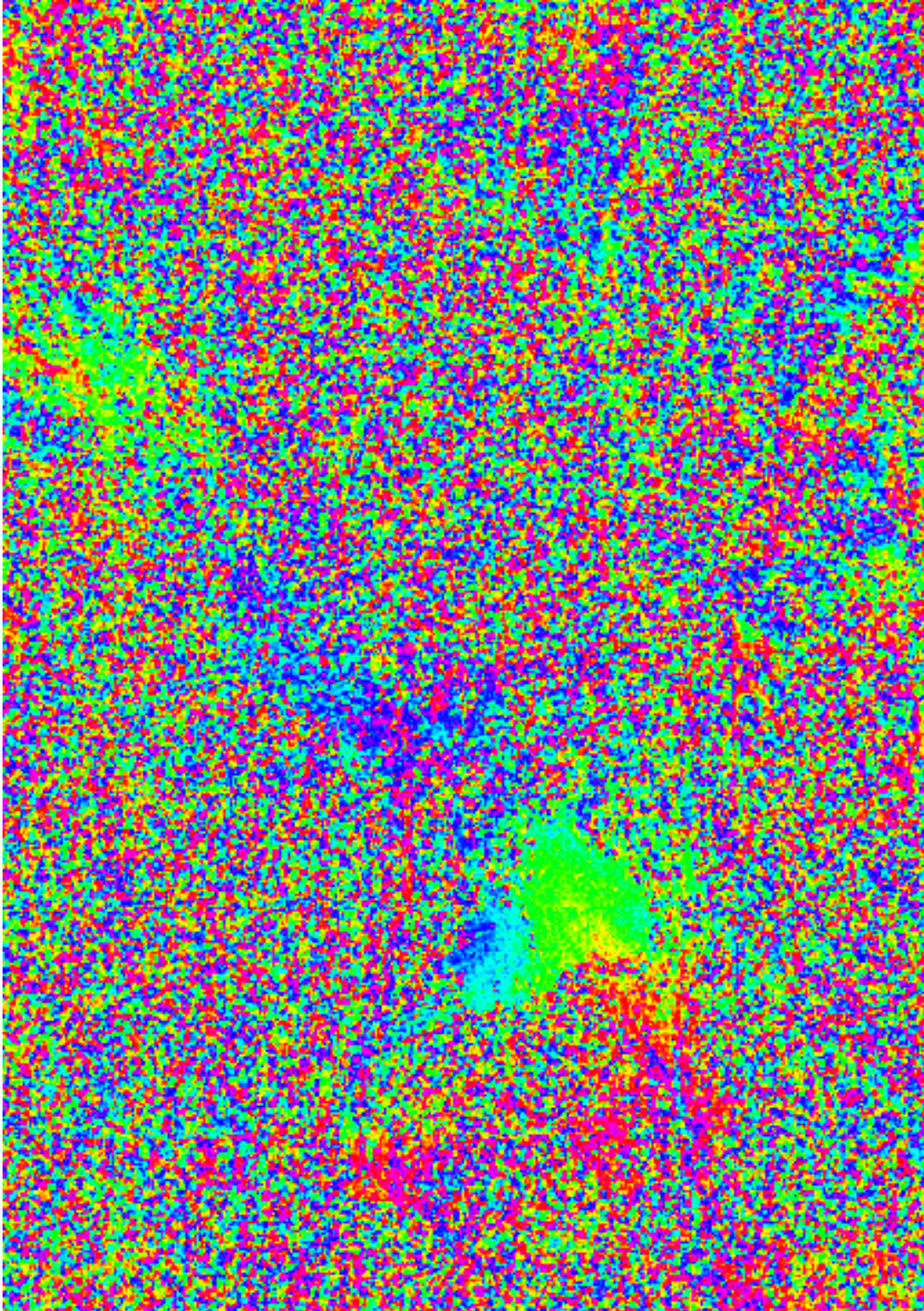


Figure 66. Larger area of Interferogram from Run 11. See Appendix B text for details.

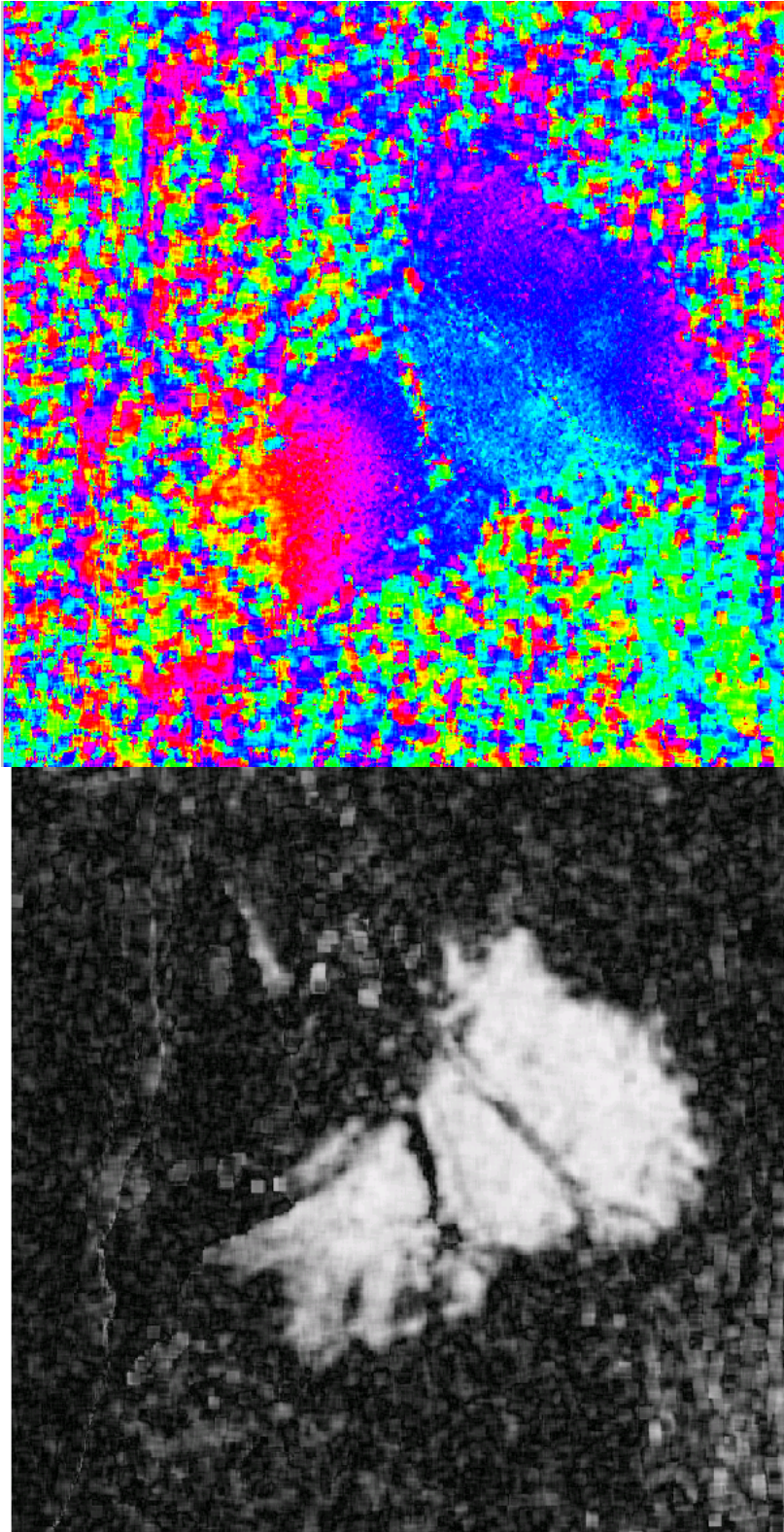


Figure 67. Interferogram (upper) and coherence (lower) images from Run 12. See Appendix B text for details.

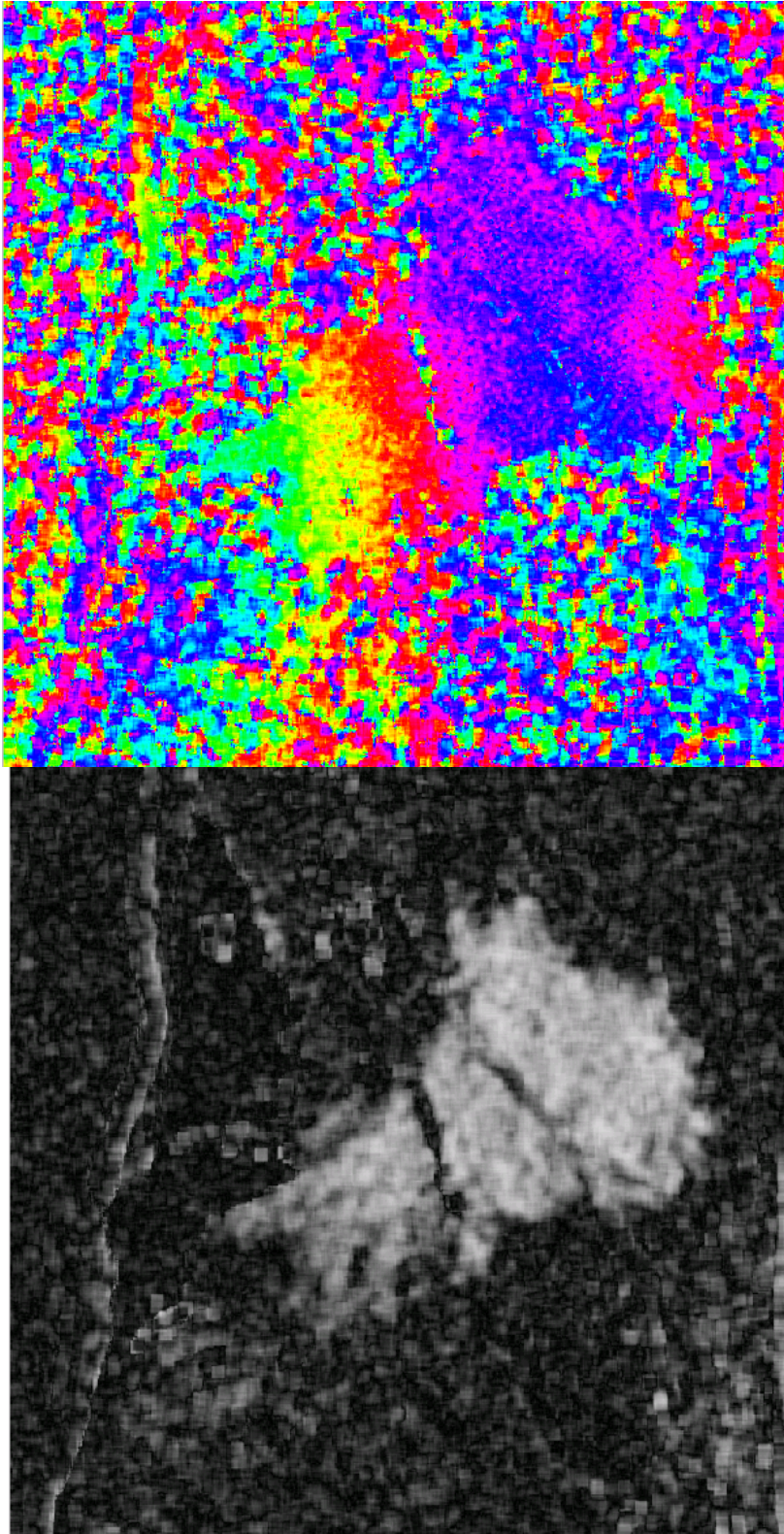


Figure 68. Interferogram (upper) and coherence (lower) images from Run 13. See Appendix B text for details.

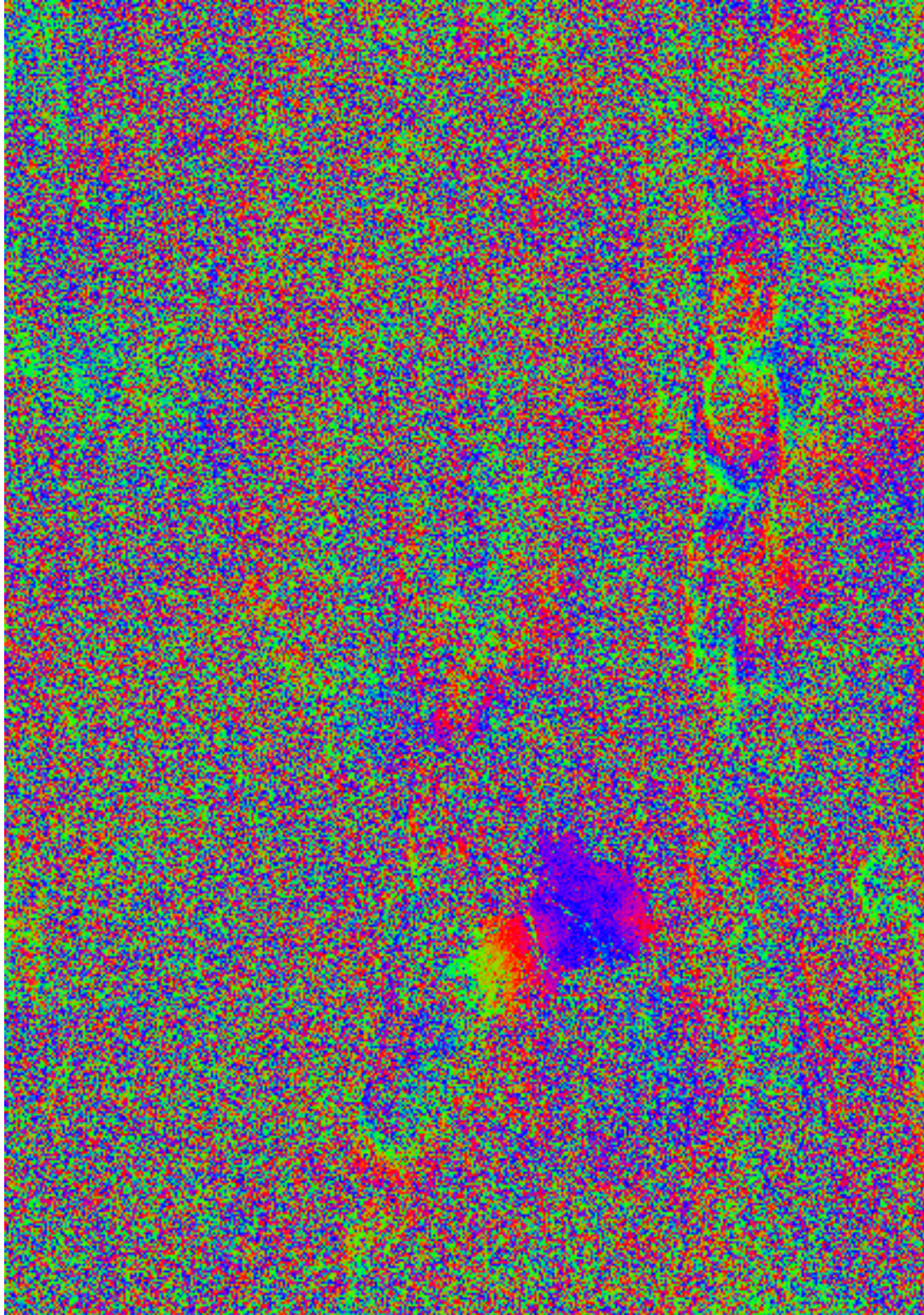


Figure 69. Larger area of Interferogram from Run 13. See Appendix B text for details.

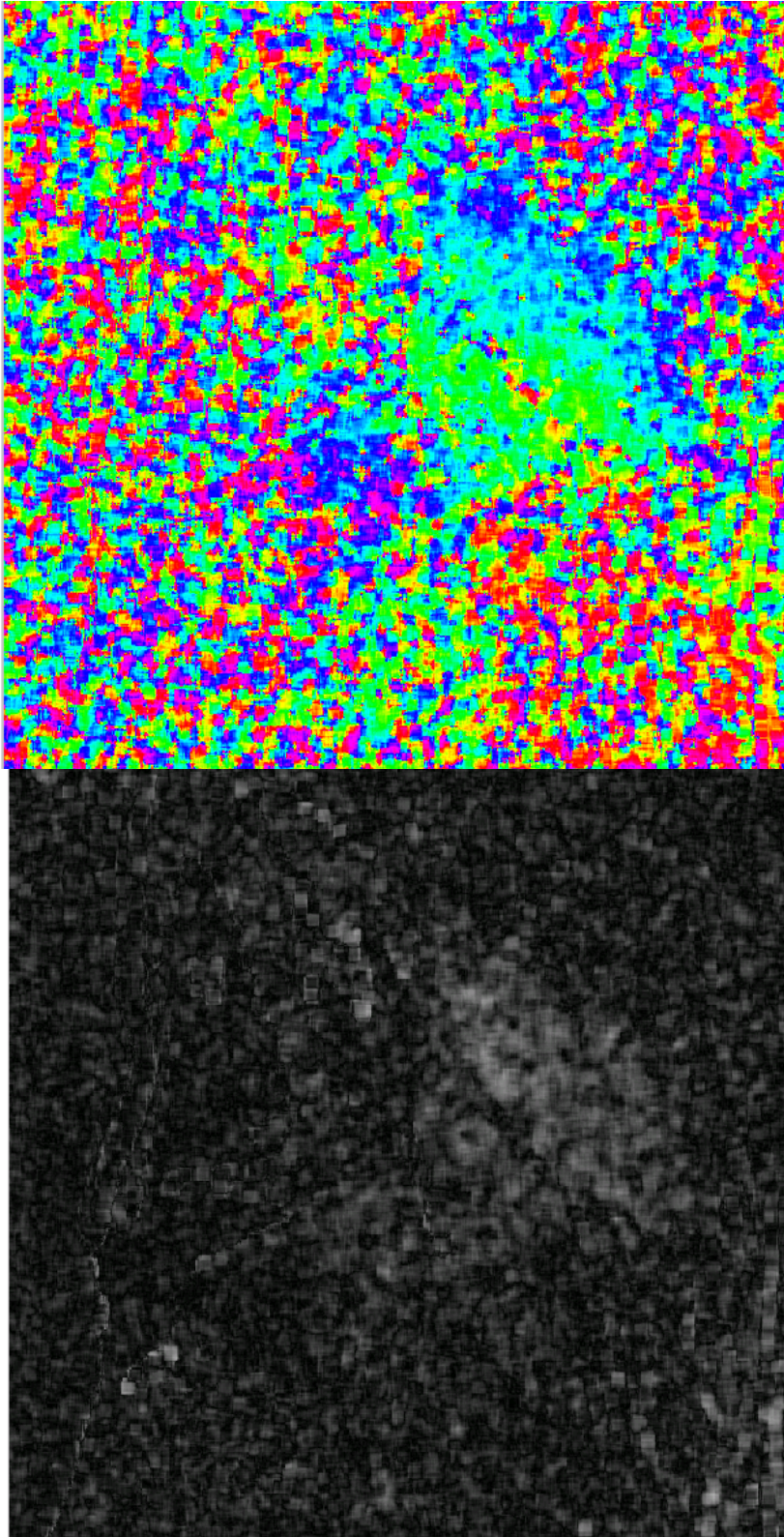


Figure 70. Interferogram (upper) and coherence (lower) images from Run 14. See Appendix B text for details.

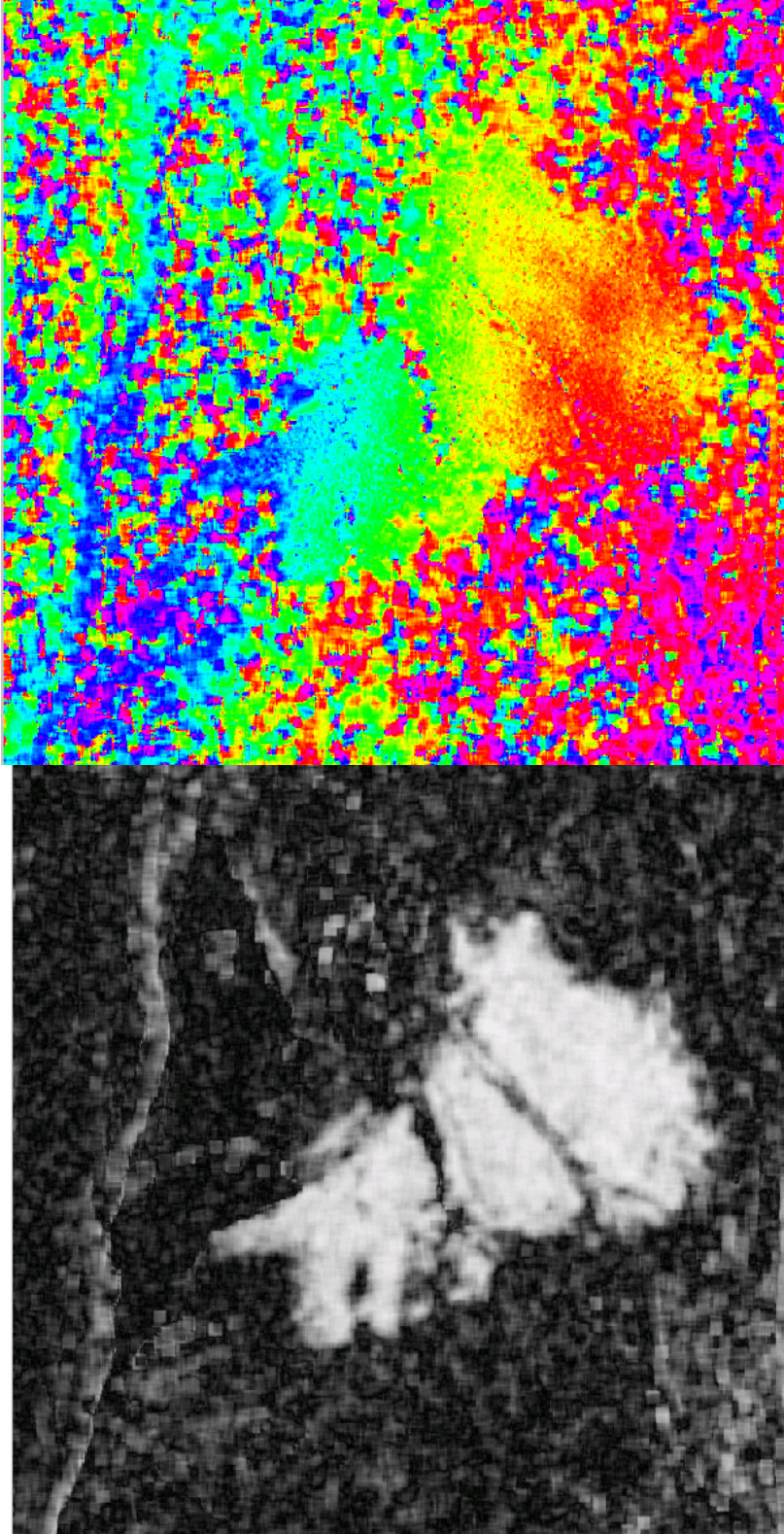


Figure 71. Interferogram (upper) and coherence (lower) images from Run 15. See Appendix B text for details.

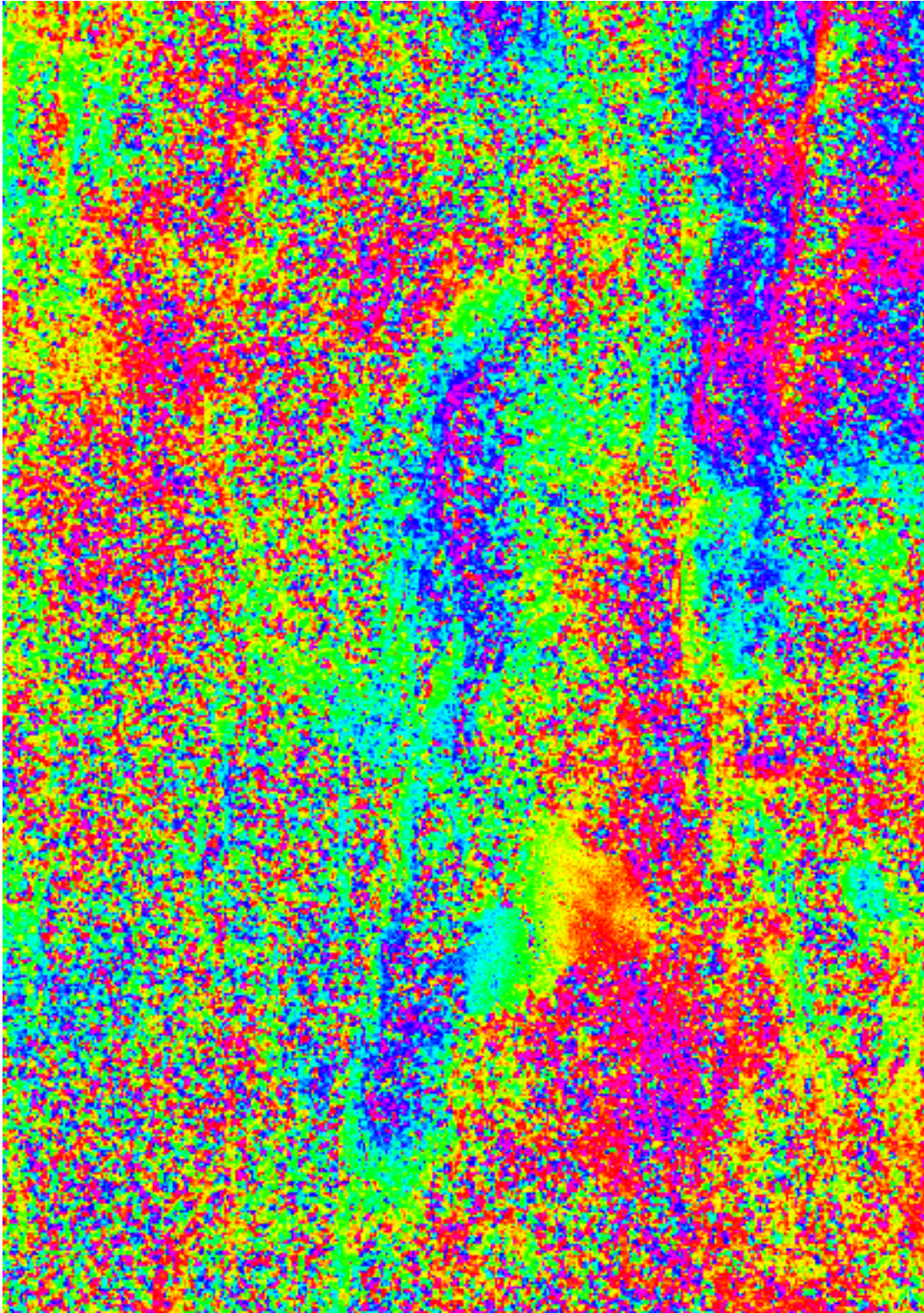


Figure 72. Larger area of interferogram from Run 15. See Appendix B text for details.

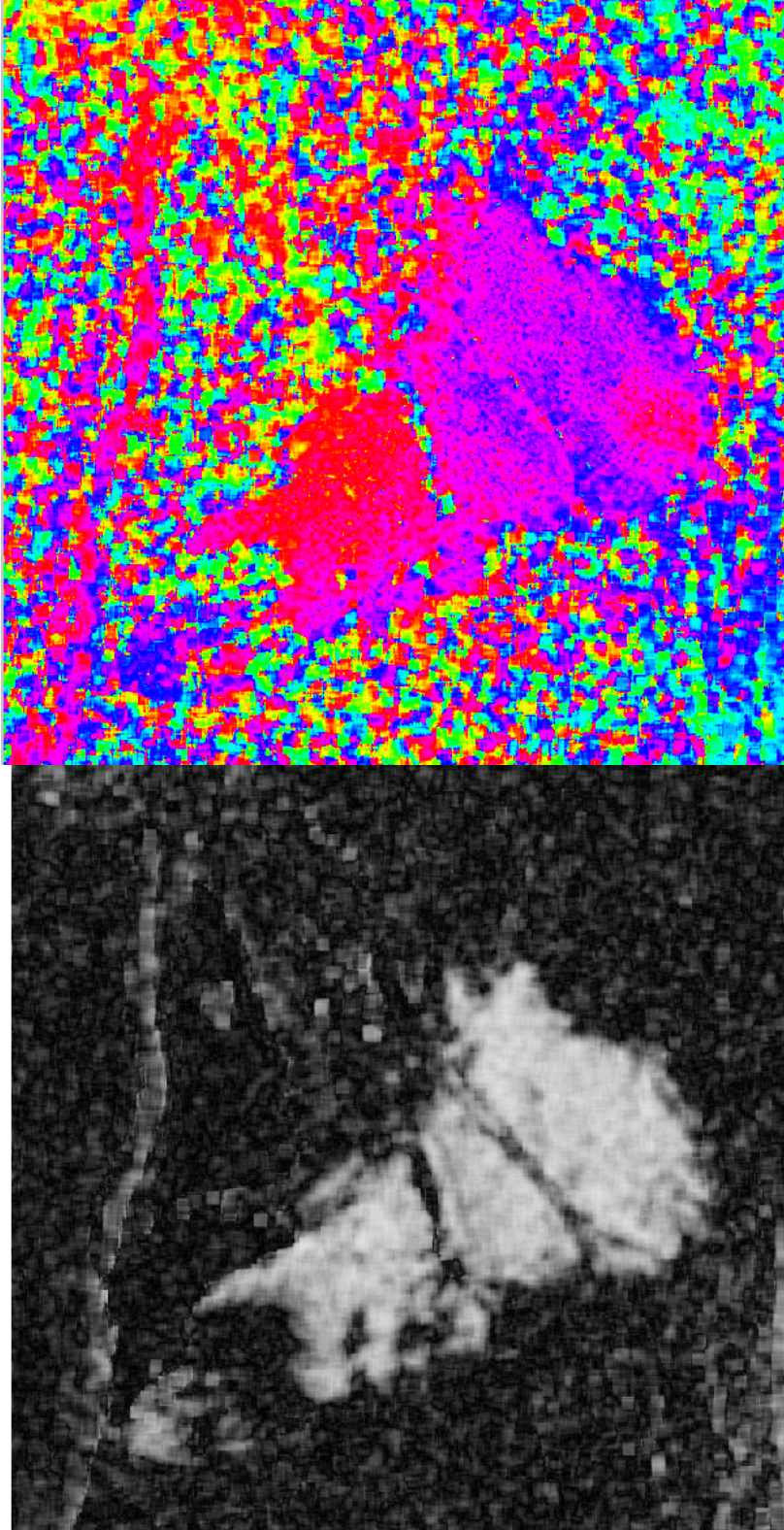


Figure 73. Interferogram (upper) and coherence (lower) images from Run 16. See Appendix B text for details.

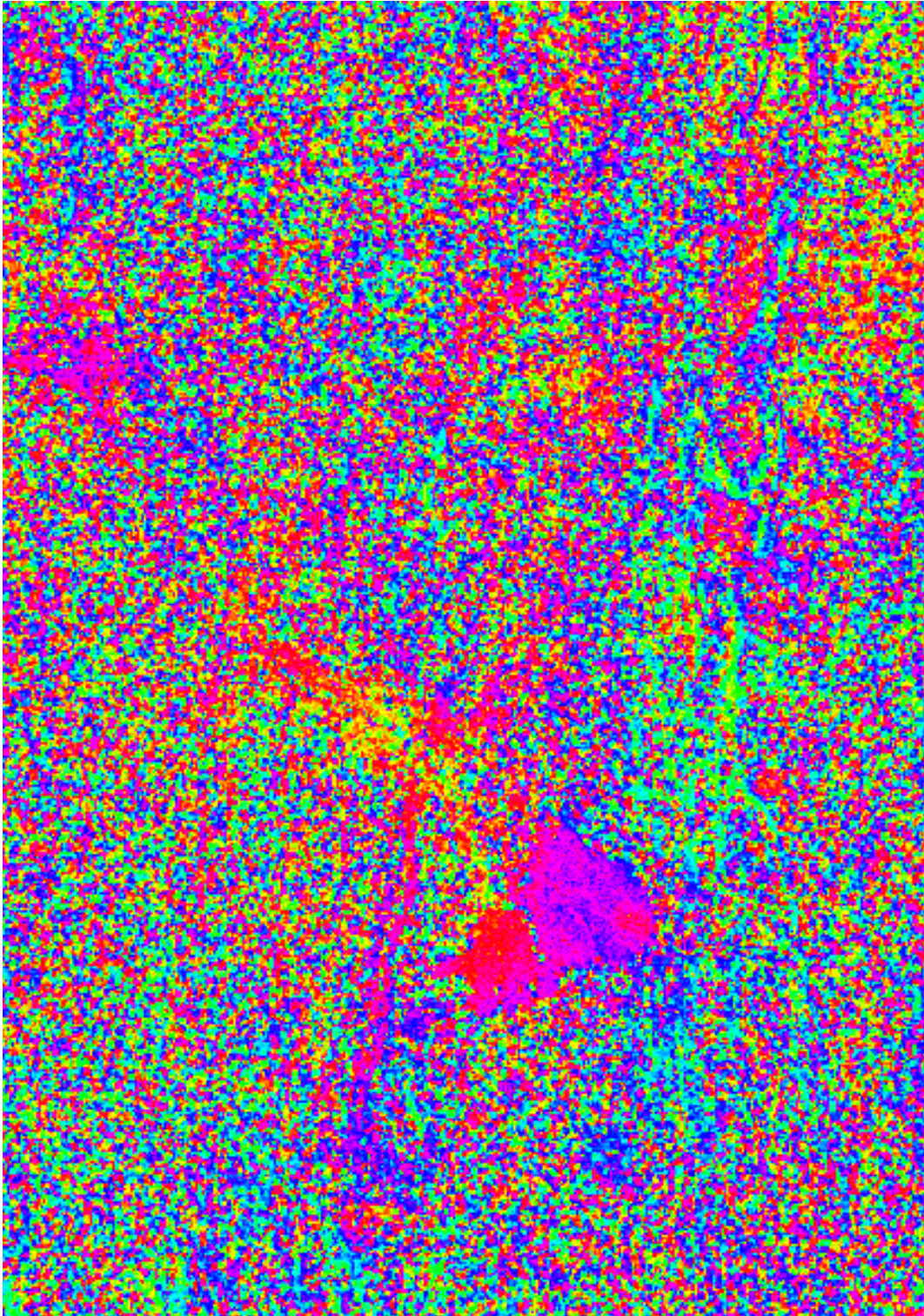


Figure 74. Larger area of Interferogram from Run 16. See Appendix B text for details.

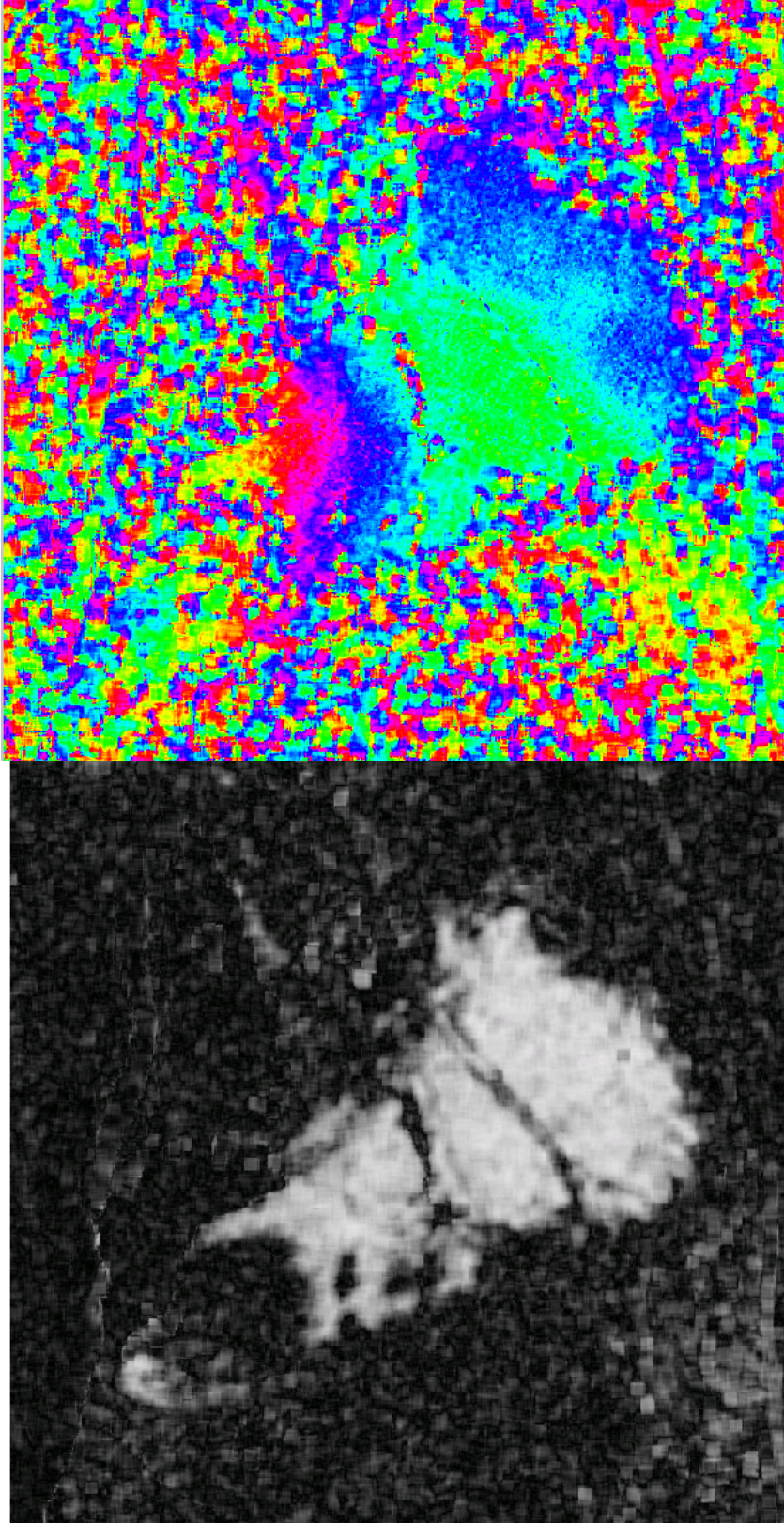


Figure 75. Interferogram (upper) and coherence (lower) images from Run 17. See Appendix B text for details.

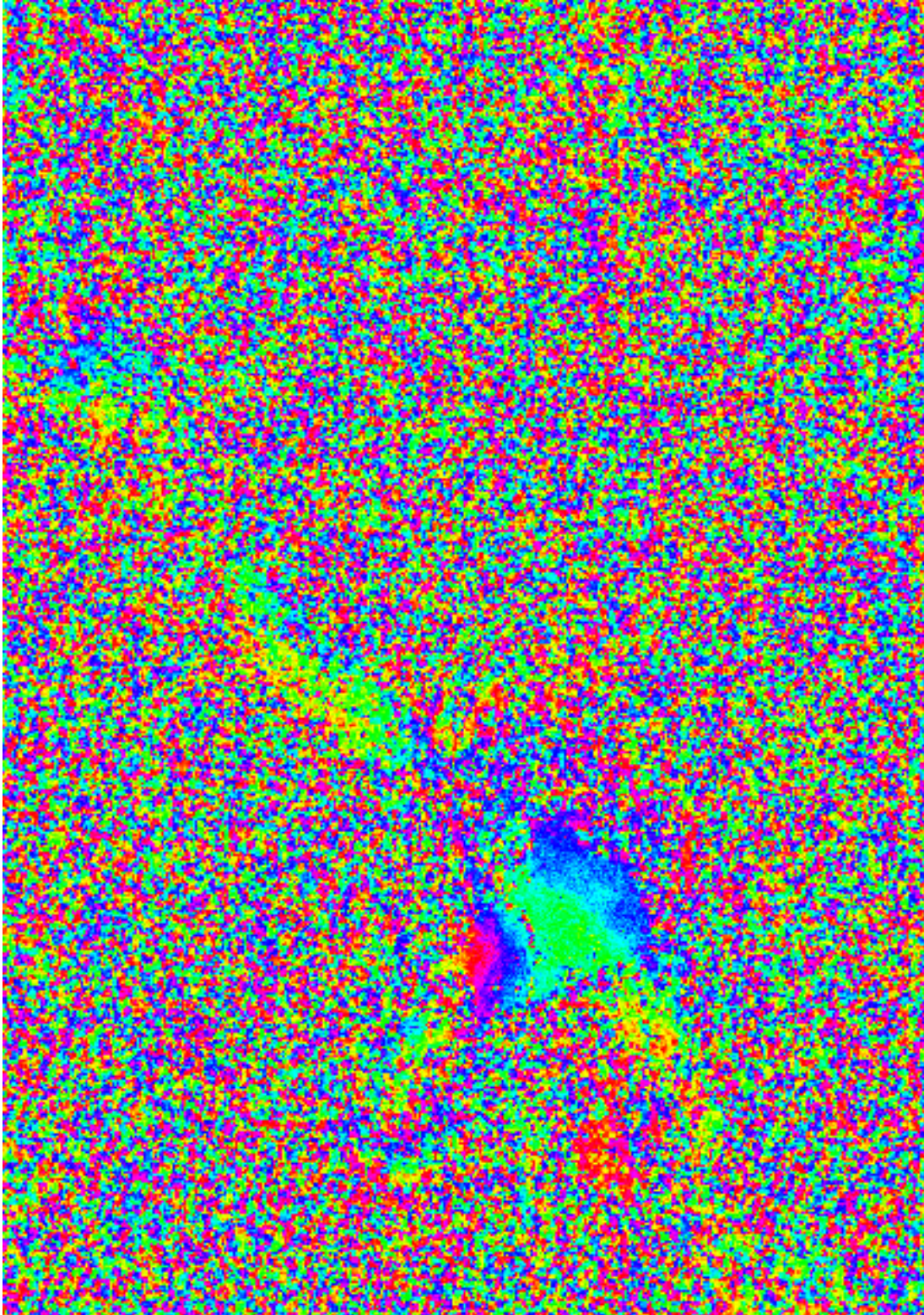


Figure 76. Larger area of Interferogram from Run 17. See Appendix B text for details.

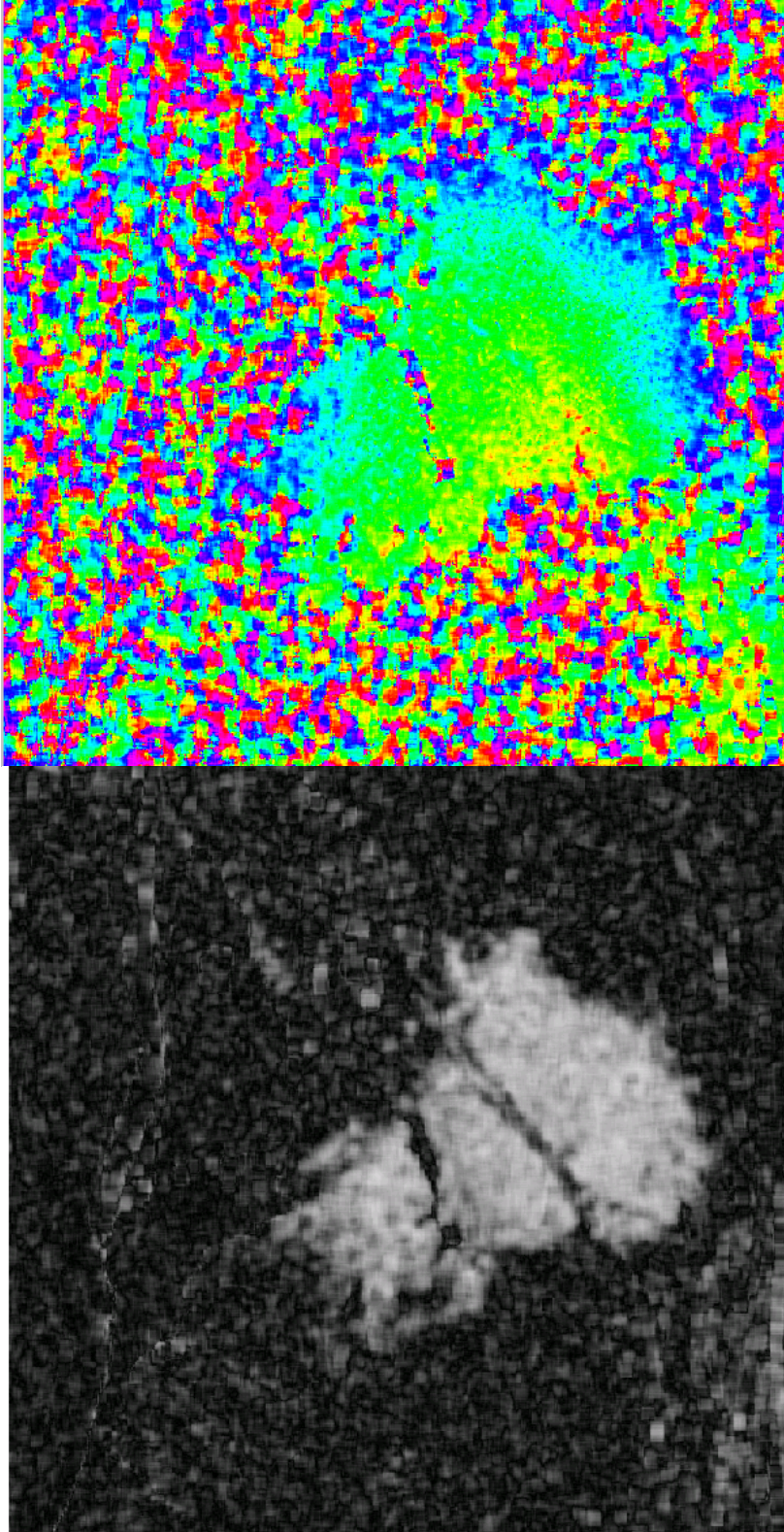


Figure 77. Interferogram (upper) and coherence (lower) images from Run 18. See Appendix B text for details.

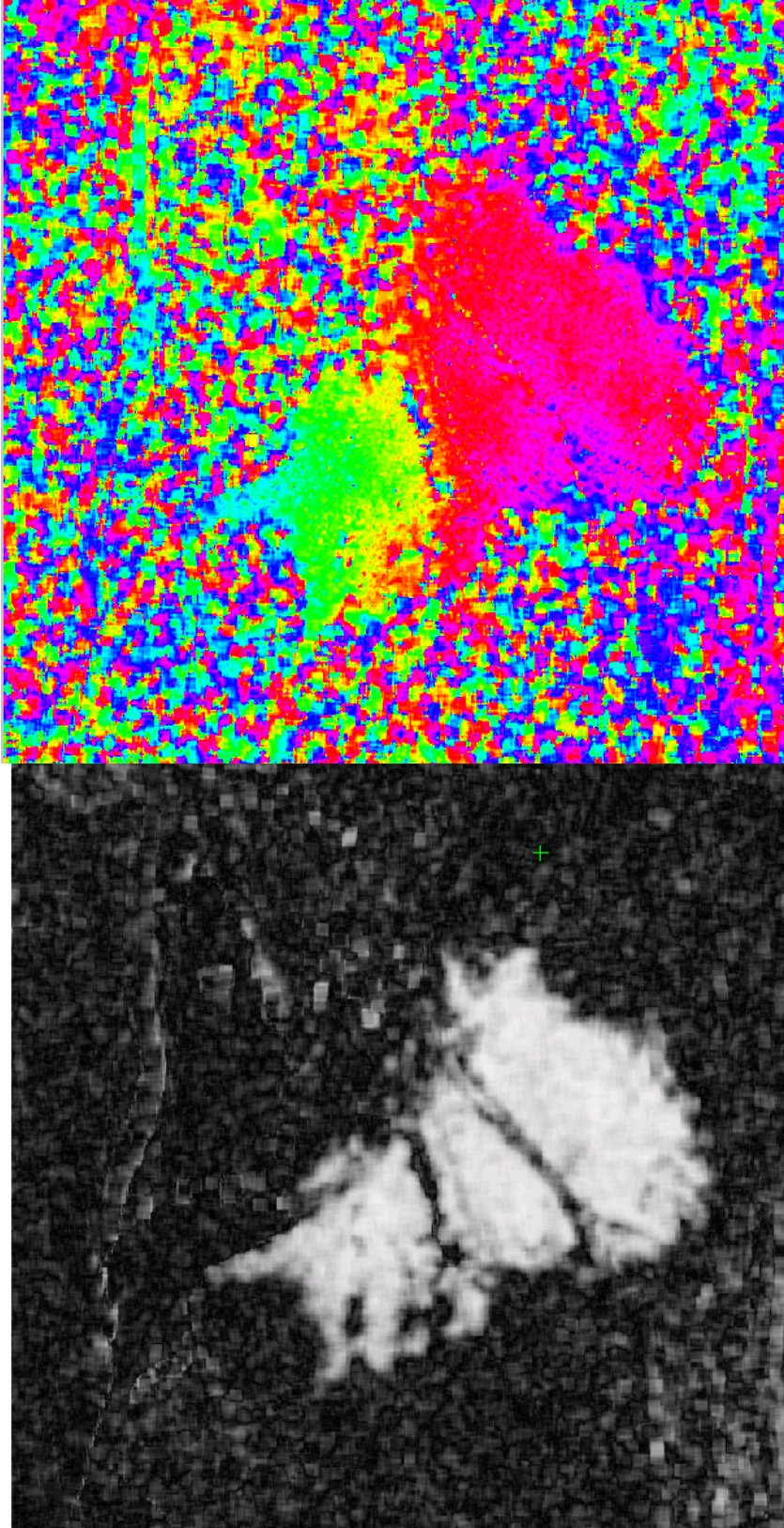


Figure 78. Interferogram (upper) and coherence (lower) images from Run 19. See Appendix B text for details.

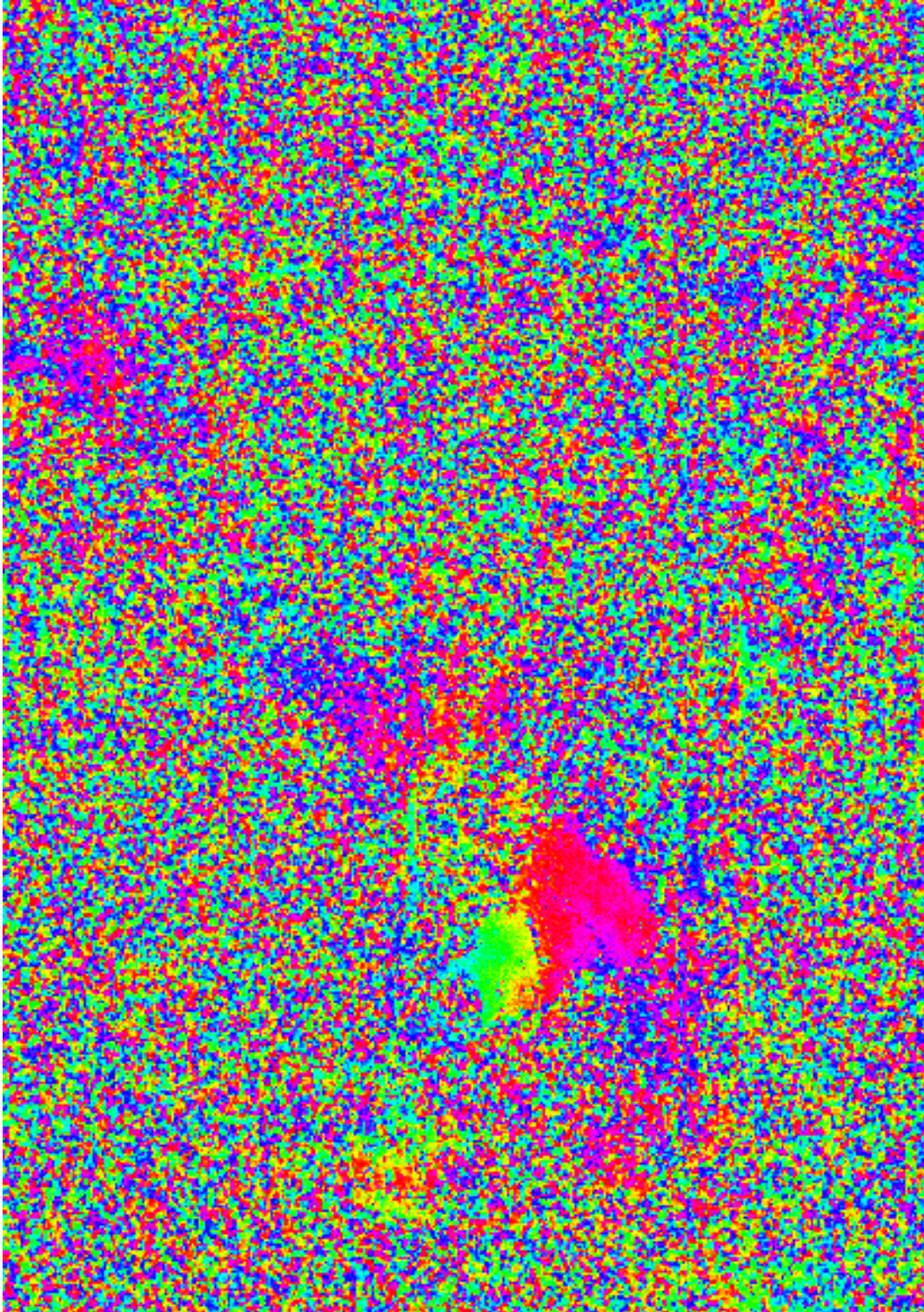


Figure 79. Larger area of Interferogram from Run 19. See Appendix B text for details.

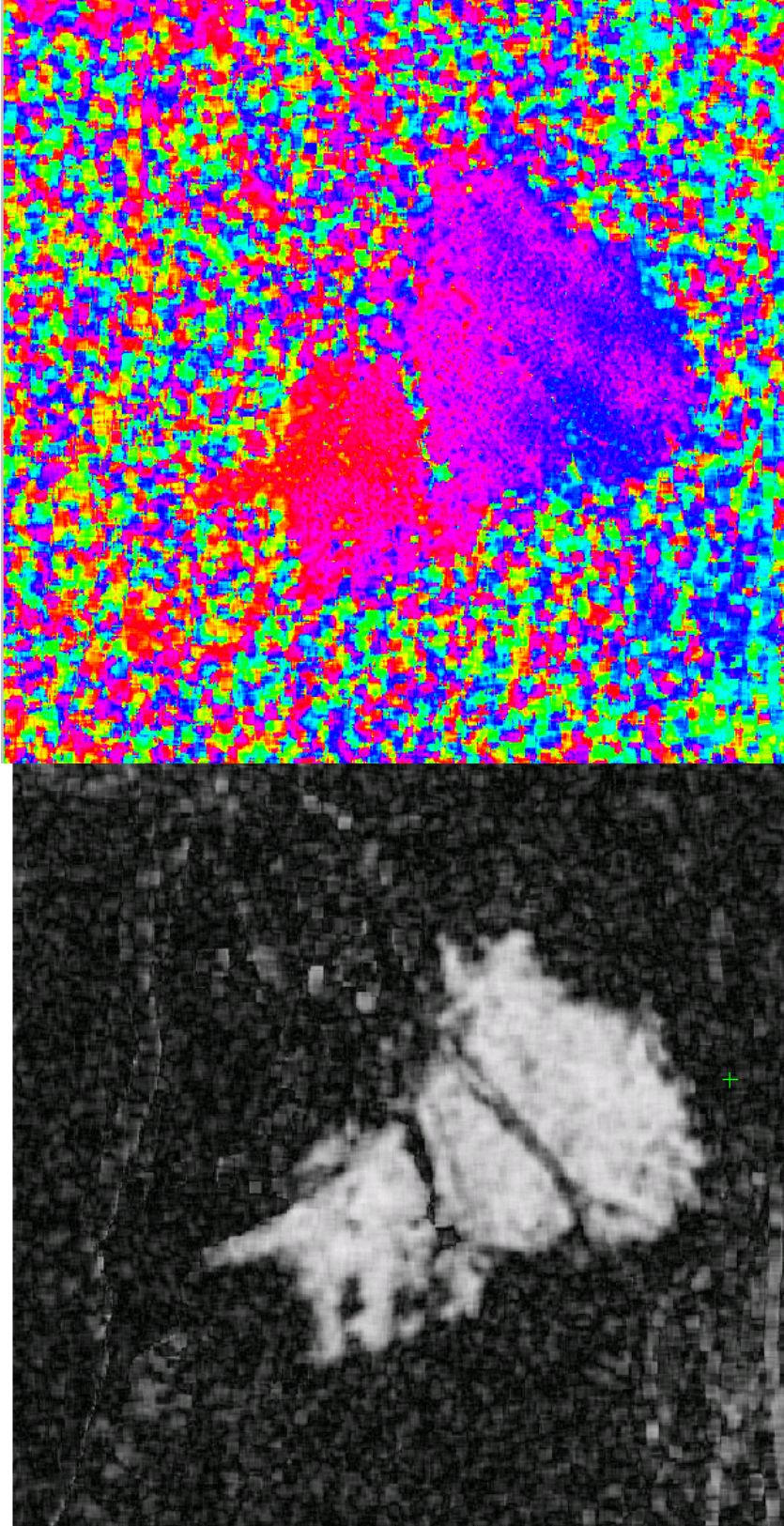


Figure 80. Interferogram (upper) and coherence (lower) images from Run 20. See Appendix B text for details.

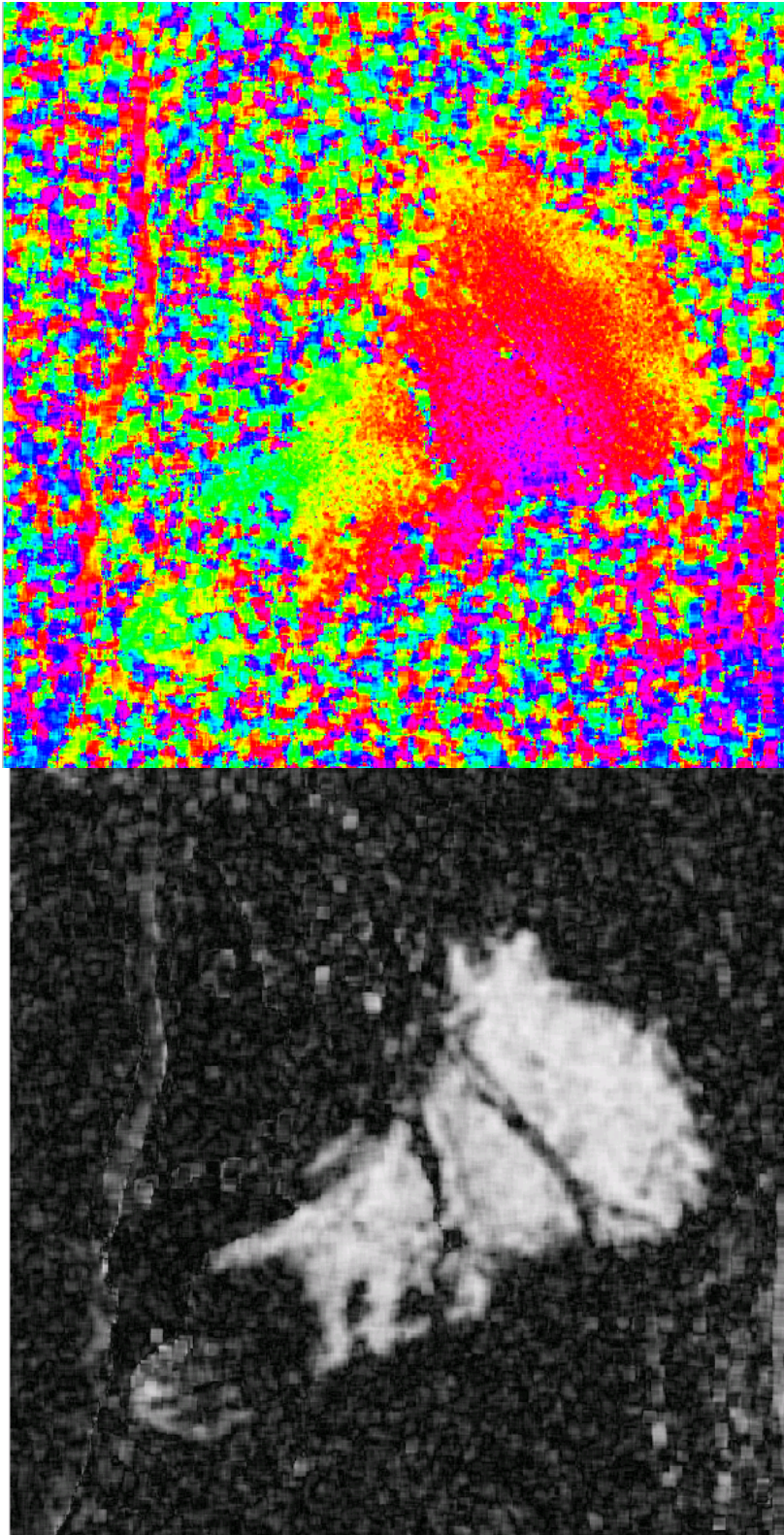


Figure 81. Interferogram (upper) and coherence (lower) images from Run 21. See Appendix B text for details.

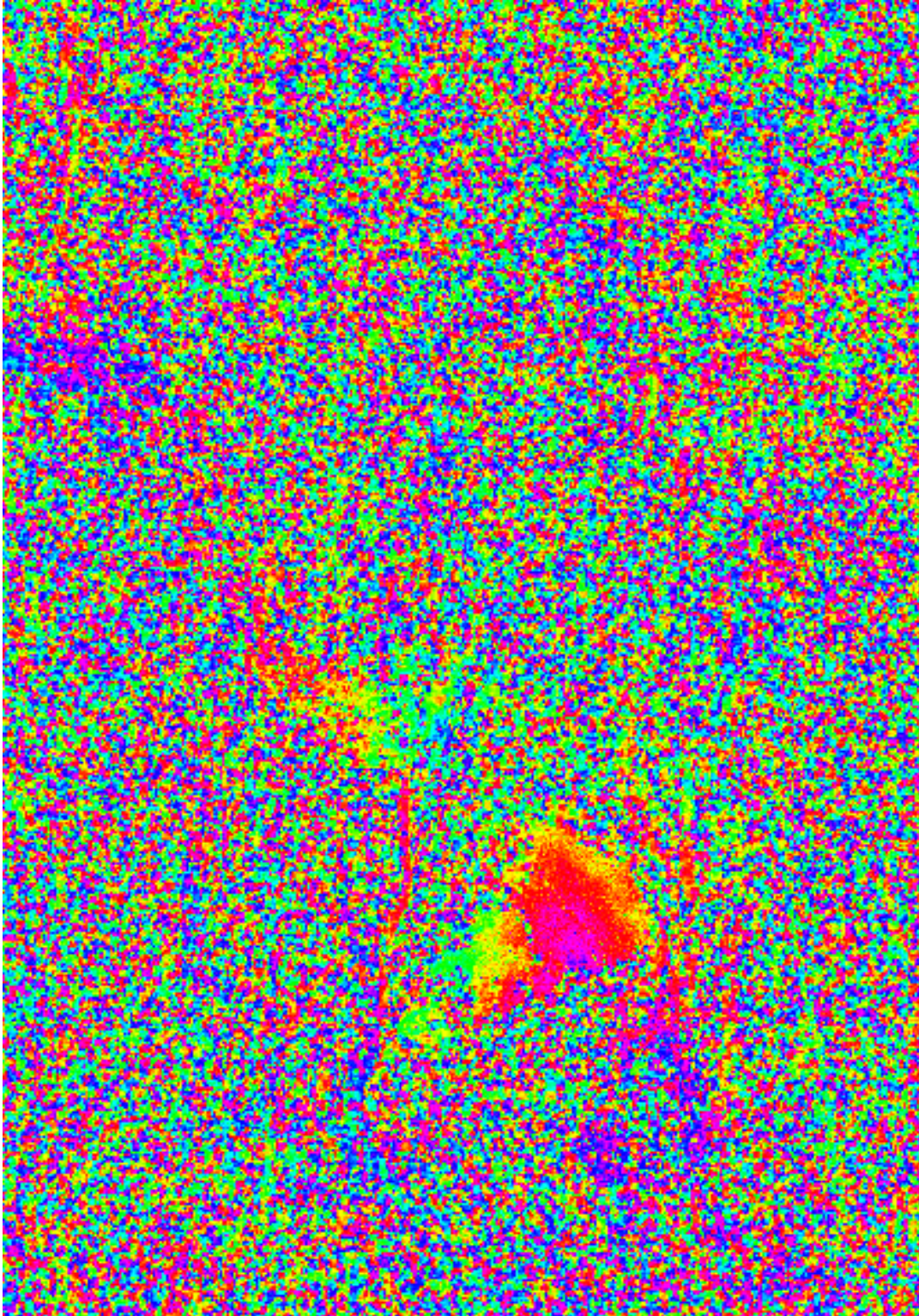


Figure 82. Larger area of Interferogram from Run 21. See Appendix B text for details.

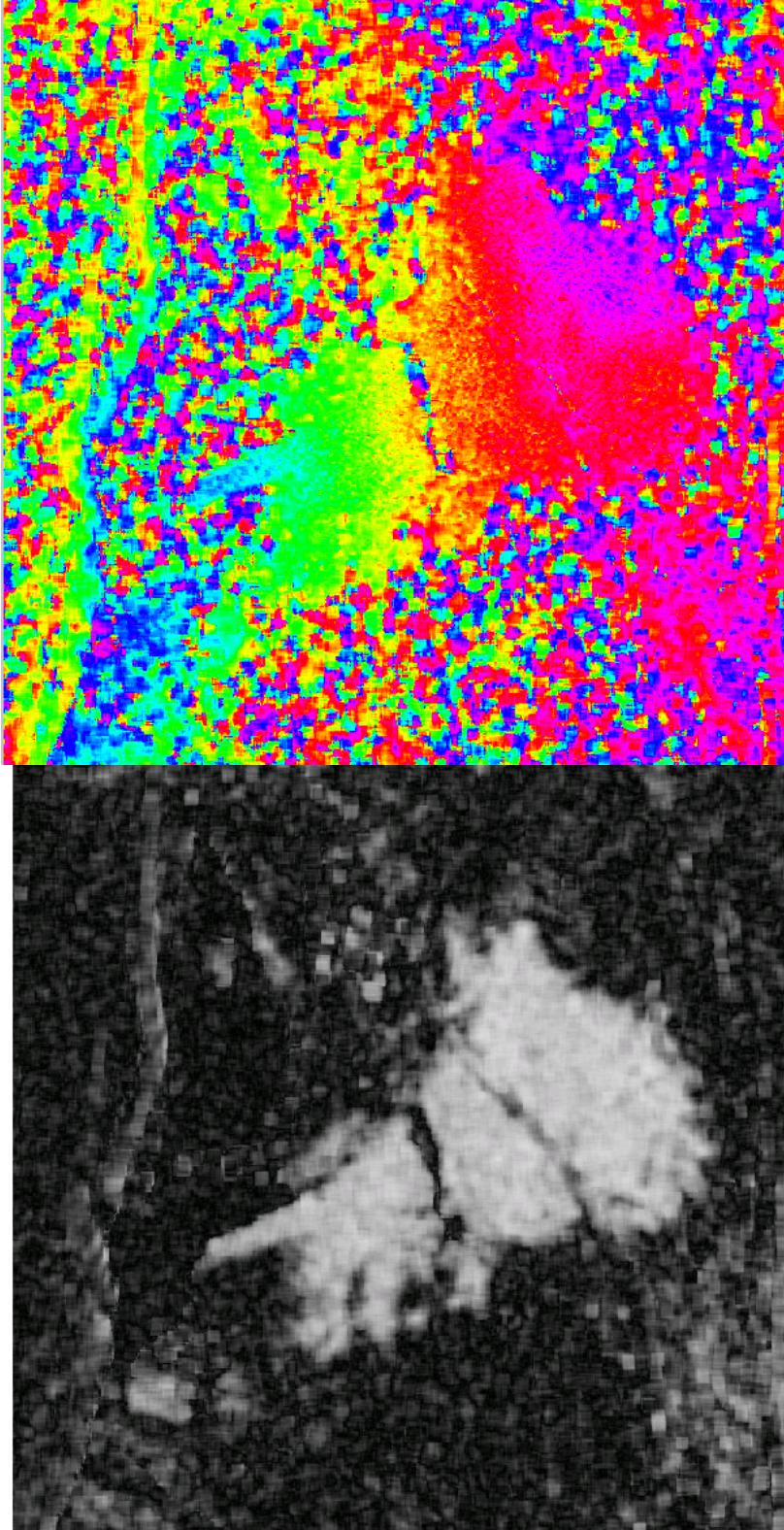


Figure 83. Interferogram (upper) and coherence (lower) images from Run 22. See Appendix B text for details.

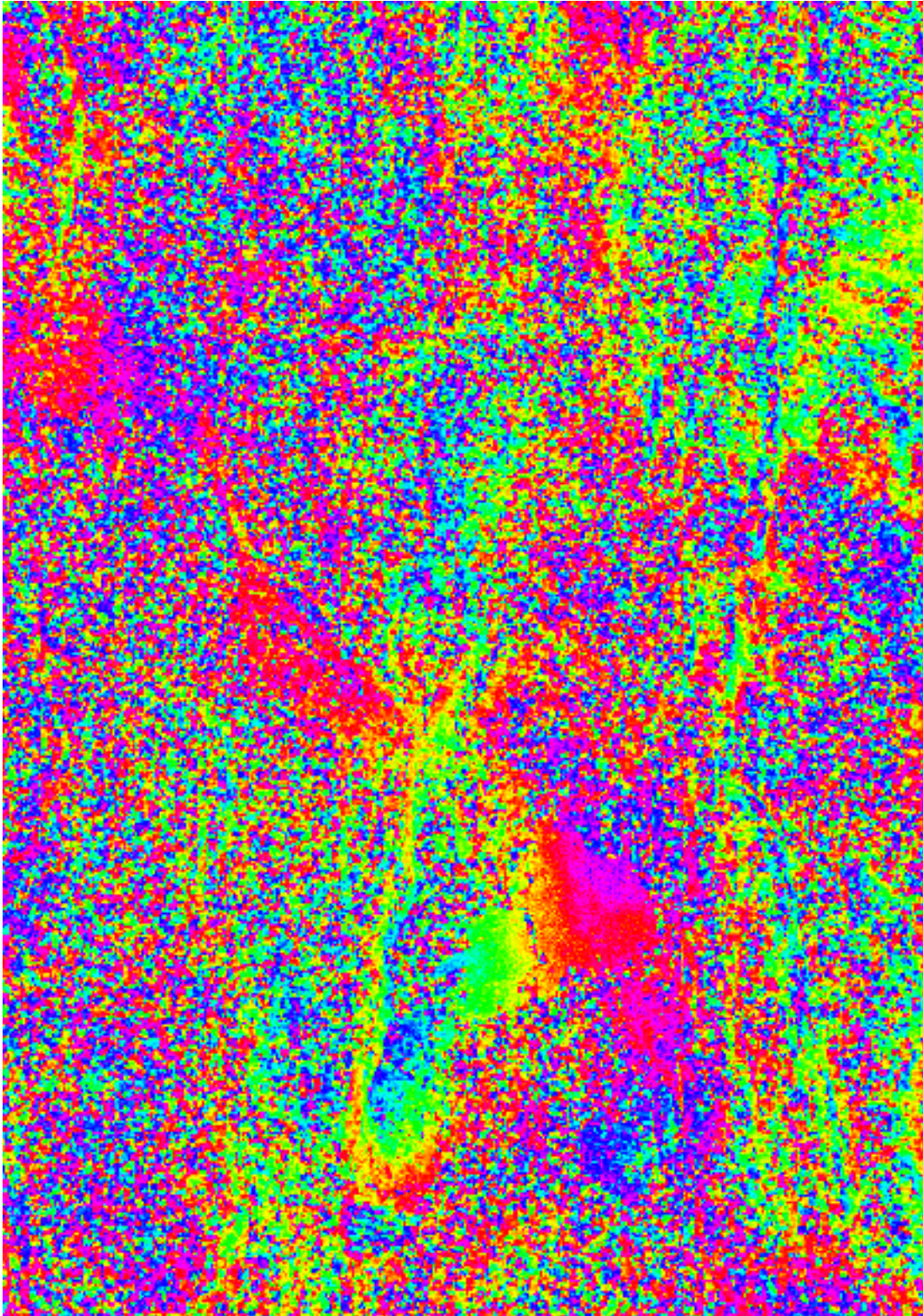


Figure 84. Larger area of interferogram from Run 22 showing atmospheric effect. See Appendix B text for details.

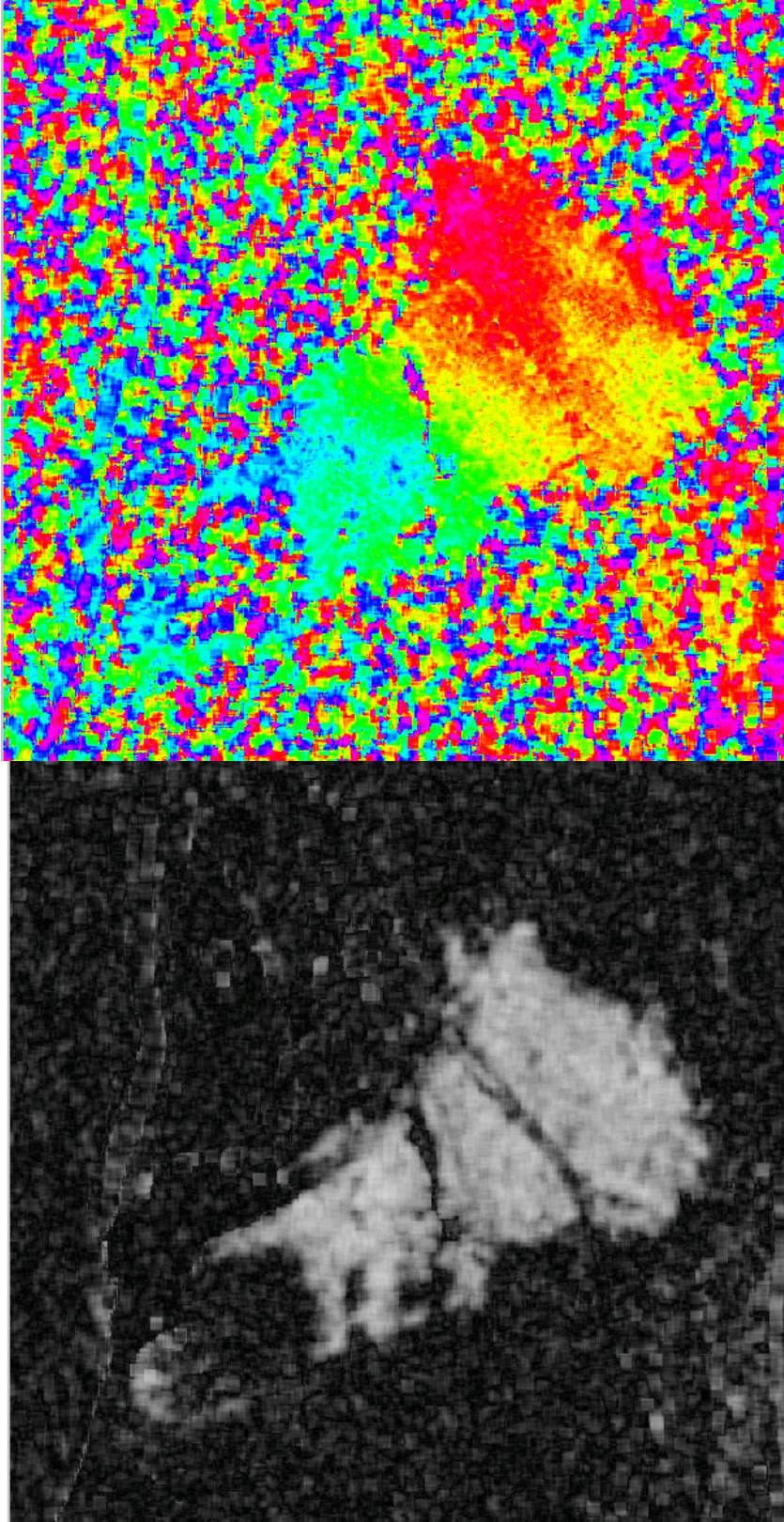


Figure 85. Interferogram (upper) and coherence (lower) images from Run 23. See Appendix B text for details.

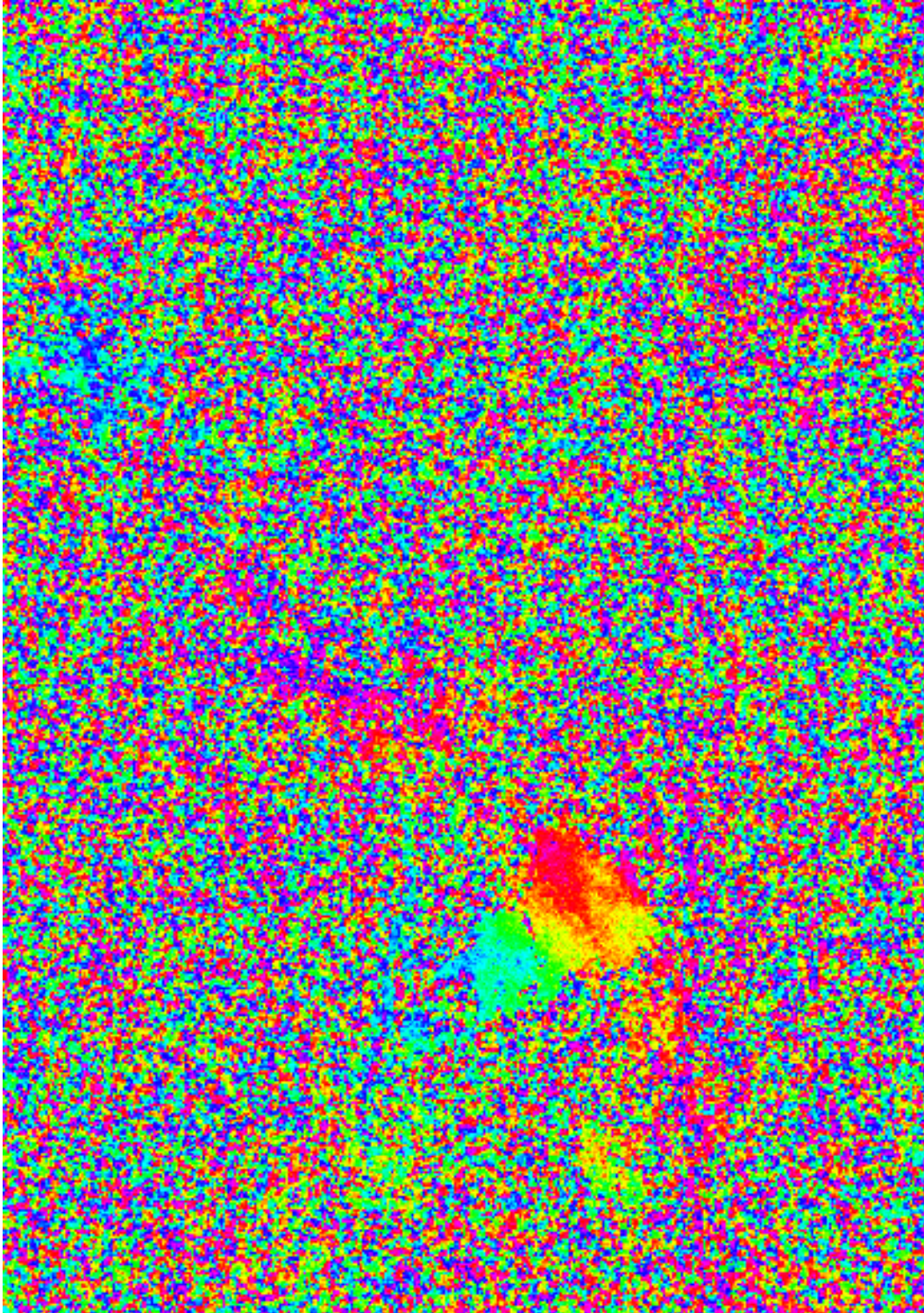


Figure 86. Larger area of interferogram from Run 23. See Appendix B text for details.

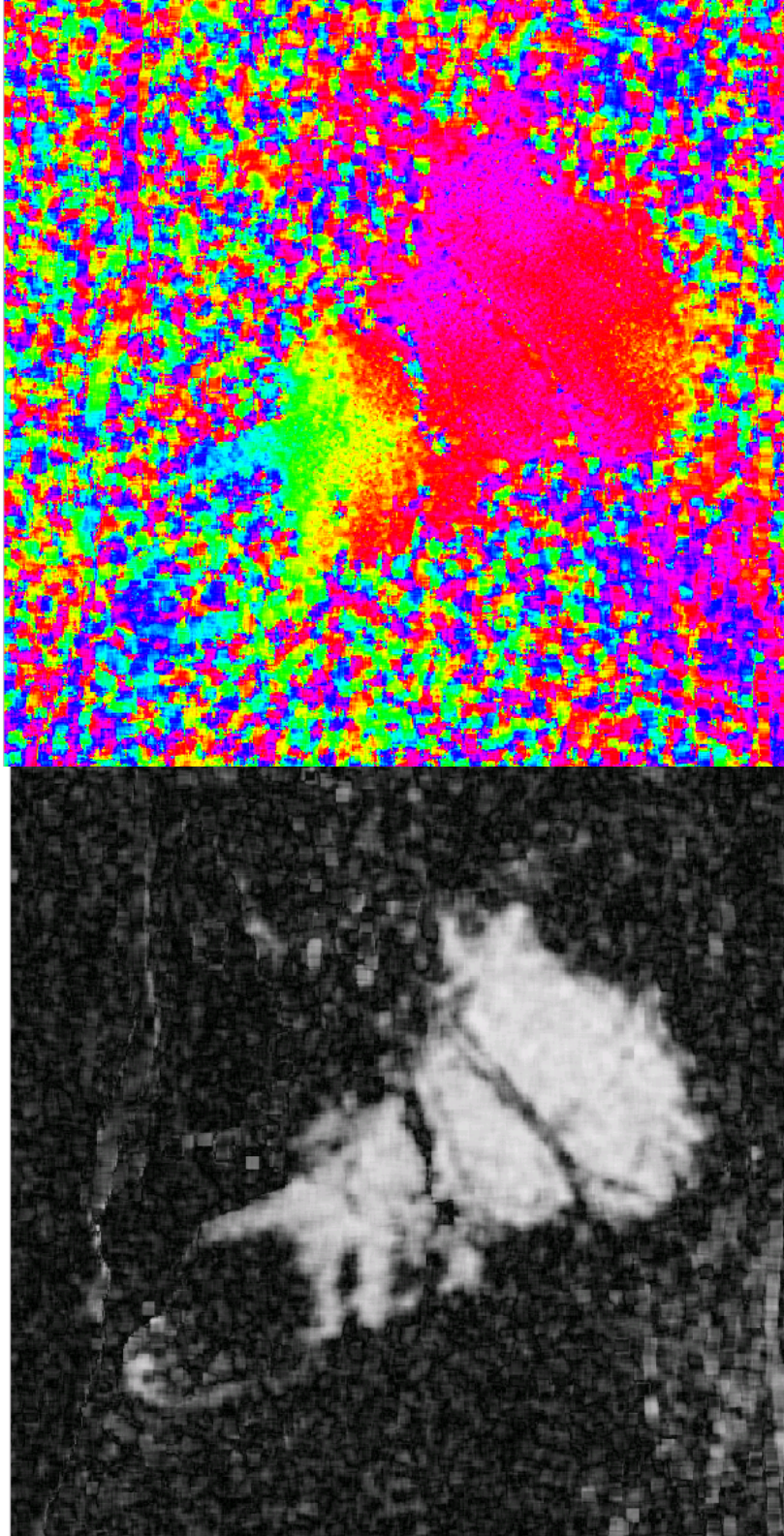


Figure 87. Interferogram (upper) and coherence (lower) images from Run 24. See Appendix B text for details.

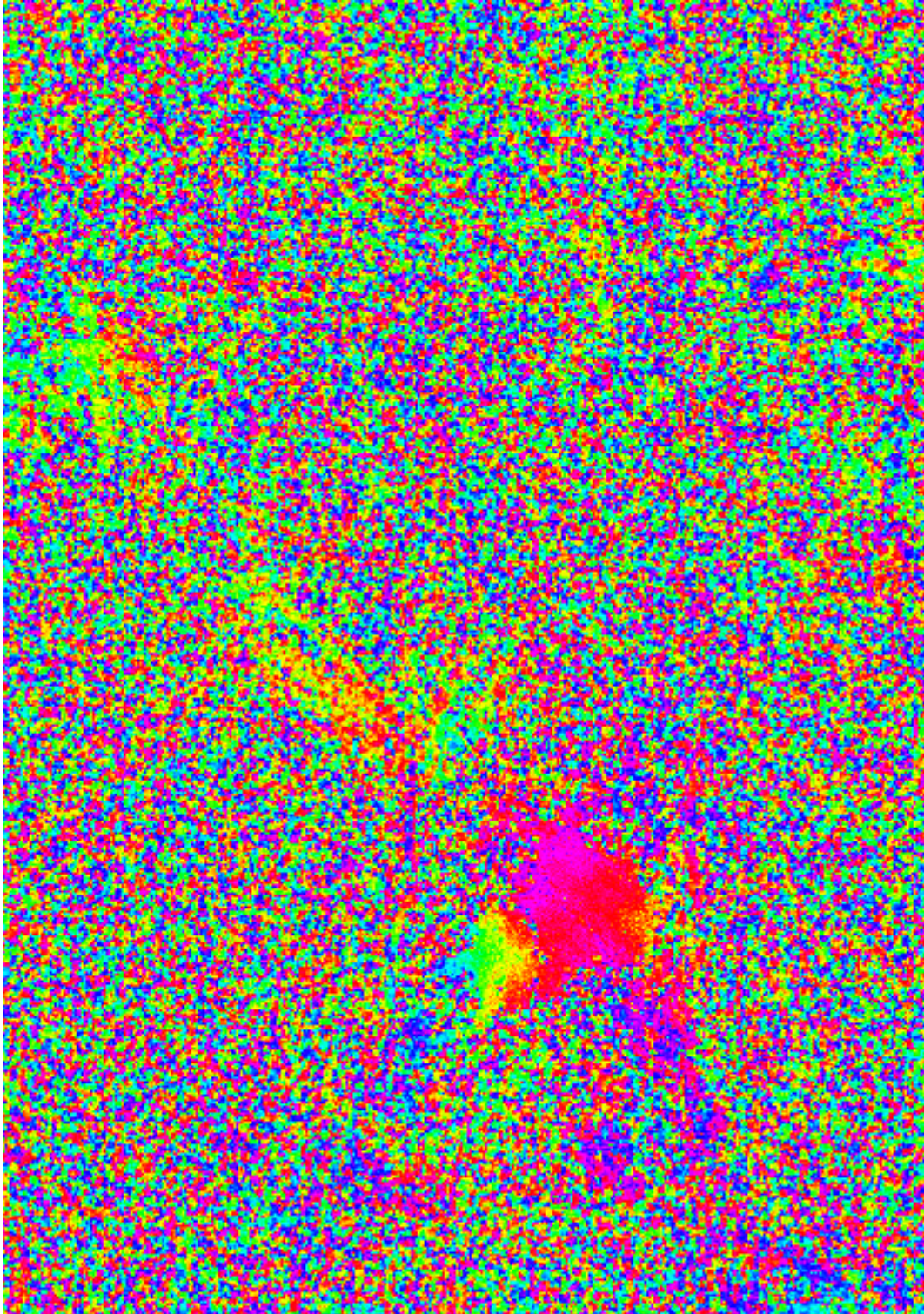


Figure 88. Larger area of interferogram from Run 24. See Appendix B text for details.

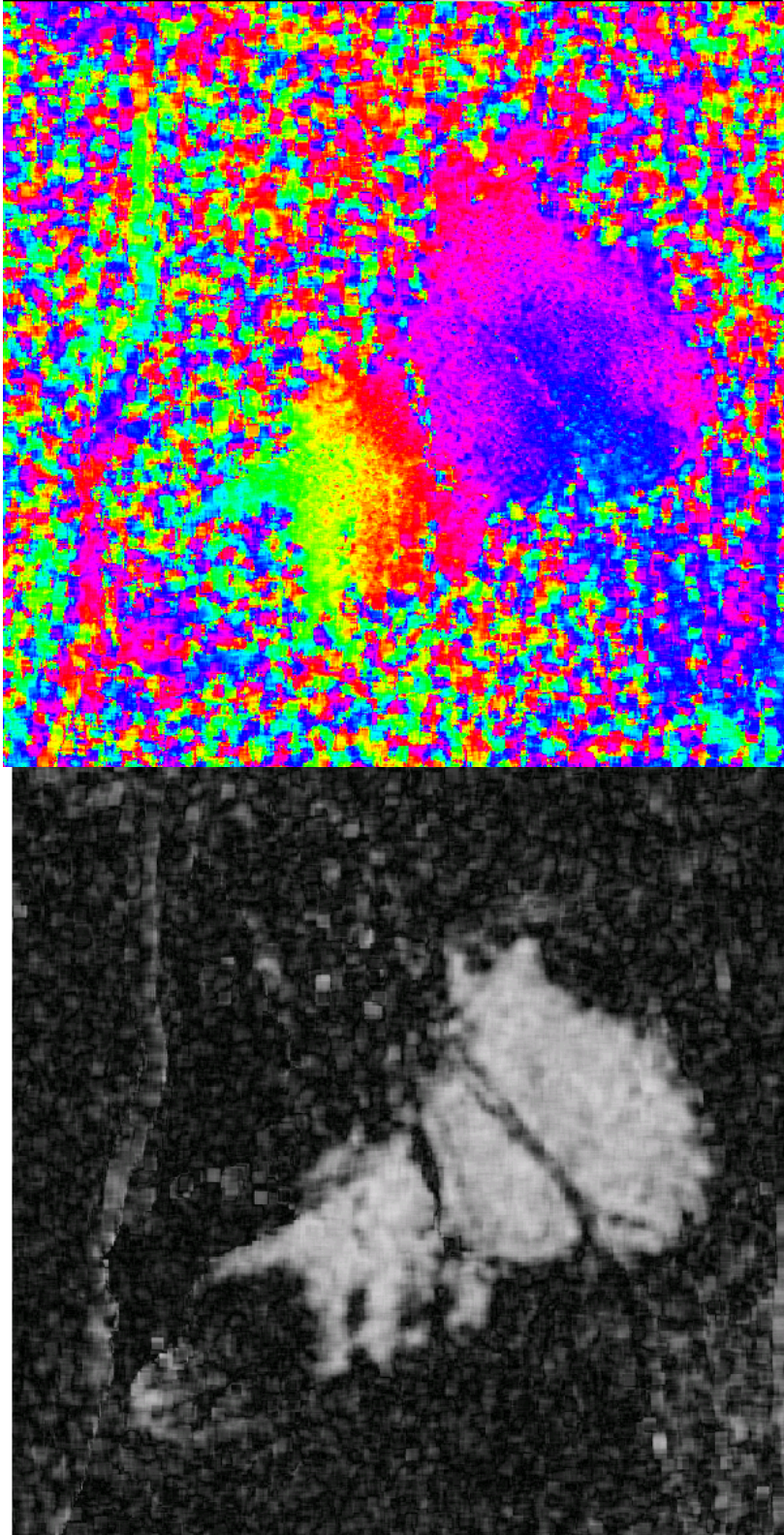


Figure 89. Interferogram (upper) and coherence (lower) images from Run 25. See Appendix B text for details.

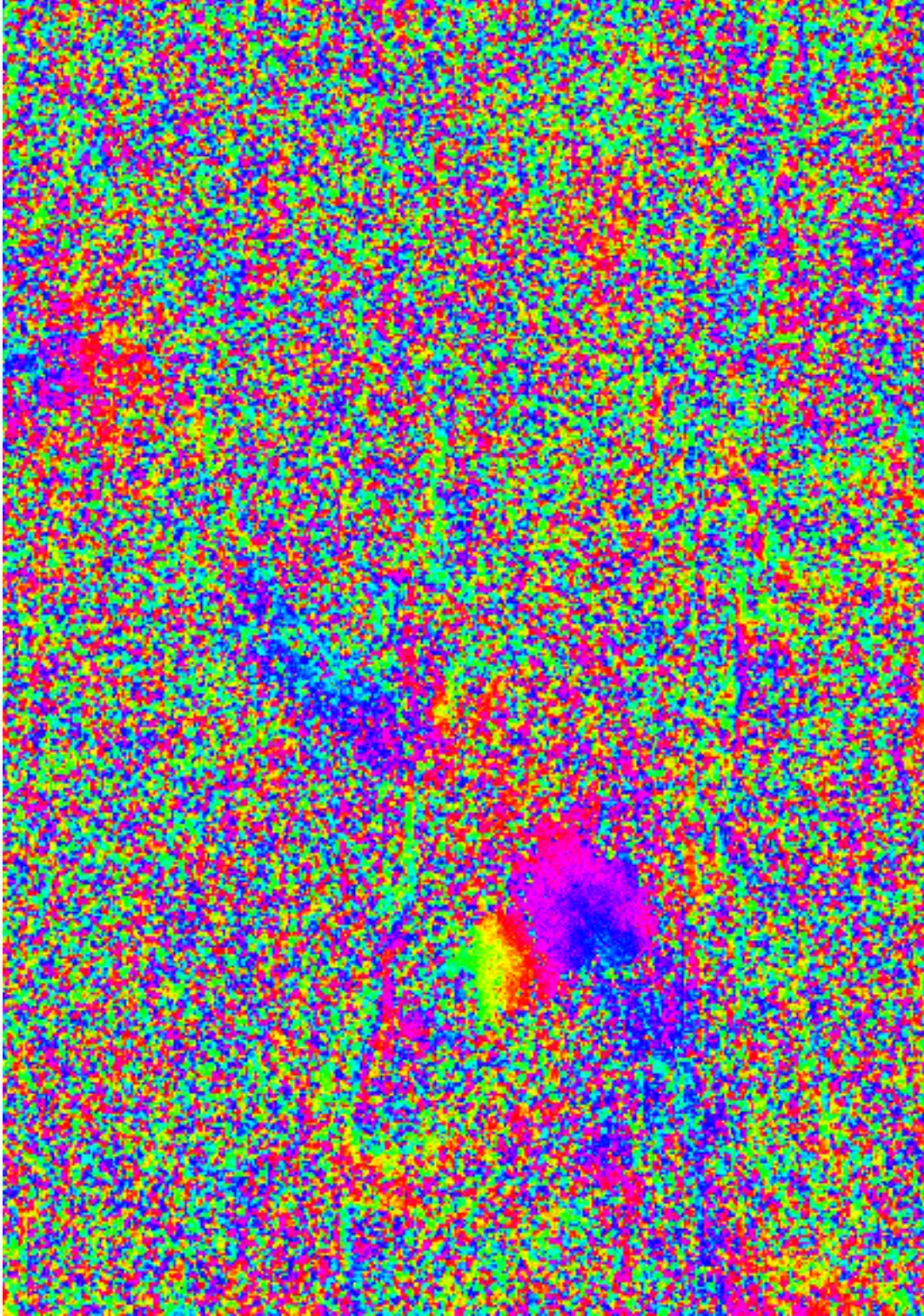


Figure 90. Larger area of interferogram from Run 25. See Appendix B text for details.

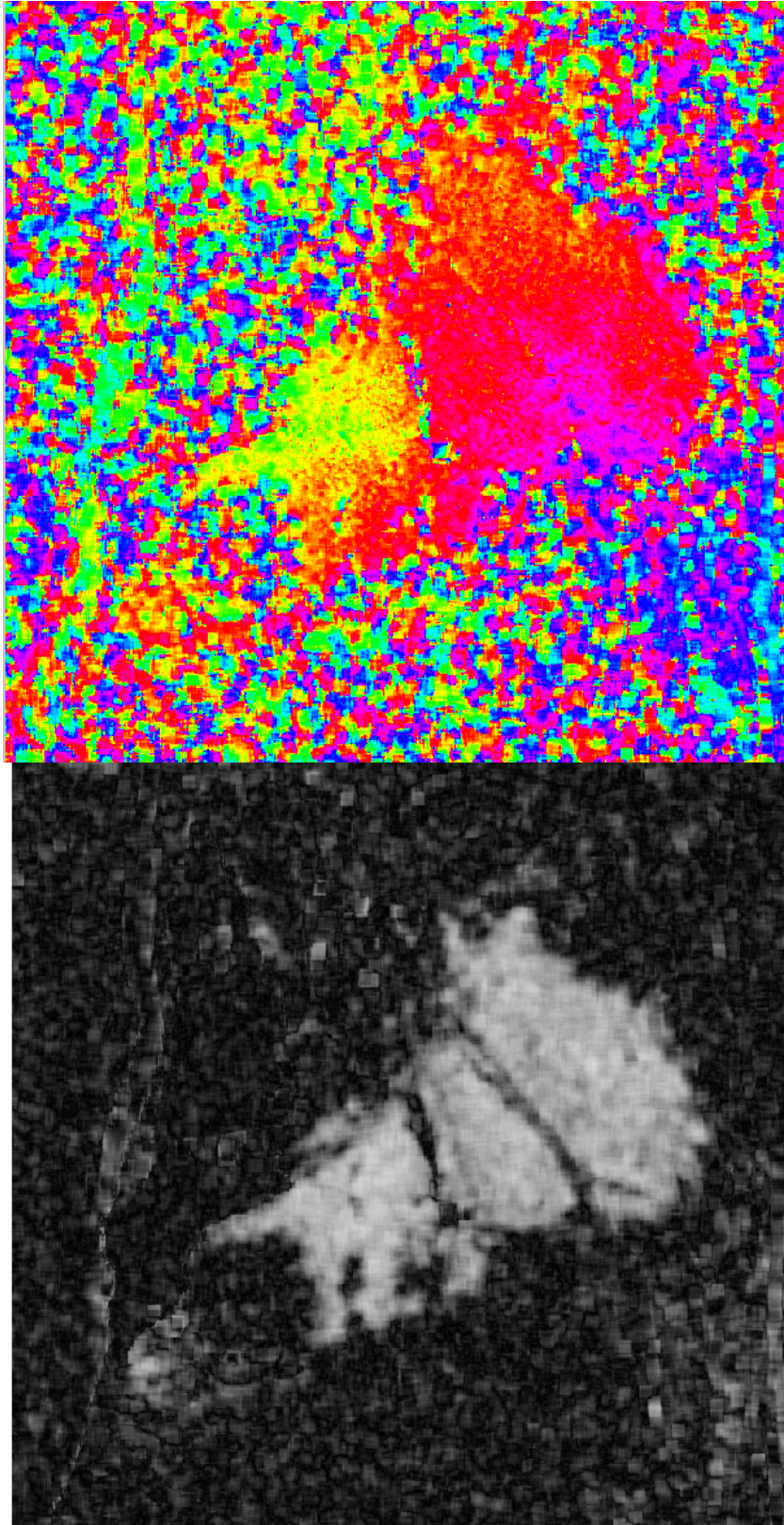


Figure 91. Interferogram (upper) and coherence (lower) images from Run 26. See Appendix B text for details.

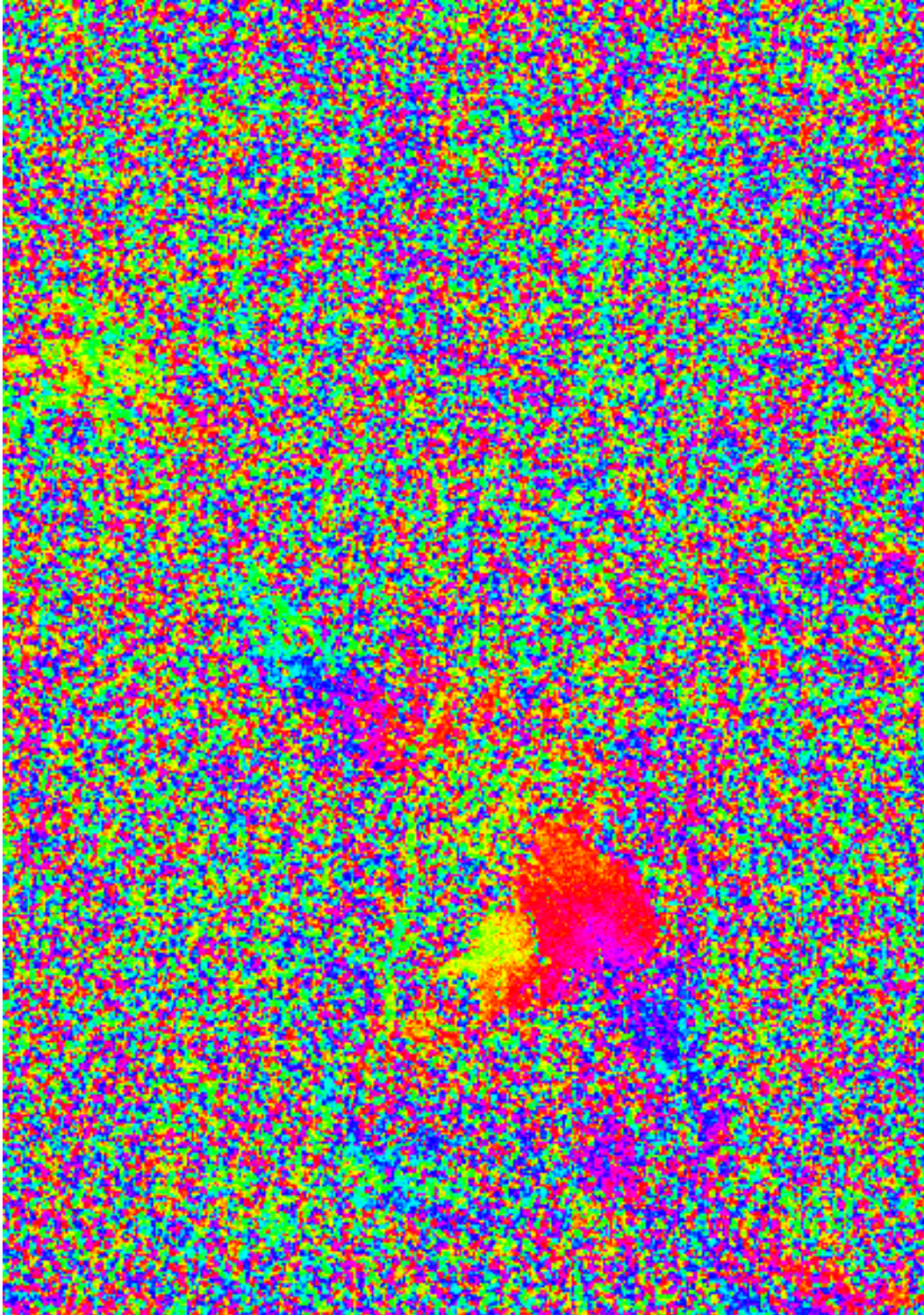


Figure 92. Larger area of interferogram from Run 26. See Appendix B text for details.

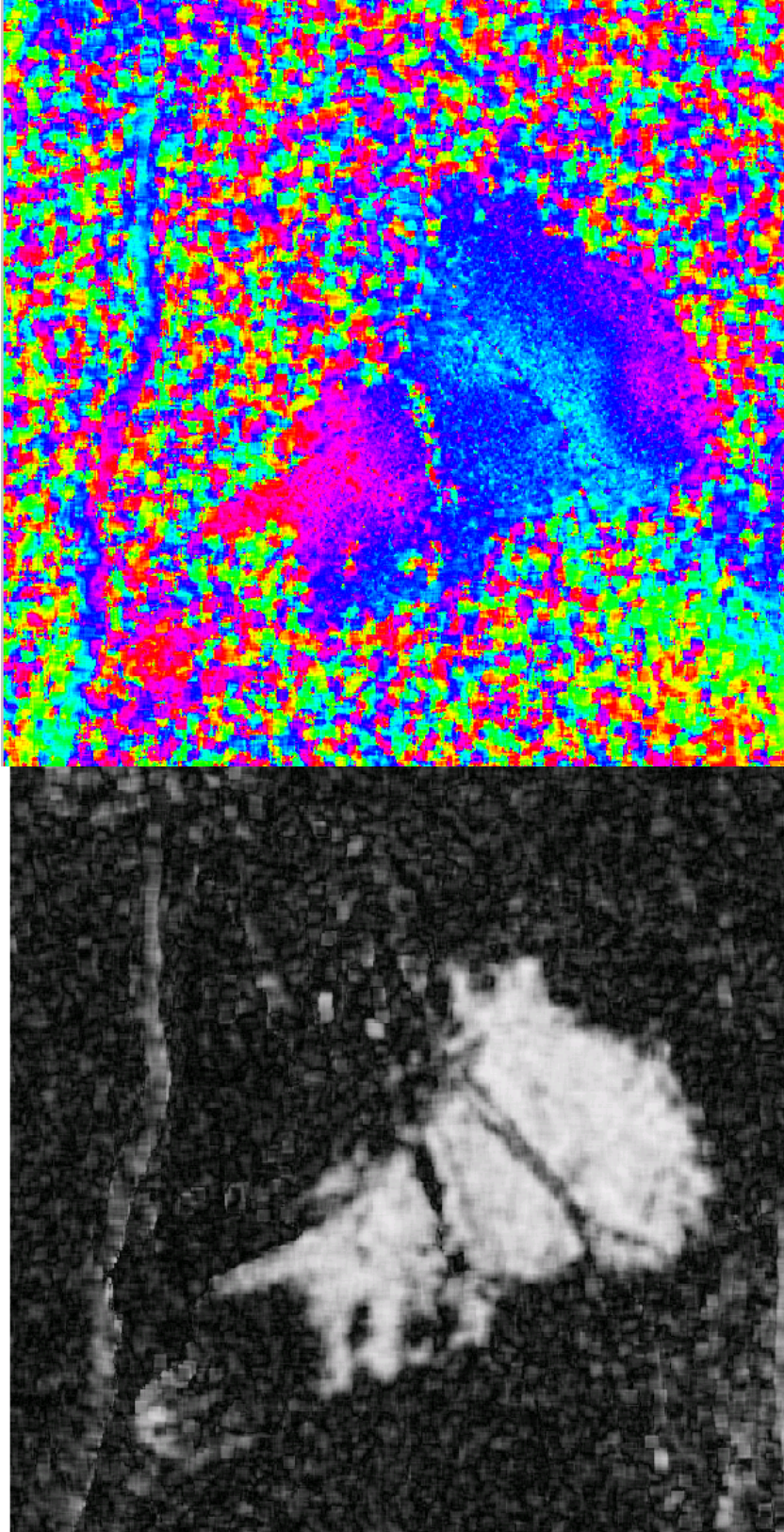


Figure 93. Interferogram (upper) and coherence (lower) images from Run 27. See Appendix B text for details.

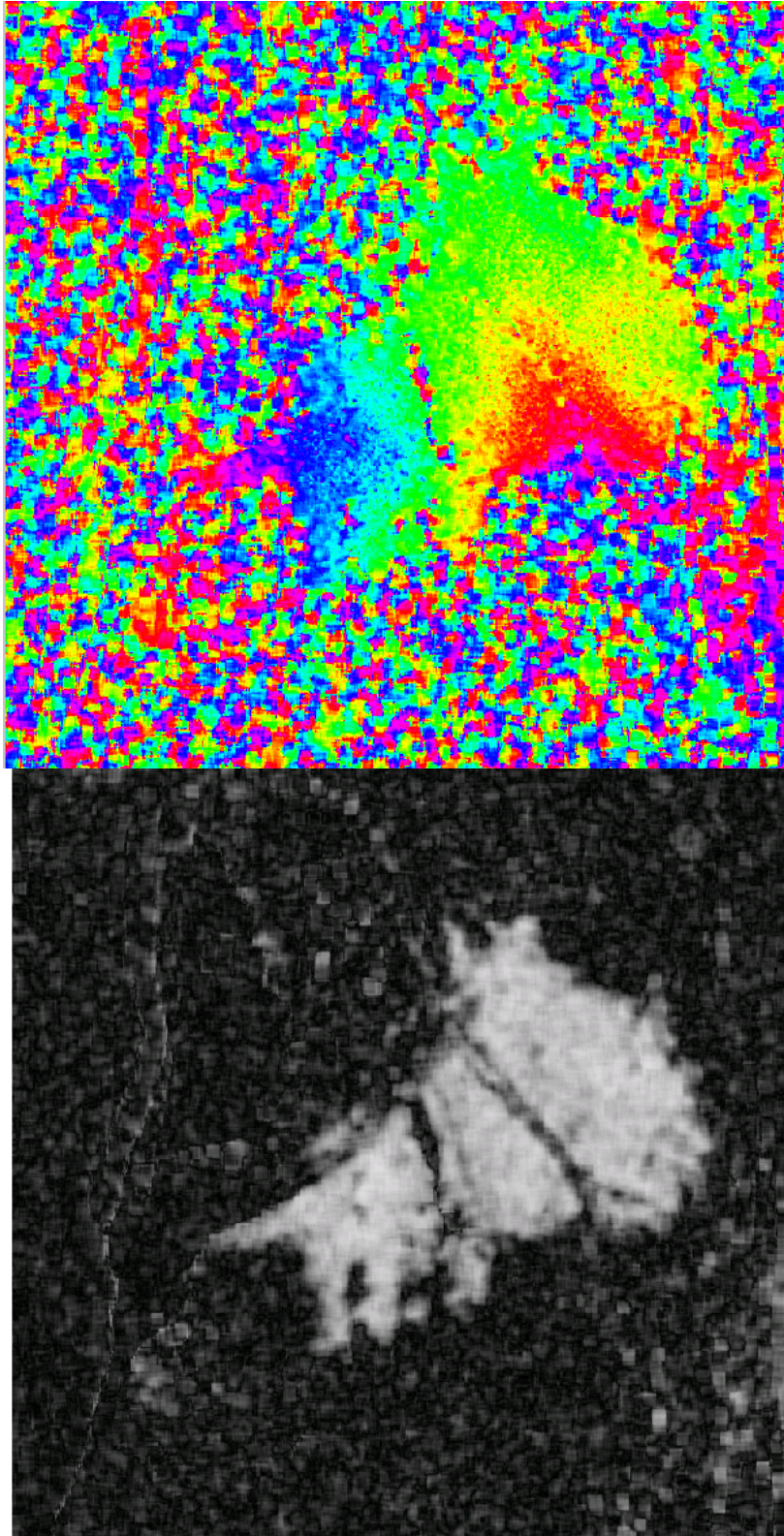


Figure 94. Interferogram (upper) and coherence (lower) images from Run 28. See Appendix B text for details.

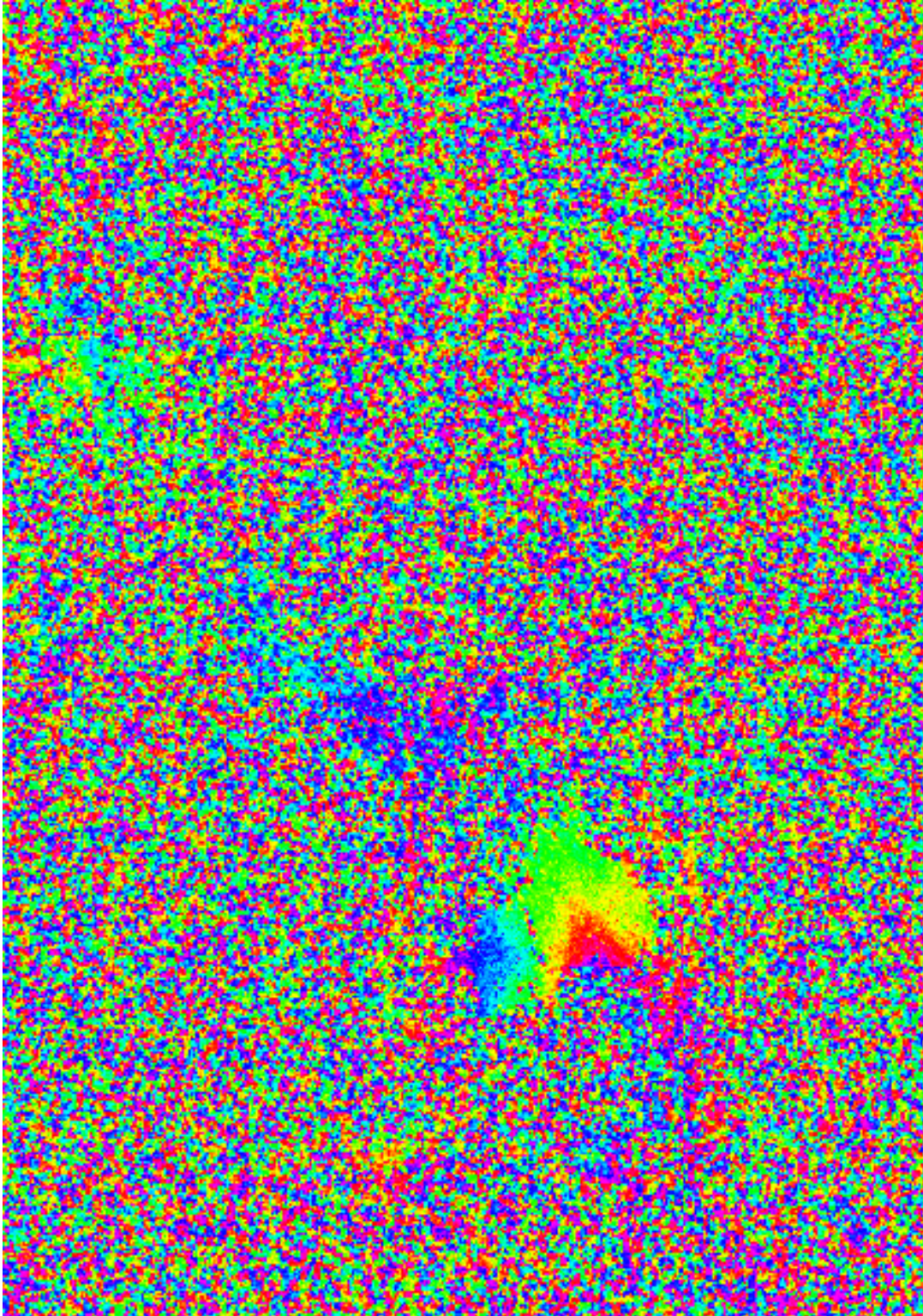


Figure 95. Larger area of Interferogram from Run 28. See Appendix B text f or details.